Evaluation of dynamic properties of geomaterials using resonant column and cyclic torsional shear tests

A thesis submitted in fulfillment of the requirements for the degree

of

Doctor of Philosophy

by **Sakshi Rohilla (2018CEZ0007)**



Department of Civil Engineering
Indian Institute of Technology Ropar
May 2024

Sakshi Rohilla: Evaluation of dynamic properties of geomaterials using

resonant column and cyclic torsional shear tests
© 2024 Indian Institute of Technology Ropar
All rights reserved.

This thesis is dedicated to *My beloved grandfather.*

Certificate

This is to certify that the thesis entitled "Evaluation of dynamic properties of

geomaterials using resonant column and cyclic torsional shear tests" submitted by

Ms. Sakshi Rohilla (2018CEZ0007) for the award of the degree of Doctor of

Philosophy to Indian Institute of Technology Ropar is a record of bonafide research

work carried out under my guidance and supervision. To the best of my knowledge

and belief, the work presented in this thesis is original and has not been submitted,

either in part or full, for the award of any other degree, diploma, fellowship,

associateship or similar title of any university or institution. In my opinion, the thesis

has reached the standard fulfilling the requirements of the regulations relating to the

degree.

Dr. Resmi Sebastian

Assistant Professor

Department of Civil Engineering

Indian Institute of Technology Ropar

Rupnagar, Punjab- 140001, India

Date: 28/05/2024

i

Declaration of Originality

I hereby declare that the work being presented in the thesis entitled "Evaluation of dynamic properties of geomaterials using resonant column and cyclic torsional shear tests" has been solely authored by me. It presents the result of my independent investigation/research conducted during the period from January 2019 to May 2024 under the supervision of Dr. Resmi Sebastian, Assistant Professor, Department of Civil Engineering, Indian Institute of Technology Ropar. To the best of my knowledge, it is an original work, both in terms of research content and narrative, and has not been submitted or accepted elsewhere, in part or in full, for the award of any degree, diploma, fellowship, associateship, or similar title of any university or institution. I also declare that any idea/data/fact/source stated in my thesis has not been fabricated/ falsified/misrepresented. All the principles of academic honesty and integrity have been followed. I fully understand that if the thesis is found to be unoriginal or fabricated, the institute reserves the right to withdraw the thesis from its archive and revoke the associated degree conferred. Additionally, the institute also reserves the right to appraise all concerned sections of society of the matter for their information and necessary action. If accepted, I hereby consent for my thesis to be available online in the institute's open-access repository, inter-library loan, and for the title and abstract to be made available to outside organizations.

Name: Sakshi Rohilla

Entry Number: 2018CEZ0007

Program: Ph.D.

Department of Civil Engineering

Indian Institute of Technology Ropar

Rupnagar, Punjab-140001, India

Date: 28/05/2024



Acknowledgements

First and foremost, I offer my deepest and most profound gratitude to Almighty God. His divine guidance, grace, and endless blessings have been the cornerstone of my strength and perseverance throughout this PhD journey. Without His mercy and wisdom, this accomplishment would not have been possible.

The journey of completing this PhD has been a profound and transformative experience, one that I could not have navigated alone. My deepest gratitude goes to those who have walked alongside me, offering wisdom, support, and encouragement.

First and foremost, I extend my heartfelt thanks to my PhD supervisor, Dr. Resmi Sebastian. Her invaluable guidance, insightful feedback, and unwavering belief in my potential have been the pillars of this work. Her patience and dedication have inspired me to persevere through the most challenging moments of this journey.

I am profoundly grateful to the esteemed faculty of my department, whose mentorship and support have been instrumental in shaping my academic path. Dr Deepak Kashyap, who served as Chairperson at the time of my admission, has been a beacon of wisdom and integrity, deeply influencing my approach to both research and life. Dr Naveen James, our previous Head of Department, along with Dr Putul Halder, Dr Raheena M., Dr Rahul T.M., Dr Reet Kamal Tiwari, Dr Sagar Rohidas Chavan, our current HOD, Dr. Sayantan Ganguly, and Dr. Aaditya Bhamidipati have each played a crucial role in my development as a researcher, offering guidance, encouragement, and support.

Beyond the confines of my department, I have been fortunate to receive mentorship from extraordinary individuals. Prof. S.K. Das from the Mechanical Engineering Department, former Director of IIT Ropar, has profoundly impacted my academic perspective, teaching me to view challenges as opportunities for growth. I also sincerely thank Dr. Jitendra Prasad and Dr. S.S. Padhee, whose insights and encouragement have enriched my research.

The support and camaraderie of my close friends and colleagues have been a constant source of strength and joy throughout this journey. Dr Niharika Bhootna, Dr Aditi Jain, Mr Sudhendhu Nath Tiwari, Mr Hrishikesh Paul, Mr Subal Beura, and Mr Rahul

Rohilla have been more than just friends; they have been my confidants and allies. Their unwavering support lifted me up in times of doubt. Their presence has been a cherished blessing, making this journey as memorable as it has been rewarding.

Outside the academic sphere, I hold dear the friendships of Mrs Mansi Panjeta, Mrs Shivani Garg, Mrs Shivani Shingari, Mrs Anita Rohilla, Mr Sanoop Suresh Kumar, Mr Kapil, Mr Rajesh Prajapati, Mr Rahul Goswami. These individuals have enriched my life with their warmth, understanding, and steadfast companionship, offering a sanctuary of support beyond the academic rigour.

I am equally indebted to the dedicated office staff, particularly Mr. Ashish and Mrs. Sakshi Kapoor, whose efficiency and willingness to assist have made my journey smoother. I extend my appreciation to the lab staff, especially Mr Arpit Gupta, whose genuine help has been invaluable, and to Mr Vipin Kumar, Mr Ashish Maurya, and Mr Surinder for their contributions.

The friendships I have forged within my department have been a source of great comfort and support. Ms Hafsoah Ahmad, with her boundless positivity and caring nature, has been a constant source of encouragement. My juniors and friends, Mr Kallol Saha, Mr Shubham Sharma, and Ms Bhavitha K., have not only been colleagues but true companions, sharing in the highs and lows of this journey. I am also grateful to Mr Shubham Jain, Mr Amit Kumar, Mrs Manisha Das, Mr Sachchidanand Kushwaha, Dr Peerzada Zafar, Mr Safdar Amini, Mr Saurav Saikia, Mr Onkar Mishra, Mrs Bhawna Thakur, and Mrs Hafsa Nazir for their friendship and support.

My labmates have been an integral part of my research journey. Dr Ankit Tyagi, Dr Veena U., Mr Manoj Kannan, Mr Sachchidanand Kushwaha, Mr Niraj Sahare, Mr Mrityunjay Jaiswal, Mrs Gayathri Prasad, Mr Kallol Saha, and Mr Mani Shankar have been a source of invaluable collaboration, stimulating discussions, and a sense of camaraderie that has greatly enriched my research experience.

Words cannot adequately express the gratitude I feel towards my family. My beloved grandfather, the Late Mr Jai Bhagwan Rohilla, remains a guiding light in my life, his memory a source of inspiration. My father, Mr Narinder Rohilla, and my mother, Mrs Rajdulari Rohilla, have been my unwavering pillars of strength, offering unconditional love and support. My brother, Mr Ramandeep Rohilla, my sister-in-law, Mrs Bhavna

Rohilla, and my nephew, Mr Meetansh Rohilla, have been a source of boundless joy and encouragement, their love sustaining me through every challenge.

I would also like to sincerely thank Mr. Naresh Ji and Mr. Jitender Ji from Aimil Consulting Company for their technical expertise and assistance, particularly concerning the Resonant Column Apparatus, which has been an indispensable tool in my research.

Finally, I cannot conclude without acknowledging my steadfast companion throughout this research journey—the Resonant Column Apparatus. This apparatus has been more than just a tool; it has been a trusted partner, surviving floods and delivering critical insights with unwavering reliability.

To all who have guided, supported, and believed in me, I offer my deepest and most heartfelt thanks. Your contributions have been invaluable, and I am forever grateful for the role each of you has played in this journey.



Lay Summary

When dynamic forces act on soils and rocks, they create vibrations that can impact buildings and other structures. By studying how these materials behave under such conditions, we can better predict and mitigate the potential damage from natural disasters and human activities. This research is particularly relevant for geotechnical engineering, which involves designing foundations, tunnels, and other structures that interact with the ground.

The primary aim is to investigate how various factors like strain amplitude (the extent of deformation), confining pressure (pressure from surroundings), and loading frequency (rate of applied force) influence the dynamic properties of soils and rocks. Additionally, the study explores the potential of using natural rubber latex (NRL) as a material to enhance the damping properties of rocks, thereby improving their ability to absorb energy.

To achieve these goals, the research uses two main testing methods:

- 1. Resonant Column (RC) Testing: This method involves applying torsional vibrations to cylindrical samples to measure their shear modulus (stiffness) and damping ratio (energy dissipation).
- 2. Cyclic Torsional Shear (CTS) Testing: This technique applies cyclic shear stresses to samples to evaluate their dynamic response under different loading frequencies. Materials used in the study include gypsum plaster to simulate rocks and dry sand to represent soil. The impact of NRL, derived from rubber trees, is also tested by grouting it into the rock joints to see how it changes their dynamic behaviour.

The key findings of the thesis are as follows:

- 1. Soil Behavior: Increasing the strain amplitude generally decreases the shear modulus and increases the damping ratio. Higher confining pressure tends to increase shear modulus and reduce the damping ratio.
- 2. Rock Behavior: For intact rocks, higher strain levels reduce shear modulus and increase the damping ratio. Higher loading rates lead to a more dynamic response with increased shear modulus and reduced damping ratio.
- 3. Jointed Rocks: The presence of more joints reduces shear modulus and increases the damping ratio. Confining pressure and loading frequency significantly influence these properties.

4. NRL Impact: Introducing NRL into rock joints decreases shear modulus but significantly increases the damping ratio, indicating better energy absorption. The effectiveness of NRL is particularly notable under varying joint spacing and confining pressures.

This research provides valuable insights for engineers designing structures in seismic regions or areas with heavy machinery. The findings suggest that incorporating materials like NRL in rock joints could enhance the stability and safety of these structures by improving their ability to dissipate energy. Future studies can build on these results to optimize the use of NRL in various geological settings. By understanding the dynamic properties of geomaterials under different conditions, we can develop better predictive models and design strategies to ensure the resilience and durability of engineering projects.

Abstract

Geomaterials, such as soil and rock, form the foundation of many structures. Understanding how they respond to dynamic forces is essential for designing safe and resilient buildings, roads, and other infrastructure. This research is particularly relevant for regions prone to seismic activity and areas with significant human-made vibrations. In this thesis, the dynamic properties of geomaterials, specifically soils, and rocks, under varying dynamic loading conditions using Resonant Column and Torsional Shear (RCTS) equipment, have been investigated. The study encompasses the dynamic properties of sands and rocks, examining the impact of variables such as strain amplitudes, confining pressures, and loading frequencies. A critical aspect of the study is the evaluation of natural rubber latex (NRL) as a damping material in rock joints, which offers potential benefits in enhancing stability and energy dissipation in geotechnical applications.

The deformational behaviour of sands indicates that increased strain amplitude decreases shear modulus while increasing damping ratio and higher confining pressures result in a higher shear modulus and lower damping ratio. The study also shows that higher relative densities lead to an increased shear modulus and decreased damping ratio. In dynamic response tests of intact rock, higher strain levels reduce shear modulus and increase the damping ratio. Loading rates also play a significant role, with higher rates reducing shear strain but increasing shear modulus and decreasing damping ratio.

The investigation of jointed rocks reveals that the number of joints significantly affects their dynamic properties. More joints lead to a lower shear modulus and higher damping ratio. Additionally, the study demonstrates that increasing the loading frequency and confining pressure generally results in a higher shear modulus and lower damping ratio. Surface roughness and joint orientation also influence these properties, with higher roughness and joint orientation increasing shear modulus and decreasing damping ratio.

The study employs advanced methodologies such as photogrammetry for estimating joint roughness coefficients (JRC), which proves to be a cost-effective and accurate alternative to traditional methods. Regression analyses using models like the modified

hyperbolic model and Ramberg-Osgood model are utilized to fit experimental data and predict dynamic responses under various conditions.

The comprehensive experimental and analytical approach provides valuable insights into the dynamic behaviour of geomaterials, which is essential for designing and assessing the safety and stability of geotechnical structures subjected to dynamic loads. The findings emphasize the significance of material-specific properties and testing conditions in predicting and enhancing the performance of geomaterials in engineering applications.

The research concludes that NRL-grouted joints exhibit superior energy dissipation and stability, making them beneficial for various geological settings. Future research directions include optimizing the use of NRL in different contexts and further refining predictive models for dynamic behaviour based on the gathered experimental data.

This study contributes to the broader understanding of the dynamic properties of geomaterials, aiding in the development of more reliable and resilient geotechnical engineering solutions.

Keywords: Geomaterials, Resonant column testing, cyclic torsional shear testing, Shear modulus, Damping ratio, Natural rubber latex, Regression analysis

Table of Contents

Certificate	i
Declaration	iii
Lay Summary	ix
Abstract	xi
List of figures	xviii
List of tables	xxiv
Chapter 1	1
Introduction	1
1.1 General Background	1
1.2 Wave propagation through geomaterials	2
1.2.1 Wave propagation through soils	3
1.2.2 Wave propagation through rocks	3
1.3 Research challenges	6
1.4 Scope and objectives of the study	6
1.5 Organization of the Thesis	8
Chapter 2	11
Literature Review	11
2.1 Introduction	11
2.2 Dynamic properties of geomaterials	11
2.3 Factors affecting the dynamic response of geomaterials	16
2.3.1 Cyclic shear strain	17
2.3.2 Stress/Strain rate	18
2.3.3 Duration of excitation	19
2.3.4 Moisture content	19
2.3.5 Confinement	21
2.3.6 Frequency	21
2.4 A review of previous research on rocks	23
2.4.1 Empirical models for rock joint shear strength	23
2.4.2 Seismic anisotropy and wave propagation in fractured rocks	23
2.4.3 Joint surface roughness and acoustic properties	24
2.4.4 Grouting, weathering, and jointed rock masses	27
2.4.5 Advanced modeling and empirical relations	28
2.5 Non-linear stress-strain models	28

2.5.1 Hardin-Drnevich	29
2.5.2 Seed-Idriss	30
2.5.3 Ramberg-Osgood	30
2.6 Summary	31
Chapter 3	33
Materials and Methodology	33
3.1 Introduction	33
3.2 General background	33
3.2.1 Resonant column testing in torsion	35
3.2.2 Determination of shear modulus (G) from RC testing	38
3.2.3 Determination of shear strain (γ) from RC testing	39
3.2.4 Determination of damping ratio (D) from resonant column testing	39
3.3 Cyclic torsional shear testing	41
3.3.1 Determination of shear modulus and damping ratio from cyclic torsion	nal
shear testing	43
3.3.2 Determination of shear strain from cyclic torsional shear testing	45
3.4 Suitability of using RCA in rock mechanics	48
3.5 Materials used for the testing	49
3.5.1 Sutlej River sand	49
3.5.2 Gypsum plaster specimen	53
3.6 Summary	56
Chapter 4	57
Dynamic Characterization of Sutlej River Sand: Insights from Resonant	
Column and Cyclic Torsional Shear Tests	
4.1 Introduction	
4.2 Test plan for RC testing	
4.2.1 Results of RC testing	
4.2.2 Regression analysis on results of RC testing	
4.3 Test plan for CTS testing	
4.3.1 Results of CTS testing	
4.3.2 Regression analysis on results of CTS testing	
4.4 Normalized shear modulus (G/G _{max})	
4.5 Damping Ratio (D)	71
4.6 Summary	74
Chapter 5	75

Dynamic behaviour of intact rock: Insights from resonant column app	aratus75
5.1 Introduction	75
5.2 Resonant column testing	76
5.3 Cyclic torsional shear testing	76
5.3.1 Influence of loading waveform	77
5.3.2 Impact of frequency on the loading rate	78
5.3.3 Impact of the amplitude of torque on the loading rate	79
5.4 Experimental observations and results	81
5.4.1 Influence of loading rate on dynamic properties	83
5.4.2 Curve fitting models	87
5.4.3 Normalized modulus reduction and material damping ratio	89
5.5 Summary	91
Chapter 6	93
Quantification and Analysis of Rock Joint Roughness Using Advanced Techniques	_
6.1 Introduction	
6.2 Background	93
6.2.1 Determination of JRC using visual interpretation	
6.2.2. Determination of JRC using the statistical approach	
6.2.3 Fractal dimension approach	98
6.3 Surface profiling techniques	99
6.3.1 Surface profiling using a profilometer	99
6.3.2 Surface profiling using a 3D scanner	99
6.3.3 Surface profiling using smartphone photogrammetry	100
6.4 Comparison of Photogrammetry technique and other methods	103
6.5 Summary	108
Chapter 7	111
Dynamic Response of Jointed Rock Masses: Effects of Joint Spacing, OPTESSURE, and Loading Frequency	_
7.1 Introduction	
7.2 Test Plan	111
7.3 Results	
7.3.1 Resonant Column Testing	
7.3.2 Cyclic torsional shear testing	
7.4 Analysis and Discussions	

7.4.1 Effect of confining pressure	116
7.4.2 Effect of loading frequency	118
7.4.3 Ramberg-Osgood material model	119
7.5 Summary	122
Chapter 8	123
Dynamic Properties of Jointed Rocks: Influence of Loading C	
Joint Characteristics	
8.1 Introduction	
8.2 Specimen preparation	123
8.3 Testing plan	127
8.4 Results	128
8.4.1 Effect of loading characteristics	128
8.4.2 Effect of joint characteristics	132
8.5 Discussions	135
8.6 Summary	137
Chapter 9	139
Enhancing Energy Dissipation in Jointed Rocks: The Role of	
Latex (NRL) as an Energy-Absorbing Layer	
9.2 Materials	
9.3 Test Plan	
9.4 Results from RC testing	
9.5 Results from cyclic torsional shear testing	
9.6 Analysis and Discussions	
9.6.1 Effect of confining pressure	
9.6.2 Effect of loading frequency	
9.6.3 Curve fitting models	
9.6.4 Regression analysis	158
9.7 Summary	160
Chapter 10	163
Conclusions	163
10.1 Introduction	163
10.2 Conclusions	
	164

10.2.2 Determination of the dynamic response of intact rock under v	
amplitudes and loading frequencies	164
10.2.3 Investigation of the surface roughness of jointed rocks using 3 processing techniques.	_
10.2.4 Determination of dynamic properties of jointed rocks under v and loading characteristics	
10.2.5 Exploration of the dynamic properties of jointed rocks when i natural rubber latex (NRL)	
10.3 Scope for future work	167
Appendix A	169
A.1 Calibration of RCA	169
A.2 Need for corrections to be applied	172
A.3 Corrections for Resonant Frequencies	173
References	177
List of Publications	197

List of figures

Figure 2. 1 Shear strains mobilized in in-situ and common laboratory techniques
(Ishihara, 1996)
Figure 2.2 Schematic view of Fixed-free resonant column apparatus
Figure 2. 3 Frequency dependence of damping ratio within soil mass (Shibuya et al.,
1995)
Figure 3. 1 Combined resonant column and torsional shear apparatus34
Figure 3. 2 Schematic view of various components of RCA
Figure 3. 3 A typical frequency response curve for torsional vibration38
Figure 3. 4 A typical graph of free vibration decay of vibration in torsion40
Figure 3. 5 Schematic view of the proximitor arrangement of resonant column
apparatus
Figure 3. 6 Schematic view of the proximitor set-up for twist measurement44
Figure 3. 7 Typical stress-strain curve obtained from the cyclic torsional shear
testing of gypsum plaster
Figure 3. 8 Simplified illustration of twist applied at the topmost end of the testing
sample
Figure 3. 9 Representation of schematic top view of the driving arrangement47
Figure 3. 10 Representation of schematic top view of the twist and shear produced in
the specimen
Figure 3. 11 SEM images of Sutlej River sand samples
Figure 3. 11 SEM images of Sutlej River sand samples
Figure 3. 12 Particle size distribution curve for Sutlej River sand51
Figure 3. 12 Particle size distribution curve for Sutlej River sand
Figure 3. 12 Particle size distribution curve for Sutlej River sand51Figure 3. 13 Calibration plot of relative density with the height of fall53Figure 3. 14 A typical view of hardened gypsum plaster specimen55
Figure 3. 12 Particle size distribution curve for Sutlej River sand51Figure 3. 13 Calibration plot of relative density with the height of fall53Figure 3. 14 A typical view of hardened gypsum plaster specimen55
Figure 3. 12 Particle size distribution curve for Sutlej River sand 51 Figure 3. 13 Calibration plot of relative density with the height of fall 53 Figure 3. 14 A typical view of hardened gypsum plaster specimen 55 Figure 3. 15 Stress-strain curve of intact gypsum plaster in compression 55
Figure 3. 12 Particle size distribution curve for Sutlej River sand
Figure 3. 12 Particle size distribution curve for Sutlej River sand
Figure 3. 12 Particle size distribution curve for Sutlej River sand

Figure 4. 6 Normalized shear modulus and damping ratio vs. shear strain73
Figure 4. 7 Comparison of Normalised shear modulus reduction and damping ratio
curves with previous studies
Figure 5. 1 Variation of shear modulus and damping ratio of intact gypsum plaster
using RC testing
Figure 5. 2 Shear stress vs. time for different waveforms
Figure 5. 3 Impact of loading frequency on the rate of loading of different loading
waveforms
Figure 5. 4 Influence of amplitude of torque applied on the loading rate of different
waveforms80
Figure 5. 5 Variation of loading rate vs. time at the varying amplitude of torque
applied81
Figure 5. 6 Variation of shear strain under the influence of loading rate for ramp
waveform82
Figure 5. 7 Variation of shear strain under the influence of loading rate for a
sinusoidal waveform82
Figure 5. 8 Shear modulus versus loading rate for ramp and sinusoidal waveform 84
Figure 5. 9 Damping ratio versus loading rate for ramp and sinusoidal waveform 84
Figure 5. 10 Shear modulus versus shear strain at different torque amplitudes and
loading frequency for a sinusoidal waveform
Figure 5. 11 Shear modulus versus shear strain at different torque amplitudes and
loading frequency for ramp waveform
Figure 5. 12 Damping ratio versus shear strain at the different magnitude of torque
and loading frequency for a sinusoidal waveform
Figure 5. 13 Damping ratio versus shear strain at the different magnitude of torque
and loading frequency for ramp waveform
Figure 5. 14 Normalised modulus reduction curve and obtained fitted curves90
Figure 5. 15 Damping ratio vs. shear strain curve along with fitted curves91
Figure 6. 1 Determination of JRC for different lengths of specimens
Figure 6. 2 An example of profiling of a jointed rough surface using a profilometer
99

Figure 6. 3 A typical representation of an image obtained from 3D scanning	.100
Figure 6. 4 The workflow of smartphone photogrammetry	.101
Figure 6. 5 Typical view of the 3D surface profile obtained from smartphone	
captured images, (a) Dense 3D reconstruction of 2D images obtained from	
VisualSFM (b) Point cloud of the 3D surface obtained from CloudCompare 2.9.1	
stereo.	.103
Figure 6. 6 View of measured dimensions of the 3D dense reconstructed surface	
using CloudCompare 2.9.1 stereo	.103
Figure 6. 7 A typical description of 12 scan lines over the top of the jointed surface	ce.
	.104
Figure 6. 8 Pictorial view of replicated gypsum specimen with an indent at the	
surface, reference line, and reference point on (a) original surface, (b) surface pro	ofile
from photogrammetry technique, and (c) surface profile from 3D scanning	.105
Figure 6. 9 An illustration of the surface profile of a scan line of three various	
jointed rough surfaces obtained from profilometer, 3D scanning, and	
photogrammetry technique	.107
Figure 7. 1 Typical view of plain jointed Gypsum plaster specimens	.112
Figure 7. 2 Variation of shear modulus with the shear strain of plain jointed	
specimens under resonant column testing	.113
Figure 7. 3 Variation of damping ratio with the shear strain of plain jointed	
specimens under resonant column testing	.114
Figure 7. 4 Variation of shear modulus with the shear strain of plain jointed	
specimens under cyclic torsional shear testing	.115
Figure 7. 5 Variation of damping ratio with the shear strain of plain jointed	
specimens under cyclic torsional testing.	.115
Figure 7. 6 Variation of shear modulus with confining pressure for plain jointed	
specimens	.117
Figure 7. 7 Variation of damping ratio with confining pressure for plain jointed	
specimens	.117
Figure 7. 8 Variation of shear modulus with the frequency of loading for plain	
jointed specimens	.118

Figure 7. 9 Variation of damping ratio with the frequency of loading for plain
jointed specimens
Figure 7. 10 Normalised modulus reduction and damping ratio curve of the plain
jointed specimen under RC testing
Figure 7. 11 Normalised modulus reduction and damping ratio curve of the plain
jointed specimen under CTS testing
Figure 8. 1 A visual representation of surface profiles designed for different Joint Roughness Coefficients, including (a) JRC=6-8, (b) JRC=12-14, and (c) JRC=18-20
Figure 8. 2 A typical representation of 3D-printed moulds featuring diverse surface
profiles and different orientation angles, including (a) a frontal perspective, (b) a side
view, and (c) a standard view of moulds alongside their mirrored counterparts125
Figure 8. 3 Flowchart illustrating the process for preparing 3D moulds
Figure 8. 4 A visual representation of the gypsum plaster specimen prepared using a
3-D mould
Figure 8. 5 The flow chart of the testing program of the study
Figure 8. 6 Modulus reduction and damping ratio curve in jointed rock specimens
with varying Joint Roughness Coefficient (JRC) of (a) JRC = 6-8, (b) JRC = 12-14,
and (c) JRC = 18-20
Figure 8. 7 Changes in shear modulus and damping ratio with varying shear strain
under different confining pressures for joint orientations of (a) θ =30°, (b) θ =45°, and
(c) $\theta = 60^{\circ}$
Figure 8. 8 Variation in shear modulus and damping ratio examined across different
frequencies of loading for joint orientations of (a) θ =30°, (b) θ =45°, and (c) θ =60°.
Figure 8. 9 Variation in shear modulus and damping ratio across varying joint
roughness coefficients for joint orientations of (a) $\theta = 30^{\circ}$, (b) $\theta = 45^{\circ}$, and (c) $\theta = 60^{\circ}$.
Figure 8. 10 Changes in shear modulus and damping ratio examined across different
joint orientations at Joint roughness coefficient of (a) JRC= 6-8, (b) JRC=12-14, and
(c) JRC=18-20.

Figure 9. 1 Tensile test of NRL with UTM
Figure 9. 2 Tensile stress-strain curve of NRL
Figure 9. 3 Variation of Poisson's ratio with strain
Figure 9. 4 Typical view of dry and wet NRL specimen in briquette mould for
ductility test
Figure 9. 5 Variation of shear modulus and damping ratio of NRL at different strain
levels using RC testing
Figure 9. 6 Typical view of plain jointed and NRL grouted jointed Gypsum plaster
specimens
Figure 9. 7 Variation of shear modulus with strain level for various thicknesses of
NRL-grouted layer
Figure 9. 8 Variation of damping ratio with strain level for various thicknesses of
NRL-grouted layer
Figure 9. 9 Comparison of equivalent shear wave velocity obtained from theoretical
and experimental results
Figure 9. 10 Comparison of equivalent damping ratio obtained from theoretical and
experimental analyses
Figure 9. 11 Variation of shear modulus with the shear strain of NRL grouted jointed
specimens under resonant column testing
Figure 9. 12 Variation of damping ratio with the shear strain of NRL grouted
specimens under resonant column testing
Figure 9. 13 Shear stress- shear strain curves obtained from CTS testing at (a)
varying loading frequencies keeping the amplitude of shear strain constant, (b)
varying amplitudes of shear strain keeping loading frequency constant150
Figure 9. 14 Variation of shear modulus with the shear strain of NRL grouted jointed
specimens under cyclic torsional shear testing
Figure 9. 15 Variation of damping ratio with shear strain of NRL grouted specimens
under cyclic torsional testing
Figure 9. 16 Variation of shear modulus with confining pressure for NRL grouted
jointed specimens
Figure 9. 17 Variation of damping ratio with confining pressure for NRL grouted
jointed specimens

Figure 9. 18 Variation of shear modulus with the frequency of loading for NRL
grouted jointed specimens
Figure 9. 19 Variation of damping ratio with the frequency of loading for NRL
grouted jointed specimens
Figure 9. 20 Normalised modulus reduction and damping ratio curve of NRL
grouted jointed specimen under RC testing
Figure 9. 21 Normalised modulus reduction and damping ratio curve of NRL
grouted jointed specimen under CTS testing
Figure A. 1 Basic configuration of calibration bar and additional mass in fixed-free
torsional RCA
Figure A. 2 Calibration bars and additional weights used to obtain corrections in
torsional vibrations
Figure A. 3 Calibration plot used to calculate the mass polar moment of inertia of the
driving plate using the aluminium calibration bars
Figure A. 4 Calibration plot used to calculate the mass polar moment of inertia of the
driving plate using steel calibration bars
Figure A. 5 Correction factors obtained in torsional vibrations for aluminium
calibration bars
Figure A. 6 Correction factors obtained in torsional vibrations for steel calibration
bars

List of tables

Table 2. 1 Soil behavior and shear strain level (Ishihara, 1996)	18
Table 2. 2 General Trends in Attenuation (After Badali and Santamarina, 1992)	22
Table 3. 1 Index properties of Sutlej Sand	50
Table 3. 2 EDX analysis of Sutlej River sand	52
Table 3. 3 Engineering properties of the gypsum plaster	56
Table 4. 1 Experimental arrangement for RC testing	
Table 4.2 a Maximum Shear Modulus (MPa) in different test conditions at a strain	
level of 0.001% (RC)	59
Table 4.2 b Shear Modulus (MPa) in different test conditions at different strain	
levels (RC)	60
Table 4.2 c Shear wave velocity in different test conditions at different strain level	S
(RC)	60
Table 4.3 Outcomes of regression analysis on resonant column testing at varying	
strain levels	63
Table 4.4 Outcomes of regression analysis of variation of G at varying shear strain	l
amplitude (RC)	63
Table 4.5 Experimental arrangement for CTS testing	64
Table 4.6 Shear Modulus in different test conditions at different strain levels (CTS	5)
	65
Table 4. 7 Results of regression analysis for variation of G with the loading	
frequency at different strain levels	69
Table 4. 8 Results of regression analysis performed on modified hyperbolic model	70
Table 4. 9 Outcomes of regression analysis performed for damping ratio	72
Table 5. 1 Shear modulus and material damping ratio at a specific value of torque	
amplitude and frequency of loading	.85
$\textbf{Table 5. 2} \ \text{Curve fitting parameters of } G/G_{max} \ \text{for modified Hyperbolic model} \$.91
Table 5. 3 Curve fitting parameters of G/G _{max} for the Ramberg-Osgood model	.91

Table 6. 1 Standard JRC profiles provided by Barton and Choubey 1977 enhanced
through P _{max} and surface description
Table 6. 2 Review of literature of empirical equations to determine JRC using Z_2 at a
sampling interval of 0.25 mm
Table 6. 3 Review of literature of empirical equations to determine JRC using D 98
Table 6. 4 Description of camera specifications used in capturing images. 101
Table 6. 5 Summary of Z ₂ , obtained for 3D scanned and photogrammetry profiles
using Tse & Cruden, (1979)
Table 6. 6 Summary of D obtained for 3D scanned and photogrammetry profiles
using Lee et al., 1990
Table 6. 7 Summary of the JRC observations 108
Table 7. 1 Results obtained from curve fitting performed for plain jointed specimens
under RC testing
Table 7. 2 Results obtained from curve fitting performed for plain jointed specimens
under CTS testing
Table 8. 1 Testing condition of the specimens 128
Table 8. 2 List of models examined for different variables 135
Table 8. 3 Outcomes of goodness-of-fit measures obtained from the regression
analysis
Table 8. 4 Outcomes of goodness-of-fit measures obtained from the regression
analysis of theoretical transformed relation
Table 9. 1 Basic properties of Natural Rubber Latex used in the study
Table 9. 2 Shear modulus and damping ratio of natural rubber latex and intact
gypsum plaster147
Table 9. 3 Results obtained from curve fitting performed for NRL grouted specimens
under RC testing

Table 9. 4 Results obtained from curve fitting performed for NRL grouted specime	ens
under CTS testing	157
Table 9. 5 Results of regression analysis of RC testing	159
Table 9. 6 Results of regression analysis of CTS testing	159
Table A. 1 Actual and obtained resonant frequencies in torsional vibrations for	
aluminium calibration bar	174
Table A. 2 Actual and obtained resonant frequencies in torsional vibrations for stee	el
calibration bar1	174

Chapter 1 Introduction

1.1 General Background

In geotechnical engineering, parameters such as shear and Young's moduli, alongside material damping, hold significance in the design of the substructure and superstructure against cyclic and dynamic loads. Historically, researchers have mainly focused on understanding soil behaviour during earthquakes. However, in recent years, there has been a growing interest in addressing challenges posed by low-amplitude vibrations from human activities, like vehicular traffic, machine operations, pile-driving, and blasting.

The strain amplitude plays a vital role in predicting the behaviour of geomaterials, regardless of whether the strain is static or dynamic. Hence, measuring deformational characteristics across small (0.001% to 0.1%) to large (0.1% to 10%) strain ranges has become essential in dynamic and static analyses.

Soil-structure and rock-structure systems often experience cyclic loads beyond their elastic limits, while soil-pavement systems are frequently loaded beyond elasticity. In these cases, the effects of cyclic loading become crucial in determining the deformational characteristics of soils and rocks. While previous research has explored cyclic and dynamic tests to understand this effect, most studies were conducted at relatively high strains exceeding 0.05%. However, limitations in accurately measuring hysteresis loops have hindered the exploration of behaviour in the elastic region and the transition zone between elastic and plastic behaviour.

Each external force acting on a rock-structure or soil-structure system produces a different loading pattern, resulting in a wide range of loading frequencies from very low (e.g., around 0.05 Hz for ocean storm waves) to very high (e.g., above 100 Hz for vehicular traffic and machine vibrations). Notably, laboratory and field-testing techniques have different frequency characteristics. For example, resonant column tests capture deformational characteristics at resonant frequencies (typically 20 to 350 Hz), while torsional shear tests measure stress-strain loops at lower frequencies (typically 0.1 Hz to 10 Hz). Field seismic tests, such as SASW (spectral analysis of surface waves) and cross-hole methods, can generate frequencies up to about 400 Hz.

1.2 Wave propagation through geomaterials

Wave propagation through geomaterials, such as soil and rock, is governed by complex interactions of mechanical properties and structural characteristics. These materials exhibit diverse behaviours, from elastic responses to non-linear deformations, influencing wave velocity, attenuation, and dispersion. Understanding these phenomena is crucial for geotechnical and seismic engineering, aiding in designing resilient structures and effective hazard mitigation strategies in the face of seismic events and dynamic loading. Examples of areas where seismic waves play an important role are:

- Determination of dynamic properties In cross-hole seismic tests, the wave velocity between parallel boreholes is measured and can be used to determine the excavation disturbed zone (EDZ) around a drift (Malmgren et al., 2007) or the degree of anisotropy of a rock mass (Emsley et al., 1997). Tomography is a method where the wave velocity is measured along a line between a source and receivers where the source is moved between measurements, thus creating a ray-tracing pattern. It can be used to determine the quality factor Q (Watanabe & Sassa, 1996). In laboratory tests, wave propagation through rock samples determines properties such as Young's modulus, Poisson's ratio, wave velocity, anisotropy ratio, etc. (Brown, 1981).
- Blasting This is used to excavate, break, or remove rock. A side-effect is the creation of shock waves travelling through the air and vibrations propagating through the ground. Both might annoy nearby residents and damage structures. The guidelines specify recommended levels of vibrations (SS ISO 14837-1 (2005); SS-1S0 2631-1460 (1997)).
- Earthquakes A sudden movement along a fault plane in the Earth's crust arising from releasing stored elastic strain energy. The released energy radiates as seismic waves and devastates nearby land and cities.
- Mining-induced seismicity A seismic event is a sudden release of energy that
 radiates as mechanical waves and occurs in mines when the rock deforms or fails.
 The mining-induced seismicity is expected to increase as mining progresses
 towards greater depths. The reinforcement provided in the construction is exposed

- to even larger dynamic loads and must, therefore, be able to yield and absorb the load to maintain a high level of safety (Larsson, 2004).
- Traffic-induced vibration and noise Among residential, commercial, and cultural
 areas in modern cities, multilevel roads, railways, and subways form a
 multidimensional traffic system producing noise and vibrations that annoy the
 building occupants. National and international guidelines specify recommended
 levels of noise and vibrations (e.g., ISO 2361-2 (1989)).
- These are just some examples to illustrate the diversity of applications where waves play an important role. Regardless of how and where waves appear, understanding their behaviour might provide valuable information to improve safety, applications, or regulations (to name a few). For rocks, with its heterogeneous composition, it is also essential to understand the effect of discontinuities on wave propagation.
- **1.2.1** Wave propagation through soils: The soil strata are frequently subjected to different kinds of vibrations, such as that caused by earthquakes, water waves, traffic loads, wind power plants, construction-related equipment, pile driving, and machine vibrations. The strain induced in soils due to traffic and machinery is usually of low amplitude and generally lies in a range of 0.0001% to 0.001%, whereas the vibrations induced by the earthquake motions often lie in a strain range of 0.01% to 0.1% which can even trigger up to 1% during an occurrence of severe earthquakes (Silver & Seed 1971; Iwasaki & Tatsuoka, 1977; Woods, 1978; Borden et al., 1996; Chowdhury & Dasgupta, 2008). The evaluation of dynamic soil properties, namely, shear modulus (G) and damping ratio (D) in a strain range of 0.0001% to 0.1%, are often required while performing the analysis for structures subjected to various vibrations. The shear modulus and damping of soils are influenced by various loading/vibrations and material factors such as strain amplitude, vibration/loading cycles, void ratio, confining pressure, plasticity index, gradation, and over-consolidation ratio.
- **1.2.2** Wave propagation through rocks: The effect of rock mass composition on wave propagation is scale-dependent. For small-scale samples, the rock is normally considered intact. The heterogeneity due to the mineral composition, microcracks, and pores is important at this scale. The most substantial impact on typical rock constructions, such as large-scale tunnels, comes from individual discontinuities

combined with borders between geologically (or geomechanically) distinct regions or various rock types. Due to the different behaviours, wave propagation in intact rock and rock masses is briefly reviewed in the subsequent sections. The following physical properties are said to have an impact on the propagation of elastic waves in rocks (Lama & Vutakuri, 1978):

- Rock type The wave velocity is normally higher in dense and compact rocks than
 in less dense and compact rocks. Large velocity variations can be observed for the
 same rock type, e.g., in limestone, the P-wave velocity can range from 3500 to
 6000 m/s due to texture variations.
- Texture Rocks consisting of minerals supporting high velocities also support a
 high velocity, and vice versa. For example, increased hornblende content increases
 the velocity of the rock, while increased quartz content decreases the velocity
 (Ramana & Venkatanarayana, 1973).
- Density Increased density generally increases P- and S-wave velocity, although
 the S-wave increase is lower. Small grains, few pores, and tight interlocking
 increase density, shear, and Young's modulus, thus increasing velocity.
- Porosity Pores are interstitial spaces between grains in a sedimentary rock, cavities in an igneous rock, or voids caused by solution in water. Microcracks develop when grains crack or shift concerning one another due to changes in the internal stresses. Increased porosity decreases wave velocity (Lama & Vutakuri, 1978; Ramana & Venkatanarayana, 1973; Youash, 1970).
- Anisotropy An anisotropic material has properties (physical, dynamic, and mechanical) that vary with direction (Amadei, 1996). Anisotropy in rock is caused by layering (i.e., sedimentation), the presence of regularly spaced cracks (small scale), or discontinuities (large scale). Both P- and S-wave velocities are affected by velocity anisotropy (Paterson, 1978).
- Confining stresses Increasing confining stress tends to close cracks and decrease
 the porosity of the intact rock, leading to increased contact between grains due to
 tighter interlocking. This increases Young's modulus and the velocity of both Pand S-waves. The increase is greater at low stresses and is, therefore, more
 prominent for porous and loose rocks than for compact rocks. Moreover, the wave

- velocity is higher during unloading than loading since cracks remain closed during unloading (Lama & Vutakuri, 1978).
- Water Content P-waves in rock propagate through the mineral structure and the pores. Since the P-wave velocity in water is several times higher than in air, the velocity generally increases in saturated hard rocks (Lama & Vutakuri, 1978; Paterson, 1978). The velocity in water-saturated highly porous rocks is lower than in less porous rocks since the P-wave velocity in water is lower than that of the mineral structure. The S-wave velocity is nearly insensitive to water saturation because it only propagates through the mineral structure.
- **1.2.2.1** Wave propagation through intact rock: The wave propagation in intact rock (i.e., small sample) depends on material properties such as the mineral content, the size and shape of the mineral grains, and the presence of pores and microcracks. These properties influence the Young's modulus and density of the rock, thereby affecting the propagation of P- and S-waves. External factors such as prevailing stresses and degree of saturation also affect the wave propagation in intact rock.
- 1.2.2.2 Wave propagation through rock masses: Propagating waves are attenuated due to energy losses from friction within the material they travel through. In a rock mass additional wave attenuation occurs due to the presence of discontinuities together with impedance differences between geological regions. Propagating waves are subjected to reflection and refraction at a discontinuity or an interface between regions. Another crucial factor is the frequency, or wavelength, of the propagating wave. The wave is predominantly reflected when the frequency is high (resulting in a short wavelength). Conversely, when the frequency is low (resulting in a long wavelength), the wave is primarily transmitted across the discontinuity (Pyrak-Nolte et al., 1990b; Boadu & Long, 1996). At a "welded" interface between geological regions, wave frequency does not affect the amplitude of the reflected and refracted waves.

The effect of an individual discontinuity on wave propagation depends on the following factors: (i) roughness of the surface, (ii) infill mineral, (iii) opening of a discontinuity, (iv) thickness of the infill, (v) compressive strength of the contact surfaces, (vi) normal and shear stiffness and (vii) water – pressure and flow. The surface roughness of a discontinuity provides resistance when the two surfaces are in contact and when the discontinuity is subjected to shear forces. The compressive

strength of contact surfaces is generally lower than that of the surrounding rock. Water might circulate in a discontinuity, transforming minerals, causing weathering and the creation of infill material. Increasing the thickness of the infill material results in decreased contact between the surfaces of the discontinuity, which reduces its strength. Additionally, water might build up pressure, leading to increased aperture, thereby decreasing the shear strength of the discontinuity.

In a rock mass, numerous discontinuities are usually randomly oriented or with dominant orientations, creating discontinuity sets. For a randomly jointed rock mass, it is difficult to account for the effect of individual discontinuities. For a rock mass intersected by discontinuity sets, properties such as normal spacing between the discontinuities within each set and the number of sets of discontinuities influence wave propagation. Propagation of waves across multiple parallel discontinuities includes multiple reflections and refractions at each discontinuity (Zhao et al., 2006) thus making the wave propagation more complex than for a single discontinuity.

1.3 Research challenges

- How do the properties of soils affect the propagation of waves?
- How does intact rock respond upon propagation of waves?
- How do geological features such as discontinuities affect wave propagation in rock?
- How do rock mass properties influence the propagation of waves?
- What properties are important for wave propagation in discontinuous rock masses, and how should the influence of discontinuities be considered in the analysis of dynamic problems?

1.4 Scope and objectives of the study

Studying the dynamic properties of geomaterials is crucial for several reasons. Firstly, it provides insights into how soils and rocks behave under dynamic loading conditions such as earthquakes, landslides, and construction activities. This understanding is essential for designing resilient infrastructure to withstand such forces, ensuring public safety. Secondly, knowledge of dynamic properties allows for predicting and mitigating geological hazards. By understanding how geomaterials respond to seismic

events or heavy rainfall, engineers and geologists can assess the risk of landslides, liquefaction, or slope failures and take appropriate measures to minimise potential damage and loss of life.

Furthermore, studying dynamic properties aids in developing innovative construction techniques and materials. By researching how geomaterials respond to dynamic loading, engineers can design more efficient foundations, earthquake-resistant structures, and protective measures, ultimately improving the durability and resilience of infrastructure. Overall, the study of dynamic properties of geomaterials is important for enhancing public safety, reducing the risk of geological disasters, and advancing the field of civil and geotechnical engineering.

This study aims to investigate the deformational behaviour of soils and rocks across a range of shearing strain levels varying from 0.0001% to 0.1%, employing resonant column/torsional shear (RCTS) equipment. Soil specimens, including dry sand, synthetic rock material, and gypsum plaster, were tested. The research examines the influence of strain amplitude, loading frequency, and confining pressure on the dynamic response of these materials. The study is structured around the following objectives to achieve its goals:

- 1. To understand the deformational behaviour of sands under diverse conditions, including varying relative densities, confining pressures, and strain amplitudes, and provide modulus reduction and damping ratio curves for sand.
- 2. To perform resonant column and cyclic torsional shear testing techniques to investigate the dynamic behaviour of rocks under various experimental settings. To examine the deformative behaviour of intact rock at various loading frequencies first. Proceed with the investigation of the dynamic behaviour of jointed rock, taking joint spacing into account. To understand the non-linear response of jointed rocks, use the Ramberg-Osgood and modified hyperbolic models.
- 3. To utilise cost-effective photogrammetry techniques to precisely determine the joint roughness coefficient of frictional joints in jointed rocks.
- 4. To understand the deformational characteristics of horizontally jointed rocks with different joint spacings under varying confining pressures and loading frequencies.
- 5. To examine the deformational response of frictional jointed rocks under different loading and joint conditions.

6. To determine the dynamic properties of jointed rocks infilled with natural rubber latex (NRL), focusing on the damping characteristics of the NRL-infilled rocks.

These objectives aim to comprehensively understand the dynamic response and deformative behaviour of different geomaterials under varying experimental conditions, from sands to jointed rocks, incorporating aspects such as joint roughness, joint spacing, and the influence of infill materials like NRL.

1.5 Organization of the Thesis

The thesis is organised into ten chapters.

Chapter 1 contextualises the subject matter, emphasising the importance of wave propagation in soils and rocks. It provides an overview of the thesis, delineating its scope and objectives.

Chapter 2 comprehensively reviews existing literature pertinent to the field, summarising relevant studies and methodologies.

Chapter 3 details the materials and methods utilised in the study, including the preparation of model materials and the testing apparatus, discussing their applicability in soil and rock mechanics.

Chapter 4 delves into the dynamic characteristics of Sutlej River sand, aiming to develop tailored modulus reduction and material damping ratio curves for specific site conditions. Advanced soil tests are conducted using the Resonant Column (RC) apparatus and Cyclic Torsional Shear (CTS) test across various strain amplitudes and experimental settings.

Chapter 5 aims to understand the comprehensive behaviour of intact rock under dynamic and cyclic loading, employing resonant column and cyclic torsional shear testing techniques. Two modelling approaches, the modified hyperbolic model and the Ramberg-Osgood models, are utilised to analyse the non-linear viscoelastic characteristics of rocks under different loading conditions.

Chapter 6 describes the assessment of the joint roughness coefficient of jointed rocks using cost-effective photogrammetry techniques, extracting surface profiles, and estimating JRC values through visual interpretation, statistical approaches, and fractal dimension analysis.

In Chapter 7, the investigation focuses on the effect of joint spacing on the dynamic response of jointed rocks. This involves conducting Resonant Column (RC) and Cyclic Torsional Shear (CTS) testing on plain-jointed rocks under various conditions, assessing the influence of joint spacing on its dynamic properties.

In Chapter 8, the study delves into the impact of joint orientation and joint roughness on the dynamic properties of jointed rocks. This part uses RC and CTS testing methodologies to examine how rock joint characteristics such as orientation, roughness, and loading characteristics such as frequency affect the dynamic response.

Chapter 9 demonstrates the role of NRL in mitigating the non-linear response of rock masses under medium and high-strain dynamic loading conditions. The study uses RO and MH models to analyse experimental data from RC and CTS tests on NRL-grouted specimens, summarising the relationship between joint spacing, confining pressure, loading frequency, and strain amplitude.

Finally, Chapter 10 summarises the research findings, draws major conclusions, and discusses avenues for future research.

Chapter 2 Literature Review

2.1 Introduction

Chapter 2 of the provided document offers an extensive literature review on the laboratory testing of geomaterials, focusing primarily on the methods and factors influencing their deformational properties. Over the past decade, significant advancements have been made in laboratory testing techniques to determine the dynamic properties of soils. These techniques are categorized into cyclic tests, where inertia is negligible, and dynamic tests, which involve wave propagation. The chapter elaborates on these fundamental concepts, discussing their capabilities and limitations. The literature review delves into various factors affecting the dynamic response of soils, particularly at low-strain amplitudes. It examines analytical models such as the Hardin-Drnevich, Seed-Idriss, and Ramberg-Osgood models, which are used to describe the nonlinear stress-strain relationship of soils at intermediate strain levels. The document reviews previous studies on the effects of loading cycles, frequency, and small-strain measurements on the deformational characteristics of soils. Additionally, the chapter addresses the determination of dynamic shear modulus and damping ratio using both in-situ and laboratory-based techniques. Laboratory methods, while more precise, face challenges at extremely low strain levels, which are discussed alongside solutions such as resonant column and pulse velocity techniques. The review also covers the impact of joint surface roughness on acoustic properties and the effects of weathering and grouting on jointed rock masses. The chapter concludes with a discussion on advanced modelling approaches and empirical relationships for predicting wave behaviour in jointed rock masses, highlighting the importance of accurate joint geometry representation in geotechnical engineering applications.

2.2 Dynamic properties of geomaterials

In most modern geotechnical engineering practices, the damping ratio and dynamic shear modulus are determined using different methods. Various in situ and laboratory-based techniques are employed for this purpose. Generally, laboratory methods yield more precise results when compared to in-situ approaches, albeit they entail certain

limitations and underlying assumptions. Particularly, conducting measurements at extremely low strain levels poses a challenge in laboratory settings. Only resonant column and pulse velocity techniques (such as bender elements and ultrasonics) enable data acquisition at these minute strain levels. The disparity in strain levels achievable between common in-situ and laboratory techniques is depicted in Figure 2.1.

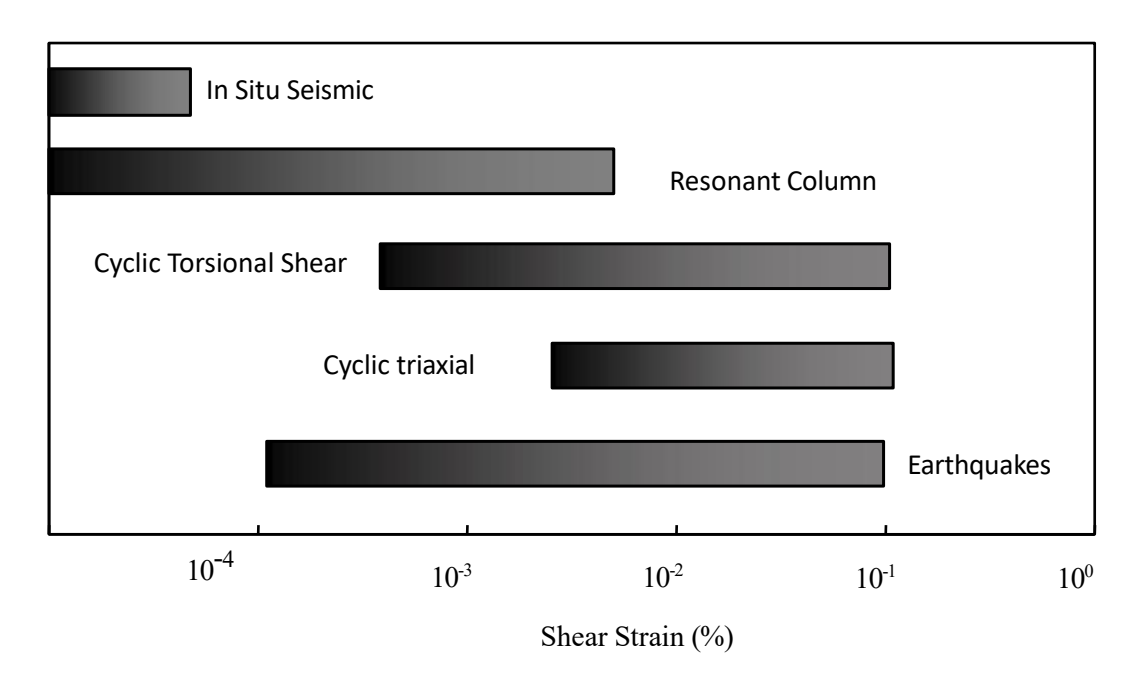


Figure 2. 1 Shear strains mobilized in in-situ and common laboratory techniques (Ishihara, 1996)

The resonant column apparatus enables the testing of a sample under axisymmetric loading, both in steady-state vibration and free vibration modes (refer to Figure 2.2). There are several types of resonant columns, which can be identified by their vibration modes and boundary conditions. Wilson and Dietrich (1960) developed a fixed-free resonant column to measure longitudinal and torsional vibrations. Hardin and Richart (1963) introduced a resonant column apparatus with free-free boundary conditions to measure torsional and longitudinal vibrations. Har (1965) devised a resonant column apparatus capable of applying deviatoric axial loads. These devices were primarily designed for operation under small strains (around 10⁻⁵). Drnevich (1967) later developed a free-fixed resonant column allowing for strains exceeding 10⁻⁴. Subsequent designs combined resonant column and torsional shear for measuring dynamic soil properties across shear strains ranging from 10⁻⁶ to 10⁻¹ (Drnevich, 1978; Drnevich et al., 1978; Isenhower, 1980).

During the resonant column test, a cylindrical specimen, either solid or hollow, undergoes harmonic excitation via an electromagnetic driving system. In the fixed-free setup, the specimen is anchored at the base and free at the top. A mass, known as the driving plate, attached to the top of the specimen, is actuated by coils and magnets. This setup enables exciting the soil in torsional, flexural, and axial modes of vibration, under varying confinements and shear strain levels.

In the fixed-free configuration of the resonant column, the distribution of angular rotation (φ) along the specimen is given by a quarter-sine function if the mass polar moment of inertia of the driving plate tends to zero ($I_o = 0$). Conversely, the distribution of angular rotation approaches a straight line as the ratio of the mass polar moment of inertia of the specimen (I), and the drive plate I/I_o tends to zero (Figure 2.2).

Resonant column measurements yield two key parameters: resonant frequency and damping coefficient. Wave velocity and attenuation are subsequently computed from these measurements. The calculation of the damping coefficient assumes an equivalent, uniform, linear viscoelastic specimen akin to the Kelvin-Voigt model (Hardin, 1965; Hardin & Scott, 1966). While this model predicts a response similar to that observed in sand specimens, damping in sands is not necessarily viscous in nature (Hardin, 1965; Hardin & Scott, 1966). Determining the frequency dependency of wave velocity and attenuation poses challenges due to issues associated with measuring high resonant modes (alternative approaches discussed in Stoll, 1979).

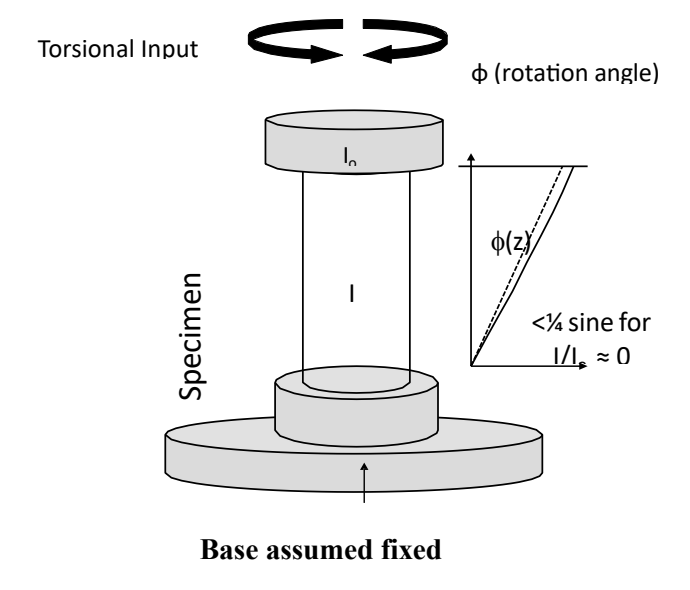


Figure 2.2 Schematic view of Fixed-free resonant column apparatus

The presence of a rigid mass atop the sample plays a crucial role in determining both the shear wave velocity and the shear strain during resonance calculations. When the rigid mass approaches zero, the initial mode resembles a quarter sine wave, leading to non-uniform shear strain distribution across the height of the sample. Conversely, as the mass of the rigid component tends towards infinity relative to the mass of the sample, the initial mode approximates a straight line, resulting in consistent shear strain at a specific radius (Woods, 1978).

Various factors influencing resonant column test outcomes have been investigated, including the impact of ageing from cyclic loading (Drnevich & Richart, 1970), interactions between the specimen and end platens (Drnevich, 1978), restraint imposed by the end platens (Alarcon-Guzman, 1986), and membrane penetration effects (Frost, 1989; Drnevich, 1985; recommending that the latex membrane thickness be less than 1% of the specimen diameter). Typically, these factors prove insignificant when the shear strain amplitude remains small ($\gamma < 10^{-4}$). Moreover, assuming in-plane strain conditions during data interpretation is permissible under conditions of minor deformation.

In conventional resonant column testing, this solution is derived by considering an elastic medium with a minimal damping ratio. The equation takes the following form (Lai et al., 2001):

$$\frac{T_o(\omega)e^{-i\phi(\omega)}}{\varphi(\omega)} = J_P \rho \omega^2 H \frac{1}{\sqrt{\frac{\rho \omega^2 H^2}{G_S} tan\left(\sqrt{\frac{\rho \omega^2 H^2}{G_S}}\right)}} - J_o \omega^2$$
(2.1)

where T_o is the applied harmonic torque, φ is the rotation angle of the specimen, φ is the phase lag between torque and rotation angle, G_S is the shear modulus, ρ is the density, J_P is the polar moment of inertia, H is the height of the specimen, and ω is the excitation frequency. At resonance, the excitation frequency $\omega = \omega_o$ and due to negligible damping, the response of the system (rotation) becomes so large that the left-hand side of Equation 2.1 tends to zero. At this condition, the solution becomes (Lai et al., 2001).

$$\frac{J}{J_o} = \sqrt{\frac{\rho \omega_o^2 H^2}{G_S}} tan\left(\frac{\rho \omega_o^2 H^2}{G_S}\right)$$
 (2.2)

The damping ratio in conventional resonant column tests is defined as the ratio between system damping and critical damping. From the equation of motion of a single degree of freedom system with viscous damping, the damping ratio is expressed as:

$$\xi = \frac{C}{C_c} = \frac{C}{2\sqrt{km}} \tag{2.3}$$

where C_c is the critical damping coefficient, C is the viscous damping coefficient [N/(m/s)], and k and m are the stiffness and mass of the system, respectively. The critical damping represents the limit between harmonic and non-harmonic motion; the system is over-damped for $\xi > 1$, critically damped for $\xi = 1$, and under-damped for $\xi < 1$.

The resolution of Equation 2.2 provides the elastic shear modulus of the specimen material, while its material damping ratio necessitates a separate assessment. However, within a viscoelastic medium, the dynamic properties are interdependent and must be concurrently assessed. An effective approach involves substituting the shear modulus in Equation 1 with the complex shear modulus, utilizing the viscoelastic correspondence principle discussed previously. By solving Equation 2.1 based on the complex modulus, it becomes possible to ascertain frequency-dependent dynamic properties. This process, known as the non-resonance method in resonant column testing, facilitates the determination of such properties (Lai et al., 2001). Both conventional and non-resonance methods can utilize either voltage-based or current-based measurements in resonant column testing (Cascante et al., 2003). Voltage-based measurements often yield notably high damping ratios, necessitating correction. Cascante et al. (2003) offered transfer functions for accurately determining the damping ratio from measurements based on either voltage or current.

2.3 Factors affecting the dynamic response of geomaterials

Laboratory testing methods, such as bender and extender elements testing and ultrasonic pulse velocity testing, are useful techniques to find dynamic properties of soil at a particular strain level, whereas cyclic torsional shear test, cyclic direct shear test, cyclic triaxial test, and resonant column apparatus testing techniques provide the dynamic properties of soil for varying strain levels (F. E., Jr. Richart, 1970). The resonant column test approach is the highest acceptable laboratory testing technique for determining the dynamic properties of soil under a strain range of 10⁻⁴% - 10⁻¹% (F. E., Jr. Richart, 1970). Experimental studies reveal that the dynamic properties of geomaterials are strain-dependent due to their energy dissipative nature (Seed & Idriss, 1970; lo Presti et al., 1997; Drnevich et al., 1967; Stokoe et al., 1999). It was found that an escalation in the strain level causes a decline in the stiffness values (in terms of Young's modulus (E) and Shear modulus (G)) and a hike in the value of the Damping ratio (D). Many researchers have accepted that the effective confining stress, void ratio, and water content are the foremost factors influencing the dynamic properties of granular soils (Chun & Carlos, 2001; Hardin & Richart, 1963; Shiming et al., 1984).

The normalized modulus reduction curve (G/Gmax vs. γ) and material damping ratio curves (D vs. γ) are essential for the assessment of many geotechnical engineering problems. Many researchers developed standard modulus reduction and damping ratio curves (Seed et al., 1986; Seed & Idriss, 1970; Darendeli, 2001; Meng & Rix, 2003; Menq, 2003; Vucetic et al., 1991; Sun et al., 1988; Vardanega & Bolton, 2011; Puri et al., 2020). The dynamic properties of soil can be considered as key parameters for the ground response analysis, liquefaction studies, seismic hazard assessment studies, and design of structures subjected to dynamic loading (Facciorusso, 2021; Hwang, 1997), and it is essential to conduct a study on the response of the soil in the area against the dynamic loading considering the seismicity associated with the region.

Sometimes, for site-specific problems, the adoption of standard curves requires advanced dynamic testing of soils, which proves a tiresome, time-consuming, and practical constraint. To encounter this problem, the use of site-specific curves would upgrade the accuracy of many geotechnical engineering problems, i.e., designing earthquake-resistant structures, improvement in the life of structures, and fidelity of important engineering projects in the study area. The Sutlej river basin lies under a high-

risk seismic zone in the north-eastern part of Punjab state. Therefore, the dynamic characterization of the sandy soil available in the region is needed. A precise site-specific study of the Sutlej river sand is essential as the ground conditions differ from the previously available studies. This study targets the estimation of the dynamic properties of Sutlej River sand to develop site-specific modulus reduction and material damping ratio curves

The dynamic behavior of geomaterials is influenced by two primary factors, as outlined by Kramer (1996). Firstly, external factors like stress/strain path, magnitude, rate, and duration play a significant role in shaping the dynamic properties of geomaterials. Secondly, material characteristics, including soil type, particle size and shape, and void ratio, also contribute to how the material responds to dynamic loading.

2.3.1 Cyclic shear strain

Experimental findings indicate that the primary external factor influencing the dynamic behaviour of soil is the magnitude of applied stress or strain. Dynamic excitation enables the measurement of strain levels induced within the soil mass. Below the linear, cyclic threshold shear strain, as Vucetic (1994) described, soil response remains linear but not elastic due to energy dissipation, even at minimal strain levels (Lo Presti & Pallara, 1997; Kramer, 1996). This linear response is characterized by constant soil stiffness, while energy dissipation at small shear strain levels occurs due to the time lag between cyclic strain and stress, typical of viscoelastic behaviour. Moreover, soil properties remain unaffected by the number of excitation cycles below the linear cyclic threshold shear strain level (Ishihara, 1996). Observation of soil response at small strain levels reveals permanent volume changes in drained tests and pore pressure development in undrained tests (Vucetic, 1994). Although the response of soils exhibits non-linear viscoelastic behaviour at this stage, material properties undergo minimal changes, with little degradation observed over cycles.

At intermediate strain levels, also termed pre-failure, instantaneous energy losses occur over a finite period in relation to the number of cycles. Soil properties degrade not only within the hysteretic loop but also with an increase in the number of cycles (Ishihara, 1996). This behaviour is categorized as non-linear elastic-viscoplastic in the shear strain range. Energy losses occurring below the volumetric threshold shear strain are considered viscoelastic and vary with soil type. For instance, the upper range of this

threshold is 0.005% for gravels, 0.01% for sands, and 0.1% for normally consolidated high-plasticity clays (Bellotti et al., 1989; Vucetic & Dobry, 1991).

In resonant column testing, three factors limit achievable strain levels. These include limited torque in the drive system, limited travel in the drive system, and constraints in the deflection measuring system. Shortening the specimen length enables higher strains for the same drive rotation. Fabricating taller base platens allows the use of shorter specimens, offering additional benefits such as higher resonant frequencies and facilitating testing at higher frequencies without significant inertial effects. Deflection sensors impose a third limitation on strain in torsional shear testing, which can be mitigated by employing shorter specimens. Micro proximitors, commonly used to measure rotations, undergo calibration using a milling machine to ensure accurate measurements. To measure higher strains, alternatives include using less sensitive proximitors with larger linear measurement ranges or employing local strain measurements using strain gauges attached to the specimen membrane (Bae et al., 2009). The soil behaviour corresponding to various strain levels is given in Table 2.1.

Table 2. 1 Soil behaviour and shear strain level (Ishihara, 1996)

Shear Strain	Very Small, γ < 10 ⁻⁷	Small, $10^{-6} < \gamma < 10^{-3}$	Intermediate, $10^{-3} < \gamma < 10^0$	Large, > 10 ⁰
Soil Behavior	Linear elastic	Non-Linear Viscoelastic	Non-Linear Viscoplastic	Failure

2.3.2 Stress/Strain rate: The soil response is influenced significantly by external variables such as the stress/strain rate (or the frequency of excitation) and the duration (measured in the number of cycles). Numerous studies, including those by Dobry and Vucetic (1987), Vucetic and Dobry (1991), Shibuya et al. (1995), Malagnini (1996), and Lo Presti et al. (1996), have delved into the impact of frequency on soil response. These investigations have revealed that the frequency effect varies depending on the strain level. Typically, stiffness rises with frequency, with low plasticity soils demonstrating the least sensitivity to frequency fluctuations. Furthermore, research indicates that the damping ratio exhibits frequency dependence within certain bandwidths while remaining frequency-independent in others. This finding has been highlighted in studies by Hardin and Drnevich (1972), Shibuya et al. (1995), and Lo Presti and Pallara (1997).

Shibuya et al. (1995) proposed a conceptual diagram to illustrate these findings (refer to Figure 2.3):

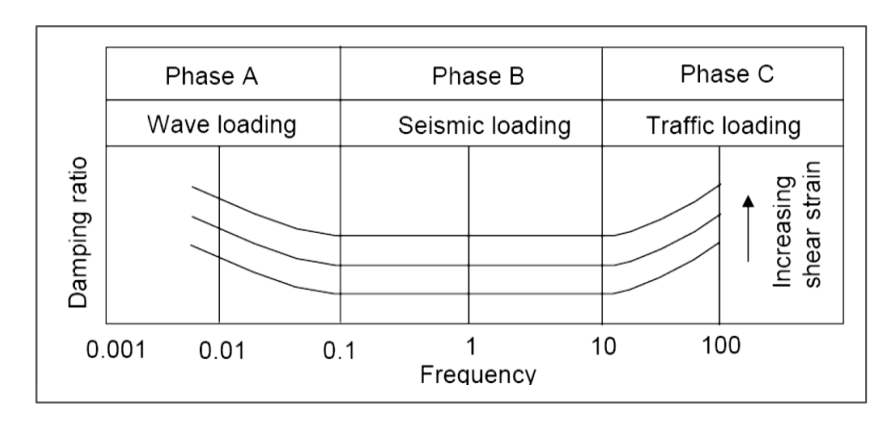


Figure 2. 3 Frequency dependence of damping ratio within soil mass (Shibuya et al., 1995)

2.3.3 Duration of excitation: The duration of excitation, also called the number of cycles, can significantly influence how soil responds to dynamic excitation. Research findings indicate that in clayey soils and dry sands, the impact of cycle numbers is minimal at very low strain levels (Shibuya et al., 1995; Lo Presti & Pallara, 1997). However, this influence becomes more pronounced as shear strain levels increase. For sandy soils, increasing the number of cycles leads to a rise in stiffness under drained conditions but a decrease under undrained conditions (Dobry & Vucetic, 1991). The reduced stiffness is linked to decreased effective stress caused by elevated pore pressure. Several factors, including cyclic pre-straining, creep, relaxation, anisotropy, digenetic processes, degree of saturation, and drainage conditions, can impact the deterioration of dynamic properties.

2.3.4 Moisture content: When a seismic wave accelerates the soil mass, it causes differential inertial forces on the fluid and soil particles. Winkler and Nur (1982) state that this leads to the development of viscous shear stresses within the pore fluid, which decreases as the distance from the pore wall increases. There is a strong coupling between the solid and liquid phases for compressional waves, whereas shear waves exhibit a lack of coupling. Dynamic stiffness and damping characteristics were relatively consistent across saturation ratios between 25% to 75%. However, as saturation approaches full capacity, modulus values decrease sharply, and damping in

loose samples increases significantly compared to unsaturated levels. Drained tests showed that the most significant changes in shear modulus and damping occur within the initial 30 cycles. Vertical consolidation stress was identified as the primary parameter affecting shear modulus and damping ratio in sand. Similarly, relative density or void ratio notably impacts dynamic stiffness and damping under drained and undrained conditions. Furthermore, the influence of shear strain amplitude is essential for interpreting results from both types of tests (Jafarzadeh, 2011).

The attenuation and dispersion of low-strain waves ($\gamma < 10^{-6}$) are influenced by fluid saturation levels and the frequency content of the wave (Murphy, 1983; Winkler & Nur, 1982). Water-saturated rocks have an increased dependence on strain amplitude (Winkler & Nur, 1979). In partially saturated media, additional mechanisms such as droplet flow and gaseous phase compression contribute to attenuation increase with saturation, with attenuation decreasing as the medium reaches full saturation (Winkler & Nur, 1979).

Differences in attenuation between compressional and shear waves in fully and partially saturated media arise from how waves interact with cracks and pores. In fully saturated media, uniform compression by compressional waves limits substantial fluid flow, while shear waves cause compression in some areas and dilation in others, enhancing fluid flow. Consequently, shear waves exhibit higher attenuation than compressional waves in fully saturated media, with compressional energy loss being twice that of shear energy loss. Moreover, the compressibility of gas-water mixtures amplifies fluid-flow mechanisms in compression (White, 1975; Murphy et al., 1982).

At low strains, low saturation slightly increases attenuation due to fluid-flow mechanisms, but at high strains, frictional losses dominate, leading to significant attenuation increases (Winkler & Nur, 1982). Hornby and Murphy (1987) studied changes in both bulk and shear moduli with heavy hydrocarbon saturation, proposing the use of the V_p/V_s ratio to distinguish between oil-saturated sands ($V_p/V_s < 2.5$) and shales ($V_p/V_s > 2.5$). Changes in attenuation for compressional and shear modes with saturation provide a diagnostic tool: $Q_p/Q_s > 1$ indicates full saturation, while $Q_p/Q_s < 1$ indicates partial saturation (Winkler & Nur, 1979), where Q_p and Q_s refer to the quality factors of P and S-wave velocity respectively. This tool is valuable for field measurements, especially when determining absolute attenuation values is challenging.

Thus, attenuation provides saturation-independent information that complements velocity measurements in assessing medium saturation.

2.3.5 Confinement: One of the most consistent observations in laboratory settings is the decrease in attenuation as confining pressure increases within the near-surface pressure range. This trend stabilizes notably with elevated pressure, where attenuation remains constant regardless of frequency or saturation condition (Johnston, 1981). This phenomenon can be elucidated by the augmentation in both the quantity and durability of contacts, alongside the decline in fluid flow and elastic dispersion as pores and cracks close under heightened pressure (Winkler & Nur, 1982; Jones, 1986). In the context of clays, heightened confinement leads to amplified shear wave velocities and reduced attenuation. This reduction primarily stems from a decreased void ratio during primary consolidation and the reinforcement of particle bonding post-consolidation (Stokoe, 1980). Time exerts a more pronounced influence on attenuation compared to shear wave velocity (Stokoe, 1980; Lodde, 1982).

2.3.6 Frequency: Stoll (1978) demonstrated that the reduction of wave intensity in fully saturated soils varies with frequency. This research posited that energy dissipation can be attributed to two main factors: the lack of elasticity in the soil structure itself and the interaction between the fluid within the pores. At lower frequencies, losses primarily stem from the properties of the soil structure, while at higher frequencies, losses are predominantly due to viscous interactions. The definitions of "high" and "low" frequencies depend on the specific characteristics of the soil being studied.

For instance, the frequency at which the peak attenuation of shear waves occurs in sand (with a porosity of 40%) shifts from 500 Hz to 5000 Hz as the intrinsic permeability decreases from 10^{-6} cm² to 10^{-7} cm² (Stoll, 1978). Stoll's subsequent work in 1984 found that in dry Ottawa sand, attenuation remains relatively consistent across a frequency range from 2 Hz to 1000 Hz. However, in saturated Ottawa sand, attenuation increases with frequency, peaking at lower kilohertz frequencies. These findings align well with predictions from Biot's model, except for cases involving low permeability silts, where Biot's theory falls short in explaining the frequency dependence of attenuation (1/Q) (Stoll, 1979).

Kim et al. (1991) utilized a torsional shear device and a resonant column with shear strain levels below 10-5 to observe that damping effects in dry sand remain consistent

across frequencies ranging from 0.1 Hz to 100 Hz. Conversely, compacted clay exhibits frequency-dependent damping effects beyond 10 Hz. A summarized overview of attenuation trends concerning increasing strain, confinement, and frequency is presented in Table 2.2. Identifying the parameters influencing attenuation is crucial in exploring the underlying physical principles governing wave propagation.

Table 2. 2 General Trends in Attenuation (After Badali and Santamarina, 1992)

Parameter	Material condition	Attenuation Parameter	Attenuation Trend	Measurement Device	Material	References
		Damping Ratio	Increase	Longitudinal Oscillations	Clean Sand	Hardin, Drnevich 1972
Strain	Dry	Logarithmic Decrement	Increase	Torsional Column	Ottawa Sand	Bae, 2009
			Increase	Longitudinal Oscillations	Ottawa Sand	Bae, 2009
	Saturated		Increase (Saturant Glycerin)	Longitudinal Oscillations	Ottawa Sand	Bae, 2009
			Increase	Torsional Column	Ottawa Sand	Jafarzadeh 2011
			Increase	Torsional Column	Silt	Jafarzadeh 2011
Confinement	Dry	Damping Ratio	Decrease	Longitudinal Oscillation	Clean Sand	Drnevich H1ardin,
		Logarithmic Decrement	Decrease	Torsional Column	Ottawa Sand	Cabalar, 2009
			Decrease	Torsional Column	Soil	Cabalar, 2009
			Decrease	Longitudinal Oscillation	Ottawa Sand	Cabalar, 2009
	Saturated		Decrease (Saturant Glycerin)	Longitudinal Oscillation	Ottawa Sand Test 19	Hall, Richart 1963
		Amplitude Ratio	Increase	Transmission Line	Sandstone Limestone	Khan, 2005
Frequency	Dry	Logarithmic Decrement	Increase then Decrease	Torsional Column	Sand and Silts	Khan, 2011
			Increase	Torsional Column	Fire Island Sand	Khan, 2011
	Saturated		Parabolic Downward	Resonance Column	Sand	Khan, 2011

2.4 A review of previous research on rocks

The study of rock joint behaviour and its influence on various geotechnical and geophysical properties has been a significant area of research. This literature review synthesizes key findings from several influential studies, providing a comprehensive understanding of the mechanisms governing rock joint interactions and their implications.

2.4.1 Empirical models for rock joint shear strength

Barton and Choubey (1977) introduced an empirical law of friction for rock joints, aiming to predict shear strength using three key parameters: joint roughness coefficient (JRC), joint wall compressive strength (JCS), and residual friction angle (ϕ_r). Their extensive testing on over 100 joint samples validated the accuracy of predicting both ϕ_r and peak shear strength angles. They also observed that JRC and JCS tend to decrease with increasing joint length, subsequently affecting shear strength, dilation angle, and stiffness of the joints.

Kahraman (2002) created artificial fractures on rock samples with various surface roughness levels, defined by the fracture roughness coefficient (FRC). His experiments revealed a strong polynomial relationship between FRC values and P-wave velocities, indicating that higher roughness (FRC) reduces P-wave velocities. This study underscores the significant impact of fracture roughness on the acoustic properties of rocks.

2.4.2 Seismic anisotropy and wave propagation in fractured rocks

Schoenberg and Sayers (1995) presented a method to incorporate geologically realistic fractures into seismic propagation models by summing the compliance tensors of unfractured rock and each fracture set. This approach helps understand seismic anisotropy, crucial for determining in-situ stress orientations. Ultrasonic experiments on simulated fractured media supported his findings, demonstrating orthorhombic elastic behaviour in isotropic background rock due to equal normal and shear compliances.

Fratta and Santamarina (2002) investigated long-wavelength shear wave propagation in rock masses with joints filled with softer gouges under low confinement. Using a slender column with gouge-filled joints excited in the first torsional vibration mode, the study highlighted the potential of wave propagation methods to assess jointed rock

masses, emphasizing the anisotropic nature and its impact on wave velocity and damping.

Li and Ma (2010) focused on rock joints and blast wave interaction, using momentum conservation and displacement discontinuity methods to analyze oblique blast waves and rock joints. Their derived wave propagation equation and parametric studies provide insights into the effects of joint stiffness and incident wave on transmission and reflection.

Sebastian and Sitharam (2016) studied wave propagation in jointed rock masses, focusing on wave frequency, stress conditions, and induced strain levels. Using a resonant column apparatus, their findings indicated that wave velocity reductions and damping across joints are influenced by friction and filling, with confining stress and strain levels playing significant roles in weak rocks.

Sebastian and Sitharam (2018) discussed the nonlinear elastic behaviour in rocks, using resonant column tests and numerical simulations to show stiffness reduction with increasing strain levels. The study emphasized the significant effect of joint orientation and spacing on wave propagation.

2.4.3 Joint surface roughness and acoustic properties

Researchers have performed many studies to quantify the joint roughness coefficient. Bandis et al. 1981; and Du et al. 2009 provided empirical correlations to estimate the JRC. Maerz et al. 1990; Tatone and Grasselli 2010; and Zhang et al. 2014 used a statistical approach for the JRC quantification. Lee et al. 1990; Fardin et al. 2004; Shirono and Kulatilake 1997; Kulatilake et al. 2006; Babanouri et al. 2013; Li and Huang 2015 used the fractal dimension approach to determine the JRC.

Barton and Choubey 1977 introduced a parameter, the Joint roughness coefficient (JRC), which is widely used in the characterization of joint roughness. This method of determination of JRC requires a profile comb or profilometers. The joint profiles can be characterised, and the JRC values can be obtained over a scale range from 0 to 20 based on comparing profiles obtained using the profile comb and the standard profiles provided by Barton and Choubey 1977. For the profiles longer than 10 cm in the field, Bandis et al. 1982 provided a chart to scale up the profile in the field with the standard profiles.

However, the method has a limitation as the profiles are two-dimensional, and these profiles are only ten in number, and one has to compare the surface profile of the joint against these ten profiles with visual interpretation.

The tilt angle test (or self-weight gravity shear test) is another simple technique to identify the roughness of jointed rock specimens. However, collecting desired rock specimens is a cumbersome task as it involves very high cutting and transportation costs (Hu and Cruden 1992). The method is based on the JRC-JCS model and involves back calculation of JRC from the shear strength parameters (Du 1994). Rahim 2018 performed tilt angle tests on different shapes of rock samples, i.e., cylindrical, square, Stimpson type, and discs; and noticed that square base slabs is the most relevant one among different types of tilting angle tests. The limitation of the tilt angle test is that it can only be used for the rock specimens of size less than 30 cm.

Z2 is the most widely used statistical parameter based on slope-based characteristics to estimate JRC. However, the Z2 value is a sampling interval dependent parameter. Tse and Cruden 1979 proposed the regression correlations between Z2 and JRC at sampling intervals of 0.25mm and 0.5 mm. Gao and Wong 2015 studied the effect of small, medium, and large sampling intervals (i.e., 0.27 mm, 0.54 mm, 1.08mm) on Z2 and JRC estimation. Mandelbrot 1977 presented the concept of fractal dimension and postulated that planar curves might also carry specific peculiar geometrical characteristics and the length of those curves depends on the size of the measuring unit employed. Further, Lee et al. 1990 used the fractal dimension approach to identify the JRC of 10 standard profiles provided by Barton and Choubey 1977. Turk et al. 1987; Bae et al. 2011; Maerz and Franklin 1990; Lee et al. 1990; Chen, 2016 also used the fractal dimension approach to estimate the JRC of standard profiles and provided correlations between fractal dimension (D) and JRC.

3D laser scanners are widely used to identify the three-dimensional JRC values for their high accuracy in getting the surface topography of rock masses and slopes (Fardin et al. 2001; Belem et al. 2007; Wang et al. 2019). MM Nordin et al. 2014 used the scan line technique to determine the JRC values from the 3D image extracted from laser scanning. The visual interpretation method to obtain the average JRC values from the 8 scan lines was employed for this research. Tatone and Grasselli 2010 proposed new correlations between Z2 and JRC based on the 2D and 3D profiles obtained from 3D laser techniques

at the sampling intervals of 0.044mm, 0.25 mm, 0.5 mm, and 1mm. Fan and Cao 2019 used a precise laser scanning technique to get 3D topography of 15 joint rock specimens and digitized the data to characterize joint roughness. However, this technique is expensive and therefore, cannot be used widely for the analyses. However, the 3D laser scanner is not widely used as the equipment cost is very high, which limits the practice of this method of JRC estimation.

Recently, with the evolution of computer vision theory, the 3-dimensional reconstruction of digital image algorithms has been constituted in photogrammetry (Brown and Lowe 2005; Westoby et al. 2012). The structure from motion (SFM) algorithm is purposeful in overlapping digital images, automatic feature matching, and computing the missing matches. The SFM algorithm can appreciably provide the spatial position of an object by overlapping the images and matching similar points from captured images (Lowe 2004; Carrivick et al. 2016). The revolution in the smartphone industry provided promising features in the devices with potential cameras that enable the device to provide high-quality images with high resolution. The high-quality camera of the smartphone helps to provide the 3D profile of jointed rough surfaces using the photogrammetry technique with high accuracy. The photogrammetry technique using a smartphone is an economical approach for gathering the 3D profile of the jointed rough surface, easily accessible, less time-consuming, and proposes a practical application to determine the JRC. The photogrammetry technique only requires a set of highresolution images to obtain the geometry of rock discontinuities (Guo et al. 2011). This technique has wide applications in the characterization of the geometry of slopes and their stability analysis (Ferrero et al. 2011; Firpo et al. 2011; Brideau et al. 2012). The photogrammetry technique to obtain the JRC values depends primarily on the image quality; therefore, errors are possible due to the low spatial density of data (Haneberg 2007). Though the SFM photogrammetry using a smartphone has been used in many fields, i.e., terrestrial surveys, coastal surveys, laboratory medical examinations, etc., this technique also assured massive benefits in the domain of mapping of rocks and rock discontinuities (Salvini et al. 2020; García-Luna et al. 2021; Paixão et al. 2022). Zhao et al. 2020 proposed a practical photogrammetric approach to evaluate rock joint roughness and anisotropy. Nowadays, the Photogrammetry technique is broadly used for the roughness characterization of jointed rock masses (Nilsson and Wulkan 2011; Bretar et al. 2013). Jiang et al., (2006) addressed the limitations of traditional 2-D

roughness characterization methods by introducing a 3-D fractal evaluation method using laser scanning profilometry and direct shear experiments. Their research provided a novel approach for assessing the evolution of rock joint roughness and its impact on hydro-mechanical behaviours in both 2-D and 3-D models.

Kurtuluş and Güner (2012) explored how parallel and variable directional joints impact ultrasonic pulse transmission in marble blocks, finding higher attenuation with more joints, especially in variable directional joint models.

Li and Zhu (2012) developed an RGB colour model to analyze the fractal dimension of joint surfaces, correlating P-wave velocity with fractal dimensions. Their formula for wave velocity across joints, validated by ultrasonic tests, indicated a decrease in P-wave velocity with increased joint surface roughness. This research offers a valuable method for understanding wave behaviour in geological formations.

Hotar and Novotny (2013) highlighted the application of fractal geometry in describing complex natural structures and their potential in industry. They emphasized the practicality of off-line software tools, with potential on-line integration, in industries like glass manufacturing.

Mohd-Nordin et al., (2014) used 3D image processing to enhance the Joint Roughness Coefficient (JRC) classification and assess its effect on S-wave and P-wave velocities. The study found that increasing JRC increases S-wave velocity while decreasing P-wave velocity and shear wave damping, highlighting the importance of 3D joint surface characterization for accurate wave velocity estimation.

2.4.4 Grouting, weathering, and jointed rock masses

Woo et al., (2010) examined the impact of weathering on the shear strength of rock joints, focusing on JCS and residual friction angle. Testing porphyritic granite joints from South Korea, the study revealed that weathering significantly reduces JCS and alters the residual friction angle, contributing to a better understanding of rock slope stability and the effects of weathering on engineering structures.

Kim et al., (2018) investigated the effects of grouting on the stiffness of jointed rock masses at small and mid-strain levels. Their study showed that grouting decreases stress sensitivity and enhances small-strain stiffness, with initial joint roughness influencing stress-dependent behaviour and grout properties dictating strain-dependent responses.

2.4.5 Advanced modeling and empirical relations

Wang et al. (2020) introduced a rough discrete fracture network (RDFN) model to account for joint geometry variability, which significantly influences shear properties. Their numerical tests using a particle flow code (PFC) demonstrated that considering joint roughness enhances peak shear strength predictions compared to traditional models, highlighting the importance of accurate joint geometry representation.

Varma et al., (2021) explored wave interactions with rock joints through experimental and numerical methods, focusing on factors like joint angle and stiffness. Their findings proposed empirical relationships for wave velocity estimation based on various joint parameters, providing insights into wave behavior in jointed rock masses.

Abbas and Mohd-Nordin (2022) studied the elastic response of body waves in complex geological formations with multi-oriented joints and interlayers. Their three-layer laboratory model revealed that joint orientation predominantly influences wave velocities, with P-wave and S-wave velocities decreasing significantly as joint angles approach perpendicular. These insights contribute to a semi-empirical model for predicting wave velocity under varying joint angles and interlayer ratios.

Rached et al., (2022) examined P-wave propagation in fractured rock masses under field-like conditions using a large-scale triaxial device. They found that P-wave velocities increase with stress following a power law relationship, with fracture stiffness and density dictating velocity behaviour. The study highlighted the importance of fracture geometry and spacing in determining wave propagation characteristics.

This literature review underscores the multifaceted nature of rock joint studies, encompassing empirical models, seismic anisotropy, acoustic properties, grouting effects, and advanced modeling approaches. Each study contributes to a deeper understanding of the complex behaviours of jointed rock masses, providing valuable insights for geotechnical engineering applications.

2.5 Non-linear stress-strain models

The decrease in shear modulus and increase in damping ratio with shearing strain amplitude has been well recognized over the past two decades. Several researchers proposed analytical methods to predict the nonlinear behaviour of geomaterials.

2.5.1 Hardin-Drnevich: The initial proposal was made by Hardin and Drnevich 1972a, 1972b), they proposed that shear modulus, G, at a given strain, y, can be predicted from the hyperbolic relationship:

$$G = G_{max} / \left(1 + \frac{\gamma}{\gamma_r} \right) \tag{2.4}$$

where γ_r = reference strain ($\frac{\tau_{max}}{G_{max}}$), τ_{max} = shearing strain at failure and G_{max} = Initial tangent modulus. They suggested that G_{max} can be determined either experimentally from low-amplitude resonant column tests or empirically, as discussed in the previous section. The shearing stress at failure, τ_{max} , was determined from consolidated undrained triaxial tests or empirically from:

$$\tau_{max} = \left[\left(\frac{1 + K_o}{2} \sigma_v^{'} Sin\varphi + c^{'} Cos\varphi \right)^2 - \left(\frac{1 - K_o}{2} \sigma_v^{'} \right)^2 \right]^{1/2}$$
 (2.5)

where K_o = coefficient of earth pressure at rest,

 $\sigma_{v}^{'}$ = effective vertical stress, and

c' and φ = Static strength parameters in terms of effective stress.

The relationship predicts the damping ratio:

$$D = D_{max} \left[\frac{(\gamma/\gamma_r)}{(1 + \gamma/\gamma_r)} \right]$$
 (2.6)

where D_{max} is the maximum damping ratio corresponding to very large strains. Because the above equations did not precisely describe the stress-strain relations for soils, they were modified by defining a hyperbolic strain, γ_h , by:

$$\gamma_h = \frac{\gamma}{\gamma_r} \left[1 + a * exp\left(-b \frac{\gamma}{\gamma_r} \right) \right]$$
 (2.7)

Where a and b are soil constants. Then,

$$\frac{G}{G_{max}} = \frac{1}{1 + \gamma_h} \tag{2.8}$$

$$\frac{D}{D_{min}} = \frac{\gamma_h}{1 + \gamma_h} \tag{2.9}$$

2.5.2 Seed-Idriss: Seed and Idriss (1970) suggested the following relationship between shear modulus and mean effective stress (σ_0) :

$$G = 1000 * K_2 * \sigma_o^{'0.5} \tag{2.10}$$

Where G and σ_o , are in terms of psf, and the parameter K₂ is related to void ratio and strain amplitude.

2.5.3 Ramberg-Osgood: Anderson (1974) used the Ramberg-Osgood stress-strain relationship to describe the variation in shear modulus with strain amplitude. The general form of the Ramberg-Osgood relationship is defined by:

$$G = G_{max} / \left[1 + \alpha \left(\tau / \tau_y \right)^{R-1} \right]$$
 (2.11)

where α = shape factor, τ = shearing stress, τ_y = Shearing stress at yield and R= correlation number for the Ramberg-Osgood curve.

Anderson (1974) suggested using $\alpha = 1.0$ and R = 3.0 for various clays. The yield stress was assumed to be between 40 and 80 percent of the undrained shearing stress. He found that neither the modified hyperbolic (Hardin & Drnevich, 1972) nor the Ramberg-Osgood relationship could consistently predict the high-amplitude behavior of soils over a wide range of strains tested (0.001 percent to 1 percent). However, he found that the Ramberg-Osgood relationship worked better at shearing strains less than 0.1 percent. The Ramberg-Osgood model has been extended to construct hysteresis loops using the Masing criterion (Idriss et al., 1978; Saada, 1985). The equivalent damping ratio from this Ramberg-Osgood formulation can be explicitly expressed as a function of parameters α and R as:

$$D = \frac{\left[2\alpha(R-1)(\tau/G_{max}\gamma_r)^R\right]}{\left[\pi(R+1)(\frac{\gamma}{\gamma_r})\right]}$$
(2.12)

If the coefficients of a backbone curve (stress-strain curve recorded in the first quarter cycle) at various stress levels and for a given cycle are known. In that case, the

corresponding secant modulus and damping ratio can be deduced using the Ramberg Osgood-Masing model.

2.6 Summary

The literature review presented in Chapter 2 has meticulously explored the dynamic properties and behaviours of geomaterials, emphasizing the factors that influence these properties. The synthesis of various studies underscores the complexity and multifaceted nature of geomaterial responses under dynamic loading conditions.

The dynamic response of geomaterials is predominantly influenced by external factors such as stress/strain path magnitude, rate, and duration, as well as intrinsic material characteristics like soil type, particle size and shape, and void ratio. Specifically, cyclic shear strain plays a crucial role, with experimental evidence suggesting that soil response varies significantly with the magnitude of applied stress or strain. Below the linear, cyclic threshold shear strain, soil exhibits a linear but not entirely elastic behaviour due to energy dissipation, characteristic of viscoelastic materials. At intermediate strain levels, soils demonstrate non-linear viscoelastic behaviour, with energy losses increasing with the number of excitation cycles.

External conditions such as water saturation and confining pressure also significantly affect the dynamic properties of geomaterials. Water saturation introduces mechanisms like droplet flow and gaseous phase compression, altering attenuation rates. Fully saturated media exhibit higher attenuation for shear waves compared to compressional waves due to enhanced fluid flow. Conversely, increased confining pressure generally leads to reduced attenuation, as it enhances the quantity and durability of interparticle contacts while reducing fluid flow and elastic dispersion.

Frequency plays a pivotal role in the attenuation of wave intensity in saturated soils. Lower frequencies are primarily affected by the soil structure's properties, while higher frequencies see predominant losses due to viscous interactions. The attenuation peak for shear waves in sand varies with frequency and intrinsic permeability, indicating that different soil types and conditions can significantly alter dynamic behaviour.

The development and refinement of non-linear stress-strain models, such as the Hardin-Drnevich model, have been crucial in predicting the behaviour of geomaterials under dynamic loading. These models account for the decrease in shear modulus and increase in damping ratio with increasing shear strain amplitude, providing a more accurate representation of soil behaviour under varying conditions.

The comprehensive review in Chapter 2 highlights the intricate interplay between external conditions, material properties, and dynamic responses of geomaterials. Understanding these interactions is vital for developing accurate models and effective testing methods, ultimately contributing to more reliable geotechnical engineering practices. The insights gained from this literature review underscore the need for continued research and innovation in testing techniques and analytical models to better predict and manage the dynamic behaviour of geomaterials in various engineering applications.

Chapter 3 Materials and Methodology

3.1 Introduction

Chapter 3 details the methodology employed to evaluate the dynamic properties of geomaterials using combined resonant column and torsional shear (RCTS) equipment. This sophisticated equipment, developed through the efforts of Professor Stokoe and his graduate students, is based on earlier designs and incorporates advanced features for precise testing. The chapter begins by describing the setup of the RCTS apparatus, which allows for both low-frequency cyclic and higher-frequency dynamic testing modes, which is crucial for comprehensive material behaviour analysis. Specific sections delve into the resonant column testing in torsion, where the apparatus measures shear modulus and damping ratio using established vibration theories. The design of equipment facilitates accurate shear strain and modulus calculations, leveraging sophisticated data acquisition and control systems. Detailed schematics and descriptions of the apparatus components are provided, illustrating the experimental setup and procedures. Additionally, the chapter covers cyclic torsional shear testing, explaining how torque and displacement measurements are converted into shear stress and strain, generating hysteresis loops used to evaluate material properties. The methodology ensures that various parameters affecting the dynamic response of geomaterials are meticulously measured and analyzed.

3.2 General background

Combined resonant column and torsional shear (RCTS) equipment was employed in this work to evaluate the dynamic properties of geomaterials. This equipment was developed by Professor Stokoe and his graduate students (Isenhower, 1979; Lodde, 1982; Ni, 1987; and Hwang, 1997) following earlier designs by Hall and Richart (1963), Hardin (1965), and Drnevich (1967). The RCTS equipment which was used for this research has a fixed-free configuration. The specimen rests on a fixed bottom pedestal (fixed at the bottom) and is free at the top. The driving plate, which is attached to the top cap, is made up of fixed coils that encircle magnets and are used to excite the top of the specimen with torsional vibrations without restricting it; as a result, the top of the

specimen is considered "free." A simplified diagram of the combined RCTS equipment is presented in Figure 3.1.

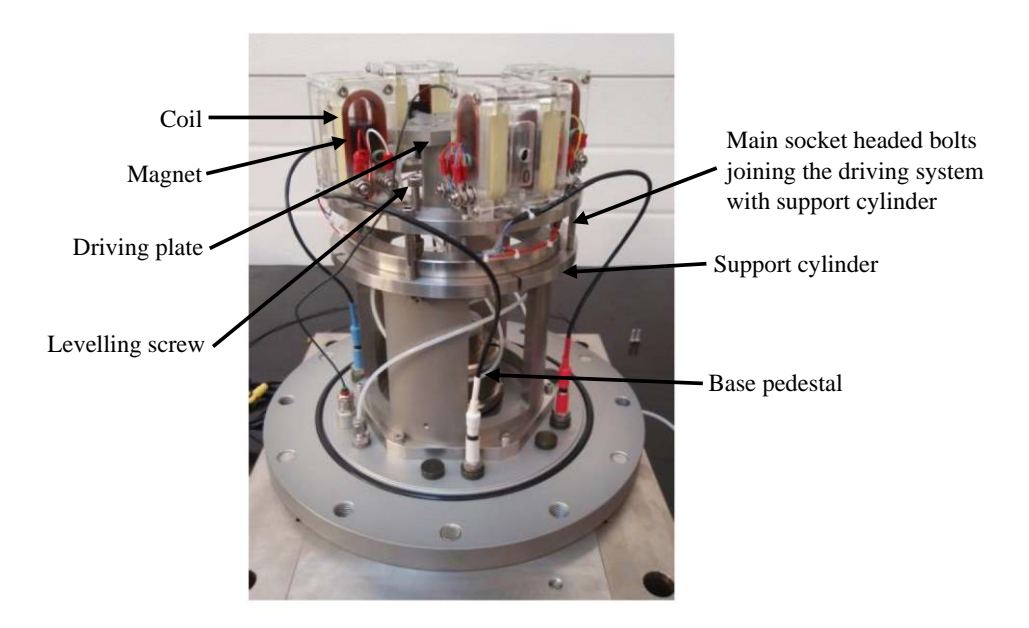
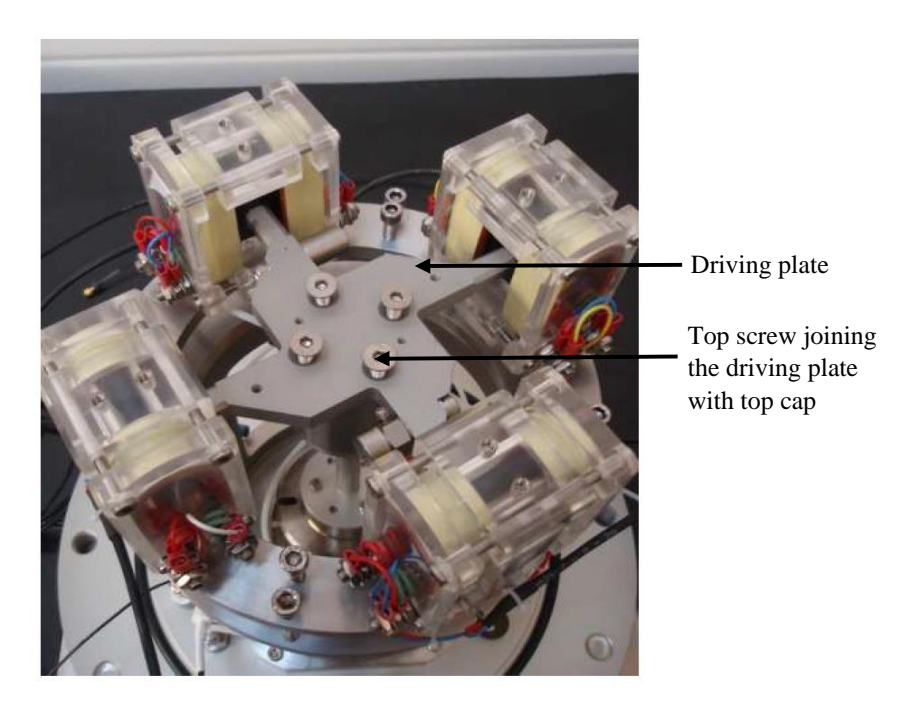


Figure 3. 1 Combined resonant column and torsional shear apparatus

Combined RCTS equipment is capable of testing a soil and rock specimen in two different modes. These modes are 1. low-frequency cyclic testing and 2. higherfrequency dynamic testing during resonance. The data collected from the two independent testing modes can effectively be compared to gain more insight into material behaviour. One of the testing modes is called the torsional resonant column (RC) test, which is based on the theory of torsional wave propagation in a fixed-free cylinder with a mass attached at the free end. In this mode, well-defined boundary conditions and specimen geometry are utilised in evaluating the shear modulus and material damping ratio in shear from measurements at first-mode resonance. The second testing mode is called the cyclic torsional shear (TS) test, which involves monitoring the applied torque and displacement at the top of the specimen. The torque is converted into shear stress, and the displacement is converted into shearing strain. Thus, hysteresis loops, utilised in evaluating shear modulus and material damping ratio, are generated. Selecting the module of torsional shear changes the frequency and amplitude of the current in the coils. The motion monitoring devices used to record the specimen response are also different. The selection of modules can be performed without changing the stress state of the specimen. These changes are performed outside the confining chamber; hence, they can be done without changing the state of stress on the specimen.

3.2.1 Resonant column testing in torsion: In the present study, the Resonant Column Apparatus (RCA) supplied by GDS Instruments UK, in which a cylindrical soil specimen is fixed at its bottom and is provided with the drive mechanism at the top, has been used. The system comprises (i) an electromagnetic drive system which consists of a four-armed plate with Sintered Neodymium Iron Boron rare-earth magnets mounted on each arm along with four pairs of precision wound coils, (ii) an internally mounted counter-balanced accelerometer with a nominal sensitivity of 31.2862 pC/g at 160 Hz, (iii) an amplifier for driving the system, (iv) a high-speed 16-bit data acquisition and control card with an interface panel, (v) GDS RCA v2 software for control and data acquisition of the RCA cell. Figure 3.2 represents a schematic diagram and the photographs of different components of the test apparatus. The RCA control box converts the digital sinusoidal waveform generated by the computer program into an analogue signal with the usage of the high-speed 16-bit data acquisition and the control card. The power amplifier amplifies the generated input signal and then transmits it back to the control box, while the amplified input signal, in turn, is then supplied to the coils of the electromagnetic drive system. This system imposes the oscillatory torque excitation onto the top of the specimen. The electromagnetic force generated due to the application of the sinusoidal voltage to the coils induces an oscillatory motion in the drive plate. The accelerometer, attached to the drive plate, measures the response of the top of the specimen. The accelerometer response is amplified by the charge amplifier and is transmitted to the control box, from where the analog voltage signal is converted to a digital signal, and it is finally analysed by using the computer program. In order to find the resonant frequency of the specimen associated with a given input voltage (maximum of 1V), the software allows running both broad and fine frequency sweep operations. The specimen can be vibrated up to a maximum frequency of 350 Hz. In the broad/fine sweep, the frequency of the specimen is varied at a specified frequency interval. This is held for a specified number of cycles, referred to as the cycle constant, and then steadily decreases in the same way as it was increased. The number of cycles for which the specimen is vibrated can be varied by changing the cycle constant value. The accelerometer amplitude is then calculated by averaging the RMS (root mean square) value for each cycle in the middle 50% of the full data set. The peak amplitude corresponding to a particular frequency increment is then calculated from the known RMS value. Finally, a graph is plotted, as shown in Figure 3.3, with peak amplitude on the vertical axis and the corresponding frequency on the horizontal axis. The frequency

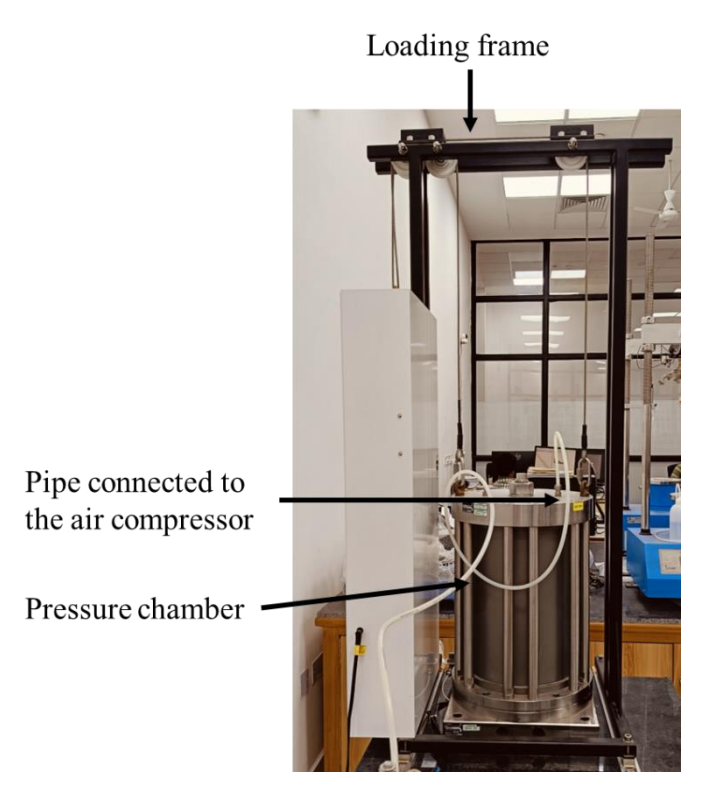
corresponding to the maximum amplitude is taken as the resonant frequency of the specimen with a given input voltage.



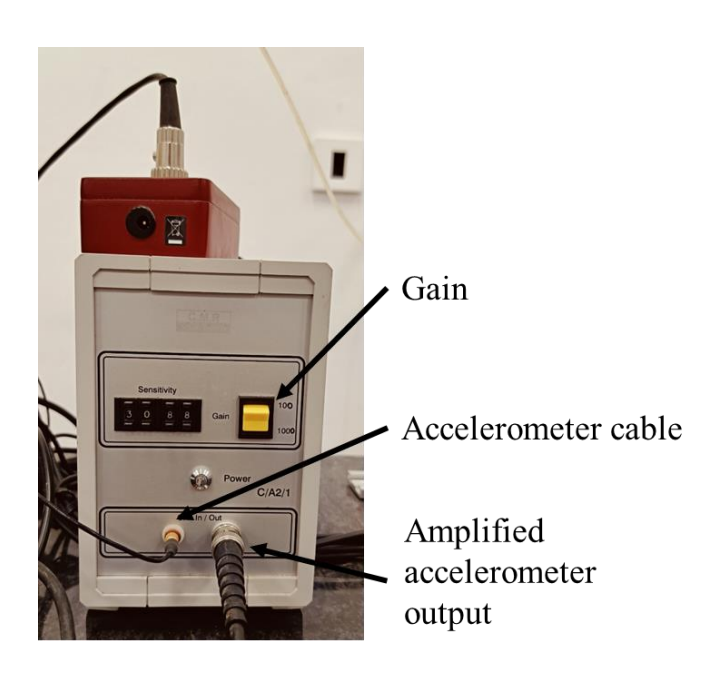
(a) Schematic view of driving plate and top screws of resonant column apparatus



(b) GDS RCA control box, data acquisition system, and the standard and pneumatic pressure controller.



(c) A typical view of the confining cell along with the loading frame



(d) A typical view of the charge amplifier with the gain value set to 100 mV/G.

Figure 3. 2 Schematic view of various components of RCA

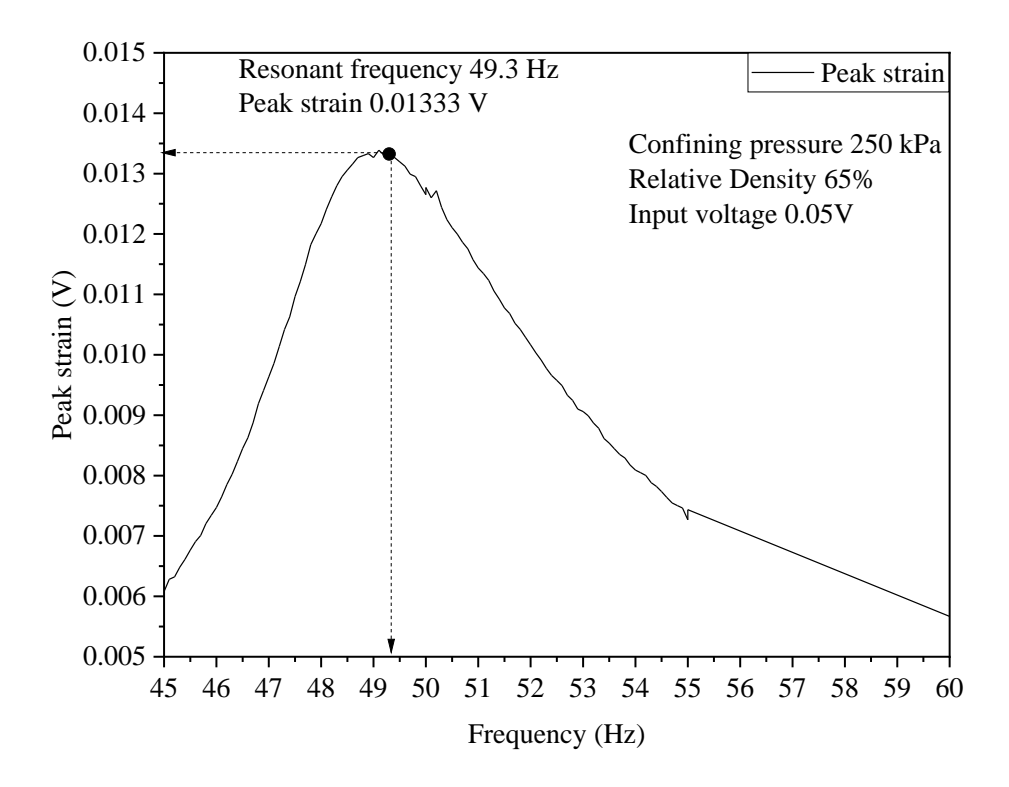


Figure 3. 3 A typical frequency response curve for torsional vibration

3.2.2 Determination of shear modulus (G) from RC testing: After the fundamental mode of vibration is established during the RC test, the shear wave velocity (Vs) of the specimen can be calculated from the measured resonant frequency by using equation 3.1. These equations are based on the theoretical one-dimensional wave propagation solution in an elastic media (Richart et al., 1970).

$$\frac{J_S}{I} = \frac{\omega_n L}{V_S} * \tan\left(\frac{\omega_n L}{V_S}\right) \tag{3.1}$$

where (i) ω_n is the torsional frequency of the specimen, (ii) L is the length of the specimen, and (iii) J_s and J correspond to the mass polar moment of the inertia (about the vertical axis) of the specimen and the additional mass (including the drive system and top cap), respectively. In the case of a solid cylindrical specimen, the mass (m_s) and diameter (d_s) are known, $J_s = \frac{m_s d_s^2}{8}$. Since the drive mechanism has a complex geometry, its mass polar moment of inertia can be obtained from the calibration exercise as discussed in Appendix A. Therefore, the shear wave velocity can be obtained from equation 3.2.

$$V_S = \frac{\omega_n * L}{\beta} = \frac{2\pi f_n L}{\beta} \tag{3.2}$$

where f_n is the resonant frequency obtained from the RC test. With the shear wave velocity and the mass density (ρ) of the specimen being known, the shear modulus can be calculated by using equation 3.3.

$$G = \rho * V_{\mathcal{S}}^2 \tag{3.3}$$

3.2.3 Determination of shear strain (γ) from RC testing: To get acceleration in ms⁻², the peak output must be multiplied by 9.81 and divided by the gain in Volts/G.

$$a = \frac{9.81V}{Gain} (ms^{-2}) \tag{3.4}$$

Where V is the voltage output from the charge amplifier in volts, gain is the charge amplifier gain in Volts/G, which is 100 for this study. The displacement of the accelerometer, $\gamma_{measured}$ is related to the angular acceleration by:

$$a = \omega_n^2 \gamma_{measured} \tag{3.5}$$

Where, $\omega_n = 2\pi f_n$, therefore, the maximum displacement γ_{measured} (in mm), which is measured using the accelerometer at resonance, is given in equation 3.6.

$$\gamma_{measured} = \frac{9.81*V}{4\pi^2 f_n^2} = \frac{0.24849*V}{f_n^2}$$
 (3.6)
V is the voltage applied in Volts, and f is the resonant frequency obtained in Hertz. The

V is the voltage applied in Volts, and f is the resonant frequency obtained in Hertz. The angle of twist measured at the top of the specimen can be obtained using the following equation 3.7:

$$\theta = \frac{\gamma_{measured}}{I} \tag{3.7}$$

Where *l* is the offset of the accelerometer from the axis of rotation with a value of 0.04325 m for the apparatus used in this study. Finally, upon consideration of the geometry of the testing sample, the shearing strain produced for a solid cylindrical specimen can be obtained as:

$$\gamma = \frac{0.8 * R * \theta}{L} = \frac{4.596 * V * R}{f_n^2 * L}$$
(3.8)

Where L is the length of the test sample (m), and R is the radius of the sample (m).

3.2.4 Determination of damping ratio (D) from resonant column testing: At small strains (in the linear range, $\gamma < 10^{-4}\%$), the material damping ratio in shear, D, of the specimen can be measured by the half-power bandwidth method as given in equation 3.9:

$$D = \frac{\omega_2 - \omega_1}{2\omega_n} \tag{3.9}$$

Where, $\omega_2 - \omega_1$ is the bandwidth in rad/sec, ω_n is the resonant frequency in rad/sec, ω_1 and ω_2 are the minimum and maximum frequencies corresponding to 1/1.414 times the maximum amplitude obtained at resonant frequency respectively.

However, due to the nonlinear behavior of geomaterial, material damping ratios estimated by the half-power bandwidth approach become erratically greater when shear strain increases, i.e., $\gamma > 10^{-4}\%$. In this instance, the free-vibration decay method is more appropriate, and the half-power bandwidth method is not appropriate (Ni, 1987). In a free vibration test, the specimen is driven with a sinusoidal force at its resonant frequency in steady-state motion. The driving force is then suddenly turned off, and the sample is allowed to vibrate freely. The relative motion between the magnets and the coils causes a change in the magnetic flux, which results in the generation of an electromotive force that opposes the motion (back-EMF). The generation of the back-EMF leads to a dissipation of energy in the system and significantly affects the measured damping ratio (Wang et al., 2003). In the present experimental setup, during the free vibration decay, the RCA software completely switches off the hardware to provide an open circuit to prevent the generation of the equipment damping errors caused by the generation of back-EMF. The material damping ratio is calculated from the free-vibration decay curve as shown in Figure 3.4.

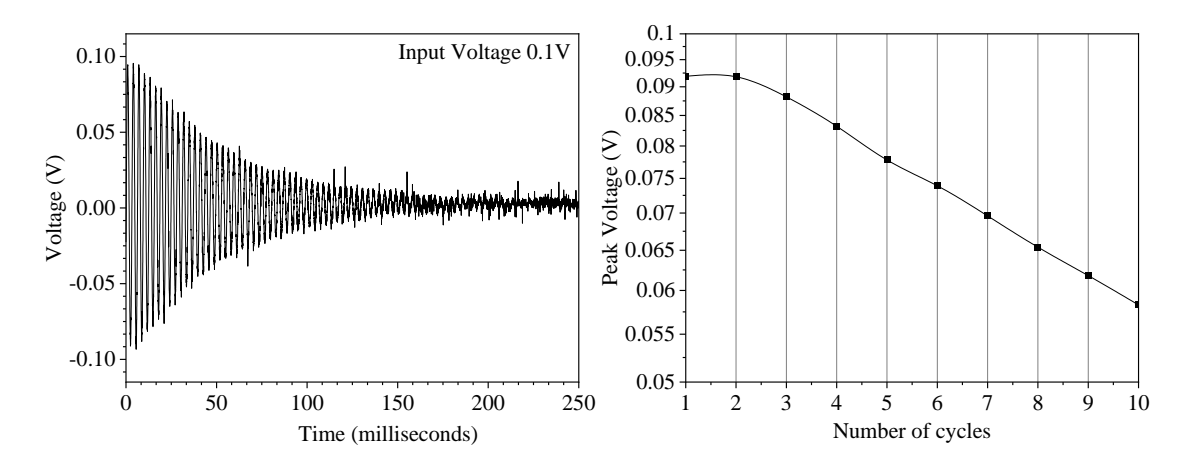


Figure 3. 4 A typical graph of free vibration decay of vibration in torsion

The logarithmic decrement, δ , is defined from the free-vibration decay curve as:

$$\delta = \frac{1}{n} \ln \left(\frac{Z_1}{Z_{n+1}} \right) \tag{3.10}$$

where n equals number of cycles between two peak points in the time record, and z_1 and z_{n+1} are the amplitudes of cycle 1 and cycle n+1, respectively (Richart et al., 1970). The material damping ratio can then be calculated using equation 3.11.

$$D = \frac{100\%}{2\pi n} ln \left(\frac{Z_1}{Z_{n+1}}\right) \tag{3.11}$$

At small strain levels ($\gamma < 10^{-4}\%$), material damping ratios measured by the free-vibration decay method generally show some scatter due to the impact of ambient noise. On the other hand, material damping ratios measured by the half-power bandwidth method show less scatter.

3.3 Cyclic torsional shear testing

Analyzing the frequency-dependent mechanical behavior of geomaterials under dynamic loading using conventional RC testing is very challenging. The non-resonance (NR) method is an appealing approach for studying the behavior of geomaterials over a range of frequencies of excitations. In this method, the shear modulus (G) and material damping ratio (D) can be estimated together at a definite excitation frequency. The conventional RC apparatus with a fixed-free configuration can be utilized to obtain the dynamic properties of geomaterials by employing the NR method under a definite frequency and amplitude of loading. The method is based on the elastic-viscoelastic correspondence principle proposed by Christensen 1971. However, the principle is limited to time-invariant boundary condition problems. This principle states that the analytical solution for any linear viscoelastic problem finds its roots in the corresponding elastic problem solution. The solution of the torsional excitation of the cylindrical specimen can be formulated by initially determining the solution for an elastic specimen, and the solution of a viscoelastic specimen can be extracted by adopting the elastic-viscoelastic correspondence principle.

The solution of a solid cylindrical, elastic rock specimen can be obtained by considering the following assumptions:

- a) The cross-section of the solid-cylindrical specimen is constant.
- b) The displacement amplitude is always proportional to the radius of the solidcylindrical specimen.
- c) The cross-sections normal to the axis of the solid-cylindrical specimen remain plane and normal to the axis during the torque application.

The governing equation of motion for a cylindrical specimen undergoing harmonic torsional excitation (Hardin, 1965) can be written as:

$$\frac{\rho}{G}\frac{\partial^2 u_\theta}{\partial t^2} = \frac{\partial^2 u_\theta}{\partial r^2} + \frac{\partial}{r}\frac{u_\theta}{\partial r} + \frac{\partial^2 u_\theta}{\partial z^2} - \frac{u_\theta}{r^2}$$
(3.12)

Where $u_{\theta} = u(r, z, t)$ is the angular displacement at the top end of the specimen in the direction of θ .

$$u_{\theta} = rf(z)g(t) = re^{i\omega t} \left(Asin\left(\frac{\Omega z}{h}\right) + Bcos\left(\frac{\Omega z}{h}\right) \right) \tag{3.13}$$

Where $\Omega = \sqrt{\frac{\rho\omega^2h^2}{G}} = \frac{\omega h}{V_S}$ and h is the height of the cylindrical specimen, and the constants A and B can be evaluated using the following boundary conditions:

a) The angular displacement at the fixed bottom end of the cylindrical specimen is zero,

$$u_{\theta}(r, h, t) = 0 \tag{3.14}$$

b) A rigid mass is attached to the top free end of the specimen (rotational moment of inertia about the z axis (vertical axis) of the cylindrical specimen, J_o), and an external torque $(T = T_o e^{i\omega t})$ is applied, which produces the angular twist θ , where $\theta(z,t) = \frac{-u_{\theta}(r,z,t)}{r}$. The twisting moment at the free end of the specimen, i.e., at z = 0 is:

$$M(0,t) = T_o e^{i\omega t} - J_o \ddot{\Theta}(0,t)$$
 (3.15)

The twisting moment M(z,t) can be obtained by integrating the non-zero stress component, i.e., $\tau_{\theta z} = G \frac{\partial u_{\theta}}{\partial z}$ over the cross-sectional area of the cylindrical specimen $(S = \pi R^2)$.

$$M(z,t) = \int_{S} \tau_{\theta z}(r,z,t) r \, ds = \frac{\pi R^4}{2} \frac{\rho \omega^2 h}{\Omega} e^{i\omega t} \left(A \sin\left(\frac{\Omega z}{h}\right) - B \cos\left(\frac{\Omega z}{h}\right) \right)$$
(3.16)

The application of the first boundary condition to equation 3.14 yields, $\frac{A}{B} = -\cot(\Omega)$. The ratio of applied torque (T) and the angular twist produced at the top of the specimen $(\theta(0,t))$ can be written as:

$$\frac{T_o e^{i\omega t}}{\theta(0,t)} = \frac{\pi R^4}{2} \cdot \frac{\rho \omega^2 h}{\Omega} \left(-\frac{A}{B} \right) - J_o \omega^2 = \frac{\pi R^4}{2} \cdot \frac{\rho \omega^2 h}{\Omega} \cot(\Omega) - J_o \omega^2$$
(3.17)

The analytical solution for viscoelastic material undergoing harmonic torsional excitation holds the same form as that for the elastic medium (Read 1950). Therefore, the elastic constants for viscoelastic material are substituted by complex-valued constants, and equation 3.17 can be expressed as:

$$\frac{T_o e^{i\omega t}}{\theta(0,t)} = \frac{\pi R^4}{2} \cdot \frac{\rho \omega^2 h}{\Omega^*} \cot(\Omega^*) - J_o \omega^2$$
(3.18)

Where $\Omega^*(\omega) = \sqrt{\frac{\rho\omega^2h^2}{G^*(\omega)}}$ and G^* is complex shear modulus, which can be expressed as:

$$G^*(\omega) = G_1(\omega) + iG_2(\omega) \tag{3.19}$$

Where $G_1(\omega)$ is the real part expressing the storage modulus and $G_2(\omega)$ is the imaginary part expressing the loss modulus. The value of shear modulus for the viscoelastic material can be expressed as $G^*(\omega)$, whose value can be obtained from the experimental observations of the magnitude of torque applied and the angle of twist produced at the free end of the specimen.

In cyclic TS testing, a slow torsional loading is applied at the top of the specimen. The loading frequency used in TS testing is much lower than resonance testing (at least 10 times less than the resonant frequency). The current in the calibrated drive coils is monitored, and the torque applied to the specimen is calculated. In the NR method, periodic torsional shear loading at a particular frequency (below resonant frequency) is enforced at the free end, i.e., top of the testing sample, with a coil-magnet driving system. The response of the tested material against the torsional shear loading is recorded in the form of an angle of twist, and a stress-strain curve is obtained corresponding to the specific excitation frequency. The dynamic properties of G and D can be elucidated from the shear stress-strain hysteresis curve.

3.3.1 Determination of shear modulus and damping ratio from cyclic torsional shear testing: An arrangement of magnets and coils connected in series helps to provide an overall torque at the top of the specimen when current flows through it. The twist of the specimen against the torque deployed at the topmost part of the specimen is measured using a set of proximitors. The proximitor arrangement consists of a proximitor probe and a sensor, as presented in Figure 3.5. The proximitor sensor is fitted at the top of the driving plate, and its probe is positioned at a definite distance from the sensor to move freely, as shown in Figure 3.6. The air gap between the proximitor sensor

and probe should not be more than 1.2 mm to measure the twist angle precisely (The GDS Resonant Column System Handbook, 2007).

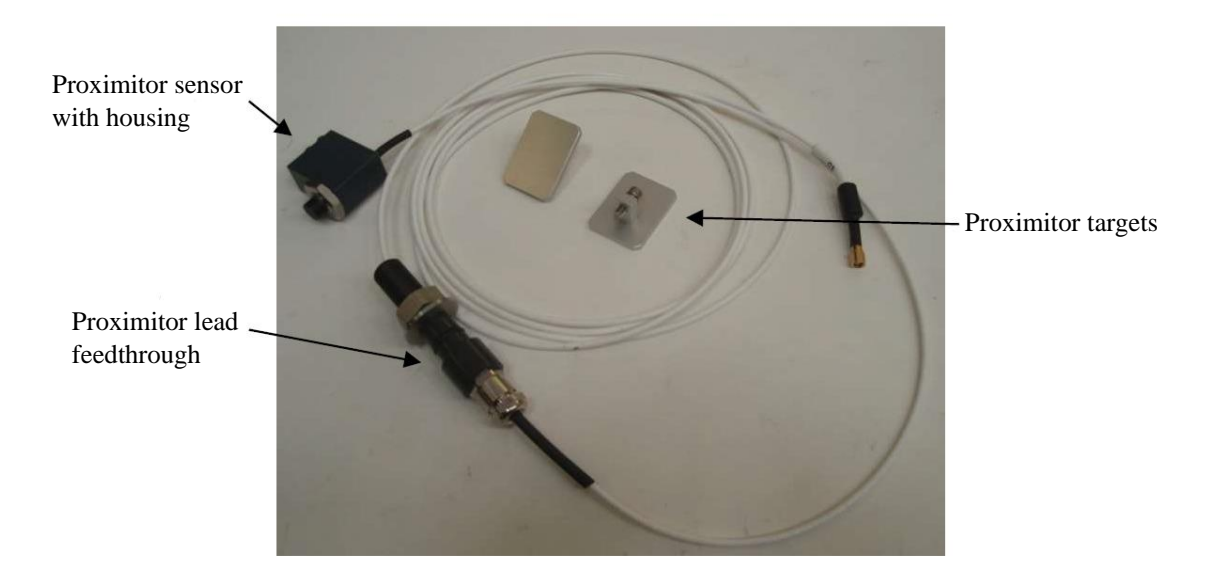


Figure 3. 5 Schematic view of the proximitor arrangement of resonant column apparatus

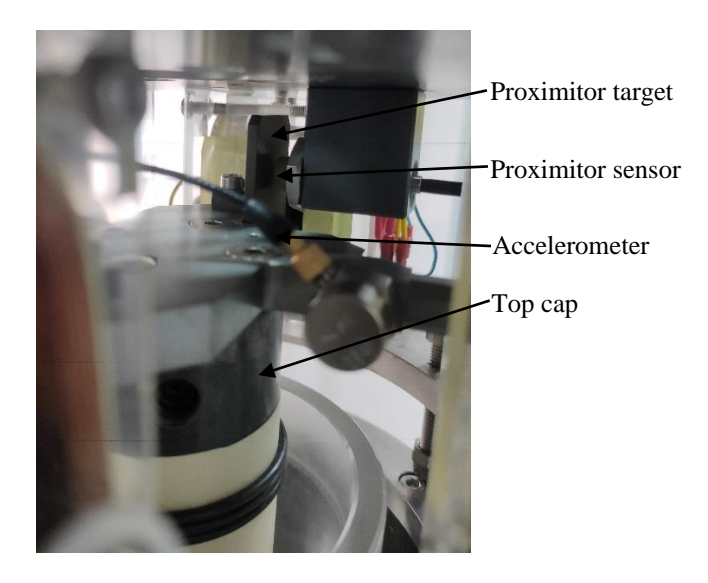


Figure 3. 6 Schematic view of the proximitor set-up for twist measurement

The response of material to one cycle of cyclic torsional shear loading is evident through the shear stress-strain hysteresis loop, illustrating energy dissipation within the specimen during loading (refer to Figure 3.7). The Figure 3.7 shown here is for 10 cycles, with each loop comprising 40 shear stress-strain points, totalling 400 points. The normalized shear modulus is derived from the 10 hysteresis loops, calculated as the ratio of maximum shear stress to the maximum shear strain produced throughout the testing.

The material damping ratio (D) is determined by the ratio of the cumulative loss area of the normalized hysteresis loops to $1/4\pi$ times the area of the triangle AOB formed by multiplying the maximum shear stress and maximum shear strain of the normalized hysteresis loop. Figure 3.7 displays the hysteresis loop obtained after normalizing the shear stress-strain data from the testing. The cumulative area of the normalized hysteresis loops is determined using equation 3.20:

Loss Area_{Normalised} =
$$\sum_{n=1}^{400} \frac{1}{2} * (\sigma'_{i+1} + \sigma'_{i}) * (\gamma'_{i+1} - \gamma'_{i})$$
(3.20)

Where, σ'_i is the normalized shear stress obtained by taking the difference of the shear stress obtained (σ_i) and the average shear stress (σ_{avg}) , where $\sigma_{avg} = \frac{\sum_{i=1}^{400} \sigma_i}{400}$; the normalized shear strain (γ_{avg}) can be obtained by taking the difference of the shear strain and the average shear strain $(\gamma_i - \gamma_{avg})$, where, $\gamma_{avg} = \frac{\sum_{i=1}^{400} \gamma_i}{400}$.

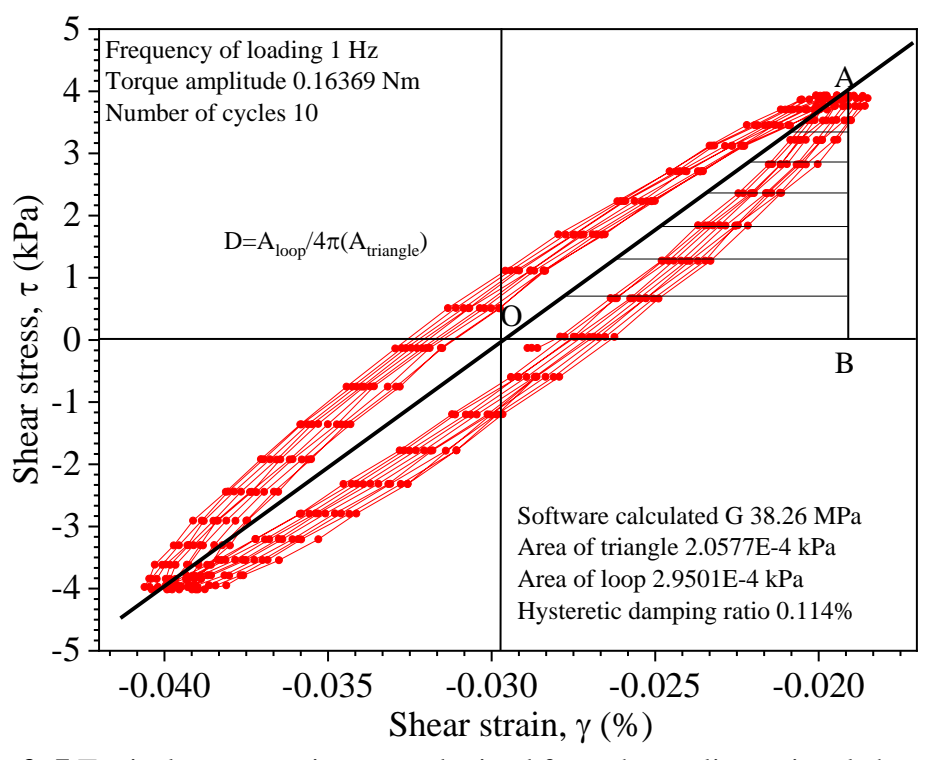


Figure 3. 7 Typical stress-strain curve obtained from the cyclic torsional shear testing of gypsum plaster

3.3.2 Determination of shear strain from cyclic torsional shear testing: When the output current flows through the coil-magnet driving system, the net torque (T) deployed at the top end of the testing specimen can be determined from the relation between the torque calibration factor $(C_t, Nm/V)$ and the applied driving voltage (V_t, V_t, V_t)

Volt). The GDS resonant column apparatus employed in this study has a calibration factor of 0.5456 Nm/V, with the maximum torque that can be applied as 0.5456 Nm.

$$T = C_t * V_t \tag{3.21}$$

The shearing stress produced in the specimen is computed as:

$$\tau = R * T/J \tag{3.22}$$

Where R is the radius of the cylindrical specimen, J is the polar moment of inertia, and T is the torque applied at the topmost end of the specimen.

The angle of twist (α) (in terms of angular deflection measured by proximitor in mm) due to the applied torque can be obtained by combining the strain calibration factor (C_s , mm/mV) and the applied output voltage (Volt). The strain calibration factor of the equipment employed in the present study is 0.000314166 mm/mV. Figure 3.8 represents the twist provided at the top end of the testing sample, and the proximitor probe displacement α is noted under the action of the twist applied.

$$\alpha = C_s * V_t \tag{3.23}$$

The maximum angle of twist (at the center of the top of the cylindrical sample in degrees) can be obtained as:

$$\theta = \frac{(360 * \alpha)}{\pi * D} \tag{3.24}$$

Where D is the gap within the center line of the rotor arm and the center of the proximitor (i.e., 0.08 m for the equipment employed), as displayed in Figure 3.9. The maximum twist angle measurable by the proximitor used in this study is 4.5°.

In the NR method, the shear stresses are applied about the z-axis of the cylindrical test specimen for which the stress distributes non-uniformly in the testing specimen. The stresses are maximum at the outer surface and zero at the center of the cylinder, as displayed in Figure 3.10. To counter the problem of the non-uniform distribution of stresses in solid test samples, Chen & Stokoe (1979) suggested the usage of the equivalent radius of 0.82*R for the amplitude of shear strain below $10^{-3}\%$ and 0.79*R for shear strain amplitudes more than or equal to $10^{-1}\%$. The amplitude of shear strain (γ) can be measured as:

$$\gamma = 0.82 * R * \theta / L \tag{3.25}$$

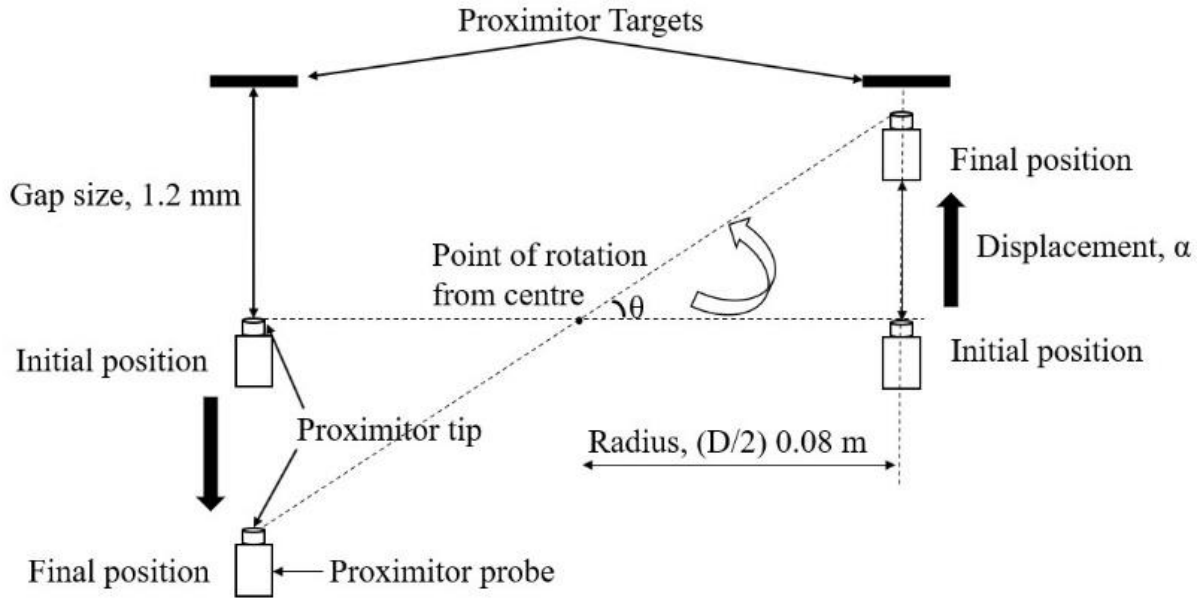


Figure 3. 8 Simplified illustration of twist applied at the topmost end of the testing sample

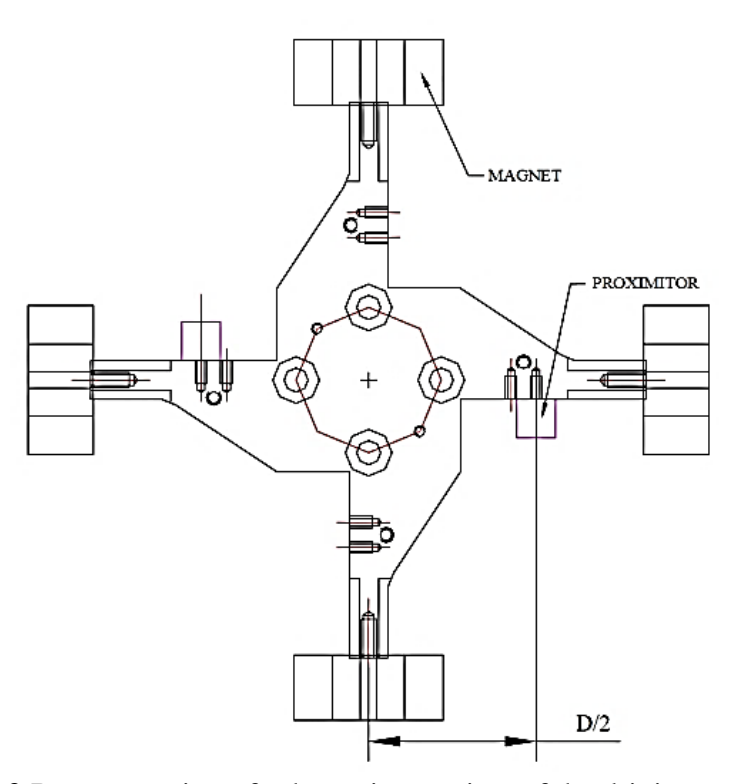


Figure 3. 9 Representation of schematic top view of the driving arrangement

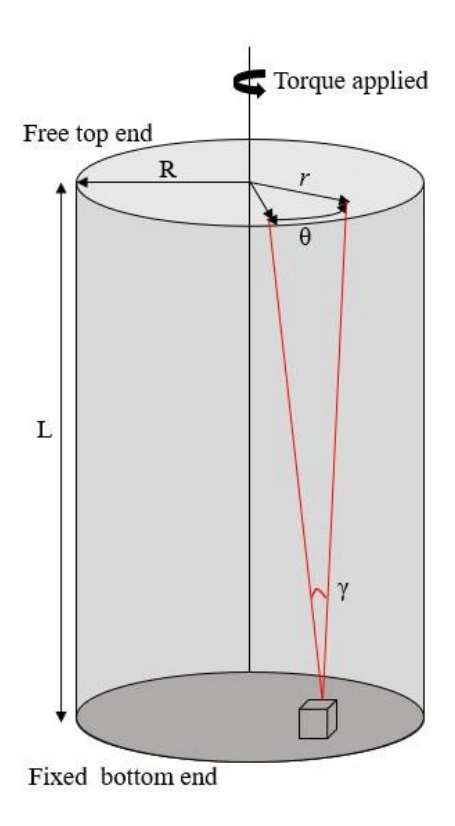


Figure 3. 10 Representation of schematic top view of the twist and shear produced in the specimen

3.4 Suitability of using RCA in rock mechanics

Resonant Column Apparatus (RCA) is typically utilized to determine the dynamic properties of soils under low strain conditions, primarily because it encounters difficulties when testing rigid samples. To mitigate these issues, in this study, Point of Plasticity (POP) samples were employed instead of rocks, which helped alleviate problems related to sample stiffness, yielding resonant frequencies within the expected range for this apparatus. Nonetheless, the apparatus required validation against specified stiffness criteria.

Common challenges encountered when testing rigid samples include sample stiffness surpassing certain thresholds, inadequate fixation of the bottom pedestal, coupling issues between the sample and end platens, and overestimation of damping due to the generation of back electromotive force (EMF) from magnets and solenoids. When rigid samples are tested for resonance, the natural frequencies of both the apparatus and samples may interfere, undermining the assumption of a fixed apparatus base. ASTM guidelines stipulate that the base can only be considered fixed if its mass exceeds the specimen mass by a factor of 100, as per Ashmawy and Drnevich's (1994)

recommendations. Similarly, ASTM D 4015-92 (2000) specifies fixity conditions for the bottom pedestal.

The adherence of the RCA setup to these fixity conditions was verified and found to be satisfactory. Drnevich (1978) advises that the shear modulus of the testing sample should not exceed 10% of the material's modulus from which the apparatus is constructed, a criterion validated against the shear moduli of POP and stainless-steel samples.

To prevent slippage of stiff samples from the base platens during vibration application, epoxy resins were applied to secure them, enhancing the linear mode shape of vibration. Furthermore, to counteract the adverse effects of back EMF, which can lead to energy dissipation during damping tests, the RCA used in this study allowed for an open circuit during free vibration decay, preventing the generation of back EMF.

Despite compliance with stiffness limits, sample stiffness may still cause underestimation of natural frequencies during RCA testing, potentially affecting shear and compression wave velocities. Corrections were, therefore, devised to adjust the obtained resonance frequency values and obtain accurate natural frequencies of the samples.

3.5 Materials used for the testing

This thesis involves extensive use of resonant column and cyclic torsional shear testing to investigate the dynamic properties of soil and simulated rock samples. Detailed information regarding the material properties of these samples, as well as the specific methodologies employed in the testing process, is provided in the subsequent sections.

3.5.1 Sutlej River sand: For the present study, the soil samples representing poorly graded sand with sub-angular-shaped particles were procured from the Sutlej Riverbank, Punjab, India. The index properties of the soil used for the experiments are presented in Table 3.1. The high-resolution images of sand particles were extracted using scanning electron microscopy (SEM), depicting the sub-angular nature of the particles as shown in Figure 3.11. The previous studies revealed that the particle shape of soil significantly affects the collapse settlement of soil subjected to shearing and wetting (Mahinroosta & Oshtaghi, 2021). The energy-dispersive X-ray diffraction (EDX) analysis of the soil sample indicated that the primary components of sand were

silica and tantalum compounds, as shown in Table 3.2. Tantalum, renowned for its ability to store and release energy and high resistance to corrosion properties, is also used as a substitute for Platinum. Ben-Moshe et al., 2013 stated that the presence of metal oxides holds a significant role in pedogenesis. The grain size distribution curve for the soil and the limiting gradation curves for liquefaction susceptible soil (Tsuchida, 1970) are shown in Figure 3.12, where Sutlej River fine sand was observed to fall in the most liquefiable zone, proposing a need for the dynamic analysis of soil.

Table 3. 1 Index properties of Sutlej Sand

Type of sand	Fine-grained sand
USGS classification	SP
Specific gravity (G _s)	2.60
Degree of roundness of particles	Sub angular
Maximum dry unit weight (γ _{dmax}) g/cc	1.62
Minimum dry unit weight (γ _{dmin}) g/cc	1.45
Maximum void ratio (e _{max})	0.79
Minimum void ratio (e _{min})	0.60
D ₁₀ (mm)	0.18
D ₃₀ (mm)	0.24
D ₆₀ (mm)	0.33
Uniformity coefficient, Cu	1.85
Coefficient of curvature, C _c	0.99

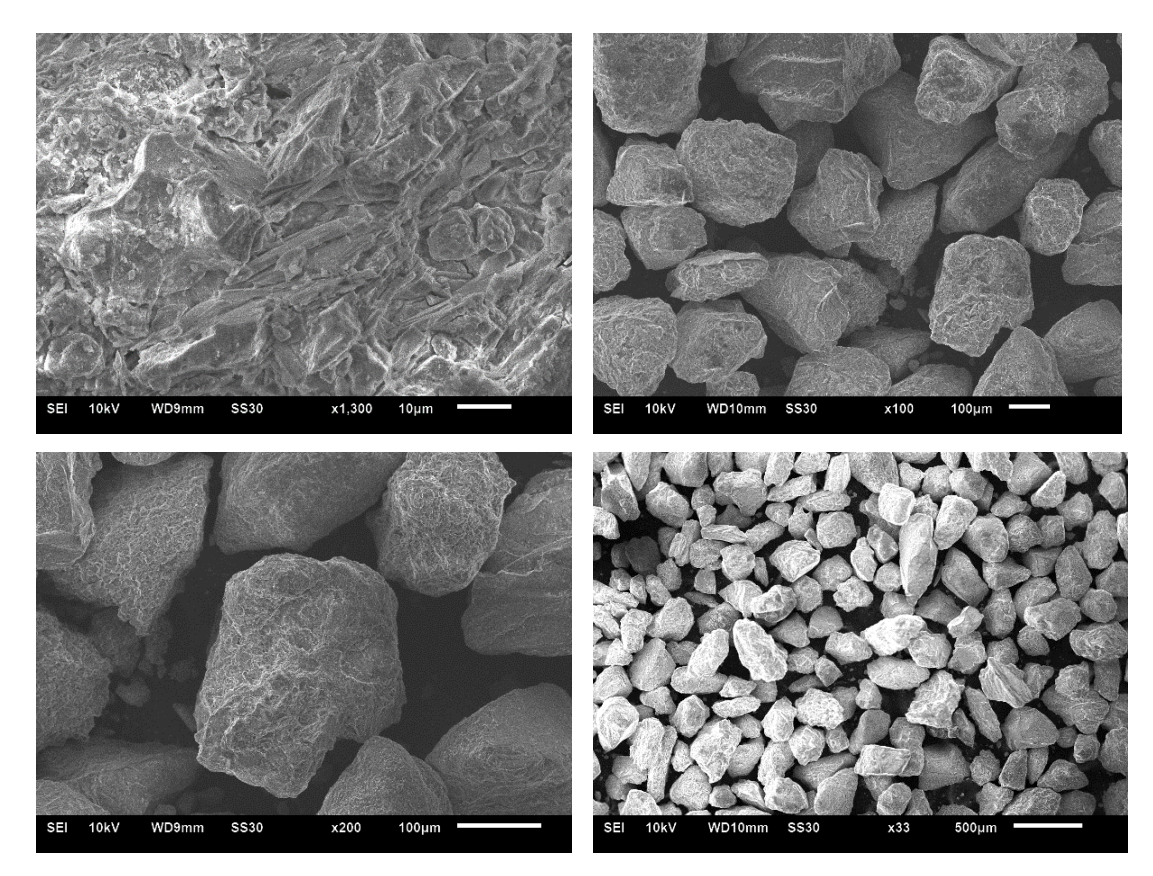


Figure 3. 11 SEM images of Sutlej River sand samples

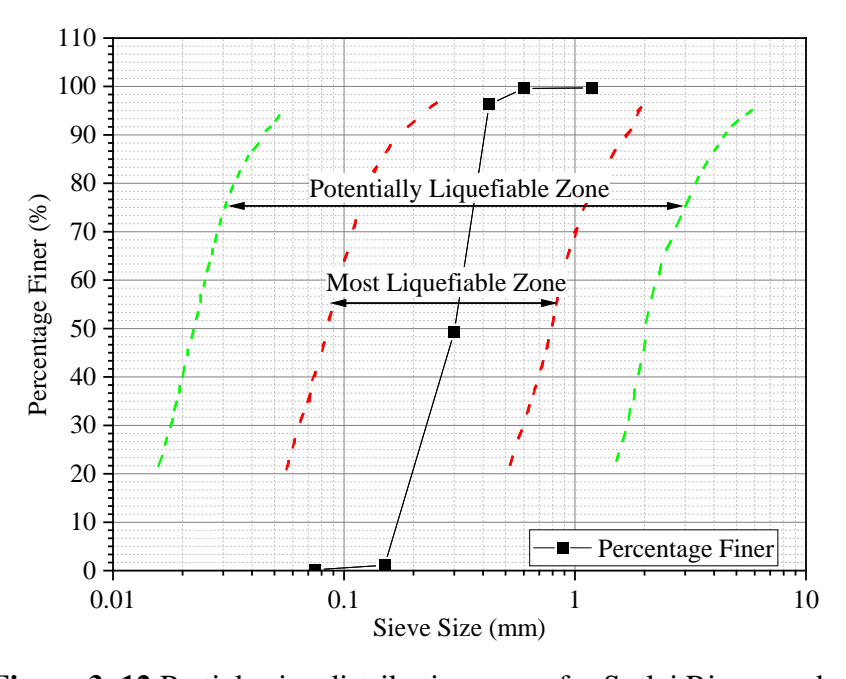


Figure 3. 12 Particle size distribution curve for Sutlej River sand

Table 3. 2 EDX analysis of Sutlej River sand

Element	Atomic	Mass (%)	Mass Normalized
	Number		(%)
Oxygen	8	88.78	51.91
Magnesium	12	1.20	0.70
Aluminium	13	6.12	3.58
Silicon	14	50.10	29.29
Potassium	19	1.18	0.69
Iron	26	5.65	3.31
Tantalum	73	19.99	10.52
	Sum	173.02	100.00

For conducting the dynamic testing of Sutlej River sand using the resonant column apparatus (RC) and the cyclic torsional shear test (CTS), soil samples of uniform relative density were required. The pluviation technique (Vaid & Negussey, 1984; Cresswell et al., 1999) was adopted to achieve uniformity in the relative density of the testing samples. The samples were prepared using the thin-walled cylindrical split mould of 38 mm internal diameter and 114 mm height. The initial calibration exercise was necessary to establish a relationship between the relative density of the specimen and the related fall height. The pluviation technique demonstrated by Kumar and Madhusudhan (2010) was adopted in the present study. The sand was allowed to fall freely in the PVC tubes from the nozzle of a funnel. These tubes had a diameter of 35 mm and the lengths were varied to achieve different relative densities values. To ensure the uniformity of the specimen, sand was permitted to fall freely from the funnel onto the apex of a wire mesh of 2.5 mm aperture size, which was placed on the top end of a vertical PVC tube. The calibration plot of height and relative density for Sutlej River sand is shown in Figure 3.13. With the help of a calibration plot, the heights of fall were determined for different relative densities used to perform the testing.

The oven-dried sand was initially cooled in a desiccator for more than 2 hours, and this sand was poured into five equal layers from a controlled height to the cylindrical split mould placed at the base of the resonant column apparatus. The cap (50 mm diameter) was then positioned on the specimen. A thin layer of silicon grease was applied to the

side of the cap, and the membrane was sealed onto the cap using the O-rings. Using a spirit level ensured that the top cap remained absolutely horizontal. A vacuum (less than 50 kPa) was exerted from the bottom of the specimen so that the sand specimen remained intact without any confining pressure. The dimensions of the specimen were accurately measured with the Vernier calipers having a least count of 0.02 mm. To account for the thickness of the latex membrane, necessary correction was also applied. This was done by measuring exactly the diameter of a 38 mm metallic mould, both with and without the inclusion of the stretched membrane. The membrane thickness was half the difference between the two diameter readings. The specimen was placed in a silicon oil bath using a Perspex cylinder. The drive system was rigidly connected to the top cap by four screws and fixed to the support frame after the coils were carefully aligned such that the magnets were centered and free to move within the coils. The accelerometer was connected following which the cylindrical pressure chamber was placed and fixed to apply the confining pressure. After the required confining pressure was applied, the vacuum created earlier was released.

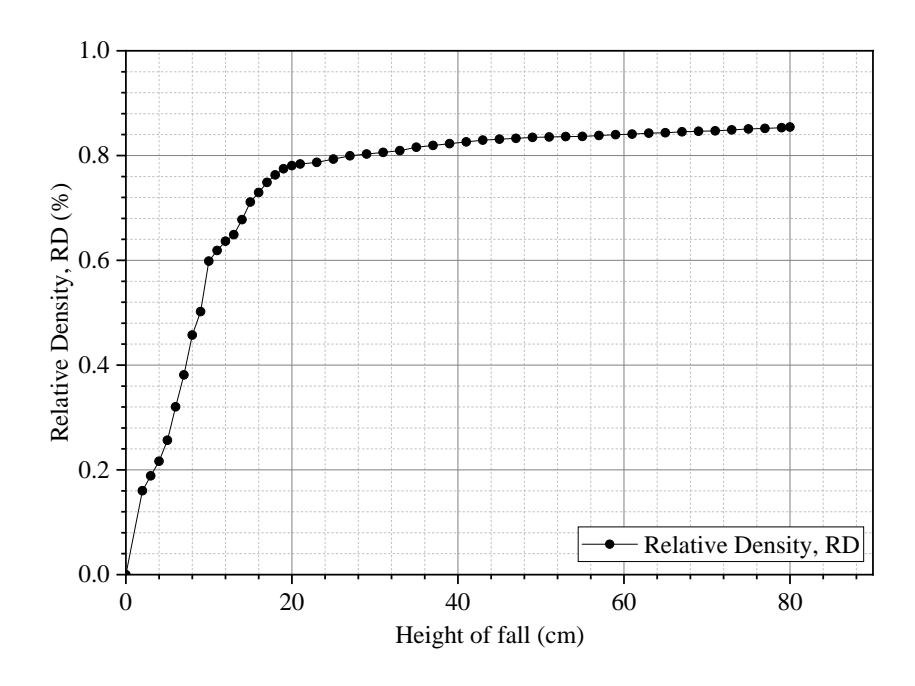


Figure 3. 13 Calibration plot of relative density with the height of fall.

3.5.2 Gypsum plaster specimen: Adopting model materials for conducting studies in rock mechanics is very common, as obtaining jointed rock samples is practically difficult and expensive. Plaster of Paris samples have the advantages that they are easily reproducible, easily available, and economical. Ramamurthy and Arora (1994) used

Plaster of Paris samples for simulating rocks, whereas Cha et al. (2009) used dental gypsum discs to study rock behavior during wave propagation and measured wave velocities across them. Indraratna and Haque (2000) also used gypsum plaster as a model material for studying the shear behavior of rock joints.

Plaster of Paris (POP), or gypsum plaster, is produced by heating gypsum to about 150° C (gypsum is a crystalline sedimentary rock). When the dry plaster powder is mixed with water, it reforms into gypsum plaster. All laboratory experiments were conducted on hardened gypsum plaster samples simulating soft rocks in the present work. The material manufactured by the same manufacturer and batch number was utilized to maintain consistency across all samples. To ensure consistent material properties of gypsum plaster across different testing conditions, it was necessary to experiment with various plaster of Paris (POP) to water ratios, given the variations in the shape and size of the specimens. The samples required for testing were prepared by pouring POP-water mix into prefabricated split moulds and removing the set samples after a few hours. Then, the samples were dried under normal room temperature and humid conditions for 13-15 days to attain constant weight. Among the tested combinations, the 3.75:1 (POPto-water ratio) was identified as the optimal ratio, providing a workable mix with consistent properties throughout the testing process, which resulted in a gypsum plaster density of 1.69 g/cc after 15 days. A hardened gypsum plaster sample is shown in Figure 3.14. Uniaxial compressive strength (UCS) tests were carried out on representative samples with a length-to-diameter ratio of 2:1, following ASTMD7012-23, keeping the strain rate of UCS equipment as 1.25 mm/minute. In compliance with ASTM E122-17, an average UCS value has been obtained based on testing three specimens to ascertain the UCS value of the intact gypsum plaster specimen. Figure 3.15 depicts the uniaxial compressive stress-strain curve of hardened gypsum plaster utilized in this investigation. The engineering properties of the prepared samples are given in Table 3.3. The Uniaxial Compressive Strength (UCS) of the intact sample indicates that the material comes under the class of 'very weak rock' (Grade R1) as per the classification of intact rocks by ISRM (1978). Based on the modulus ratio (ratio of tangent modulus at 50% of failure stress to UCS), the material falls under the class 'L' (low modulus ratio), and based on UCS, it belongs to the class of 'E' (Very low strength) as per Deere – Miller's (Deere & Miller, 1966) classification of intact rocks.

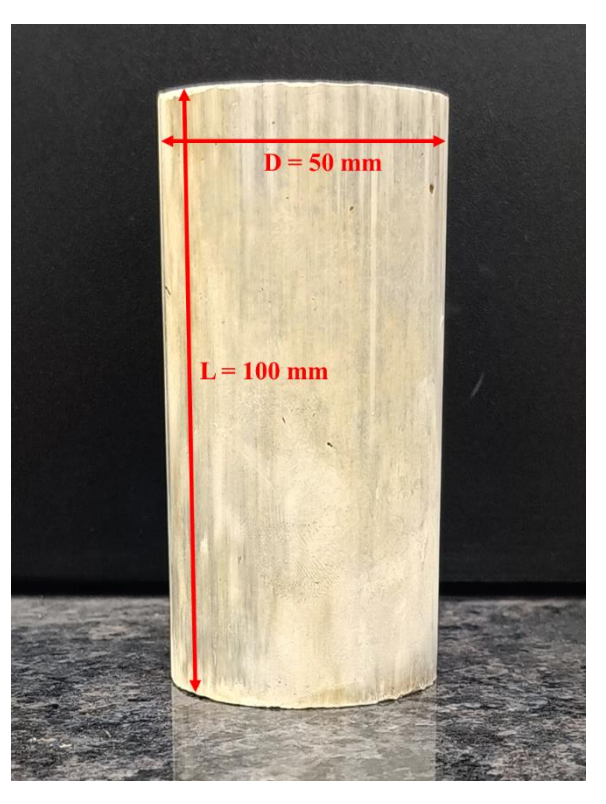


Figure 3. 14 A typical view of hardened gypsum plaster specimen

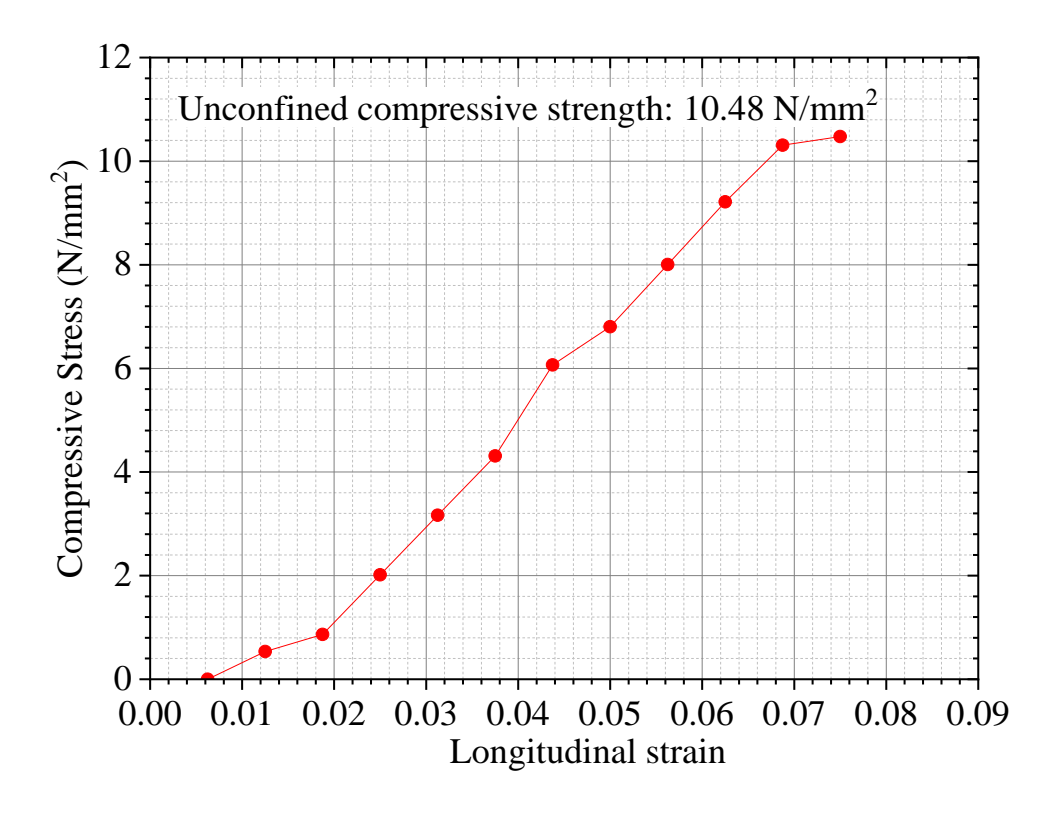


Figure 3. 15 Stress-strain curve of intact gypsum plaster in compression

Table 3. 3 Engineering properties of the gypsum plaster

Material	Gypsum plaster
Dimensions, shape	Diameter = 50 mm, height = 100 mm,
	Cylinder
Density (g/cc)	1.695
Young's Modulus (GPa)	1.702
Unconfined compressive strength (MPa)	14.38
Poisson's ratio	0.23
ISRM classification	Low strength

3.6 Summary

Chapter 3 outlines a robust methodology for assessing the dynamic properties of geomaterials using the RCTS equipment. The chapter meticulously details the experimental setup, including the design and components of the resonant column and torsional shear apparatus. By employing both resonant column and cyclic torsional shear tests, the methodology provides a comprehensive analysis of shear modulus and damping ratio. These tests are critical for understanding the material behaviour under different stress and strain conditions. The resonant column tests focus on determining shear wave velocity and modulus through torsional vibration theories, while cyclic torsional shear tests provide insights into material damping through hysteresis loop analysis. The chapter emphasizes the precision and reliability of the measurements, facilitated by advanced data acquisition systems. The concluding remarks highlight the importance of this methodology in providing accurate and reliable data on geomaterial properties, which are essential for various geotechnical engineering applications. This detailed methodological framework sets a solid foundation for further research and practical applications in the field of dynamic material testing.

Chapter 4

Dynamic Characterization of Sutlej River Sand: Insights from Resonant Column and Cyclic Torsional Shear Tests

4.1 Introduction

Chapter 4 delves into the dynamic properties of Sutlej River sand through rigorous experimental analysis. The chapter outlines the methodology and results of Resonant Column (RC) tests and Cyclic Torsional Shear (CTS) tests conducted to assess the behavior of sand under varying strain amplitudes, confining pressures, and relative densities.

The RC tests focus on the sand's response at low to medium strain amplitudes, utilizing a modified Stokoe-type apparatus to determine shear modulus and damping ratio across different experimental setups. The data collected cover a range of relative densities (35%, 55%, 65%, and 75%) and confining pressures (50 kPa to 250 kPa), providing a comprehensive understanding of the material's dynamic characteristics under controlled conditions.

In parallel, CTS tests investigate the sand's behavior at medium to high strain amplitudes and under cyclic loading at various frequencies (0.1 Hz to 10 Hz). These tests reveal critical insights into how shear modulus and damping ratio evolve with changes in strain amplitude, loading frequency, and confining pressure. The results demonstrate a significant dependency of these properties on loading frequency and strain amplitude, with detailed regression analyses elucidating the correlations.

The chapter culminates with the development of normalized shear modulus and damping ratio curves specific to the site conditions of Sutlej River sand. By comparing these experimental results with established models, such as those proposed by Seed and Idriss (1970) and Darendeli (2001), the study underscores the necessity for site-specific calibration of these models to ensure accuracy in geotechnical applications.

4.2 Test plan for RC testing

The primary goal of the present study is to explore the effect of relative density and confining pressure on the dynamic properties of Sutlej River sand at varying strain levels using resonant column tests. For conducting the experiments, a cylindrical sand specimen diameter of 38 mm and height of 114 mm were used. All the tests were conducted at varying shear strain amplitudes ranging from $10^{-5}\%$ to $10^{-3}\%$. A total of 20 test conditions have been studied for different combinations of relative density conditions, i.e., 35%, 55%, 65%, and 75%, and confining pressures ranging from 50 kPa to 250 kPa in steps of 50 kPa. The experimental conditions for RC tests are shown in Table 4.1.

Table 4. 1 Experimental arrangement for RC testing

		Relative	Density achieved	Confining stress
No.	Test ID	density (%)	(g/cc)	(kPa)
1	SSP-RC1	35	1.503	50
2	SSP-RC2	35	1.503	100
3	SSP-RC3	35	1.503	150
4	SSP-RC4	35	1.503	200
5	SSP-RC5	35	1.503	250
6	SSP-RC6	55	1.537	50
7	SSP-RC7	55	1.537	100
8	SSP-RC8	55	1.537	150
9	SSP-RC9	55	1.537	200
10	SSP-RC10	55	1.537	250
11	SSP-RC11	65	1.555	50
12	SSP-RC12	65	1.555	100
13	SSP-RC13	65	1.555	150
14	SSP-RC14	65	1.555	200
15	SSP-RC15	65	1.555	250
16	SSP-RC16	75	1.573	50
17	SSP-RC17	75	1.573	100
18	SSP-RC18	75	1.573	150
19	SSP-RC19	75	1.573	200

20	SSP-RC20	75	1.573	250

4.2.1 Results of RC testing: It was observed that for all the test conditions, the maximum shear moduli (G_{max}) were obtained when the amplitude of shear strain was near $10^{-5}\%$, as shown in Table 4.2a, where the behavior of sand is nearly linear and, at a particular value of shear strain amplitude (for example, 0.01%), the G value increases appreciably with the increment in confining stress for all relative densities explored as shown in Table 4.2b (for shear strain amplitudes of 0.0001% and 0.001%). Table 4.2 c shows the variation of shear wave velocity with strain amplitude at different confining pressures. The shear modulus and damping ratio curves for different experimental conditions are shown in Figures 4.1 and 4.2. These curves depict that an increment in the magnitude of shear strain amplitudes brings on a declination in the shear modulus value. Additionally, with an increase in shear strain, there is an attenuation of the influence of confining pressure and the relative density on the modulus of the material. The G values were anticipated to enhance remarkably with an advancement in the relative density and confining pressure for a particular strain level.

Table 4.2 a Maximum Shear Modulus (MPa) in different test conditions at a strain level of 0.001% (RC)

Strain level		Maximun	Maximum Shear Modulus at varying confining pressure			
(%)	RD		(kPa)			
0.00001 %	(%)	50 kPa	100 kPa	150 kPa	200 kPa	250 kPa
	35	78.4	86.8	103.3	115.0	125.5
	55	90.8	95.5	100.4	108.4	113.7
	65	114.0	122.5	129.5	135.3	150.2
	75	128.8	141.2	163.8	175.4	174.4

Table 4.2 b Shear Modulus (MPa) in different test conditions at different strain levels (RC)

Strain level (%)		Shear Modulus at varying confining pressure				
	RD			(kPa)		
0.0001 %	(%)	50 kPa	100 kPa	150 kPa	200 kPa	250 kPa
	35	73.1	84.4	99.5	113.7	123.1
	55	84.2	92.6	99.3	107.2	111.9
	65	104.2	117.8	124.3	133.7	146.4
	75	116.4	134.9	161.7	170.3	157.9
0.001 %	35	58.3	67.4	82.6	94.2	102.8
	55	65.6	71.7	80.3	86.2	90.0
	65	75.3	82.4	91.5	98.9	104.6
	75	78.2	92.5	115.6	115.5	115.1

Table 4.2 c Shear wave velocity in different test conditions at different strain levels (RC)

Strain level, %		Shear wave velocity at varying confining pressure (m/s)				
	RD (%)	50 kPa	100 kPa	150 kPa	200 kPa	250 kPa
	35	228.338	240.259	262.102	276.547	288.896
0.00001%	55	243.003	249.213	255.527	265.512	271.925
	65	270.741	280.653	288.56	294.951	310.768
	75	286.13	299.587	322.673	333.903	332.95
	35	220.485	236.914	257.236	274.979	286.12
0.0001%	55	234.005	245.4	254.123	264.038	269.764
0,000	65	258.842	275.216	282.707	293.202	306.811
	75	272.008	292.827	320.598	329.013	316.808
0.001%	35	196.904	211.714	234.374	250.291	261.466
	55	206.548	215.938	228.522	236.768	241.931

65	220.038	230.178	242.556	252.173	259.338
75	222.951	242.48	271.072	270.954	270.485

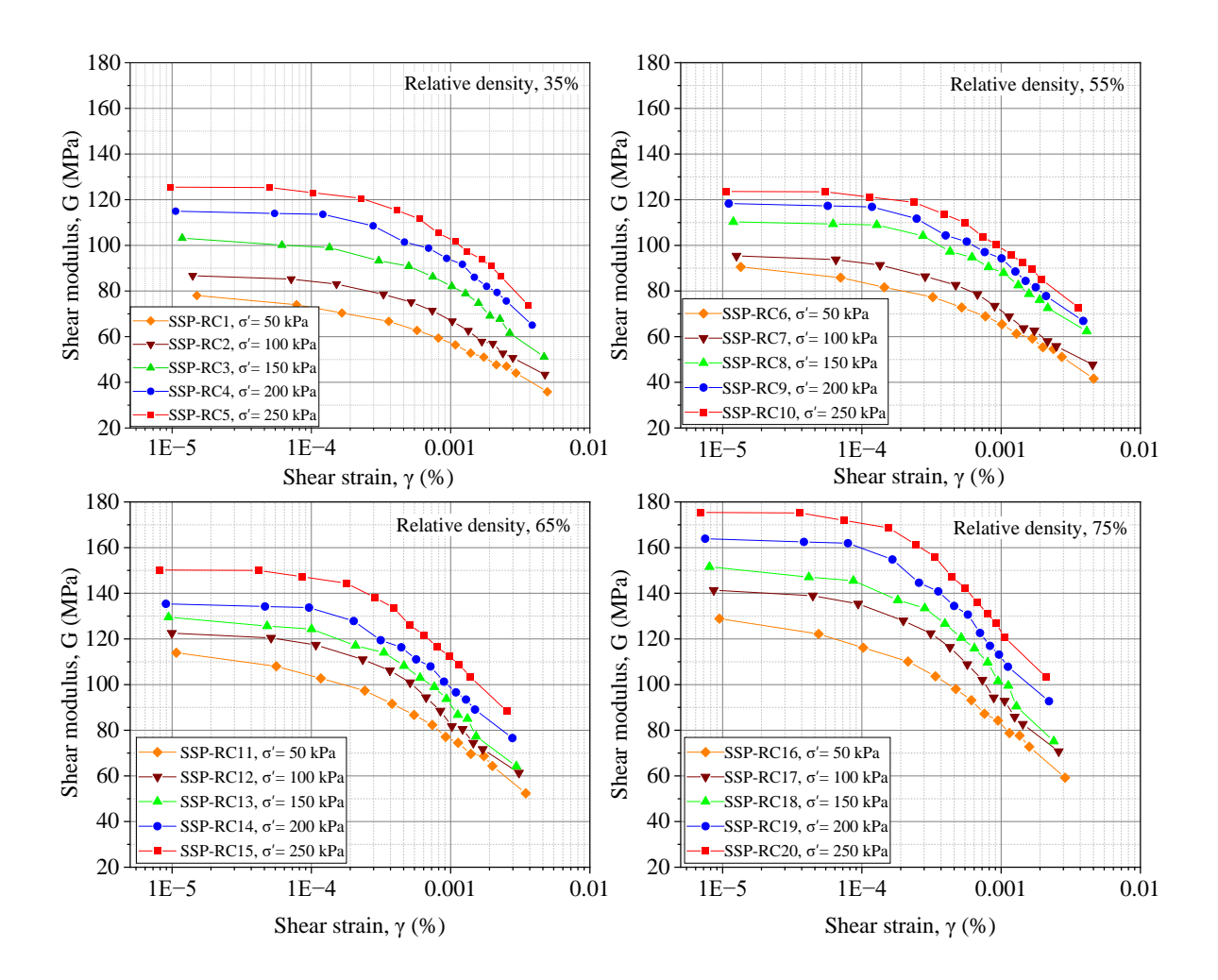


Figure 4.1 Shear modulus vs. shear strain amplitudes (RC) under varying confining pressure and relative density.

The material damping ratio (D) obtained from the RC testing of sand at different strain levels under varying confining pressure and relative density is shown in Figure 4.2. It can be elucidated from the observations that the material damping ratio of sand specimens rises with the increase in the strain levels with concavity upwards, and as the confining pressure and relative density value escalate, the damping ratio value decreases.

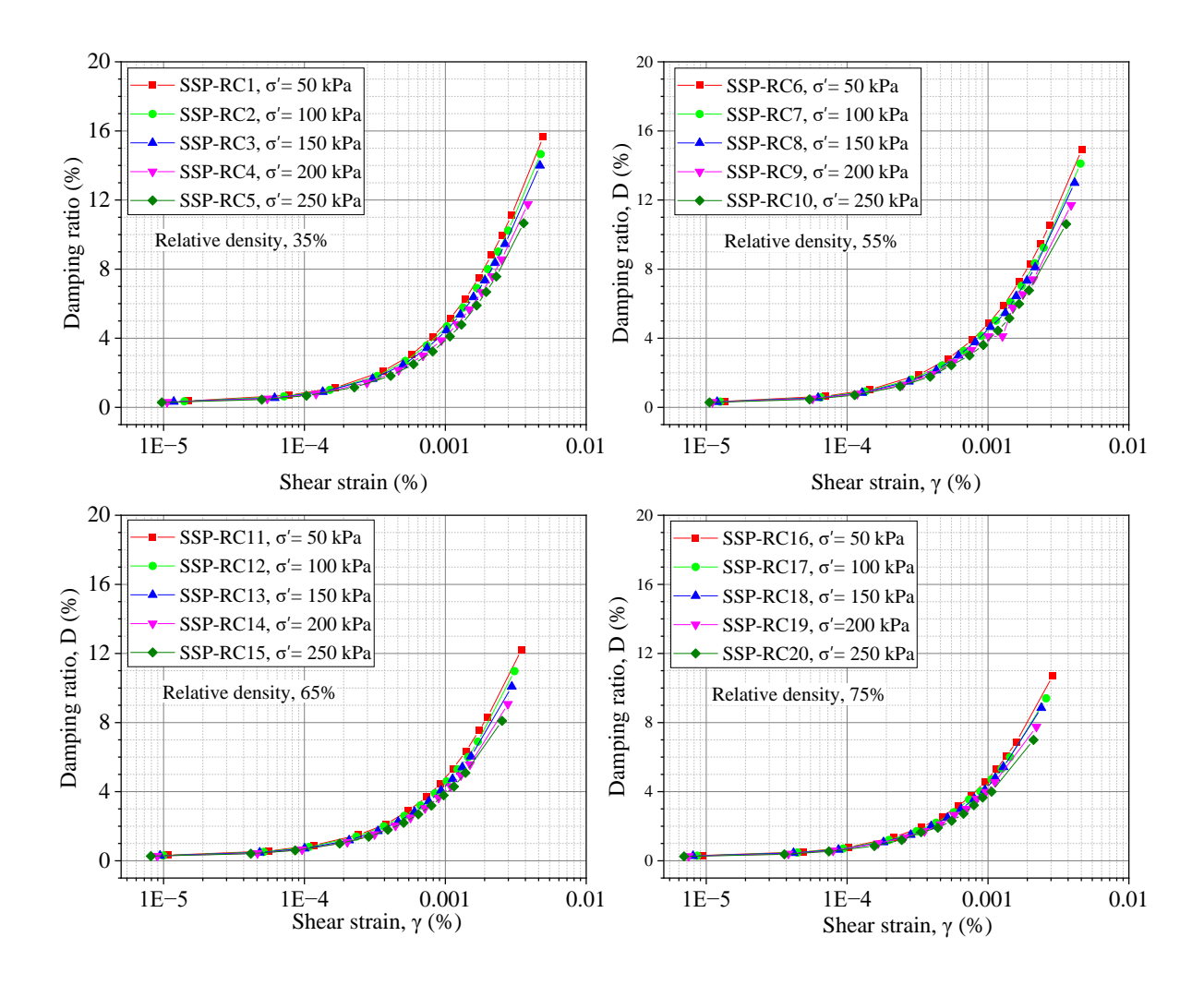


Figure 4.2 Shear strain versus material damping ratio for RC tests

4.2.2 Regression analysis on results of RC testing: The regression analysis has been performed by fitting the outcomes of tests conducted for different experimental conditions in the correlation suggested by Hardin and Richart (1963), which is given by:

$$G_{max} = A * F(e) * (\sigma')^a$$
(4.1)

where A, is the coefficient reliant on the type of soil; F(e), is a function of void ratio (e) and relative density; σ' , the effective confining pressure (kPa); a, the stress exponent; and G_{max} , the maximum shear modulus obtained (MPa).

The outcomes of the regression evaluation carried out are presented in Table 4.3. The equations of G_{max} in reference to effective confining pressure (σ') and relative density (in terms of void ratio, e) can be brought into play for estimating the G_{max} in the scarcity of any field test results such as SPT value or shear wave velocity (V_s) data. Nevertheless, it has been noticed that the equation suggested by Hardin and Richard (1963) for G is

also valid for the higher shear strain amplitudes, and the trend can be conveniently calculated at specific shear strain amplitudes. It has been observed from the regression analysis that the laboratory test results give a good fitting with the correlation suggested by Hardin and Richard (1963).

Table 4.2 Outcomes of regression analysis on resonant column testing at varying strain levels

Shear Strain level	F(e)	Coefficient A	a	\mathbb{R}^2
0.00001%	-1.131	6771.23	0.51	0.83
0.0001%	-1.1	6770.15	0.5	0.85
0.001%	-0.79	6770.12	0.47	0.89

The shear modulus of soil is also sensitive towards other parameters such as structural anisotropy (K, 1979; Hardin & Blandford, 1989), particle characteristics (Bui, 2009; Gye-Chun et al., 2006a), OCR (Kenneth & E, 1968; Kokusho et al., 1982), confinement time (Anderson & Stokoe, 1978), bonding/cementation, etc. Based on the study performed, to account for the influence of relative density, confinement, and strain amplitude, an empirical equation has been recommended for evaluating G. The fundamental yet salient form of the proposed equation is:

$$G = (\sigma')^a * (\gamma)^b * (e)^c$$
(4.2)

Where γ , is the shear strain amplitude (%); a, is the effective confining pressure exponent; b is the shear strain exponent; c is the relative density exponent.

The laboratory test results have been fitted in the proposed regression equation. The parameters obtained from the regression analysis of the present study are shown in Table 4.4.

Table 4.3 Outcomes of regression analysis of variation of G at varying shear strain amplitude (RC)

Coefficient a	Coefficient b	Coefficient c	\mathbb{R}^2
0.10	-0.49	-0.55	0.975

4.3 Test plan for CTS testing

The Cyclic torsional shear test (CTS) was conducted on Sutlej River Sand to study the influence of low-frequency cyclic loading. The tests were sequentially rendered over a range of relative densities (35%, 55%, 65%, and 75%) and the effective confining pressures (i.e., 50 kPa to 250 kPa). The CTS tests were performed by driving the excitation coils for 10 cycles with the lowest excitation voltage possible, corresponding to the strain amplitude near 0.01%. The excitation voltage increased gradually for a range of strain amplitudes to reach 1% for subsequent tests at each confining pressure. The testing was performed over a spectrum range, i.e., 0.1 Hz, 0.3 Hz, 0.5 Hz, 1 Hz, 3 Hz, 5 Hz, and 10 Hz. The experimental conditions for CTS tests are shown in Table 4.5.

4.3.1 Results of CTS testing: It was determined that the shear modulus (G) values of the sand specimen raised along with an enhancement in the relative density and for all the confining pressures tested and depleted with its concavity upwards with an increment in strain level as shown in Figure 4.3. Furthermore, the impact of relative density and confining pressure on G values is no more substantial at higher strain levels, i.e., above 0.1%. The results of the test performed in different experimental conditions are shown in Table 4.6.

The material damping ratio values obtained from CTS testing show that the increase in the shear strain amplitude leads to a rise in the damping ratio with its concavity downwards, and the same trend is observed for all relative densities tested, as shown in Figure 4.4. The damping ratio values declined with a rise in the confining pressure. It was noticed that after a certain level of strain amplitude (i.e., above 0.1%), the effect of relative density and confining on the declination of the damping ratio diminishes.

Table 4.4 Experimental arrangement for CTS testing

		Relative density	Density achieved	Confining stress
No.	Test ID	(%)	(g/cc)	(kPa)
21	SSP-TS1	35	1.503	50
22	SSP-TS2	35	1.503	100

23	SSP-TS3	35	1.503	150
24	SSP-TS4	35	1.503	200
25	SSP-TS5	35	1.503	250
26	SSP-TS6	55	1.538	50
27	SSP-TS7	55	1.538	100
28	SSP-TS8	55	1.538	150
29	SSP-TS9	55	1.538	200
30	SSP-TS10	55	1.538	250
31	SSP-TS11	65	1.555	50
32	SSP-TS12	65	1.555	100
33	SSP-TS13	65	1.555	150
34	SSP-TS14	65	1.555	200
35	SSP-TS15	65	1.555	250
36	SSP-TS16	75	1.573	50
37	SSP-TS17	75	1.573	100
38	SSP-TS18	75	1.573	150
39	SSP-TS19	75	1.573	200
40	SSP-TS20	75	1.573	250

Table 4.5 Shear Modulus in different test conditions at different strain levels (CTS)

Strain range	Relative					
(%)	Density	Shear Modulus at various confining pressure (kPa)				
0.01%	(%)	50 kPa	100 kPa	150 kPa	200 kPa	250 kPa
	35	32.2	38.3	44.5	53.6	59.2
	55	36.7	41.5	48.1	50.8	53.2
	65	41.2	46.2	47.1	53.9	59.1

	75	43.3	47.4	60.7	61.7	72.3
0.1%	35	8.6	7.6	8.5	9.2	9.4
	55	9.4	7.5	8.6	9.3	9.7
	65	9.4	7.8	8.7	9.4	10.2
	75	9.4	7.9	8.8	9.5	10.5

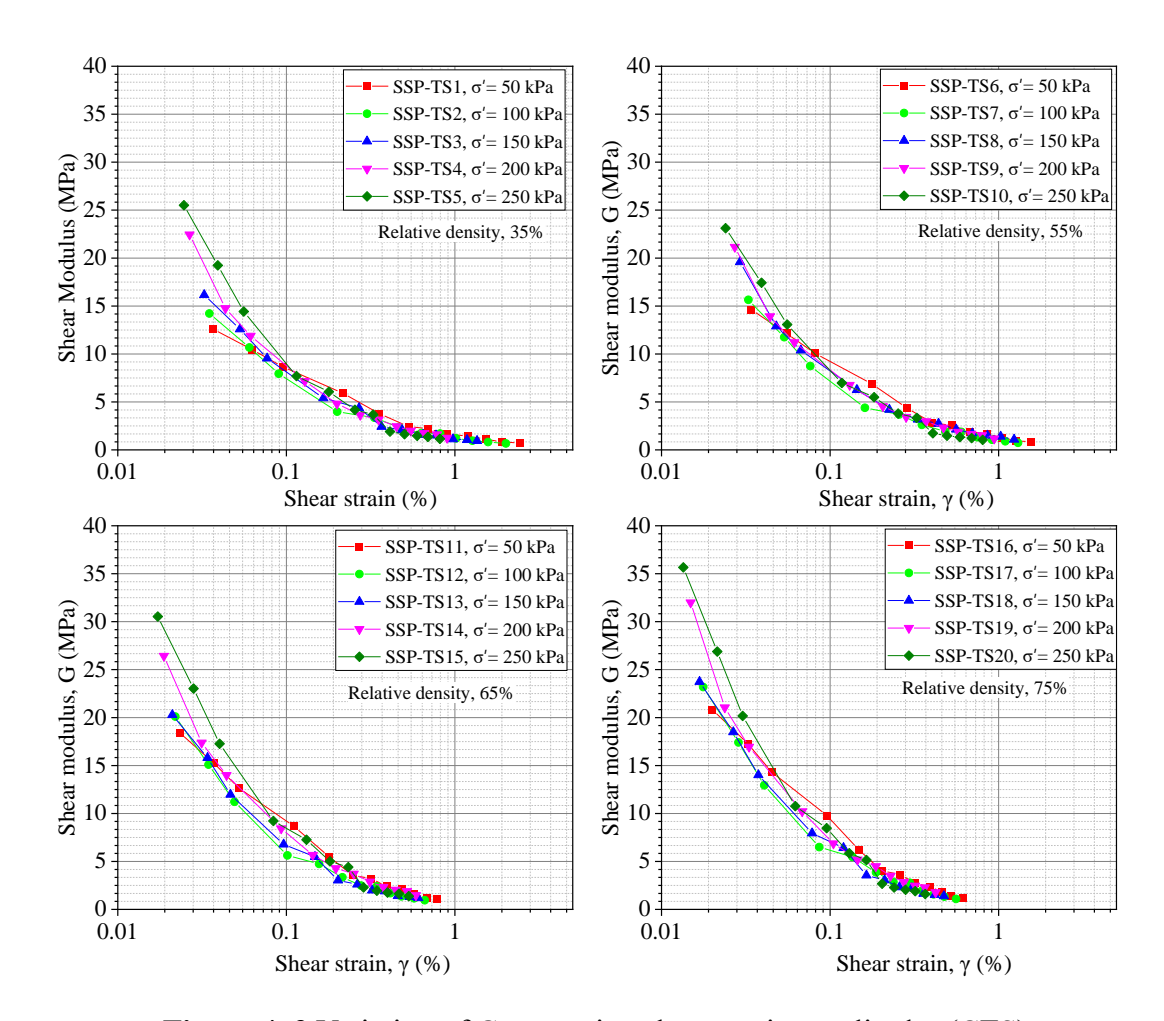


Figure 4. 3 Variation of G at varying shear strain amplitudes (CTS)

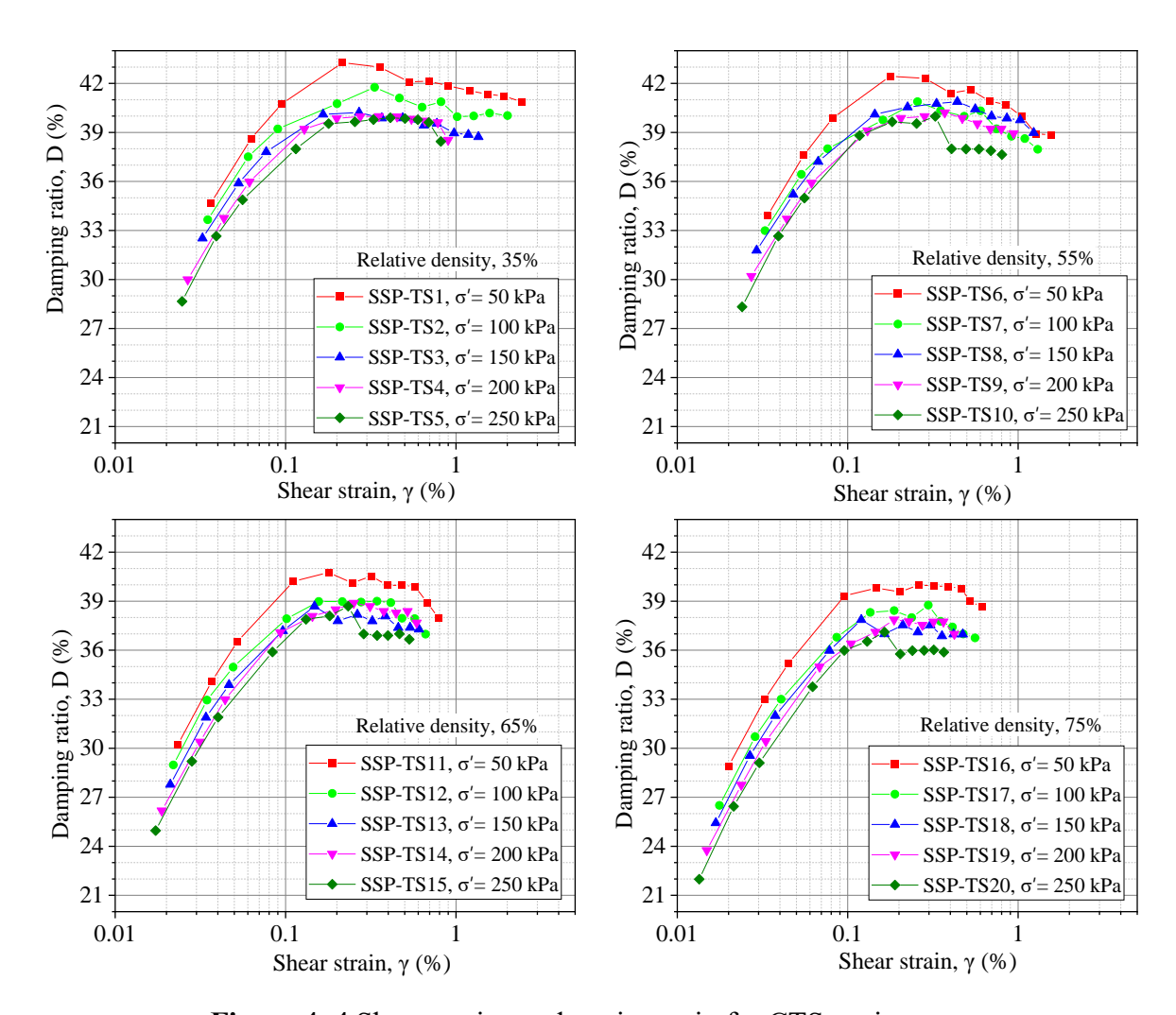


Figure 4. 4 Shear strain vs. damping ratio for CTS testing

In addition, the effect of cyclic loading frequency has also been studied over a spectrum of frequency values (i.e., 0.1 Hz, 0.3 Hz, 0.5 Hz, 1 Hz, 3hz, 5hz, and 10hz) for a definite 10 number of cycles. Figure 4.5 shows the influence of frequency of loading, strain levels, and relative densities on the shear modulus and damping ratio of sand. The result demonstrates that, for a particular relative density value, an increment in the strain level leads to a reduction in soil shear modulus and accretion in the damping ratio. For a definite strain level, as the frequency of loading increases, the shear modulus values rise, and damping ratio values fall. The same trend has been observed for all relative densities tested at all confining pressures.

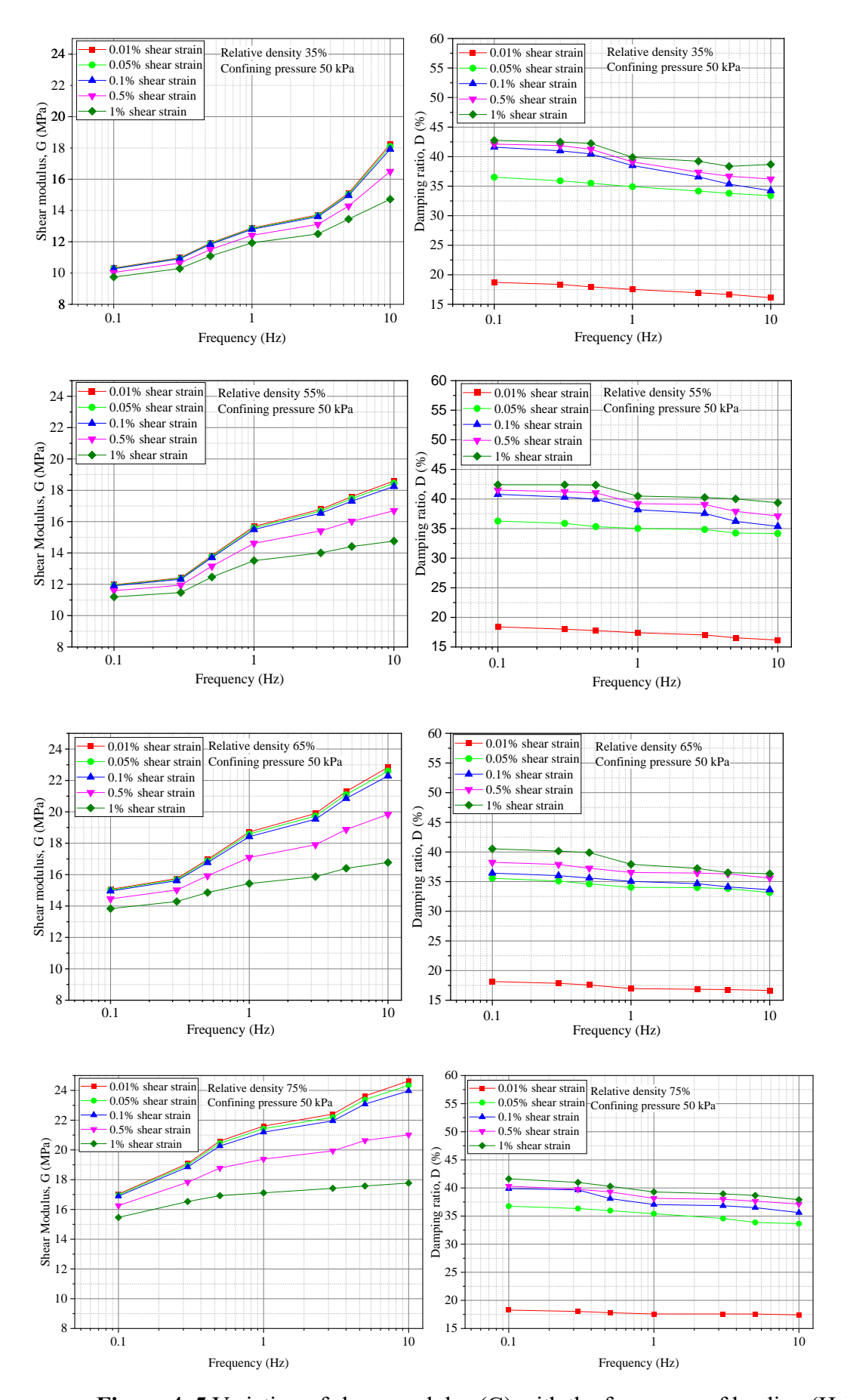


Figure 4. 5 Variation of shear modulus (G) with the frequency of loading (Hz)

4.3.2 Regression analysis on results of CTS testing: No particular pattern of increment in shear modulus and decrement in damping ratio with a rise in loading frequency was observed. Therefore, on the grounds of the performed study, to obtain the impact of relative density, confinement, and frequency of loading for estimating G, a regression analysis has been performed for various strain levels. The three-parameter regression model proposed is as follows:

$$G = (f^{a}) * (\sigma'^{b}) * (e^{c})$$
(4.3)

Where f, is the frequency of loading in Hz; a is the exponent of the frequency of loading; σ' the effective confining pressure (kPa); b, the stress exponent; e, the relative density function; and c, the relative density exponent.

Table 4.7. shows the outcomes of regression analysis performed on CTS test results for different strain levels for a constant of 10 cycles. The experimental results with the proposed regression fit well for strain levels up to the range of 1%. The regression analysis exhibits the reduction in the frequency exponent value with an increase in the strain level (i.e., from 0.01% to 1%), which demonstrates that the effect of frequency of loading on shear modulus reduces as the shear strain level rises.

Table 4. 6 Results of regression analysis for variation of G with the loading frequency at different strain levels.

Strain level	Coefficient a	Coefficient b	Coefficient	\mathbb{R}^2
			c	
0.01%	0.076	0.293	-4.063	0.99
0.1%	0.072	0.292	-4.03	0.99
1%	0.031	0.287	-3.66	0.99

4.4 Normalized shear modulus (G/G_{max})

The normalized modulus reduction $(G/G_{\text{max}}-\gamma)$ curves suggested by Bolton Seed & Idriss, 1970 and Darendeli, 2001 are considered standard curves and own wide applications in many geotechnical engineering problems. The modulus reduction curves were developed by Bolton Seed & Idriss, 1970 by gathering the data of experimentation performed and fitting it into the hyperbolic model against the reference shear strain. To develop the modulus reduction curve and to fit the experimental data, Darendeli, 2001 adopted two parameters, viz. reference shear strain (γ_{ref}) and curvature coefficient (α).

It has been noticed that the comparison of experimental results with the standard curves offered by Seed & Idriss, 1970 and Darendeli, 2001 possess an appreciable modification in the curve. Hence, for site-specific study, the parameters of the hyperbolic model require reassessment, so the regression analysis on the results of experiments performed has been carried out to establish the best fitting, as shown in Table 4.8.

The hyperbolic model correlating the shearing stress to maximum shear modulus (G_{max}) and shear strain amplitude (γ) was earliest proposed by Hardin & Drnevich, 1972 to understand the nonlinearity of shear modulus (G) values of soil corresponding to shear strain amplitude (γ). Darendeli, 2001 modified the hyperbolic model by introducing reference shear strain (γ_{ref}) (described as the strain at 50% degraded shear modulus) and the curvature coefficient (α) in the study. In the present study, the regression assessment has been committed by fitting the laboratory test results in the modified hyperbolic model, which is written as:

$$\frac{G}{G_{max}} = \frac{1}{1 + \left(\frac{\gamma}{\gamma_{ref}}\right)^{\alpha}} \tag{4.4}$$

The above two parameter values govern the outline of the modulus reduction curve. The γ_{ref} values can be gained by performing the resonant column (RC) tests and also can be obtained empirically using a correlation proposed by Meng & Rix, 2003 based on the coefficient of uniformity of soil (C_u), which is given as:

$$\gamma_{ref} = A_{\gamma} \times \left(\frac{\sigma'}{P_a}\right)^{n_{\gamma}} \tag{4.5}$$

where $A_{\gamma} = 0.12 \times C_u^{-0.6}$; $n_{\gamma} = 0.5 \times C_u^{-0.15}$; and P_a , is the barometric pressure (atm).

Table 4. 7 Results of regression analysis performed on modified hyperbolic model

σ' (kPa)	Reference strain, γ _{ref}	α	R ²
	(%)		
50	0.004	0.72	0.94
100	0.0043	0.79	0.97
150	0.0045	0.83	0.95
200	0.0049	0.87	0.96
250	0.0052	0.9	0.95

In general, the value of α rose with an escalation in the effective confining pressure. Figure 4.6 displays that with the hike in the shear strain amplitude, the shear modulus values subside, which is attributable to an increase in the magnitude of torsional vibration, resulting in lower resonant frequency and corresponding lower shear modulus. The declination rate of shear modulus with the escalation in the strain amplitude declines with the relative density and confining pressure rise. The results of this study have been collated with the standard curves (Seed & Idriss, 1970; Darendeli, 2001; Puri et al., 2020), as shown in Figure 4.7.

4.5 Damping Ratio (D)

Darendeli, 2001 suggested that the shear modulus degradation ratio affects the damping characteristics of the soil. The regression analysis has been performed for the results obtained using RCA and CTS tests and fitted against the model established by Darendeli, (2001). The material damping ratio is expressed as:

$$D_{Masing} = \frac{100}{\pi} \left[4 \times \frac{\gamma - \gamma_{ref} \ln{(\frac{\gamma + \gamma_{ref}}{\gamma_{ref}})}}{\left(\frac{\gamma^2}{\gamma + \gamma_{ref}}\right)} - 2 \right]$$
(4.6)

where, D_{Masing} is the material damping ratio associated with hysteretic Masing behaviour (Masing, 1926), which needs to be corrected using an expression as follows:

$$D_{correct} = c_1 \times D_{Masing} + c_2 \times D_{Masing}^2 + c_3 \times D_{Masing}^3$$
 (4.7)

Where c_1 , c_2 , and c_3 are the coefficients based on the curvature coefficient (α) given below

$$c_1 = -1.1143 \times \alpha^2 + 1.8618 \times \alpha + 0.2523,$$

$$c_2 = 0.0805 \times \alpha^2 - 0.0710 \times \alpha - 0.0095,$$

$$c_3 = -0.0005 \times \alpha^2 + 0.0002 \times \alpha + 0.0003$$

For higher strains, the damping value needs normalization, which can be done using the following expression:

$$D - D_{min} = \beta (G/G_{max})^{0.1} \times D_{correct}$$
 (4.8)

where β represents the scaling factor and D_{min} is the minimum damping ratio obtained from the RC and CTS tests at low strain amplitudes.

The results of the regression analysis performed for all relative density values of sand at varying conditions of confining pressure and strain levels are presented in Table 4.9. A minor decrement in the D_{min} was observed with the increment in the effective confining pressure, which is inflexible with the observations of past studies (Gye-Chun et al., 2006b; Payan et al., 2016; Senetakis et al., 2012, 2016). It was examined that the damping ratio values rise with the escalation in the shear strain amplitude and decline with an increment in the effective confining pressure for both RC and CTS tests, as shown in Figure 4.6. Moreover, it has been noticed that the degree of the rise of the damping ratio with an increase in the strain amplitude was more prominent for the CTS test than the RC test. The impact of relative density and confining pressure on the damping characteristics was negligible after a strain level of 1%.

Table 4. 8 Outcomes of regression analysis performed for damping ratio

$\sigma'(kPa)$	D _{min} (%)	β	\mathbb{R}^2
50	0.257	0.987	0.97
100	0.248	0.959	0.98
150	0.239	0.915	0.98
200	0.231	0.897	0.99
250	0.226	0.853	0.98

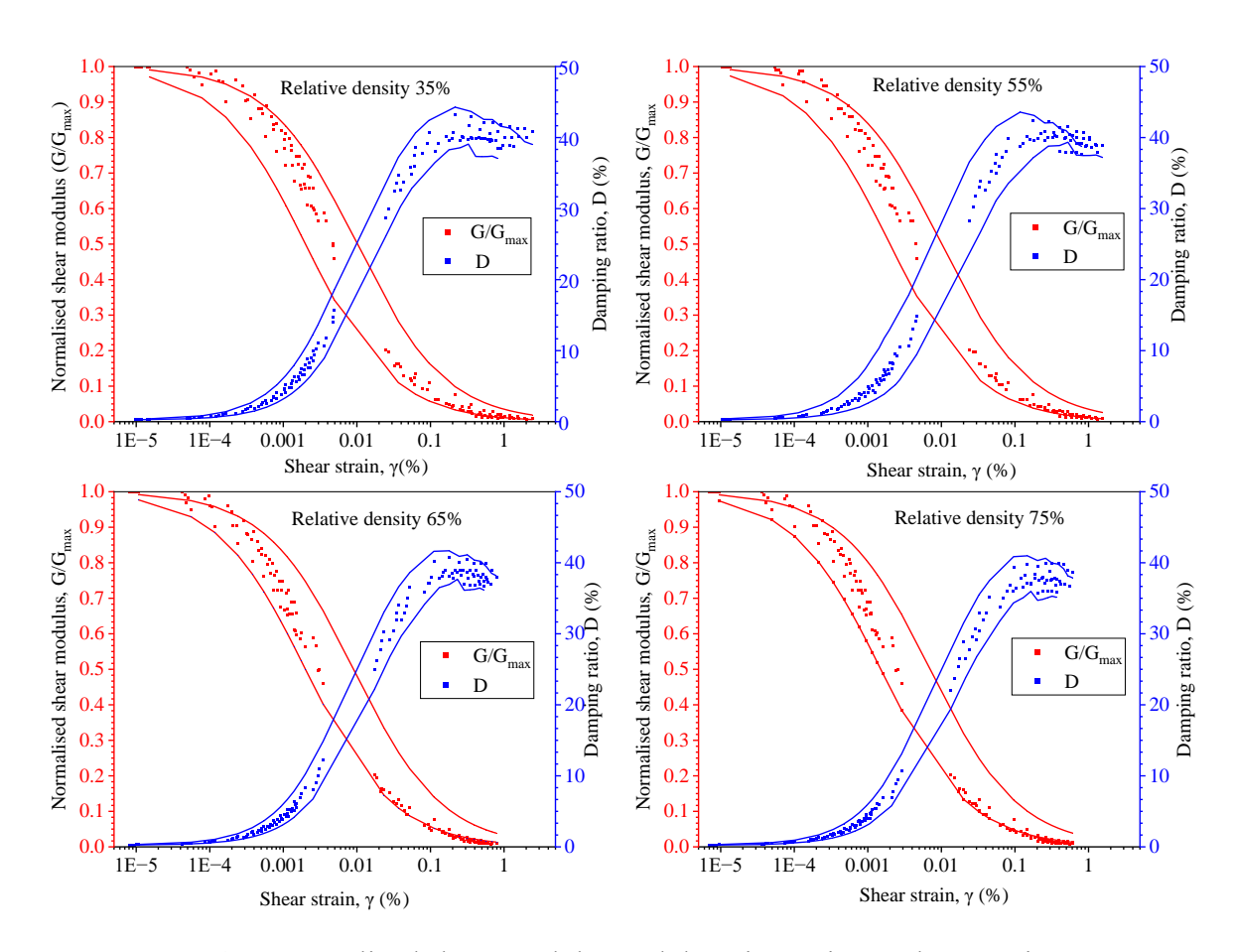


Figure 4. 6 Normalized shear modulus and damping ratio vs. shear strain

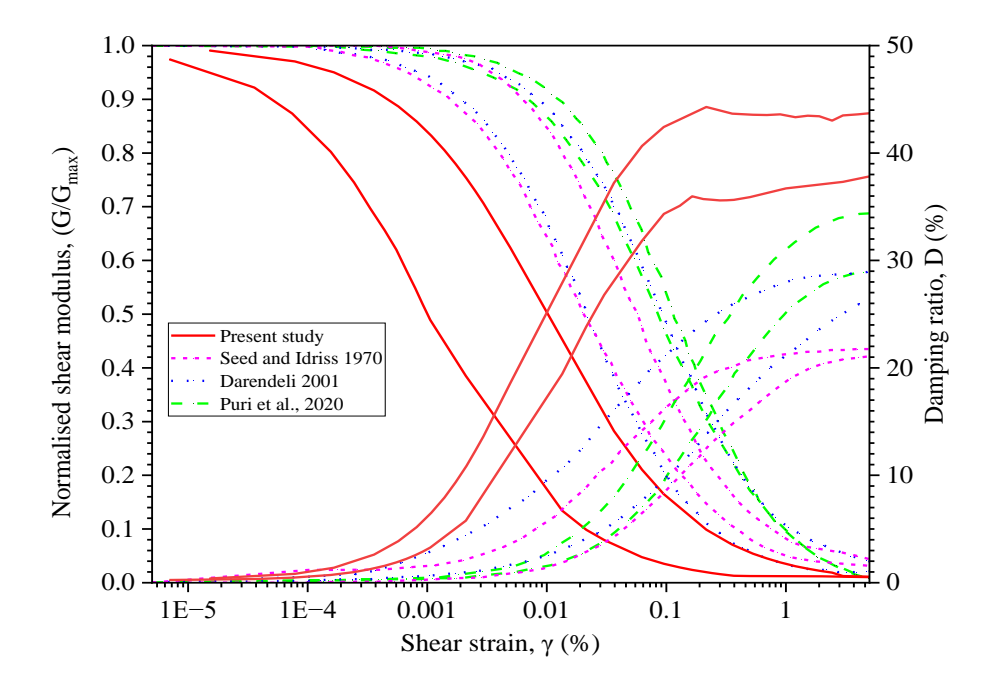


Figure 4. 7 Comparison of Normalised shear modulus reduction and damping ratio curves with previous studies

4.6 Summary

The dynamic properties of Sutlej River sand have been studied using resonant column tests (RC) and cyclic torsional shear tests (CTS) for various strain levels and have been presented in this paper. All the experiments were carried out on modified Stokoe-type resonant column apparatus in torsional mode to determine the dynamic properties of sand over a range of strain amplitudes. The site-specific shear modulus and damping ratio curves have been developed under different confining pressure and relative density conditions. A rigorous regression analysis has been performed to provide the correlation between the shear modulus at different strain levels. A correlation between the shear modulus and the loading frequency over varying strain levels has been proposed under different experimental conditions of confining pressure and relative density.

The major conclusions that are drawn from the study are:

- 1. The obtained shear modulus and damping ratio curves are similar to the standard curves reported in the literature.
- 2. The shear modulus and material damping ratio obtained from Cyclic torsional shear (CTS) tests showed remarkable dependency on loading frequency for all shear strain amplitudes.
- 3. The results from the laboratory tests indicated that the dynamic properties of Sutlej River sand are strongly controlled by variations in the shear strain amplitudes, confining pressures, and relative density.
- 4. The effect of relative density and confining pressure on the increment in shear modulus and decrement in damping ratio reduces at higher strain levels (i.e., near 1%).
- 5. The regression analysis performed on experimental results based on a modified hyperbolic model indicated that with a hike in confining pressure, the values of curvature coefficient, α, increase, and the scaling coefficient, β, decreases.
- 6. The degree of the rise of damping characteristics and fall of shear modulus with the hike in shear strain amplitude is greater for the CTS test than for the RC test.

Chapter 5

Dynamic behaviour of intact rock: Insights from resonant column apparatus

5.1 Introduction

Chapter 5 of this doctoral thesis investigates the dynamic properties of intact rock using the Resonant Column Apparatus (RCA) under various loading conditions. This chapter explores the influence of torque amplitude and loading frequency on the shear modulus and damping ratio of the rock, employing both sinusoidal and ramp waveforms. The experimental setup, described in detail, involves applying different torque amplitudes ranging from 0.00545 Nm to 0.545 Nm across a spectrum of frequencies from 0.01 Hz to 10 Hz.

Key findings presented in this chapter reveal a consistent pattern where an increase in loading rate results in a decrease in shear strain. This is attributed to the limited time available for the propagation of microcracks at higher loading rates. The data shows that the shear modulus increases with rising torque amplitude and loading frequency, indicating a significant enhancement in the material's stiffness. The chapter also compares the dynamic responses of the material under sinusoidal and ramp-loading waveforms, highlighting that while both waveforms exhibit similar trends, the sinusoidal waveform shows slightly greater dynamicity due to its higher loading rate. Furthermore, the chapter delves into the relationship between shear modulus and loading rate, applying curve-fitting models to better understand the behaviour of the material. It is noted that the damping ratio decreases as the loading rate increases, a phenomenon consistently observed across varying torque amplitudes. This comprehensive analysis underscores the significant impact of loading conditions on the mechanical properties of intact rock, providing valuable insights for its application in engineering and construction contexts.

5.2 Resonant column testing

After preparing the intact gypsum plaster specimen as per the method explained in Chapter 3, for each chosen value of the input excitation voltage, the resonant frequency and damping ratio of the specimen were determined, and the corresponding amplitude of the shear strain was then computed. The fine sweep operation was carried out with a frequency increment of 0.1 Hz for a total frequency band of 2 Hz and the value of the cycle constant was kept equal to 100. Starting from a minimum input voltage to the maximum input voltage, this exercise was repeated in order to find corresponding values of the resonant frequencies, damping ratio, and strain levels. The fundamental properties of the gypsum plaster utilized in this investigation are given in Chapter 3, Table 3.3. The variation of shear modulus and damping ratio with shear strain amplitude for intact gypsum plaster specimens is given in Figure 5.1. The experimental results demonstrate that as the amplitude of shear strain increases, the shear modulus values decrease, and the damping ratio of the material increases.

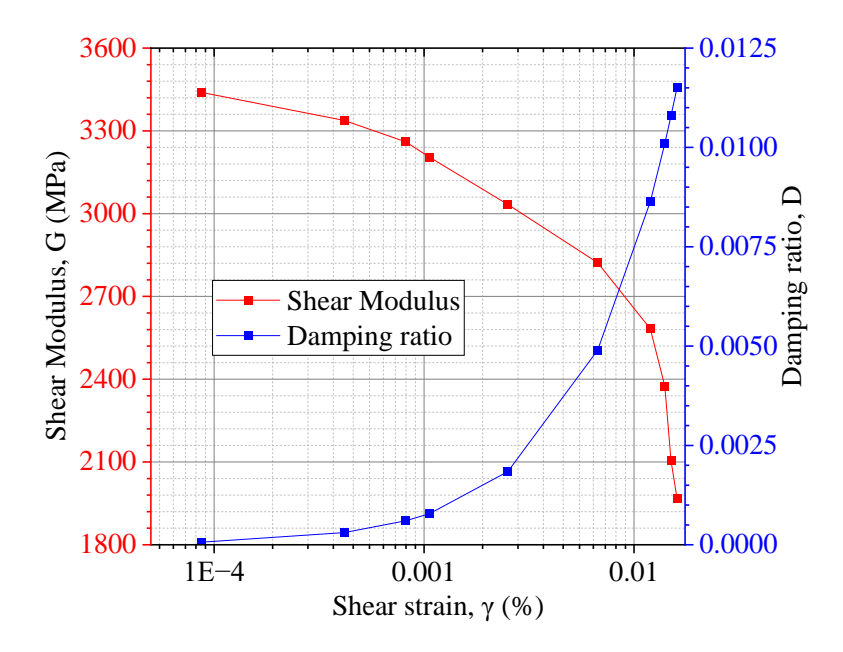


Figure 5.1 Variation of shear modulus and damping ratio of intact gypsum plaster using RC testing

5.3 Cyclic torsional shear testing

The testing procedures were conducted using the cyclic torsional shear testing module of resonant column apparatus (RCA), offering a wide frequency spectrum ranging from 0.01 Hz to 10 Hz, encompassing two distinct loading waveforms: sinusoidal and ramp.

Specifically, the sinusoidal waveform permitted excitation frequencies ranging from 0.1 Hz to 10 Hz, while the ramp waveform extended the frequency range from 0.01 Hz to 0.1 Hz.

In this study, testing was systematically carried out for both ramp and sinusoidal waveforms, spanning a spectrum of loading frequencies. These tests were performed sequentially, while the output voltage was varied across a range of values, including 0.01 V, 0.03 V, 0.05 V, 0.1 V, 0.3 V, 0.5 V, 0.7 V, 0.9 V, and 1 V. These voltage settings corresponded to varying torque amplitudes of 0.0054 Nm, 0.0164 Nm, 0.027 Nm, 0.038 Nm, 0.054 Nm, 0.164 Nm, 0.273 Nm, 0.382 Nm, and 0.546 Nm, respectively.

5.3.1 Influence of loading waveform: It has been observed that both the frequency and amplitude of loading profoundly influence the loading rate, subsequently impacting the mechanical response of materials (Xiao et al., 2008). Furthermore, it has been noted that the loading rate exhibits variations among different waveform types at specific frequencies and amplitudes of loading. Notably, Xiao et al., 2008 introduced expressions for calculating the average loading rate under quasi-dynamic loading conditions. This study focussed on two distinct loading waveforms: the ramp and sinusoidal waveforms.

For the ramp waveform, the average loading rate (as outlined by Xiao et al., 2008) can be expressed as:

$$K = 4Af \tag{5.1}$$

where, A denotes the amplitude of the load, and f represents the loading frequency.

Conversely, in the case of sinusoidal waveforms, the loading rate fluctuates over different time intervals due to continuous variations in the applied load over time, as elaborated by Xiao et al. (2008). As a result, an expression for the average loading rate is given by:

$$K = \frac{2A^2\pi f}{P} \left(\frac{\arcsin(P/A)}{2} + \frac{\sin(2\arcsin(P/A))}{4} \right)$$
 (5.2)

where P signifies the load at any given time, where P=A $\sin(2\pi ft)$.

Figure 5.2 presents the average loading curves for both the ramp and sinusoidal loading waveforms, corresponding to a loading frequency of 0.1 Hz and an applied output

torque amplitude of 0.054562 Nm. It is important to note that the slope of the loadingtime curve directly represents the loading rate inherent to each waveform.

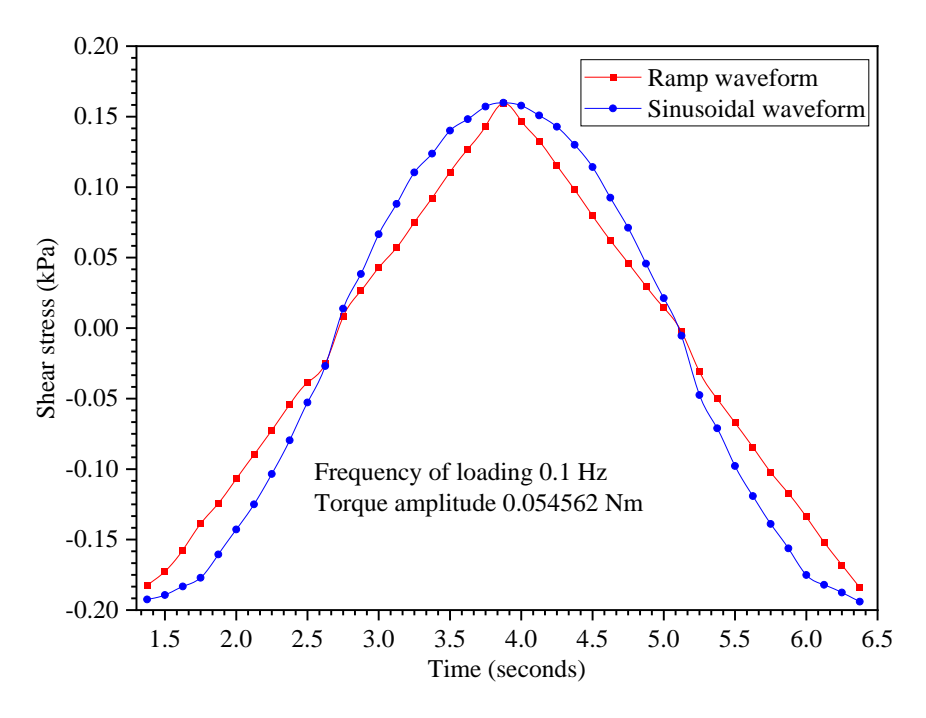


Figure 5. 2 Shear stress vs. time for different waveforms

5.3.2 Impact of frequency on the loading rate: The findings derived from the expressions formulated by Xiao et al., 2008 for both ramp and sinusoidal waveforms indicate that the average loading rate escalates in direct correlation with increasing loading frequency. The impact of 0.1, 0.5, 1, 1.5, and 2 Hz loading frequencies on the average loading rate was investigated in a study conducted by Xiao et al., 2008. In this study, the impact of frequency on the loading rate has been quantitatively assessed by applying cyclic torsional shear loading to intact gypsum plaster specimens at a spectrum of loading frequencies spanning from 0.01 Hz to 0.1 Hz, with incremental steps of 0.01 Hz. This experimentation was conducted while maintaining a consistent output torque amplitude of 0.005452 Nm.

Figure 5.3 vividly presents the average loading rate profiles for both the ramp and sinusoidal waveforms across varying frequencies. Consistent with the findings of Xiao et al., 2008, the observations indicate that the increase in loading rate with frequency is more pronounced for the sinusoidal waveform than the ramp waveform. In essence, a logarithmic progression in the loading rate has been obtained concurrently with increments in the loading frequency.

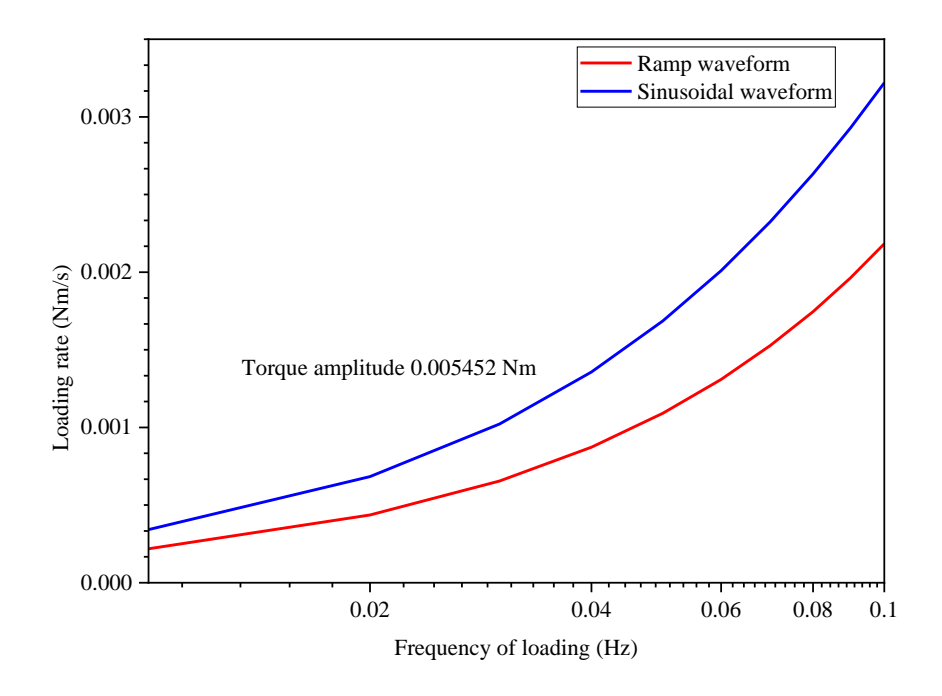


Figure 5. 3 Impact of loading frequency on the rate of loading of different loading waveforms

5.3.3 Impact of the amplitude of torque on the loading rate: The investigation yielded insightful findings regarding the profound influence of torque amplitude on the loading rate. In order to thoroughly evaluate the effect of torque amplitude on the average loading rate, a consistent loading frequency of 0.1 Hz was maintained while the amplitude of torsional loading was systematically varied. In contrast, the research conducted by Xiao et al., 2008 employed a constant loading frequency of 1 Hz to investigate the relationship between amplitude and average loading rate. This variation spanned from 0.005456 Nm to 0.545621 Nm under both ramp and sinusoidal waveforms.

Figure 5.4 presents the alterations in the average loading rate, distinctly illustrating the responsiveness of the ramp and sinusoidal waveforms to fluctuating torque amplitudes. It was discerned that the average loading rate exhibited a logarithmic dependence on the amplitude of loading, reinforcing the sensitivity of this parameter.

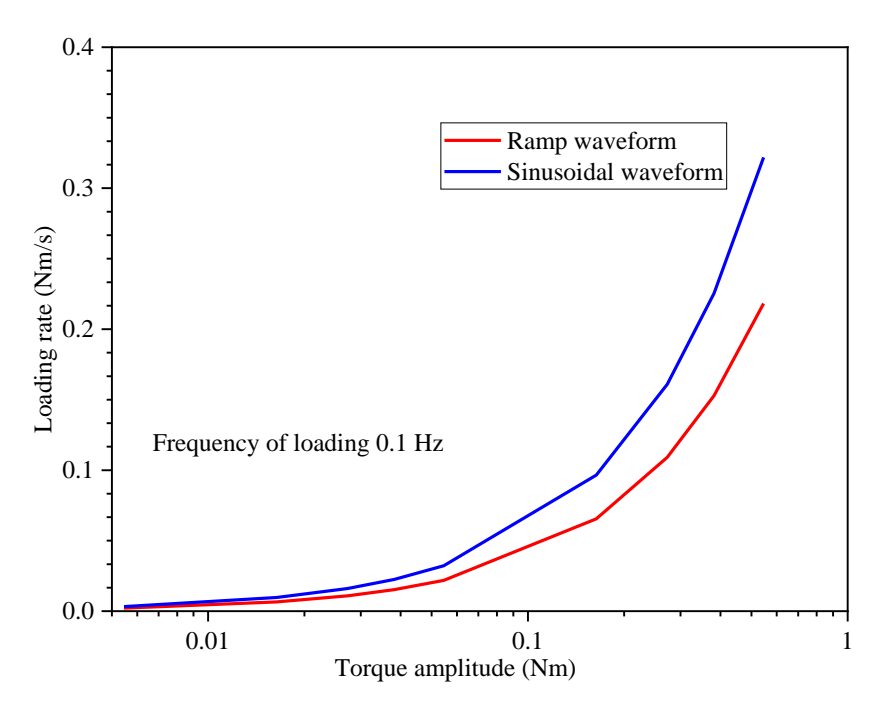


Figure 5. 4 Influence of amplitude of torque applied on the loading rate of different waveforms

In the case of the ramp waveform, the average loading rate remained constant throughout the duration of loading. However, a contrasting trend was observed for the sinusoidal waveform, as delineated in Figure 5.5. Regardless of the specific torque amplitudes applied (i.e., 0.005456 Nm, 0.05456 Nm, and 0.5456 Nm) at a consistent loading frequency of 0.1 Hz, the average loading rate progressively decreased over time for sinusoidal loading. These findings provide valuable insights into the interaction between torque amplitude, loading rate, and waveform characteristics. The current investigation results are consistent with those reported in the study conducted by Xiao et al., 2008.

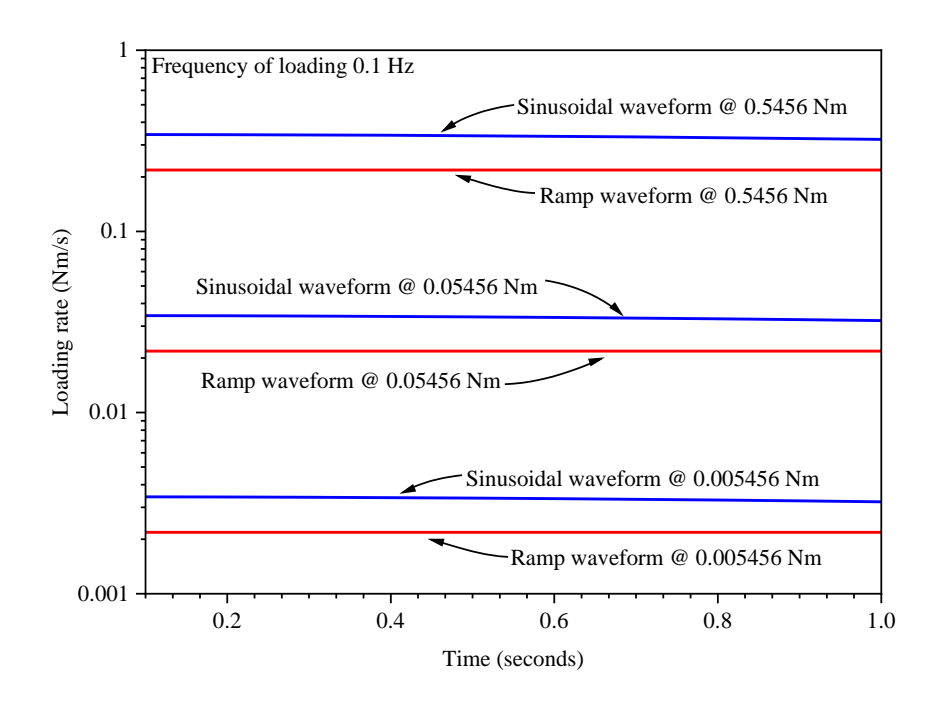


Figure 5. 5 Variation of loading rate vs. time at the varying amplitude of torque applied

5.4 Experimental observations and results

The findings underscore the substantial influence of excitation frequency and applied torque amplitude on the loading rate, thereby exerting a discernible impact on the dynamic properties of gypsum plaster. This investigation revealed a consistent reduction in shear strain within the material as the loading rate escalated, aligning with previous research outcomes (Bagde & Petroš, 2005; Li et al., 2001; Ray et al., 1999). The primary explanation for this decrease in shear strain with increasing loading rate pertains to the limited time available for the propagation of microcracks and flaws during high loading rates.

In this study, the experimental protocol involved sequential tests spanning a range of torque amplitudes, ranging from 0.00545 Nm to 0.545 Nm. These tests encompassed frequencies of 0.01 Hz to 0.1 Hz for the ramp waveform and 0.1 Hz to 10 Hz for the sinusoidal waveform.

As elucidated in Figures 5.6 and 5.7, the results consistently demonstrate a reduction in shear strain as the loading rate escalates, a phenomenon observed for both sinusoidal and ramp waveforms. The ramp and sinusoidal waveforms achieved maximum loading rates were 0.2182 Nm/s and 34.28 Nm/s, respectively, with corresponding shear strains of 0.0019% and 0.0002%.

Ultimately, the present study affirms that in the context of frequency-dependent torsional shear loading, an increase in the loading frequency and the applied torque amplitude induces a proportional rise in the loading rate.

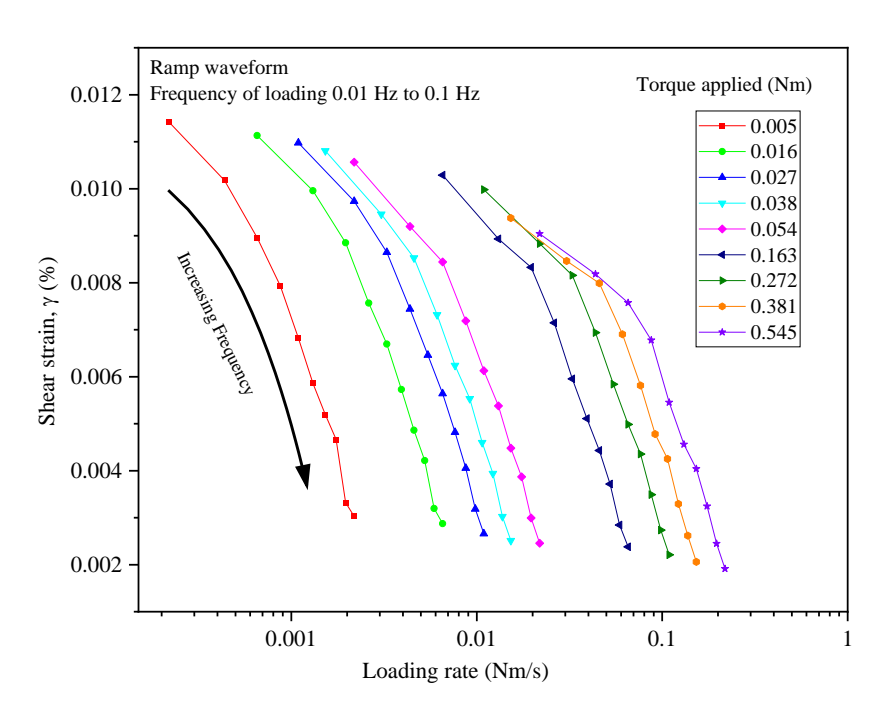


Figure 5. 6 Variation of shear strain under the influence of loading rate for ramp waveform

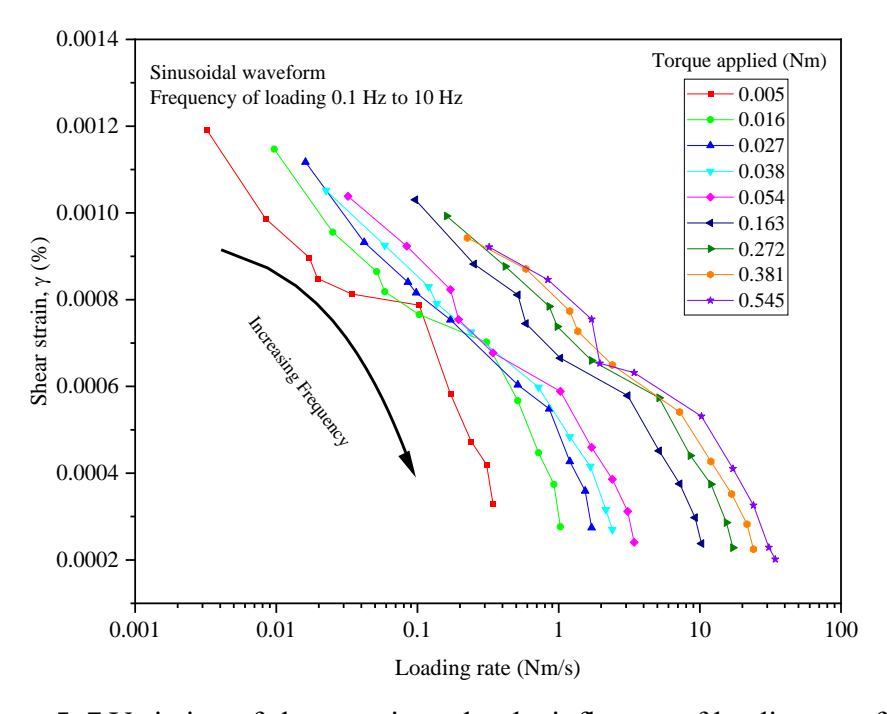


Figure 5. 7 Variation of shear strain under the influence of loading rate for a sinusoidal waveform

5.4.1 Influence of loading rate on dynamic properties: The experimental findings demonstrate a consistent trend across both ramp and sinusoidal loading waveforms. As the torque amplitude increases, the loading rate rises, thereby elevating the shear modulus of the material. A comparative analysis was conducted between these two waveforms at a fixed loading frequency of 0.1 Hz to further investigate the loading rate dynamics. The results indicate that the sinusoidal waveform exhibits slightly greater dynamicity than the ramp waveform due to its higher loading rate. However, it is noteworthy that the shear moduli obtained for both waveforms at a particular loading rate magnitude remain nearly identical. Figure 5.8 effectively illustrates the relationship between shear modulus and loading rates, with curve fitting applied to the data, revealing a nonlinear asymptotic connection.

A comparative examination of the damping ratio for both waveforms at specific loading rates reveals that the damping ratio under the ramp waveform closely aligns with that under the sinusoidal waveform. This study underscores that material damping ratio values increase as loading rates decrease for both waveforms, as portrayed in Figure 5.9, following a nonlinear logarithmic pattern.

The dynamic properties of gypsum plaster specimens were acquired over a range of strain amplitudes spanning from 0.0001% to 0.01%. Numerous experiments were conducted at various torque amplitudes across a frequency range encompassing 10 cycles. The average values of G (shear modulus) and D (damping ratio) obtained for these 10 cycles are tabulated in Table 5.1. The findings of the present study reveal that heightened torque amplitudes and loading frequencies contribute to increased loading rates, consequently leading to an escalation in G values and a decline in D values.

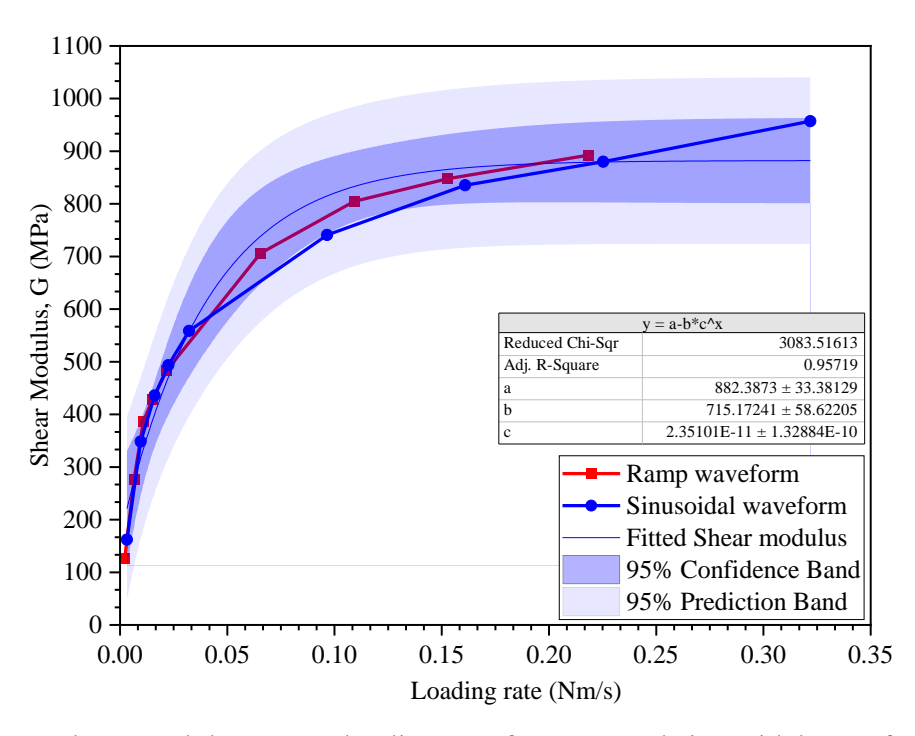


Figure 5. 8 Shear modulus versus loading rate for ramp and sinusoidal waveform

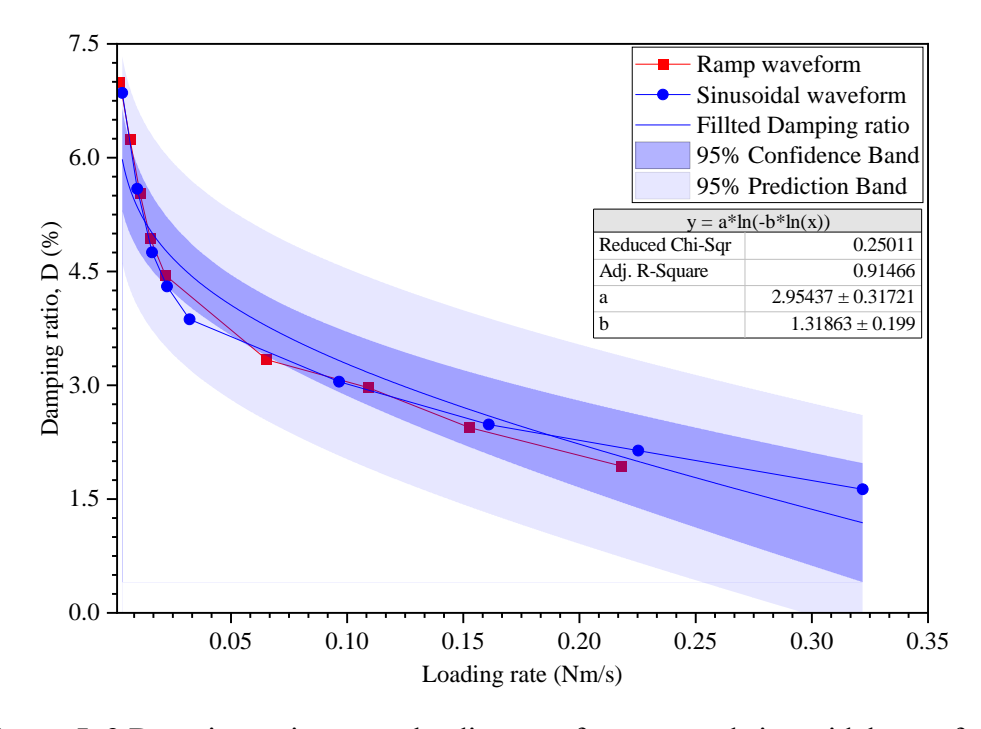


Figure 5. 9 Damping ratio versus loading rate for ramp and sinusoidal waveform

The versatility of the apparatus employed in this study, offering both ramp and sinusoidal loading waveforms, proved advantageous in characterizing dynamic properties across a broad spectrum of loading rates. Specifically, the sinusoidal waveform enabled dynamic response assessment within a shear strain amplitude range of 0.0002% to 0.001%, while the ramp waveform encompassed the shear strain levels spanning from 0.002% to 0.01%.

Table 5.1 Shear modulus and material damping ratio at a specific value of torque amplitude and frequency of loading

Type of	Torque	Frequency	Shear	Damping
waveform	amplitude (Nm)	(Hz)	Modulus	ratio (%)
			(MPa)	
Sinusoidal	0.005456	0.1	382.15	5.26
		1	569.42	4.96
		10	963.89	1.58
	0.05456	0.1	688.63	5.23
		1	1065.9	4.03
		10	1353.4	0.65
	0.5456	0.1	1047.1	5.18
		1	1461.4	3.52
		10	1742.9	0.19
Ramp	0.005456	0.01	23.88	16.54
		0.1	103.7	9.49
	0.05456	0.01	83.70	16.13
		0.1	259.53	8.85
	0.5456	0.01	171.31	15.72
		0.1	417.14	8.03

The distribution of shear modulus values for the sinusoidal and ramp waveforms is graphically depicted in Figures 5.10 and 5.11, respectively. The observations of this study show that shear modulus values decline as strain amplitudes increase for all tested torque amplitudes. Notably, applying sinusoidal waveform exhibits curves with concavity downwards at lower strain levels (0.0002% to 0.001%, Figure 5.10). In contrast, the application of the ramp waveform extends to a shear strain range of 0.002% to 0.01% and depicts concavity upwards (Figure 5.11). This behavior arises from the interplay of torque amplitude and loading frequency, where lower strain amplitudes correspond to higher loading rates, leading to reduced shear modulus. The rate of shear modulus change is more pronounced at lower strain amplitudes and diminishes as strain amplitudes increase.

Furthermore, the investigation demonstrates that the material damping ratio increases with strain amplitude for both waveforms, as delineated in Figures 5.12 and 5.13. Specifically, the damping ratio for the sinusoidal waveform ranges from 0.19% to 5.2%, corresponding to shear strain amplitudes of 0.0002% and 0.001%, respectively. Likewise, the damping ratio ranges from a maximum of 15.9% to a minimum of 8.03% for the ramp waveform, corresponding to shear strain levels of 0.01% and 0.002%, respectively. This study reveals a consistent pattern where an increase in loading rate corresponds to a reduction in the damping ratio, constantly observed across varying torque amplitudes.

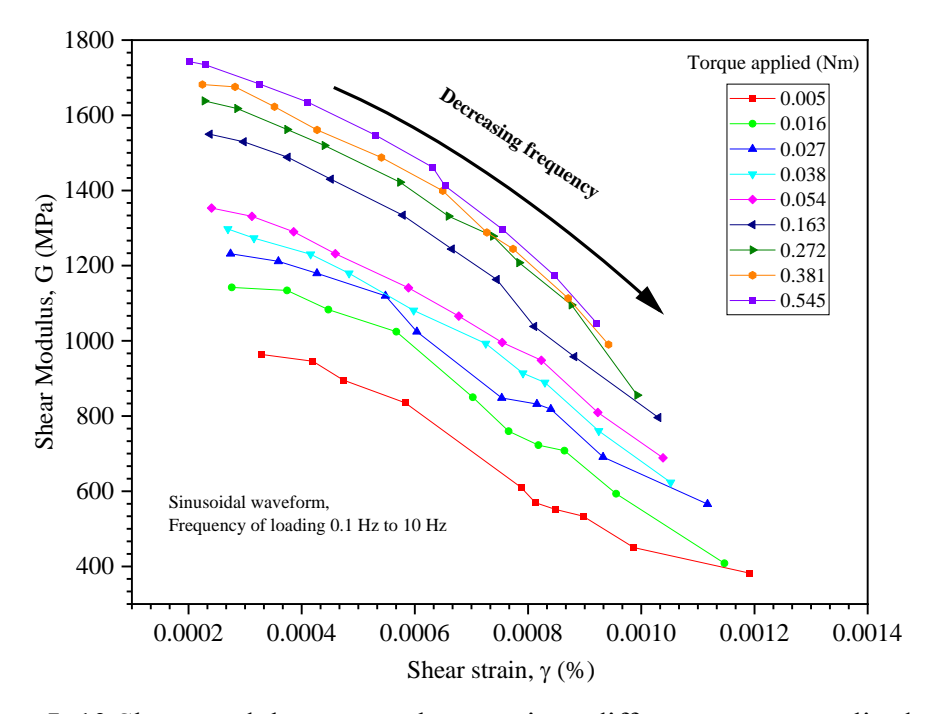


Figure 5. 10 Shear modulus versus shear strain at different torque amplitudes and loading frequency for a sinusoidal waveform

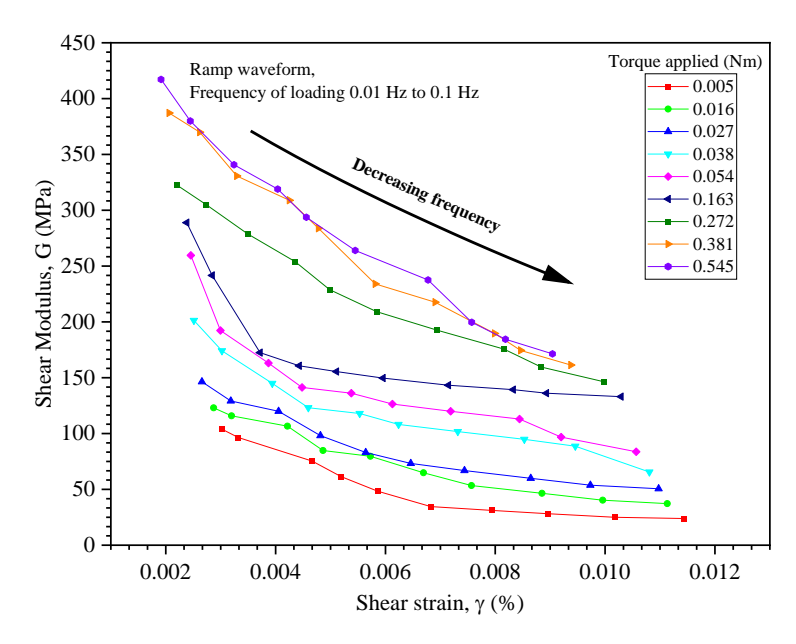


Figure 5. 11 Shear modulus versus shear strain at different torque amplitudes and loading frequency for ramp waveform

5.4.2 Curve fitting models:

5.4.2.1 Ramberg-Osgood material model: The Ramberg-Osgood (R-O) model is widely utilized to illustrate the elastoplastic response of materials (Jennings, 1965). Many researchers have used the model to understand the nonlinear dynamic properties of geomaterials (Ueng & Chen, 1992; Kouretzis et al., 2015; Izzat et al., 1978; Sireteanu et al., 2014).

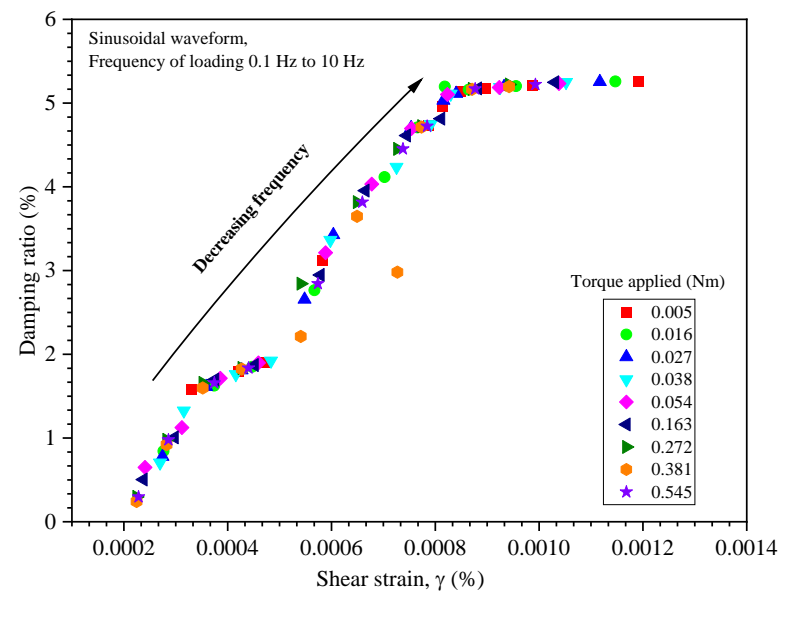


Figure 5. 12 Damping ratio versus shear strain at the different magnitude of torque and loading frequency for a sinusoidal waveform

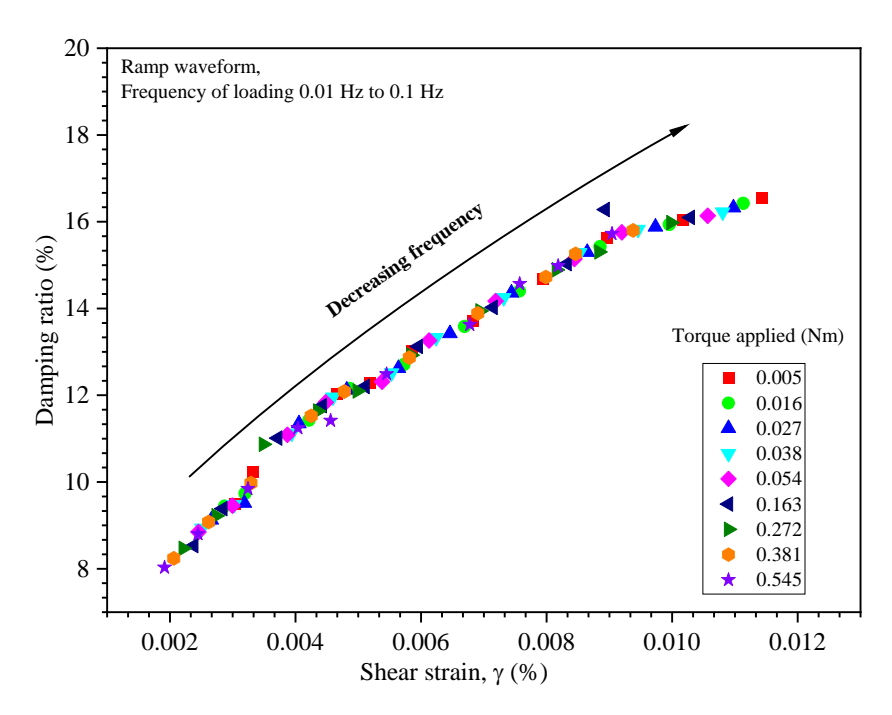


Figure 5. 13 Damping ratio versus shear strain at the different magnitude of torque and loading frequency for ramp waveform

The secant shear modulus and damping ratio from the backbone curve for the Ramberg-Osgood elastoplastic material model suggested by <u>Izzat et al. (1978</u>) can be written as:

$$\frac{G}{G_{\text{max}}} = \frac{1}{\left(1 + \alpha \left| \frac{G}{G_{\text{max}}} \frac{\gamma}{\gamma_y} \right|^{r-1}\right)}$$
 (5.3)

$$D = \frac{2}{\pi} \frac{r-1}{r+1} \alpha \frac{\left| \frac{G}{G_{\text{max}}} \frac{\gamma}{\gamma_y} \right|^{r-1}}{1 + \alpha \left| \frac{G}{G_{\text{max}}} \frac{\gamma}{\gamma_y} \right|^{r-1}}$$
(5.4)

Where γ is the shear strain; γ_y is the reference shear strain; G_{max} is the maximum shear modulus; α and r are the constants with values ≥ 0 and ≥ 1 , respectively.

The parameter γ_y is to be precisely determined as it defines the shape of the hysteresis curve and the point of maximum curvature in the backbone curve (Ueng & Chen, 1992). The magnitude of γ_y is determined using the method proposed by Ueng & Chen (1992), and the procedure is provided as follows:

1. Initially, assume a suitable value of reference strain by plotting the data, considering the point of maximum curvature from the curve, and determining the values of constants α and r as per equation 5.3.

2. The regression analysis is performed to get the best-fitting values of the data using the modified form of equation 5.3. Equation 5.3 can also be written as:

$$\log\left(\frac{G_{\text{max}}}{G} - 1\right) = \log(\alpha) + (r - 1)\log\left(\frac{G}{G_{\text{max}}} * \frac{\gamma}{\gamma_{\text{y}}}\right)$$
 (5.5)

The values of r and α can be determined from the slope and intercept from the best-fitting results.

- 3. Compute the values of reference strain from the values of α and r obtained in the previous step using equation 5.4.
- 4. If the difference between the assumed and reference strain obtained from the above analysis is significant, repeat the procedure in the above steps.

5.4.2.2 Modified hyperbolic model: Many studies on the geomaterials predicted that the dynamic shear modulus, G, declines and the damping ratio, D, rises with the increase in shear strain amplitudes (e.g., Seed et al., 1970; Seed et al., 1986; Darendeli, 2001). The hyperbolic model (Hardin, 1972) and modified hyperbolic model (Darendeli, 2001) are widely adapted to identify the nonlinear response of the geomaterials. The basic equation of shear modulus reduction and material damping ratio versus shear strain amplitude for the hyperbolic model (Hardin, 1972) has been given in Chapter 3, Sections 3.4 and 3.5.

5.4.3 Normalized modulus reduction and material damping ratio: In this research, a consistent trend has been observed wherein shear modulus values decline as shear strain amplitudes increase. This phenomenon can be attributed to the concurrent reduction in loading rate. Specifically, at lower loading rates, the specimen is afforded more time to return to its original position following cyclic loading. This extended duration increases the magnitude of strain generated within the material, ultimately resulting in a reduction in shear modulus. It is important to note that the rate of modulus degradation with strain is more pronounced at smaller strain amplitudes, ranging from 10^{-49} % to 10^{-30} %, and gradually diminishes as the strain amplitude expands to the range of 10^{-30} % to 10^{-20} %.

In the present study, the MH model (proposed by Darendeli in 2001) and the RO material model (Ramberg-Osgood, 1943) have been employed to analyze the outcomes of NR testing conducted on gypsum plaster specimens. The fitting curves derived from

the MH and RO models, in conjunction with the findings of experimental results, are presented in Figures 5.14 and 5.15.

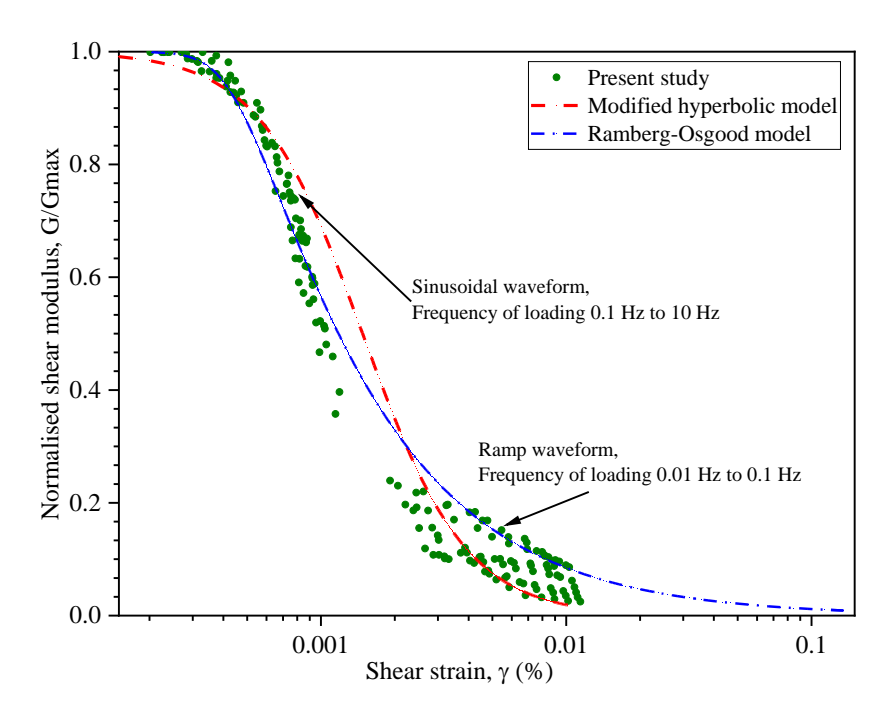


Figure 5. 14 Normalised modulus reduction curve and obtained fitted curves

The curve fitting parameters for the MH model, obtained through regression analysis, are detailed in Table 5.2. Notably, the analysis performed in this study determined the minimum damping ratio (D_{min}) and the scaling coefficient (b) to be 0.193% and 0.6197, respectively. Additionally, the fitting curve parameters for the damping ratio under the RO model, as per equation 5.18 (utilizing parameters r and α), are provided in Table 5.3.

An interesting observation that emerges from the analysis is that contrary to the results of the regression analysis conducted on the modulus reduction curve, the MH model proposed by Darendeli in 2001 offers a superior fit for the damping ratio curve compared to the RO model. This observation aligns with the findings of Park and Kishida, 2019 and underscores the suitability of the model for capturing the damping ratio behaviour in this context. However, it is noteworthy that the RO model remains a more suitable choice for representing the modulus reduction curve, emphasizing the nuanced nature of material behaviour under different loading conditions.

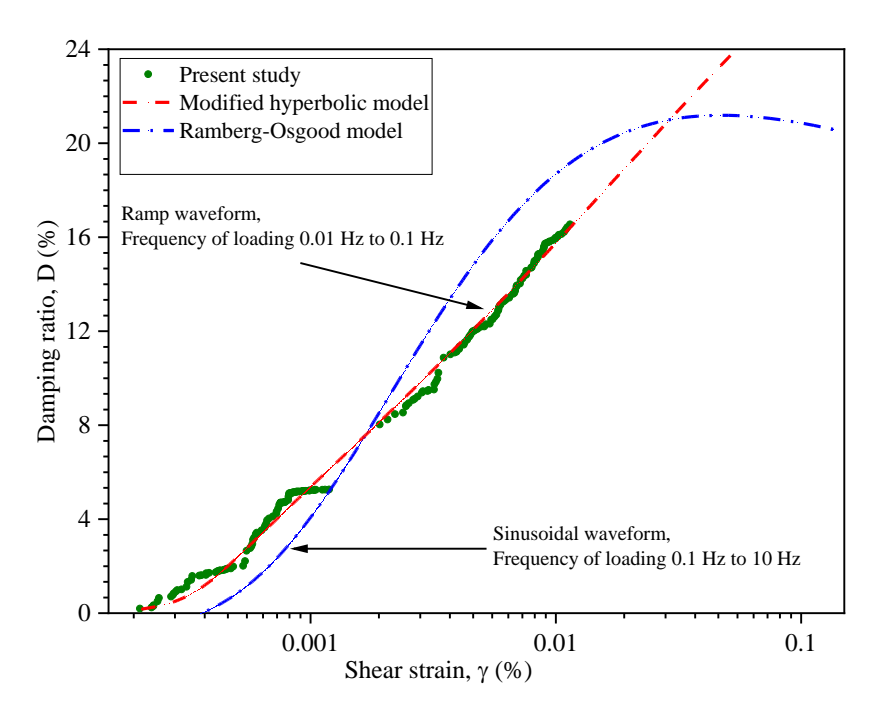


Figure 5. 15 Damping ratio vs. shear strain curve along with fitted curves

Table 5.2 Curve fitting parameters of G/G_{max} for modified Hyperbolic model

Reference strain, γ _y (%)	a	\mathbb{R}^2
0.00148	2.059	0.823

Table 5.3 Curve fitting parameters of G/G_{max} for the Ramberg-Osgood model

Reference strain, yy (%)	α	r	\mathbb{R}^2
0.00045	0.08015	7.5117	0.935

5.5 Summary

In this chapter, the dynamic properties of intact rock specimens have been determined under varying loading rates. The resonant column and cyclic torsional shear testing have been performed to comprehensively observe intact gypsum plaster specimens under vibrational and cyclic loading. It has been observed that the shear modulus values decrease, and the damping ratio increases with an increase in the strain level under resonant column testing. Furthermore, a noteworthy observation under cyclic torsional shear testing was the consistent increase in loading rate with elevating loading frequency and torque amplitude, a trend consistently observed across both sinusoidal

and ramp waveforms. Additionally, an intriguing aspect of the findings pertains to the influence of loading waveform on the loading rate. Specifically, for a fixed combination of loading frequency and torque amplitude, the sinusoidal waveform consistently exhibited a notably higher loading rate than the ramp waveform, thus substantiating the superior dynamicity of the sinusoidal waveform. Correspondingly, the analysis demonstrated that higher loading rates correlated with elevated shear modulus (G) and reduced damping ratio (D); conversely, lower loading rates exhibited the opposite effect on these parameters.

Moreover, G vs. γ and D vs. γ curves were constructed across a spectrum of shear strain amplitudes and loading frequencies, providing invaluable insights into the shear modulus degradation and damping ratio enhancement observed with increasing shear strains. For the mathematical representation of these curves, both the MH and RO models were employed, furnishing equations that elucidate the complex relationship between G/Gmax and γ and D and γ . Remarkably, curve fitting results underscore the superior suitability of the RO model for describing the modulus reduction behavior, while the modified hyperbolic model proves more adept for analyzing the damping ratio dynamics.

Chapter 6

Quantification and Analysis of Rock Joint Roughness Using Advanced Profiling Techniques

6.1 Introduction

Chapter 6 of this doctoral thesis focuses on quantifying the roughness of rock joints, a crucial factor in determining the hydrological and mechanical properties of rock masses in engineering applications. This chapter examines various methods for surface profiling and joint roughness estimation. The analysis considers three types of rock joint discontinuities, utilizing a 2D profilometer, 3D scanner, and 3D photogrammetry to extract surface profiles.

The chapter presents a comprehensive study on estimating Joint Roughness Coefficient (JRC) values for different surface profiles using visual interpretation, the statistical approach (Root Mean Square, Z_2), and the fractal dimension approach (D). Techniques from Barton and Choubey (1977), Tse and Cruden (1979), and Lee et al. (1990) are employed to assess these profiles.

The chapter delves into the methodology for determining JRC using visual interpretation, highlighting the potential for human error, and proposing alternative statistical measures to enhance accuracy. It also explores the fractal dimension approach as a modern method for quantifying roughness. The use of surface profiling techniques, including a profilometer, 3D scanner, and smartphone photogrammetry, is detailed, showcasing their application in capturing and analyzing the surface profiles of rock joints.

This chapter provides a comparative analysis of these profiling techniques, demonstrating their efficacy in accurately estimating JRC values and contributing to a deeper understanding of the roughness characteristics of rock joints. These findings are pivotal for improving the design and analysis of rock engineering projects.

6.2 Background

JRC can be obtained by comparing the surface profile of the jointed surface with the ten-typical profiles provided by Barton and Choubey 1977 via visual interpretation. The comparative study via visual interpretation is sometimes associated with human errors (Herda, 2006). Myers (1962) presented four surface roughness parameters to eliminate

human error in visual interpretation; of these, Root Mean Square (Z_2) was found to be more favourable. Tse and Cruden 1979 provided the relation between JRC and eight surface roughness characteristics and stated that the Root Mean Square (Z_2) and structure-function (SF) of the surface profile are majorly related to JRC values. Lee et al. 1990 performed regression analysis based on the roughness of profiles and stated that the value of the JRC possesses a second-degree polynomial relationship with the fractal dimension of the rough surface profile.

6.2.1 Determination of JRC using visual interpretation

The visual interpretation to estimate JRC is the simplest of all methods. The length of the jointed surface may range from a few centimeters to a few meters, and the JRC values can be scaled accordingly with the help of the chart proposed by Bandis et al., 1981. In this method, the JRC estimation is done based on qualitative as well as quantitative estimation of the surface profile, where the quantitative assessment is done based on the maximum peak-to-valley height of the surface profile, and qualitative estimation is done based on the description of the surface profile (Hotar & Novotany, 2005). The maximum peak-to-valley height obtained for each surface profile is then averaged and compared with the standard profile chart given by Barton and Choubey 1977 in Table 6.1. However, the rock masses in the field are more enormous than the standard surface profiles proposed by Barton and Choubey 1977. Thus, the surface profiles require suitable scaling to determine the value of JRC. Barton 1982 presented a chart to scale the surface profiles, as shown in Figure 6.1.

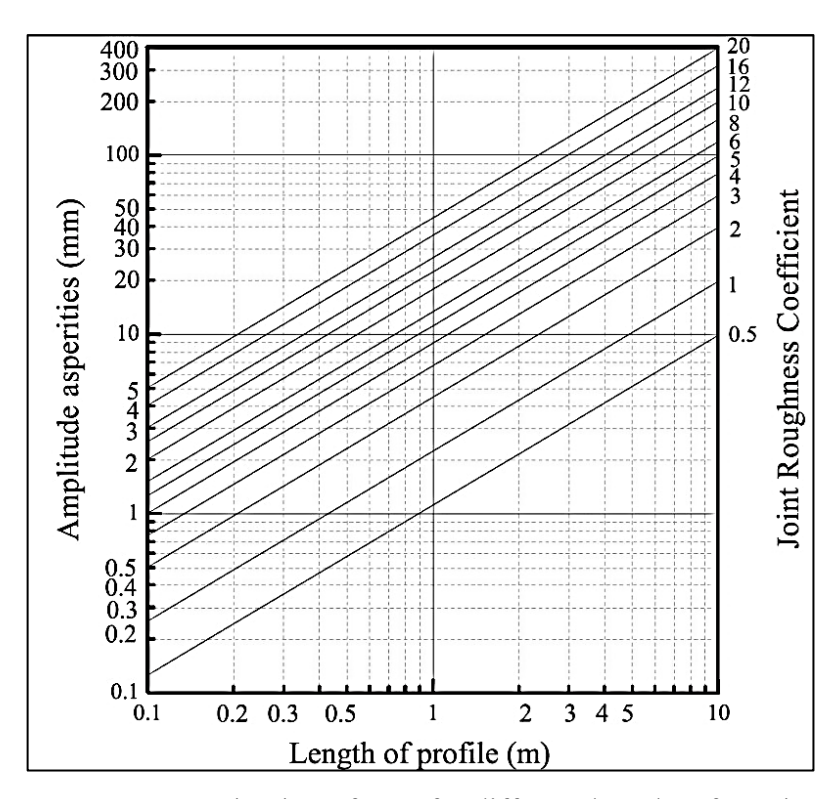


Figure 6. 1 Determination of JRC for different lengths of specimens

Table 6. 1 Standard JRC profiles provided by Barton and Choubey 1977 enhanced through P_{max} and surface description.

Surface profile (5cm)	JRC value	Surface description
	0-2	Smooth and planar, $P_{max} \sim 1.0$ mm
	2-4	Smooth and planar, $P_{max} \sim 1.5$ mm
	4-6	Undulating and planar, $P_{max}\!\sim 1.8$ $$mm$
	6-8	Rough and planar, $P_{max} \sim 3.5 \text{ mm}$
	8-10	Rough and planar, $P_{max} \sim 3.8 \text{ mm}$
	10-12	Rough and undulating, $P_{max} \sim 6.2$ mm
	12-14	Rough and undulating, $P_{max} \sim 6.5$ mm
	14-16	Rough and undulating, $P_{max} \sim 7.0$

	mm
 16-18	Rough and irregular, $P_{max} \sim 6.0$
	mm
 18-20	Rough and irregular, $P_{max} \sim 6.5$
10 20	mm

6.2.2. Determination of JRC using the statistical approach

In general, the characterization of the roughness of jointed rock surfaces considers the average deviation of the profile from the center line values. An average surface profile deviation from the center line is defined as the Root Mean Square (RMS), which is given as:

$$RMS = \left[\frac{1}{n} \int_{x=0}^{x=n} y^2 dx\right]^{1/2}$$
 (6.1)

Where dx is the spacing interval between two successive amplitudes, y is the amplitude of asperities, and n is the number of measurements. Myers 1962 used RMS as the primary tool to quantify roughness and presented Z_2 as the RMS of the first derivative of the rough profile, which is also helpful in estimating the light scattering properties of metalized surfaces. Z_3 is the RMS of the second derivative of the rough surface profile, which helps to assess the roundness of asperities of any surface. Z_4 is the percentage difference between the distance recorded along the profile when the slope is positive (the direction of movement is upwards) and the distance measured along the profile where the slope is negative. Additionally, it was discovered that, among the aforementioned parameters, Z_2 , Z_3 , and Z_4 , Z_2 is more appropriate for the frictional properties of rough surfaces than Z_3 and Z_4 .

Myers 1962 proposed various surface roughness characteristics and suggested that the Root Mean Square (Z_2) is the most effective method to predict the JRC value. The Root Mean Square of the first derivate of the surface profile can be formulated as:

$$Z_2 = \sqrt{\frac{1}{L} \int_{x=0}^{x=L} \left(\frac{dy}{dx}\right)^2 dx} = \sqrt{\frac{1}{M(Dx)^2} \sum_{i=1}^{M} (y_{i+1} - y_i)^2}$$
(6.2)

Where Z_2 is the Root Mean Square, L is the length of the surface profile, x_i and y_i are equally spaced points along with the surface profile, and M is the total number of equally spaced straight-line segments along with the surface profile.

It was noticed in many studies that the Z_2 value of a surface profile is dependent on the sampling interval. Researchers have performed several studies to develop an appealing relationship between Z_2 and JRC. Tse and Cruden 1979, proposed a correlation between Z_2 and JRC at a sampling interval of 0.5mm. Yu & Vassade, 1991; Wu et al., 2011 studied three sampling intervals, i.e., 0.25 mm, 0.5 mm, and 1 mm, to determine their influence on Z_2 . Zhang et al., 2014 developed a relationship between the Z_2 and JRC at the sampling interval of 0.5 mm, 1 mm, and 4 mm. Table 6.2 shows the correlations proposed by various researchers corresponding to the sampling interval of 0.25mm. They also found that JRC values calculated based on this fitting function were in relatively good agreement with the corresponding 10 standard profiles.

Table 6. 2 Review of literature of empirical equations to determine JRC using Z_2 at a sampling interval of 0.25 mm

Model used	Fitting relation	R	Author
$JRC = a + b * (Z_2)$	JRC = -4.51 + 60.32	0.968	Yu and Vayssade
	* (Z ₂)		(1991)
JRC	JRC = 28.43 + 28.1	0.951	Yu and Vayssade
$= a + b * log(Z_2)$	$*log(Z_2)$		(1991)
$JRC = a + b * \sqrt{Z_2}$	JRC = -16.99 + 56.15	0.967	Yu and Vayssade
	$*\sqrt{Z_2}$		(1991)
JRC	JRC = -5.05 + 64.28	0.969	Yu and Vayssade
$= a + b * tan(Z_2)$	$* tan(Z_2)$		(1991)
JRC	JRC	0.929	Tse and Cruden
$= a + b * tan^{-1}(Z_2)$	= -2.30 + 116.3		(1979)
	$* tan^{-1}(Z_2)$		

6.2.3 Fractal dimension approach

The fractal dimension approach is widely used nowadays to quantify the roughness of a jointed rock surface. Fractal dimension (D) measures variation in the curve of a surface or a bulk mass. The D value ranges from 1 to 2, corresponding to a smooth surface with JRC = 0-2 and a highly rough irregular surface with JRC = 18-20, respectively (Turk et al., 1987; Carr & Warriner, 1987). The fractal dimension (D) of any surface profile can be estimated by using the number of steps of straight-line segments (N) and the length of each step (r). Many researchers have correlated the JRC value of a surface profile with the D for the 10 standard roughness surface profiles proposed by Barton and Choubey 1977. Table 6.3 presents the empirical correlations between JRC and D.

Table 6.3 Review of literature of empirical equations to determine JRC using D

Fitting Relation	R	JRC for a smooth surface	Fractal dimension,	Author
JRC = 172.206D - 167.295	0.998	4.9114	1-1.0876	Zhou and Xiong 1996
JRC = -1138.6 + 1141.6D	-	3	1-1.0149	Turk et al. 1987
JRC = 7811778.93 D^3 - 23723041.684 D^2 + 24014672.3562 D - 8103409.7809	0.993	-0.1809	1-1.0144	Bae et al. 2011
JRC = 1870(D-1)	0.684	0	1-1.0107	Maerz and Franklin 1990
JRC = 1195.38(D-1)	_	0	1-1.0167	Lamas 1996
$JRC = 479.396(D-1)^{1.0655}$	-	0	1-1.0495	Zhou and Xiong 1996
$JRC = 85.2671(D-1)^{0.5679}$	-	0	1-1.0778	Xie and Pariseau

				1994
JRC				
$= -0.87804 + 37.7844 \frac{(D-1)}{0.015}$	0.95	-0.878	1.0005- 1.0113	Lee et al., 1990
$-16.9304 \left[\frac{D-1}{0.015} \right]^2$			1.0113	1770

6.3 Surface profiling techniques

6.3.1 Surface profiling using a profilometer

Surface profiling using a profile gauge or profilometer is the standard, comprehensible method to obtain the surface profile. A typical example of surface profiling using the profile comb and profile obtained is shown in Figure 6.2, where the width of each pin in the set of steel pins is 0.9 mm.

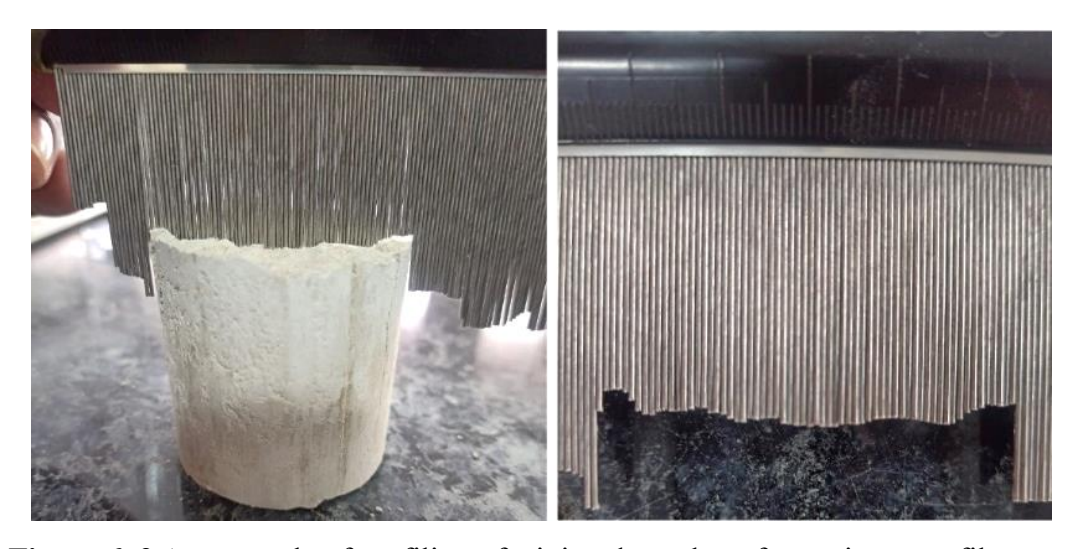


Figure 6. 2 An example of profiling of a jointed rough surface using a profilometer

6.3.2 Surface profiling using a 3D scanner

In this study, three rough surfaces were scanned to obtain the 3D profiles of the surfaces. The Steinbechler Comet L3D scanner, equipped with a compact, high-performance 3D sensor that uses innovative structured blue LED lighting 3D scanning technology, was used for scanning purposes. The resolution of the 3D scanner used was 0.024 mm.

Figure 6.3 shows the typical pictures of the rough surface obtained using 3D scanner and photogrammetry techniques.

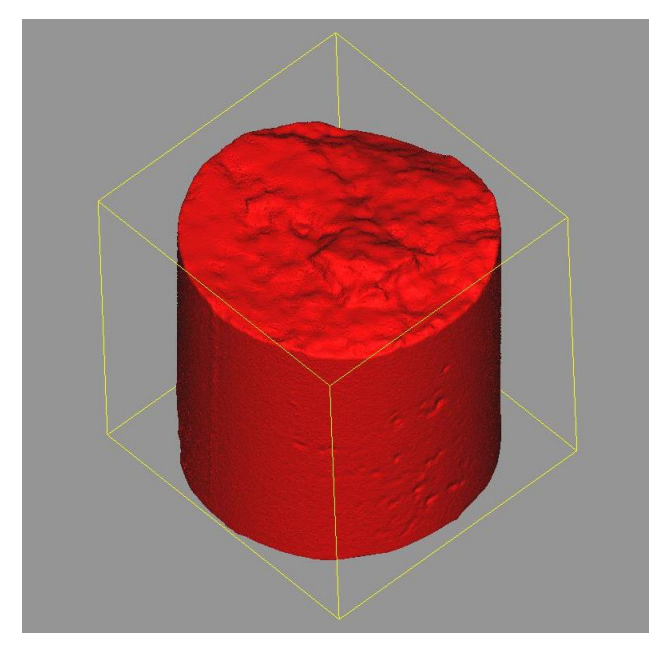


Figure 6. 3 A typical representation of an image obtained from 3D scanning.

6.3.3 Surface profiling using smartphone photogrammetry

Due to the developments in feature-matching algorithms, a technique called structure from motion is introduced in photogrammetry, which provides a 3D reconstruction of digital images. With the help of this technique, the coordinates of the object in space can be easily detected and matched using overlapping digital images. In the present study, a free tool, i.e., Visual SFM, has been used to obtain the 3D model of the rough rock surface. The construction of a 3D joint rough surface has been done in three steps, i.e., data collection followed by 3D reconstruction of jointed surface, preparation of point cloud, and assessment of point cloud. The workflow used for the smartphone photogrammetry is shown in Figure 6.4.

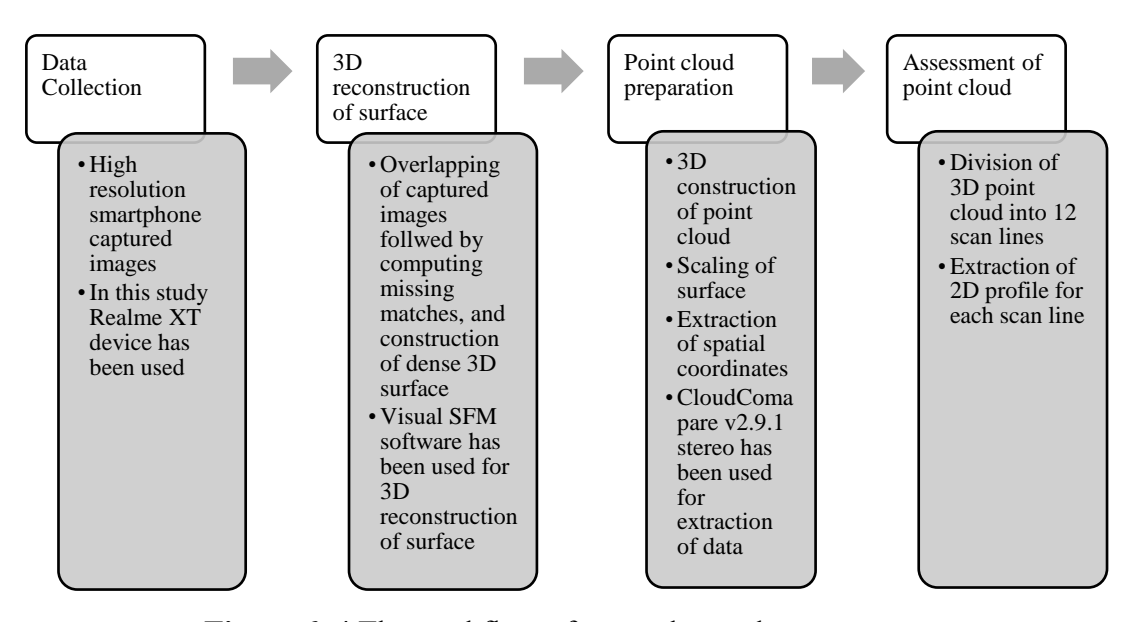


Figure 6. 4 The workflow of smartphone photogrammetry

In this study, three randomly picked jointed rock samples have been considered, and the discontinuity surfaces of all three surfaces have been replicated using gypsum to produce an artificial rock jointed surface of a circular shape having a 5 cm diameter. For replicating the jointed rough surface, the silicon gun has been used to imprint the top discontinuity surface of the rock specimen into the gypsum sample. With the aim of the economic approach of the study, the smartphone named Realme XT has been used to get the images of three jointed rough surfaces of gypsum samples prepared for the study. The specifications of the smartphone camera are provided in Table 4. The images were collected in moving smartphone capture mode (MSC) for all three samples. Many images were captured for each jointed surface at different angles, including 15°, 30°, 45°, 60°, 75°, and 90° at a 25-50 mm distance between the camera and specimen, forming a hemispherical dome of overlapping images.

Table 6. 4 Description of camera specifications used in capturing images.

Camera	Realme XT
Sensor type	Samsung GW1 Sensor
Sensor size	1/1.72" (~7.44*5.58 mm)
Aperture	f/2.25
Autofocus	Yes
Image format	JPG
Image resolution	6936*9248

After capturing the images, the 3D model of the rough surface was constructed using a software tool named VisualSFM v0.5.22, which functions along with Clustering views for Multi-View Stereo algorithms (CMVS). The 3D surface of the jointed surface has been developed in three stages, i.e., alignment of captured photographs, construction of dense point cloud, and scaling (resizing) of the 3D image. The photographs were overlapped and matched to form missing data points. Ultimately, the dense point cloud of the three jointed rough surfaces of the gypsum sample of actual size was obtained from structure from motion (SFM) models. The dense point cloud was cleared to remove the unwanted points, followed by orientation, rotation, and translation using CloudCompare v2.9.1 stereo software. Figure 6.5 shows a typical 3D surface profile obtained from smartphone-captured images.

The scaling of the point cloud has been performed by applying a suitable scaling factor to extract the desired size of the dense point cloud as that of the original specimen. To obtain a suitable scaling factor, the dimensions of the dense point cloud were measured using the 'Point-picking' tool available in CloudCompare v2.9.1stereo software. As the original dimensions of the specimen were previously known, a suitable resizing multiplication factor could be applied to the dense point cloud to get the desired size, i.e., the diameter of 50 mm, using the 'Multiply/scale' tool in the CloudCompare v2.9.1stereo. After applying a suitable multiplying factor to the dense cloud, the dimensions of the dense point cloud were measured again to verify the size. A typical picture of a dense 3D surface after scaling is shown in Figure 6.6. The scaling was done by keeping all the entities in place so that the shape of the dense point cloud was not disturbed.

The point cloud was then assessed to get the spatial coordinates of each point of the point cloud. The typical picture of the 3D model constructed using Visual SFM and point cloud obtained in CloudCompare v2.9.1 stereo is shown in Figure 6.5. Once the point cloud is obtained, the coordinates of every point of the 3D rough surface are available for the JRC estimation.

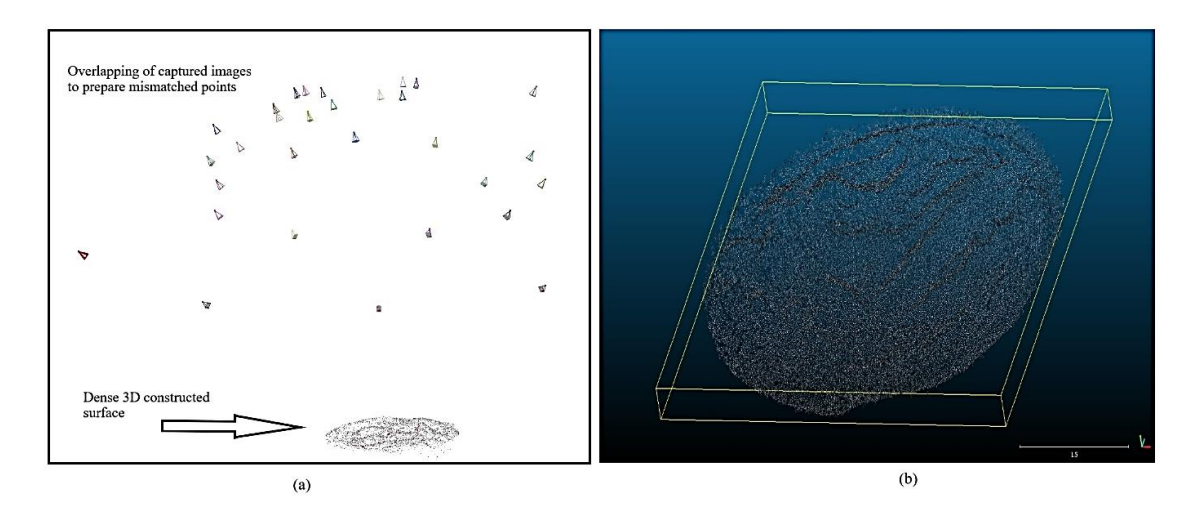


Figure 6. 5 Typical view of the 3D surface profile obtained from smartphone captured images, (a) Dense 3D reconstruction of 2D images obtained from VisualSFM (b) Point cloud of the 3D surface obtained from CloudCompare 2.9.1 stereo.

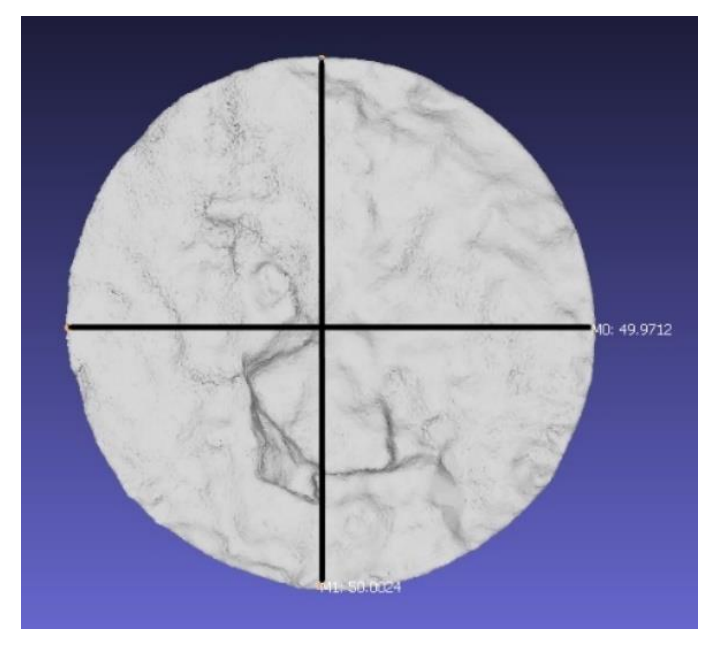


Figure 6. 6 View of measured dimensions of the 3D dense reconstructed surface using CloudCompare 2.9.1 stereo

6.4 Comparison of Photogrammetry technique and other methods

The 3D discontinuity surface has been divided into 12 scan lines that run diametrically (each 5 cm in length) to get the 2D profiles across each scan line. A typical example of a scan line is shown in Figure 6.7. A reference point was considered on the edge of the original surface, which is also visible in the 3D profile obtained from the 3D scanner and photogrammetry technique, as shown in Figure 6.8. The line passing through the reference point and the center of the original surface was treated as the first scan line.

To extract the scan line 1, one coordinate, say x, was kept fixed at 0, then moving in another axis (y) from one corner to another, i.e., from (0, 2.5) to (0, -2.5) at the sampling interval of 0.01 mm. The data obtained from the 3D point cloud was sorted to get the third coordinate (z) (i.e., the height of each point in the point cloud) corresponding to a particular combination of x and y of a specific scan line. The first scan line's coordinates (x, y, and z coordinates) were then extracted from the 3D point cloud. By taking an increment of 15° from the first scan line in the x-y plane, the x and z coordinates were gathered to get the 2D profiles of all 12 scan lines.

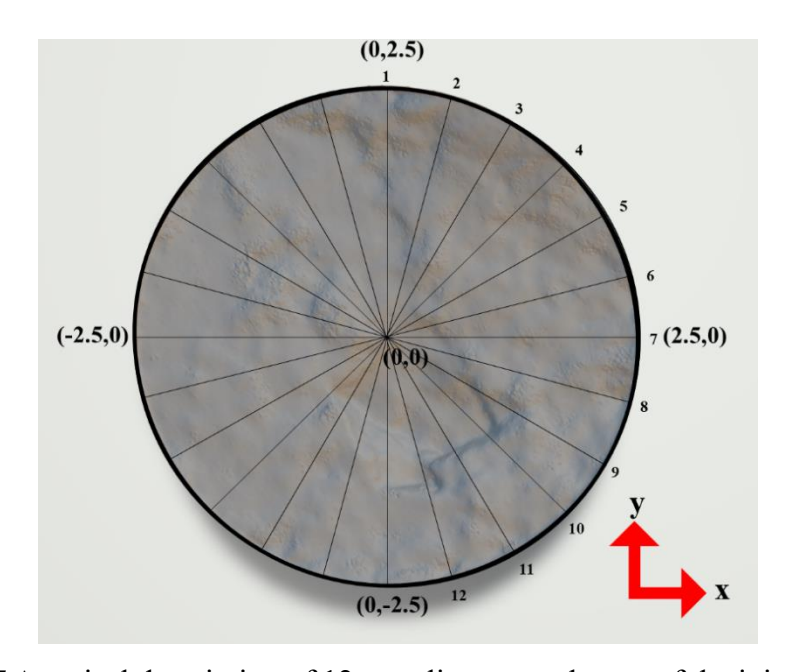


Figure 6. 7 A typical description of 12 scan lines over the top of the jointed surface.

The surface profiles of all three discontinuity surfaces have been extracted for all 12 scan lines using a profilometer, 3D scanner, and the photogrammetry technique. The surface profilometer was placed diametrically across each designated scan line of the gypsum sample, and the projection of the profilometer was then traced on the paper to get the surface profiles across all 12 scan lines. The least count of the profilometer is 0.9 mm (in the horizontal direction). The least count (minimum resolution) of the surface profile obtained from the photogrammetric technique in the horizontal direction (i.e., x and z direction) is 0.01 mm (which is the horizontal distance between the two points of the point cloud). The surface profiles obtained from the profilometer, 3D scanner, and photogrammetry technique for each scan line have been analyzed to

estimate the JRC value using visual interpretation, Z₂, i.e., RMS, and the Fractal dimension approach.

It was observed from the visual interpretation that the maximum peak-to-valley height obtained for all the 12 scan lines surface profiles using all the methods, i.e., profilometer, 3D scanner, and photogrammetry technique, are nearly the same, with a very slight difference in the surface description. Therefore, the JRC values obtained from visual interpretation (Hotar & Navatony, 2005) are nearly the same for surface profiles obtained from the profilometer, 3D scanner, and Photogrammetry techniques, and the same can be concluded for all three rock discontinuity surfaces. A typical picture of a specific surface profile obtained from the 3D scanner and photogrammetry technique is shown in Figure 6.8.

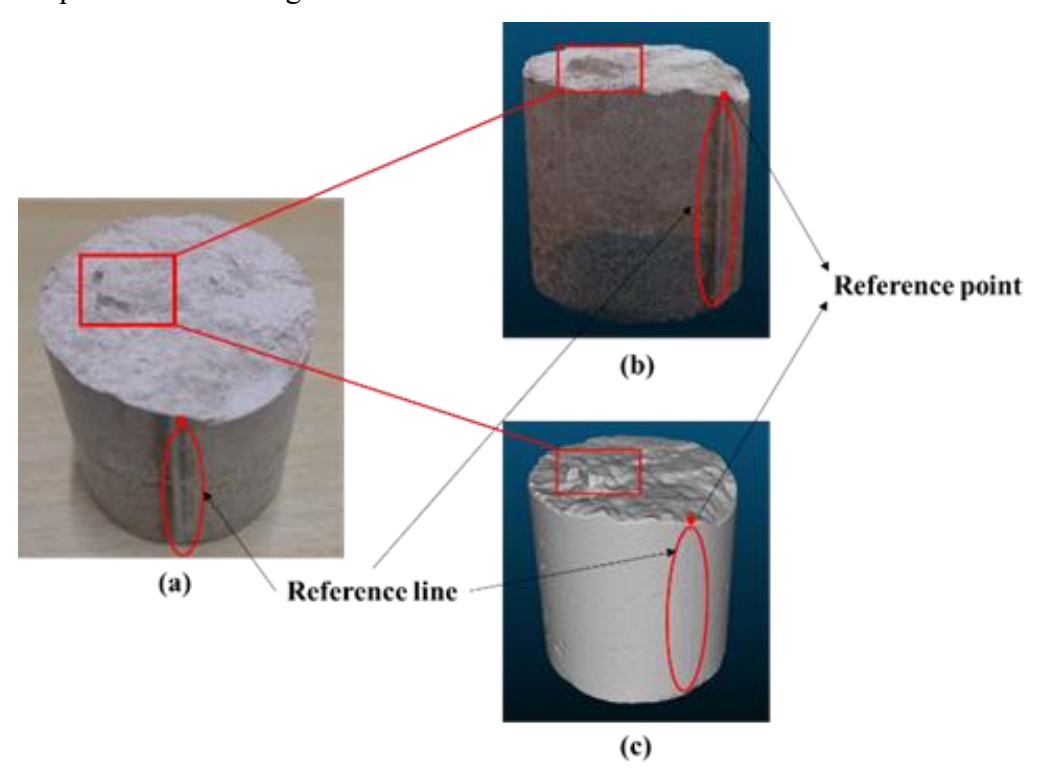


Figure 6. 8 Pictorial view of replicated gypsum specimen with an indent at the surface, reference line, and reference point on (a) original surface, (b) surface profile from photogrammetry technique, and (c) surface profile from 3D scanning

The JRC values were obtained from the Root Mean Square method, fractal approach, and visual interpretation and compared against each other. The value of the Z_2 parameter has been obtained for the profiles obtained from the 3D scanner and photogrammetric technique for all 12 scan lines with a sampling interval of 0.5 mm. In this study, the relationship between Z_2 and JRC proposed by Tse and Cruden 1979 is employed, which is stated as follows:

$$JRC = 32.20 + 32.47 \log (Z_2) \tag{3}$$

The mean values of Z_2 obtained from 12 scan lines for all the 3 rough surfaces, along with the standard deviation, are given in Table 6.5. Similarly, the fractal dimension values have been obtained with a value of r of 0.2 mm for all the 12 scan lines of the rough surfaces obtained from the 3D scanner and photogrammetry techniques. In this present study, the relation of D and JRC proposed by Lee et al. 1990 has been used, which is stated as follows:

$$JRC = -0.87804 + 37.7844 \frac{(D-1)}{0.015} - 16.9304 \left[\frac{D-1}{0.015} \right]^2$$
 (4)

The mean values of the number of steps (N) and fractal dimension (D) for the three rough surfaces, obtained for 12 scan lines, in addition to standard deviation, are given in Table 6.6.

Table 6. 5 Summary of Z₂, obtained for 3D scanned and photogrammetry profiles using Tse & Cruden, (1979)

Surface profiling method	Discontinuity surface	\mathbf{Z}_2
	Surface 1	0.145±0.006
3D scanner	Surface 2	0.193±0.010
	Surface 3	0.295±0.015
	Surface 1	0.144±0.005
Photogrammetry technique	Surface 2	0.194±0.009
	Surface 3	0.293±0.013

Table 6. 6 Summary of D obtained for 3D scanned and photogrammetry profiles using Lee et al., 1990

Surface profiling	Surface profiling Discontinuity		Fractal	
method	surface	steps, N	Dimension, D	
	Surface 1	115.2±0.16	1.030±0.0002	
3D scanner	Surface 2	114.4±0.21	1.027±0.0004	
	Surface 3	111.9±0.32	1.024±0.0003	
Photogrammetry	Surface 1	115.3±0.15	1.031±0.0002	
technique	Surface 2	114.2±0.19	1.028±0.0003	
teemique	Surface 3	111.7±0.3	1.024±0.0004	

The data points obtained in one scan line across the horizontal direction of the surface profile obtained from the 3D scanner and the photogrammetric technique are more precise than visual interpretation. The pictures of the surface profiles of all three rough surfaces obtained from the visual interpretation, 3D scanner, and photogrammetric technique are shown in Figure 6.9. It has been observed that the JRC values obtained from the visual interpretation, i.e., the method proposed by Barton and Choubey 1977 were in good comparison to the values extracted using the statistical approach provided by Tse and Cruden 1979 and Lee et al. 1990. The JRC values of the three discontinuity surfaces obtained from the photogrammetry technique comply with the JRC findings of 3D scanning and surface profilometer. The visual interpretation technique has been used to determine the JRC of the surface profiles obtained from the surface profilometer. Table 6.7 displays the JRC values for surface profiles derived from the 3D scanner and photogrammetry technology, which have been analyzed using the fractal approach, the Root Mean Square method, and visual interpretations.

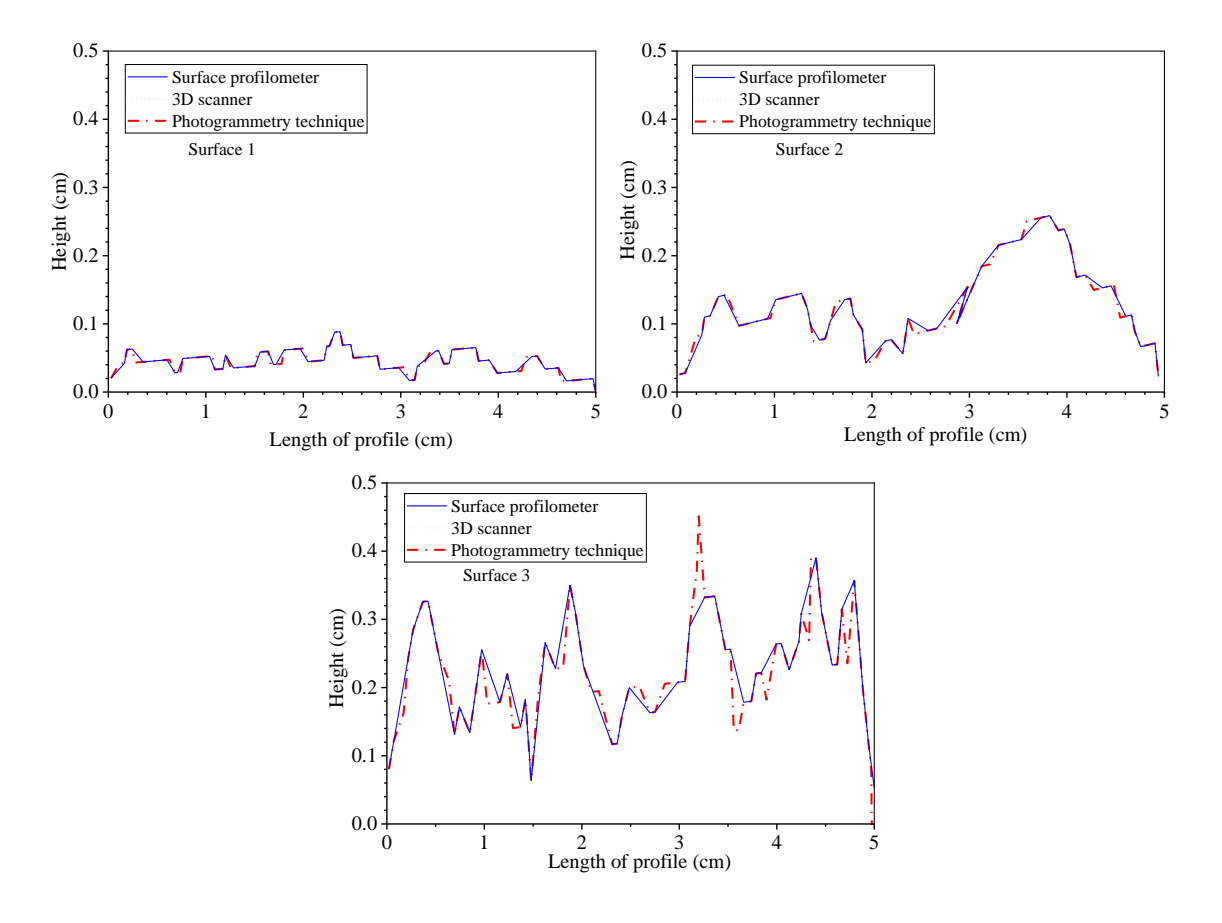


Figure 6. 9 An illustration of the surface profile of a scan line of three various jointed rough surfaces obtained from profilometer, 3D scanning, and photogrammetry technique

Table 6. 7 Summary of the JRC observations

		Joint roug	Joint roughness coefficient (J		
Surface profiling method	Discontinuity surface	Visual interpretation	RMS, Z ₂	Fractal Dimension, D	
Surface	Surface 1	4-6	-	-	
profilometer	Surface 2	8-10	-	-	
promometer	Surface 3	14-16	-	-	
	Surface 1	4-6	5±0.6	5±0.4	
3D scanner	Surface 2	8-10	9±0.7	9±0.3	
	Surface 3	14-16	15±0.7	16±0.4	
Photogrammetry technique	Surface 1	4-6	5±0.5	5±0.5	
	Surface 2	8-10	9±0.6	9±0.4	
teeninque	Surface 3	14-16	15±0.9	16±0.5	

6.5 Summary

In this study, the low-cost economic approach of the photogrammetric technique using a smartphone has been used to obtain the 3D surface profile of three jointed rough surfaces of gypsum samples to estimate JRC. Three different rough surfaces have been considered in this study, and roughness profiles have been extracted using a 2D surface profilometer and 3D scanning and photogrammetry techniques. The scan line technique has been used to get the 2D profiles from the 3D surface profiles. The surface profiles have been obtained for 12 scan lines, and quantification of JRC has been done using visual interpretations, Root Mean Square methods, and fractal dimension techniques. The surface profile obtained from the profilometer, 3D scanner, and photogrammetry techniques has been compared. Based on the study, it has been concluded that the surface profiles obtained from the photogrammetric technique using smartphones provide realistic profiling compared to the profilometer due to lower least count and higher precision. The surface profiles obtained from the smartphone photogrammetry technique agree with those obtained from the 3D scanner. The JRC values obtained from visual interpretation, Root Mean Square method, and fractal approach lie nearly in the same range for the photogrammetry technique, 3D scanner, and profilometer for all the surface profiles. Therefore, the smartphone photogrammetry technique can be considered an economic tool to estimate JRC values with good precision.

Chapter 7

Dynamic Response of Jointed Rock Masses: Effects of Joint Spacing, Confining Pressure, and Loading Frequency

7.1 Introduction

This chapter delves into the dynamic characteristics of jointed rock masses, particularly focusing on the propagation of shear waves induced by seismic or explosive activities. The research evaluates the influence of joint spacing on the dynamic response of rock by examining specimens with varying numbers of joints (1, 2, 3, and 4 joints). The experimental approach involves resonant column (RC) and cyclic torsional shear (CTS) testing on plain-jointed gypsum plaster specimens across a broad spectrum of strain amplitudes.

Key aspects explored include the effects of confining pressure (ranging from 0 kPa to 2500 kPa) and loading frequency (spanning 0.1 Hz to 10 Hz) on the shear modulus and damping ratio of the specimens. The study provides a comparative analysis of these parameters under different strain conditions. Both the Ramberg-Osgood and Modified Hyperbolic models are employed to fit the experimental data, highlighting the nonlinear behaviour of the rock specimens.

The chapter outlines the methodology, including specimen preparation and testing protocols, and presents detailed results from RC and CTS tests. Findings indicate that shear modulus decreases and damping ratio increases with higher strain amplitudes, while increased confining pressure and loading frequency enhance shear modulus and reduce damping ratio. The impact of joint number and spacing is also discussed, revealing that more joints lead to lower shear modulus and higher damping ratios.

Overall, this chapter contributes valuable insights into the dynamic behaviour of jointed rock masses, which is essential for understanding and mitigating the effects of seismic and explosive forces in geological and engineering applications.

7.2 Test Plan

Resonant column (RC) and cyclic torsional shear (CTS) tests were conducted on plain-jointed gypsum plaster specimens with joint spacings of 50 mm, 33.3 mm, 25 mm, and 20 mm, respectively, as depicted in Figure 7.1. To determine the effect of confining

pressure on plain jointed specimens, the jointed specimens were subjected to an array of confining pressure starting from 0 kPa to 2500 kPa in increments of 500 kPa. Additionally, to examine the effect of the frequency of loading on plain-jointed rock specimens, a range of loading frequency from 0.1 Hz to 10 Hz was applied under a constant confining pressure of 50 kPa. The density of specimens with plain joints was 1.69 g/cc regardless of joint spacing. For this study, the response of the jointed rock mass (either plain) is analyzed as an equivalent continuum material.

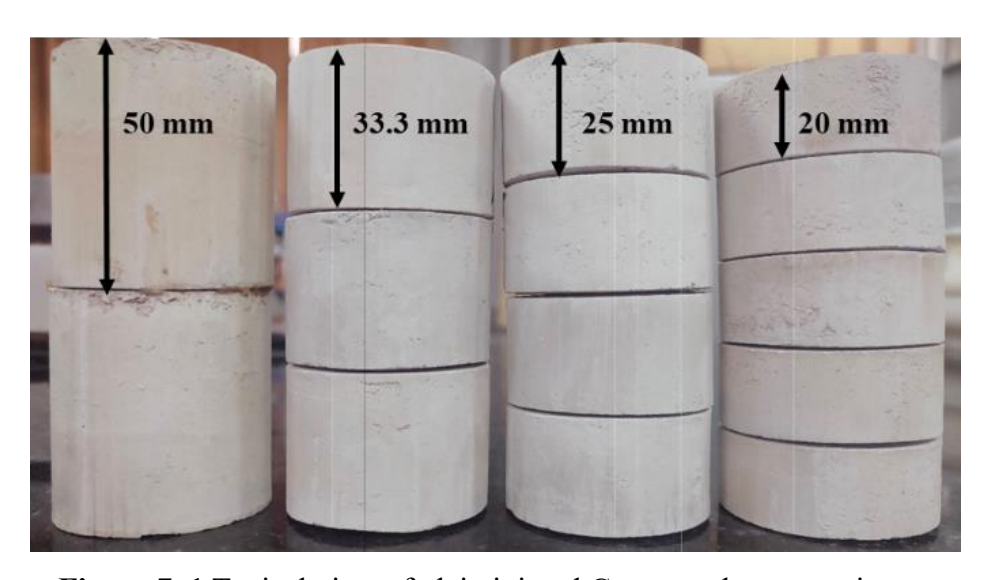


Figure 7. 1 Typical view of plain jointed Gypsum plaster specimens

7.3 Results

Resonant column testing has been conducted under a spectrum of strain amplitudes and confining pressure conditions to ascertain both the shear modulus and damping ratio. Concurrently, cyclic torsional shear testing has been executed across diverse strain amplitudes and loading frequencies to delineate the shear modulus and damping ratio. Furthermore, a comparative analysis has been undertaken on differing joint configurations to assess their dynamic responses across varying experimental parameters.

7.3.1 Resonant Column Testing: The experimental results demonstrate that as the amplitude of shear strain increases, the shear modulus values decrease, and the damping ratio of the material increases, as depicted in Figures 7.2, and 7.3. A similar trend was

found for all joint spacings and confining pressures. In particular, it has been observed that a rise in confining pressure causes a hike in the shear modulus and a decline in the damping ratio. Moreover, when the confining pressure increases, the nonlinearity related to the decline in shear modulus with the rise in the strain level decreases. At any given strain level, the shear modulus values decline with an increased number of joints.

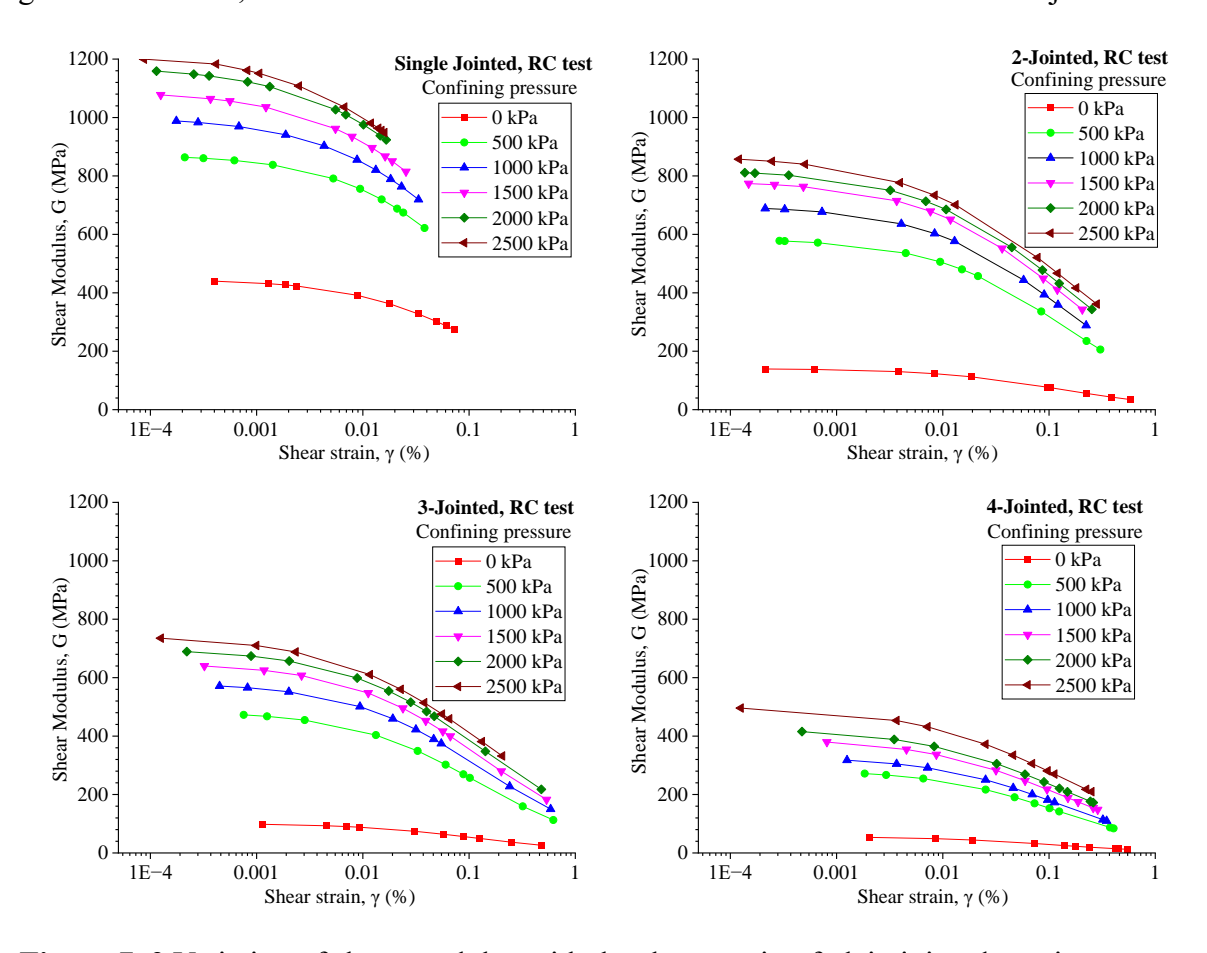


Figure 7. 2 Variation of shear modulus with the shear strain of plain jointed specimens under resonant column testing

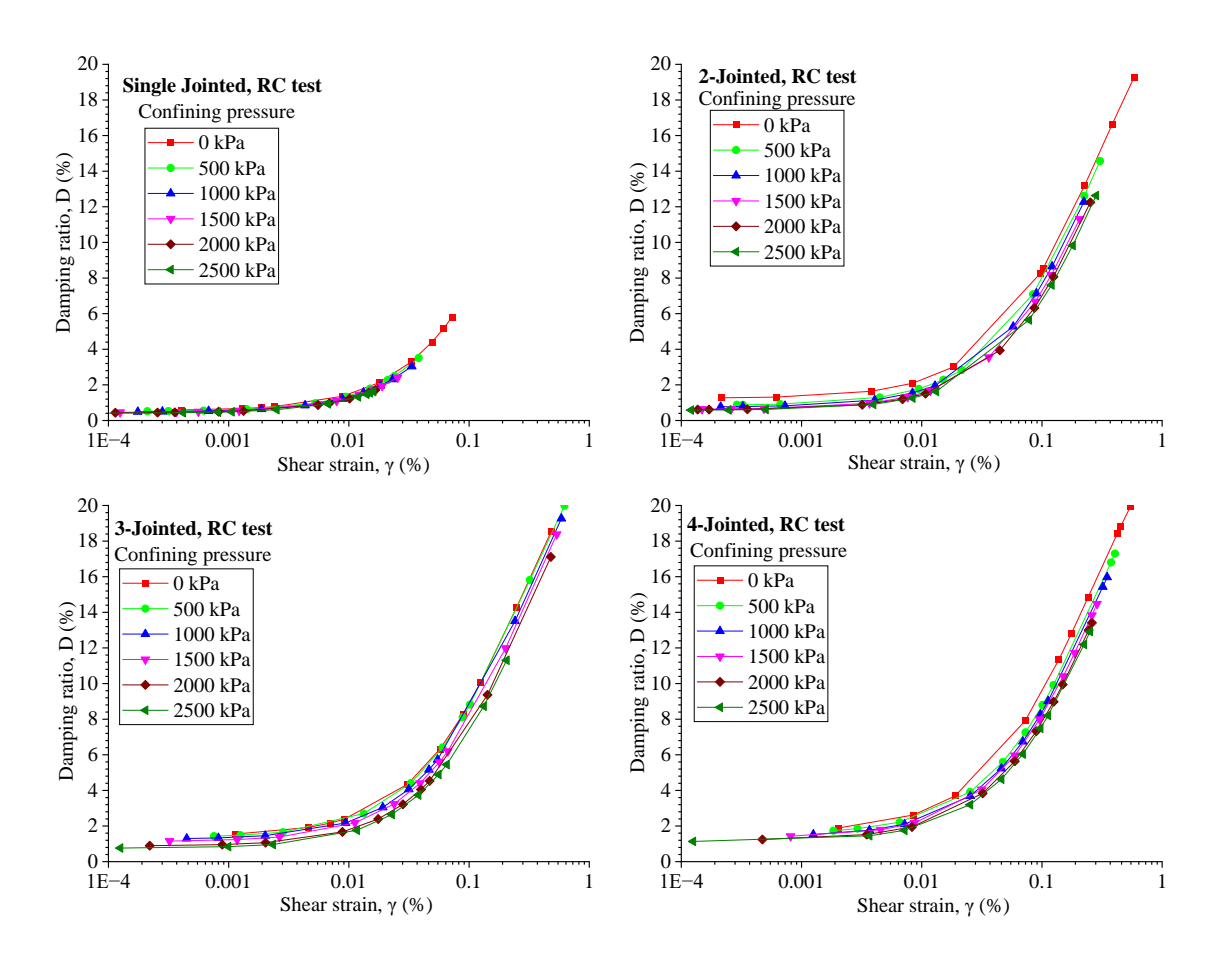


Figure 7. 3 Variation of damping ratio with the shear strain of plain jointed specimens under resonant column testing

7.3.2 Cyclic torsional shear testing: The cyclic torsional shear testing of plain jointed specimens demonstrates that the shear modulus values increase and the damping ratio values reduce as the frequency of loading rises while the amplitude of loading remains constant. In addition, an increase in strain amplitude results in a declination in shear modulus and a rise in damping ratio while the loading frequency remains the same.

The cyclic torsional shear tests were conducted at a constant confining pressure of 50 kPa with various strain amplitudes and loading frequencies. As shown in Figures 7.4, and 7.5, for all joint spacings, the shear modulus values decline with a rise in strain amplitude and hike with an escalation in the loading frequency. Compared to cyclic torsional shear testing, resonant column testing yields greater shear modulus values at a given shear strain amplitude. The reason is the higher loading rate associated with the RC test than the CTS test. In RC testing, the specimen is exposed to torsional vibrations whose loading frequency is considerably higher than the cyclic torsional shear loading applied in CTS. With an escalation in the number of joints, the influence of the loading frequency on the shear modulus diminishes.

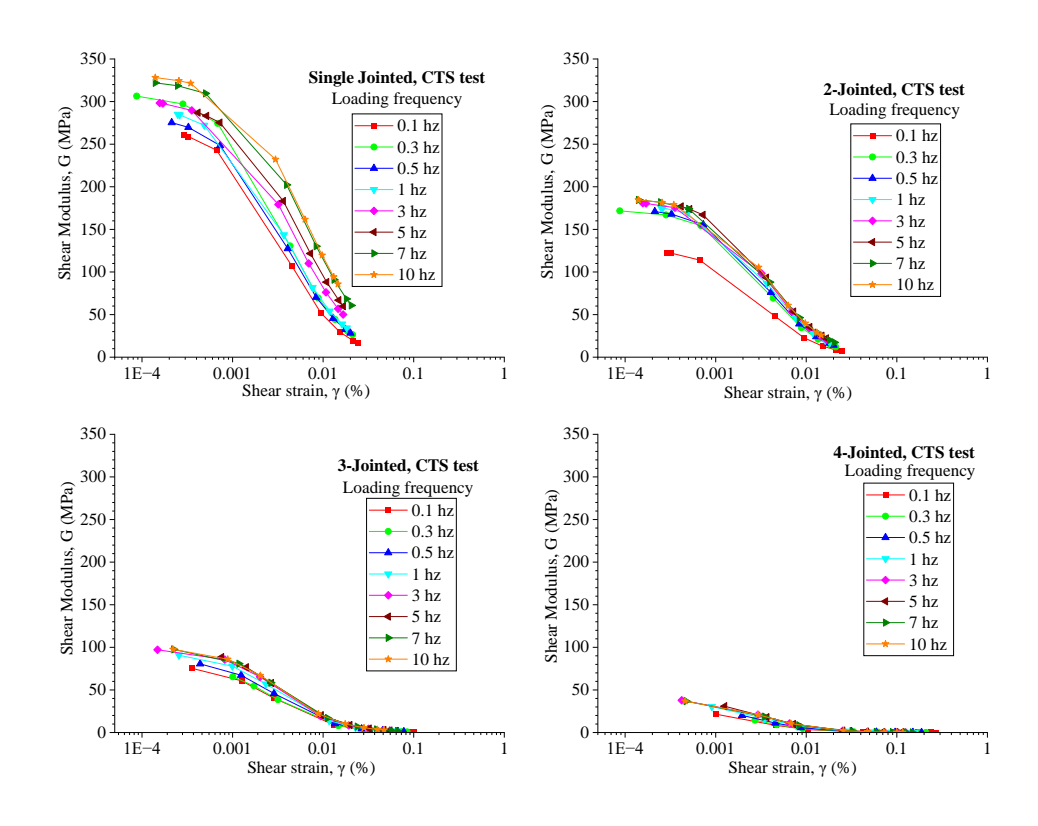


Figure 7. 4 Variation of shear modulus with the shear strain of plain jointed specimens under cyclic torsional shear testing

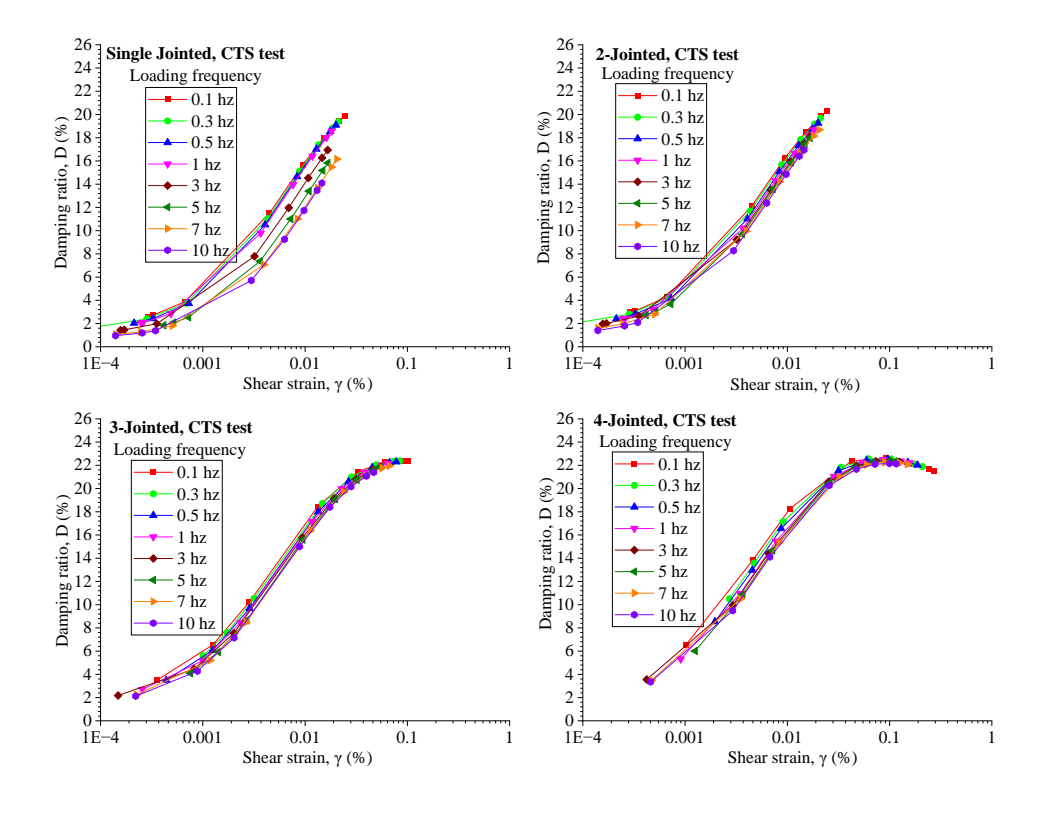


Figure 7. 5 Variation of damping ratio with the shear strain of plain jointed specimens under cyclic torsional testing

7.4 Analysis and Discussions

The dynamic properties of plain-jointed gypsum plaster specimens were evaluated across a spectrum of strain amplitudes (ranging from 10⁻⁵ to 10⁻¹%) under different levels of confining pressure and loading frequencies. The results of RC and CTS tests were analyzed in this study using the MH model (Darendeli, 2001) and the RO material model (Ramberg-Osgood, 1943).

7.4.1 Effect of confining pressure: The rise in shear modulus and decline in damping ratio with increment in the confining pressure follows a power function, which can be stated as:

$$y = a \left(\frac{\sigma_n}{1kPa}\right)^b \tag{7.1}$$

Where y is the dependent variable, which can be either shear modulus (G) or damping ratio (D), a is the constant whose value depends on the material property at the confining pressure of 1 kPa, and b is the sensitivity constant.

With an increment in the number of joints, the sensitivity of the modification in shear modulus and damping ratio to a rise in confining pressure increases. Furthermore, the dynamic characteristics of jointed rock specimens under various shear strain amplitudes are not significantly affected by confining pressure; nevertheless, a rapid increase in sensitivity was seen near the 0.1% strain level. The same pattern has been observed for all joint conditions. With a reduction in joint spacing, the value of a decreases, and b rises. The deviation in shear modulus and damping ratio with confining pressure for specimens with plain joints is depicted in Figures 7.6, and 7.7, respectively.

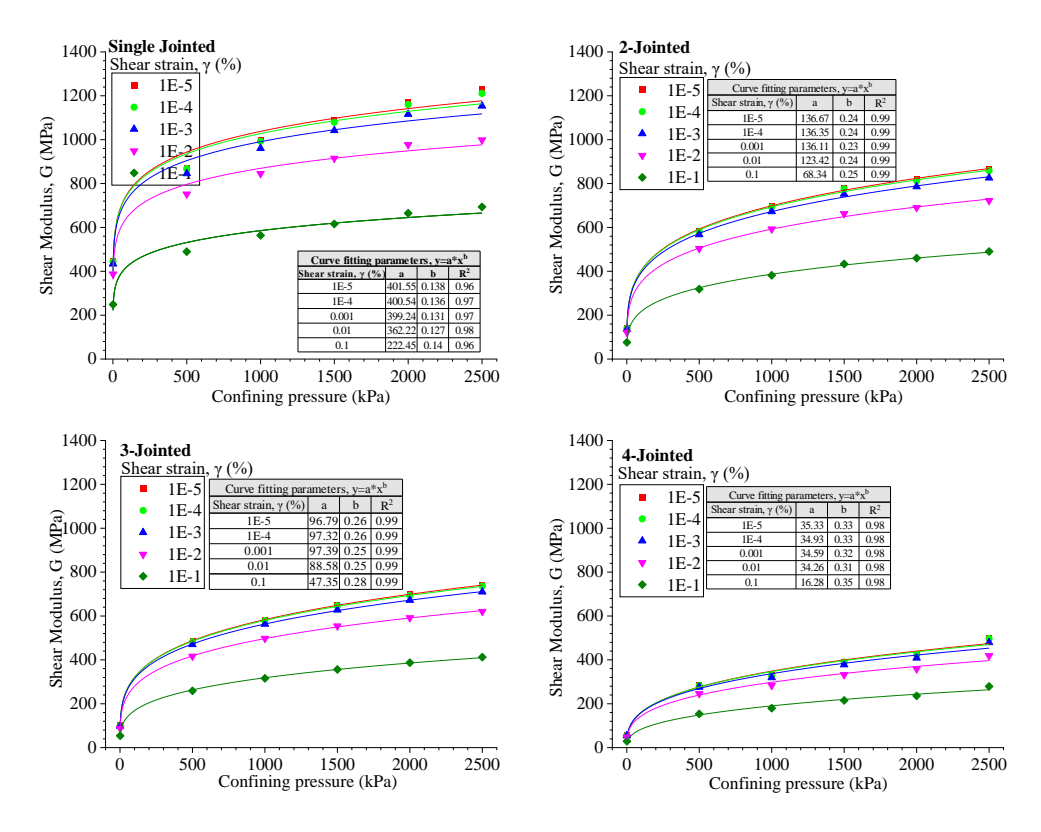


Figure 7. 6 Variation of shear modulus with confining pressure for plain jointed specimens

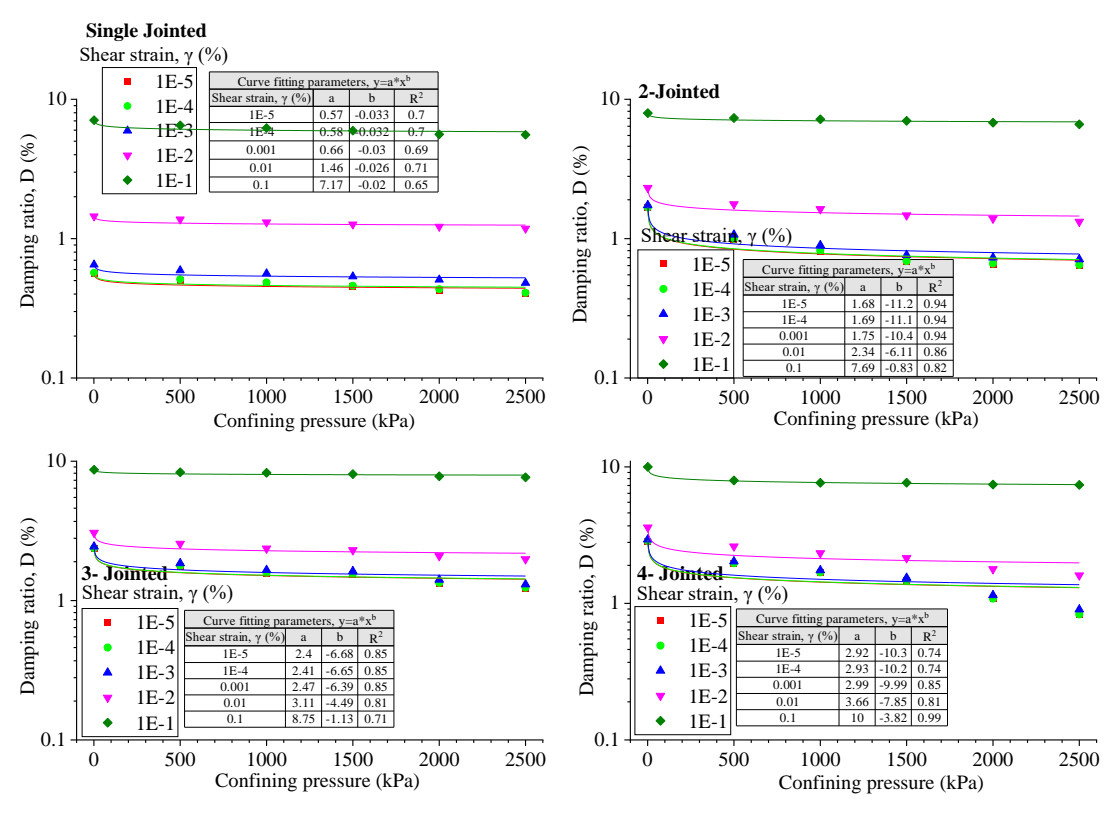


Figure 7. 7 Variation of damping ratio with confining pressure for plain jointed specimens

7.4.2 Effect of loading frequency: The experimental results from CTS testing demonstrated that the loading frequency substantially affects the dynamic characteristics of plain-jointed rock specimens. Consistent with <u>Xiao et al. (2008)</u>, increased shear modulus and reduced damping ratios have been observed as loading frequency increases.

Similarly, the influence of confining pressure on the dynamic characteristics, the modification of shear modulus, and the damping ratio with a change in loading frequency follow the power function. Increasing the shear strain amplitude enhances the sensitivity of variation in the dynamic characteristics of plain-jointed specimens with the loading frequency. The modification of shear modulus with loading frequency and damping ratio with the loading frequency for plain jointed specimens are depicted in Figures 7.8 and 7.9, respectively.

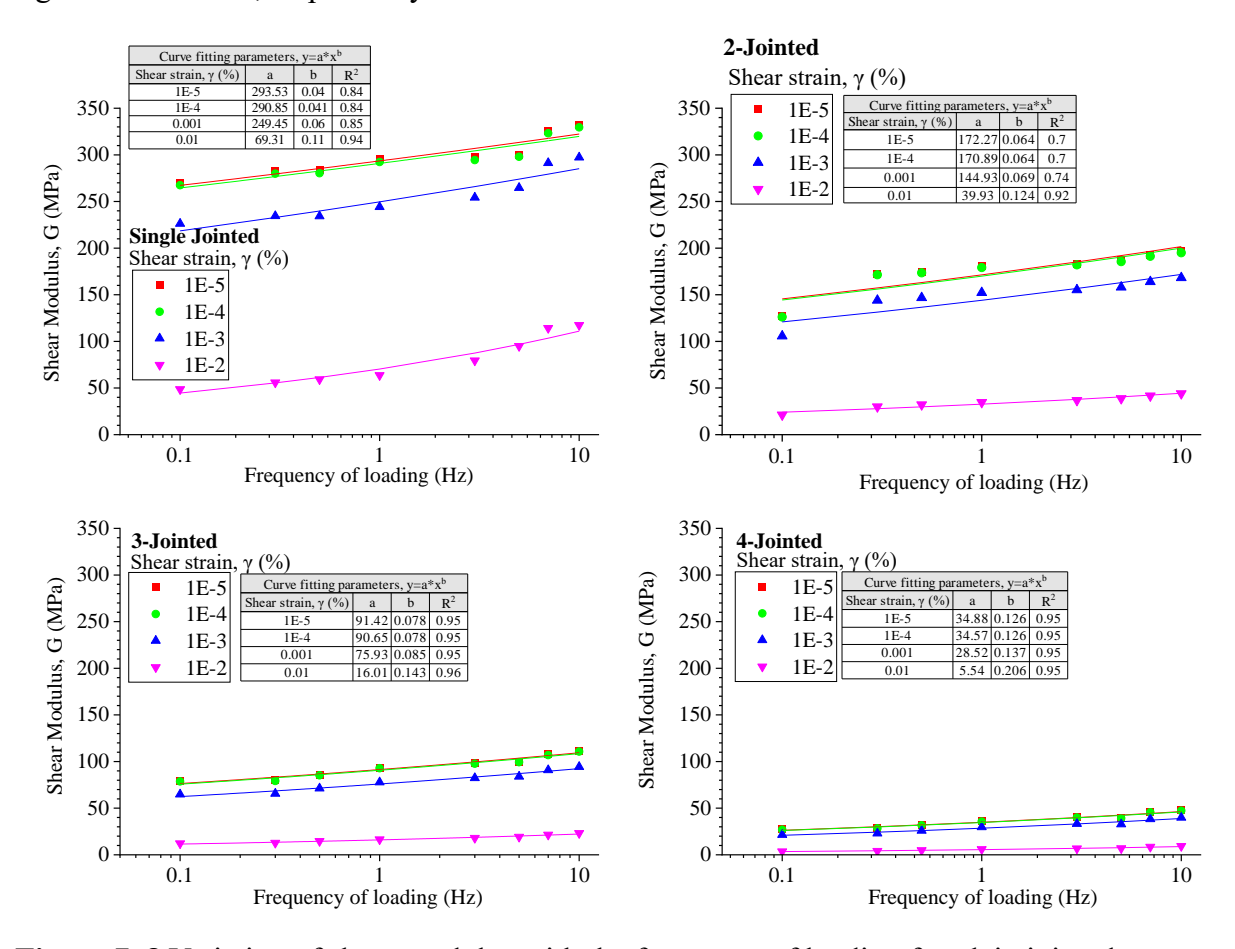


Figure 7. 8 Variation of shear modulus with the frequency of loading for plain jointed specimens

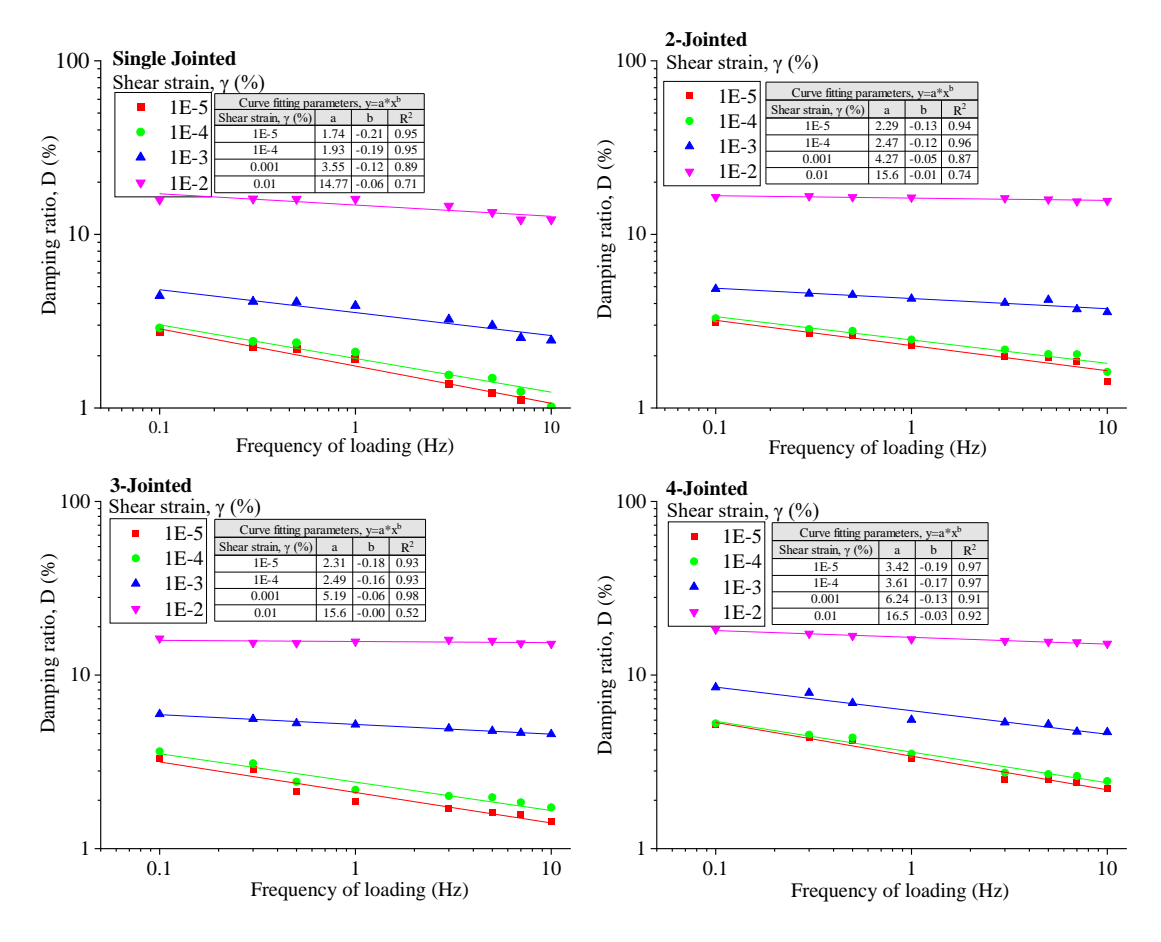


Figure 7.9 Variation of damping ratio with the frequency of loading for plain jointed specimens

7.4.3 Ramberg-Osgood material model: Normalized modulus reduction and material damping ratio curves have been obtained for plain-jointed rock specimens with varying joint spacings. The RC and CTS testing outcomes have been fitted to the modified hyperbolic and Ramberg-Osgood models. It was discovered that both the MH and RO models fit the experimental data well. While fitting the experimental results of RC testing with the MH model, it was observed that the value of ' γ_{ref} ' raised with an increment in confining pressure, and ' δ ' declined with the increase in the number of joints. Likewise, the findings of this study showed that the value of ' γ_{ref} ' increased and ' δ ' decreased as the loading frequency increased during CTS testing. The curve fitting for plain-jointed specimens subjected to RC and CTS testing is depicted in Figures 7.10, and 7.11, respectively. The values of the curve fitting parameters for the upper and lower bound curves of the MH and RO models are provided in Tables 7.1 and 7.2.

Table 7. 1 Results obtained from curve fitting performed for plain jointed specimens under RC testing

Curve fitting parameters (Resonant Column testing), plain jointed							
Number of joints		Ramberg	-Osgood Model	Modified model	hyperbolic		
		r α΄		γref	δ		
1	Upper bound	1.605	0.130	0.208	0.715		
1	Lower bound	1.524	0.297	0.110	0.705		
2	Upper bound	1.607	0.303	0.185	0.795		
2	Lower bound	1.702	0.105	0.082	0.725		
3	Upper bound	1.687	0.202	0.155	0.795		
	Lower bound	1.722	0.125	0.083	0.762		
4	Upper bound	1.717	0.223	0.149	0.802		
·	Lower bound	1.732	0.134	0.085	0.651		

 Table 7. 2 Results obtained from curve fitting performed for plain jointed specimens under CTS testing

Curve fitting parameters (Cyclic torsional shear testing), plain jointed							
Number of joints		Ramberg	g-Osgood Model	Modified hyperboli model			
		r	α´	γref	δ		
1	Upper bound	2.175	1.068	0.003	0.375		
1	Lower bound	2.252	1.264	0.006	1.195		
2	Upper bound	1.953	0.392	0.016	0.915		
	Lower bound	1.824	0.915	0.009	0.891		
3	Upper bound	1.923	0.958	0.032	0.945		
	Lower bound	1.929	0.356	0.013	0.801		
4	Upper bound	1.913	0.307	0.072	0.958		
	Lower bound	2.029	0.116	0.038	0.851		

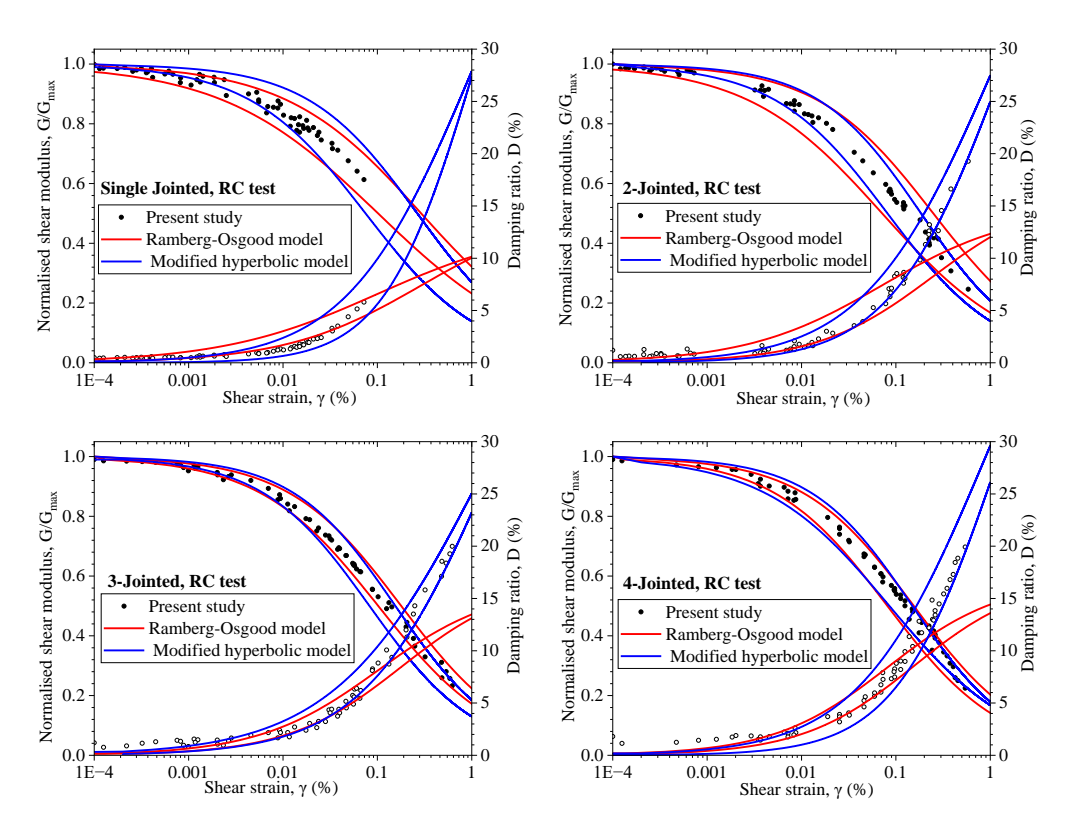


Figure 7. 10 Normalised modulus reduction and damping ratio curve of the plain jointed specimen under RC testing

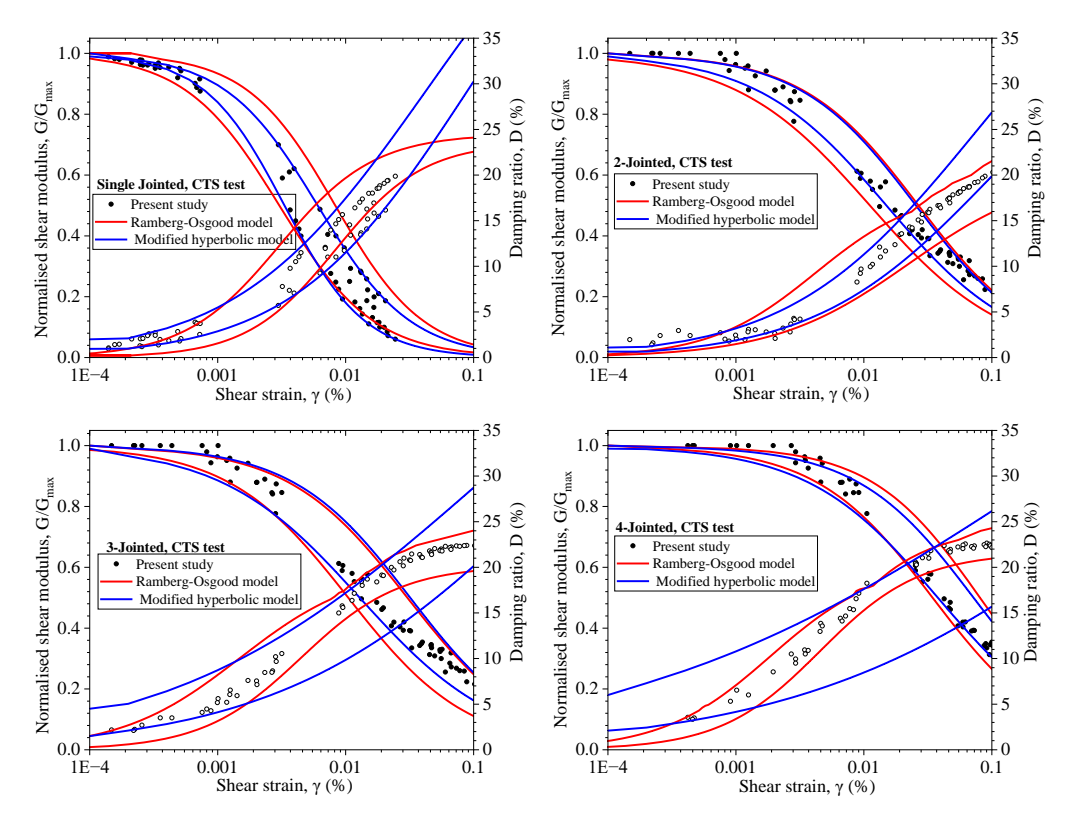


Figure 7. 11 Normalised modulus reduction and damping ratio curve of the plain jointed specimen under CTS testing

7.5 Summary

RC and CTS tests were conducted to determine the dynamic properties of the model material after the plain joints were introduced. From the study, the following conclusions are listed below:

- Comparative analysis of the RC and CTS tests revealed that, at a certain strain amplitude, the lower shear modulus and higher damping ratio values were obtained from the CTS tests than those from the RC, and this trend was observed for all joint spacing conditions.
- The increased number of joints leads to reduced shear modulus and a greater damping ratio; the same trend was observed during RC and CTS testing.
- At a specific strain amplitude, applying confining pressure raises the shear modulus and decreases the damping ratio, this outcome is observed under all test conditions.
- The impact of the loading frequency reveals that the shear modulus escalates with a hike in the loading frequency, and the damping ratio decreases.
- The RO and MH models appropriately fit the results obtained from RC and CTS testing. In addition, the nonlinearity associated with the modulus reduction and damping ratio curves reduced with rising confining pressure, loading frequency, and joint spacing.

Chapter 8

Dynamic Properties of Jointed Rocks: Influence of Loading Conditions and Joint Characteristics

8.1 Introduction

This chapter delves into the dynamic behaviour of jointed rocks under varying loading conditions, focusing on their shear modulus and damping ratio. The study utilizes both resonant column (RC) and cyclic torsional shear (CTS) testing methods to examine the effects of different loading characteristics, such as strain amplitude, confining pressure, and loading frequency, as well as joint attributes, including roughness and orientation.

The chapter begins with an overview of specimen preparation, detailing the fabrication of gypsum plaster models with specific joint roughness coefficients (JRC) and orientations. Using 3D-printed moulds, the specimens are crafted to represent JRC values of 6-8, 12-14, and 18-20, and joint orientations of 30°, 45°, and 60°. These preparations ensure a controlled environment for accurately assessing the impact of various parameters on the mechanical properties of rocks.

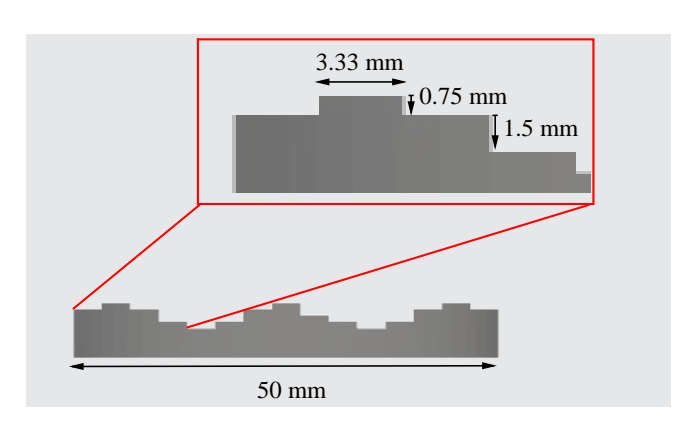
The experimental results are systematically presented, revealing key findings on how each factor influences the shear modulus and damping ratio. For instance, an increase in strain amplitude consistently reduces shear modulus while increasing the damping ratio. Similarly, higher confining pressures enhance shear modulus and reduce damping ratio, a trend that intensifies with greater joint orientation angles. Furthermore, the study observes a logarithmic increase in shear modulus and a decrease in damping ratio with rising loading frequencies.

By combining these insights, the chapter provides a comprehensive understanding of the dynamic responses of jointed rocks, contributing valuable knowledge for engineering applications and the development of predictive models for rock behaviour under various environmental conditions.

8.2 Specimen preparation

To facilitate RC and CTS testing on frictional jointed rocks with specific joint roughness and orientation, the jointed rock specimens were prepared using gypsum plaster as the model material. To introduce joint roughness, artificial surface profiles were designed that correspond to JRC values of 6-8, 12-14, and 18-20, as illustrated in Figure 8.1.

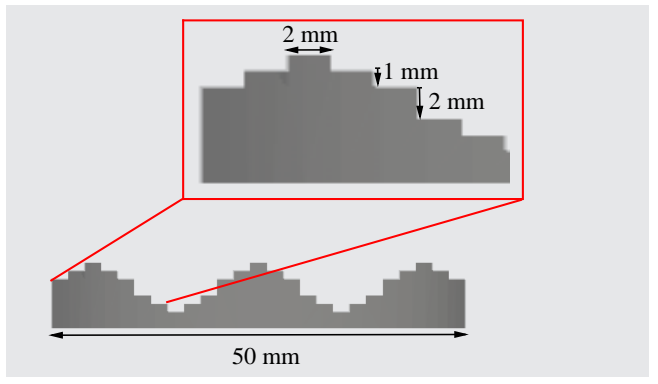
Verification of these profiles followed methodologies proposed by Barton and Choubey (1977), Tse and Cruden, 1979, and Rohilla and Sebastian, 2023. The design of first and second-order asperities meticulously addressed the waviness and unevenness characteristics of the jointed rough surface profiles. Using Acrylonitrile butadiene styrene (ABS) filament, the designed surface profiles were 3D printed to serve as moulds for crafting gypsum plaster specimens with the desired JRC and orientation. In this investigation, joint orientations of 30°, 45°, and 60° were employed, requiring 3D printing of moulds corresponding to JRC values for these angles, as depicted in Figure 8.2. The orientation angles of the joints were taken with the horizontal line as the reference baseline. The mirror image replicas of the moulds were 3D printed with a 0.1 mm clearance, ensuring matching joint profiles with a joint matching coefficient (JMC) of 1. A comprehensive flow chart detailing the specimen preparation process is presented in Figure 8.3.



(a) JRC: 6-8

Maximum peak to valley height: 2.25 mm

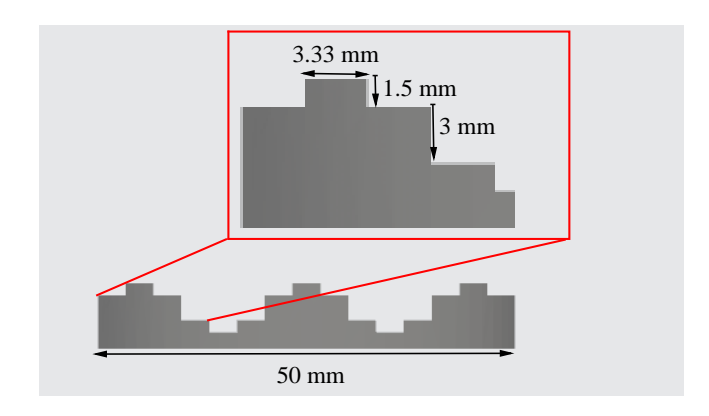
Surface Description: Rough and planar



(b) JRC: 12-14

Maximum peak to valley height: 6 mm

Surface Description: Rough and undulating



(c) JRC: 18-20

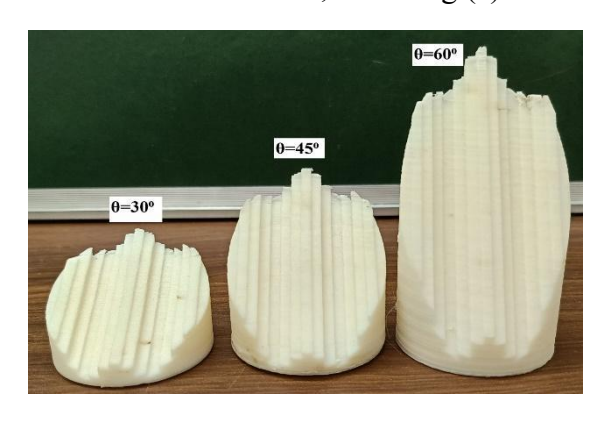
Maximum peak to valley height: 6

mm

Surface Description: Rough and

irregular

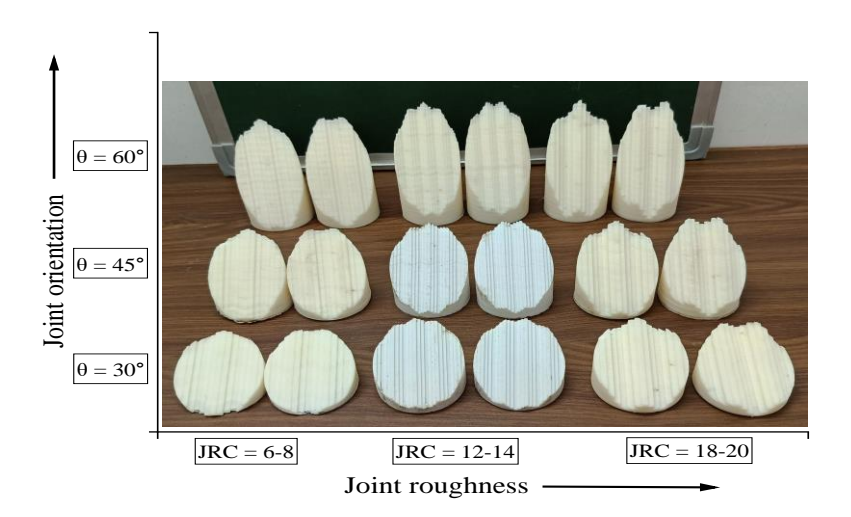
Figure 8. 1 A visual representation of surface profiles designed for different Joint Roughness Coefficients, including (a) JRC=6-8, (b) JRC=12-14, and (c) JRC=18-20





(a) Front view of the oriented 3D printed moulds

(b) Side view of the oriented 3D printed moulds



(c) Typical view of 3D printed moulds with their mirror image

Figure 8. 2 A typical representation of 3D-printed moulds featuring diverse surface profiles and different orientation angles, including (a) a frontal perspective, (b) a side view, and (c) a standard view of moulds alongside their mirrored counterparts.

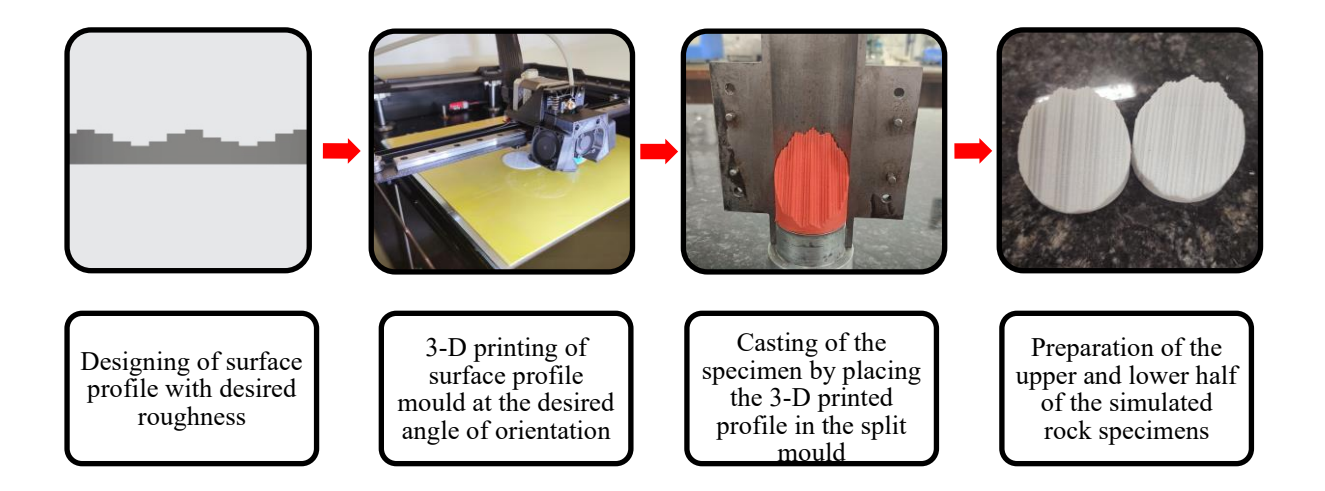


Figure 8. 3 Flowchart illustrating the process for preparing 3D moulds

The gypsum plaster specimens were cast by positioning one section of the 3D printed mould at the base of the split mould. A mixture of plaster of Paris and water was then poured from the top, allowing it to conform to the shape of the 3D mould. Simultaneously, the other portion of the 3D mould was positioned in the split mould, and the remaining half of the specimen was prepared. Figure 8.4 presents a representative image of the gypsum plaster specimen created using the 3D printed mould.

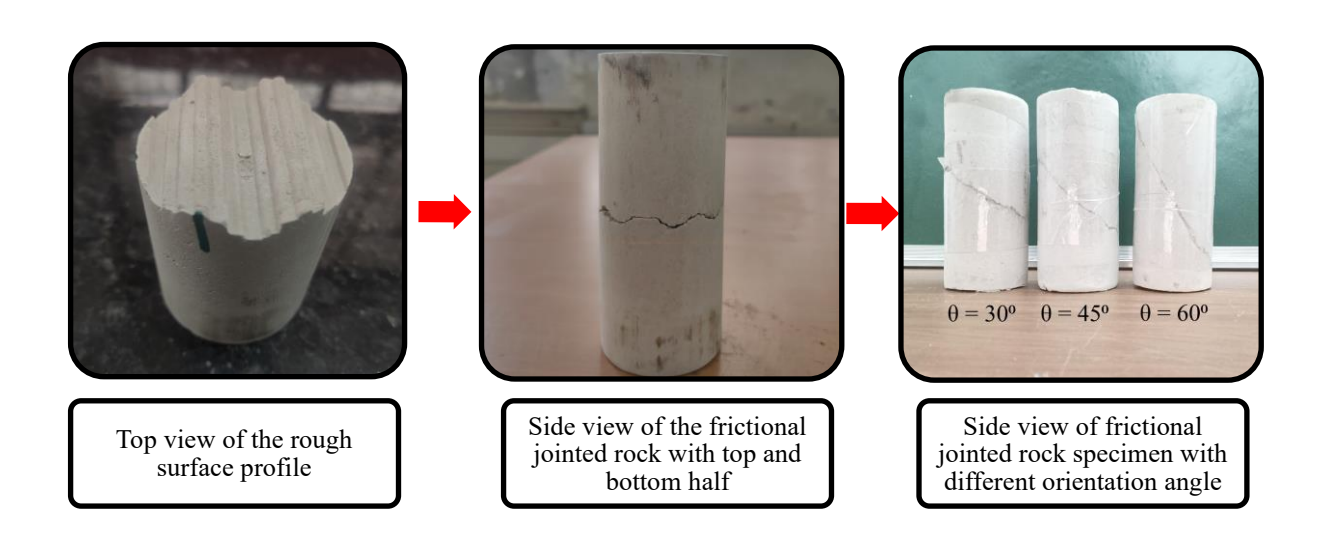


Figure 8. 4 A visual representation of the gypsum plaster specimen prepared using a 3-D mould.

8.3 Testing plan

The testing plan involved the sequential execution of resonant column and cyclic torsional shear tests, exploring a spectrum of material and loading characteristics to ascertain the shear modulus and damping ratio of the jointed model material. This study treats the shear modulus and damping ratio as dependent variables, while independent variables are categorised into material and loading characteristics. Joint characteristics include joint roughness (quantified as joint roughness coefficient, JRC) and joint orientation (expressed as the angle of the oriented joint from the horizontal base in degrees). Loading characteristics encompass independent parameters such as strain amplitude, confining pressure, and loading frequency. The testing program, outlined in Figure 8.5, illustrates the systematic approach of the testing program of the study. To assess the impact of joint roughness and orientation, JRC values of 6-8, 12-14, and 18-20 were applied over joint orientations of 30°, 45°, and 60°. Specimens were designated based on joint characteristics, as outlined in Table 8.1. Resonant column (RC) testing involved applying input voltage current ranging from 0.001V to 1V, corresponding to strain levels from 0.001% to 0.1%. A varied range of confining pressures (2500 kPa to 50 kPa) was sequentially applied for RC testing at specific strain amplitudes. Similarly, cyclic torsional shear testing was conducted over a spectrum of strain levels and confining pressure combinations, spanning a loading frequency range from 0.1 Hz to 10 Hz.

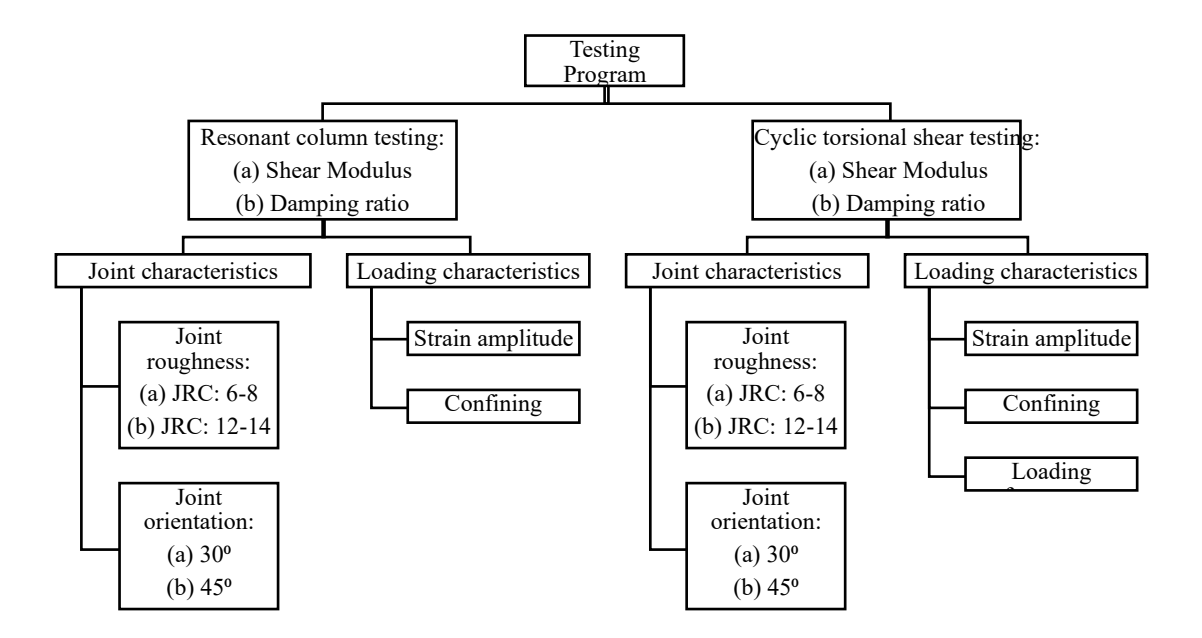


Figure 8. 5 The flow chart of the testing program of the study

Table 8. 1 Testing condition of the specimens

	Joint	Joint	Designation used	
Specimen Number	Roughness Coefficient, JRC	Orientation, θ (degrees)	Resonant column testing	Cyclic torsional shear testing
S1	6-8	30°	S1-RC	S1-CTS
S2	6-8	45°	S2-RC	S2-CTS
S3	6-8	60°	S3-RC	S3-CTS
S4	12-14	30°	S4-RC	S4-CTS
S5	12-14	45°	S5-RC	S5-CTS
S6	12-14	60°	S6-RC	S6-CTS
S7	18-20	30°	S7-RC	S7-CTS
S8	18-20	45°	S8-RC	S8-CTS
S9	18-20	60°	S9-RC	S9-CTS

8.4 Results

This section presents the findings of experimental tests conducted using resonant column and cyclic torsional shear testing methodologies. It examines how loading characteristics and joint attributes impact the shear modulus and damping ratio.

8.4.1 Effect of loading characteristics: The impact of loading characteristics investigated in this study encompasses the impact of strain amplitude, confining pressure, and loading frequency. The effects of strain amplitude and confining pressure were analysed through resonant column testing, while the influence of loading frequency was assessed using cyclic torsional shear testing.

8.4.1.1 Effect of amplitude of loading: In evaluating the impact of strain amplitude on the dynamic behavior of frictional jointed rocks, resonant column testing was executed

across a spectrum of strain amplitudes, ranging from 0.0001% to 0.1%. Multiple experiments were conducted under a specific test condition, maintaining other parameters constant. The results revealed a consistent trend across the experiments, indicating a decrease in shear modulus and an increase in damping ratio with an escalation in strain amplitude. This observed behaviour aligns with the findings reported by Sebastian and Sitharam (2015, 2016, 2018). Figure 8.6 illustrates the variation of normalised shear modulus and damping ratio with strain levels for jointed rock specimens characterised by JRC values of 6-8, 12-14, and 18-20, respectively. Notably, this trend remained consistent for all specimens, encompassing various joint orientations at 30°, 45°, and 60°.

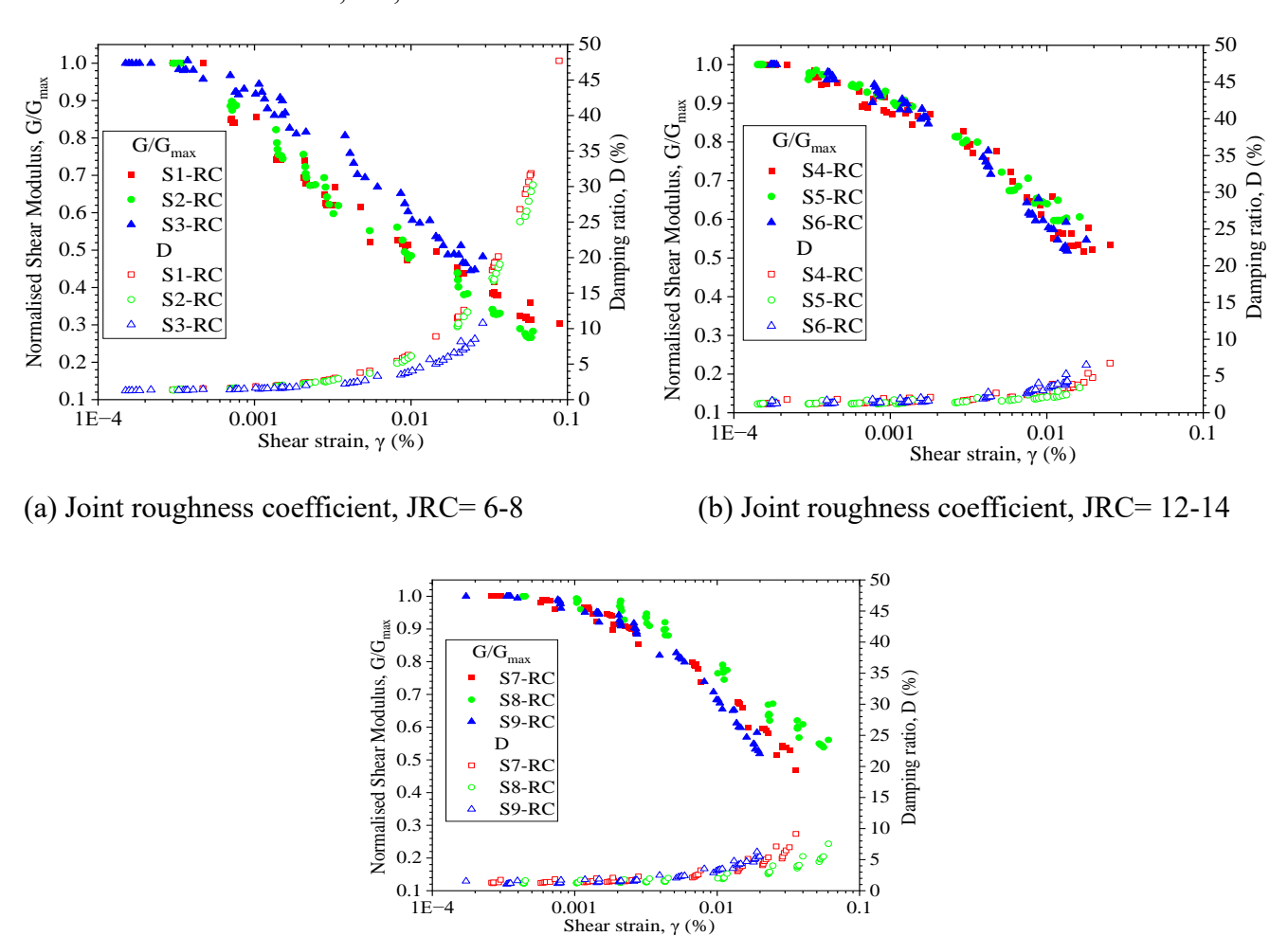
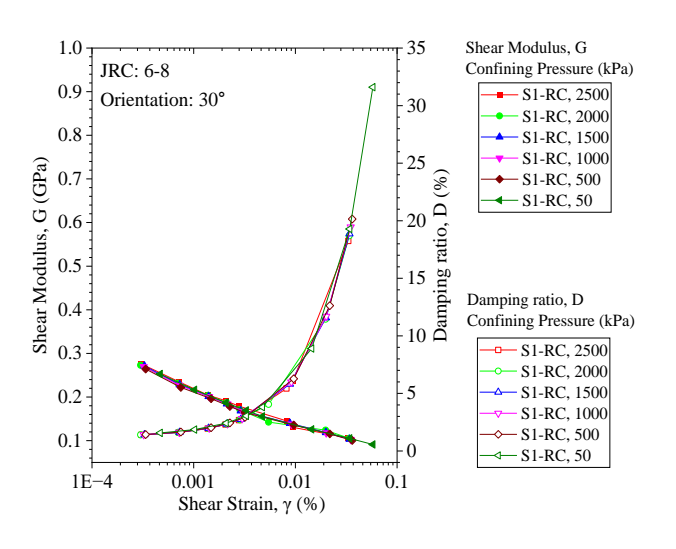
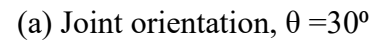


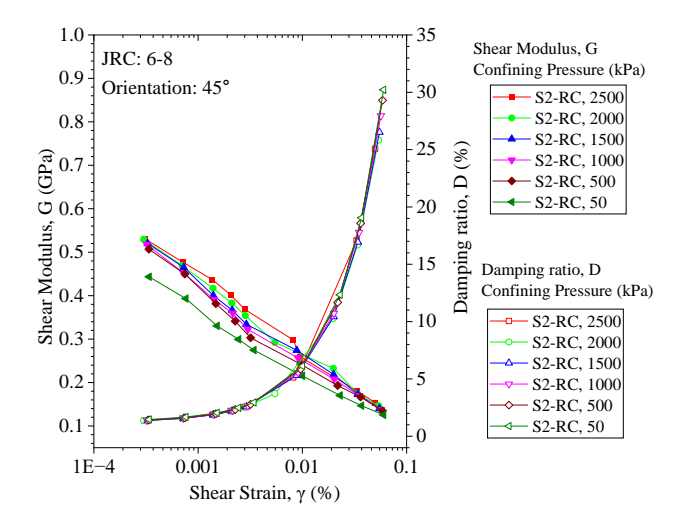
Figure 8. 6 Modulus reduction and damping ratio curve in jointed rock specimens with varying Joint Roughness Coefficient (JRC) of (a) JRC = 6-8, (b) JRC = 12-14, and (c) JRC = 18-20.

(c) Joint roughness coefficient, JRC= 18-20

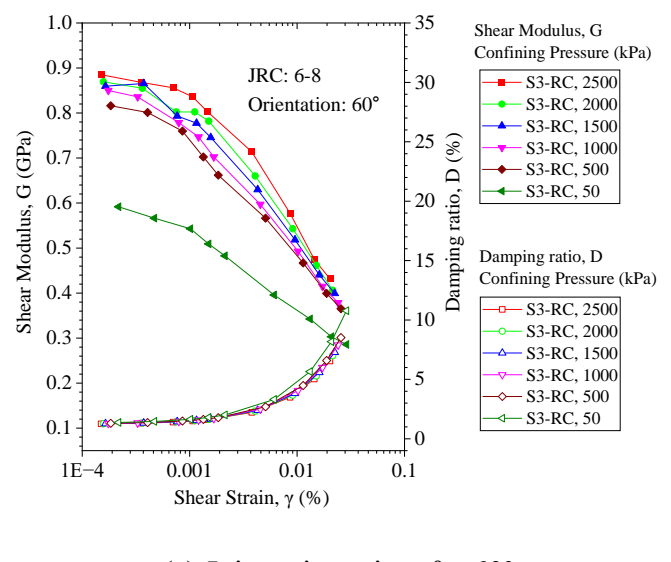
8.4.1.2 Effect of Confining Pressure: In examining the effect of strain amplitude, the study maintained constant joint characteristics (joint roughness coefficient and joint orientation) and loading features (frequency of loading), focusing on the influence of confining pressure on shear modulus and damping ratio. Testing under various confining pressures, ranging from 50 kPa to 2500 kPa, revealed distinct trends. Figure 8.7 illustrates the variations in shear modulus and damping ratio across different confining pressures for jointed rock with a constant JRC of 6-8 and joint orientations of 30°, 45°, and 60°. The results indicate a consistent pattern observed in previous studies (Cha et al., 2009; Fratta & Santamarina, 2002; Sebastian and Sitharam, 2015, 16, and 18), where an increase in confining pressure leads to an augmentation in shear modulus and a reduction in damping ratio. This behaviour is attributed to joint closure under high confining pressure, increasing stiffness, and higher modulus while diminishing the damping ratio. Comparative analysis of confining pressure effects on dynamic properties across varying joint orientations revealed a more pronounced influence with increasing orientation angles. The sensitivity of dynamic properties to increasing confining pressure was observed to escalate with greater joint orientation angles. At specific strain amplitudes, the increase in shear modulus and decrease in damping ratio with rising confining pressure were more noticeable at higher joint orientations, as depicted in Figure 8.7. Additionally, the impact of confining pressure was more evident at lower strain amplitudes (below 0.01%) and diminished as the strain amplitude increased. This trend held for other JRC values as well.







(b) Joint orientation, $\theta = 45^{\circ}$



(c) Joint orientation, $\theta = 60^{\circ}$

Figure 8. 7 Changes in shear modulus and damping ratio with varying shear strain under different confining pressures for joint orientations of (a) $\theta = 30^{\circ}$, (b) $\theta = 45^{\circ}$, and (c) $\theta = 60^{\circ}$.

8.4.1.3 Effect of Frequency of loading:_In investigating the impact of loading frequency on the dynamic response of jointed rock, cyclic torsional tests were conducted across a spectrum of frequency levels, namely 0.1 Hz, 0.3 Hz, 0.5 Hz, 0.7 Hz, 1 Hz, 3 Hz, 5 Hz, 7 Hz, and 10 Hz, while maintaining a constant of 10 cycles. Strain amplitude and Joint Roughness Coefficient (JRC) were held constant during individual tests. The variation of shear modulus and damping ratio with joint orientation (30°, 45°, and 60°) is depicted in Figure 8.8. The results revealed a logarithmic increase in shear modulus values and a decrease in damping ratio with the escalation of loading frequency. This phenomenon can be attributed to heightened loading rates associated with increased frequency, leading to an augmentation in shear modulus (G values) and a reduction in damping ratio (D values). This trend was consistent across all strain levels and JRC values. Furthermore, the rate of shear modulus increase with rising loading frequency was more pronounced at lower confining pressure levels, observed consistently for all joint orientations. Notably, no significant effect on the damping ratio of jointed rock specimens was discerned under varying loading frequencies.

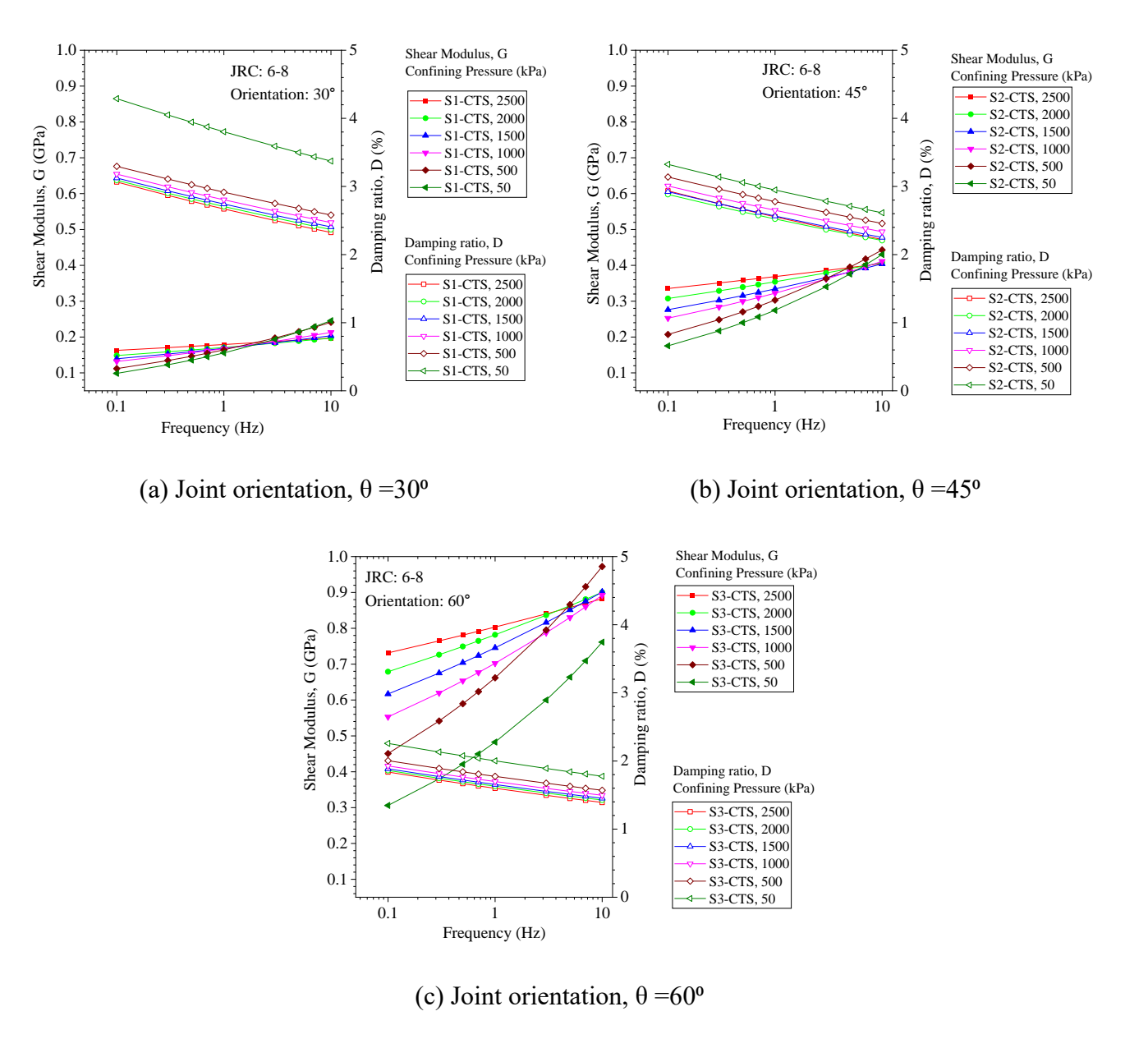


Figure 8. 8 Variation in shear modulus and damping ratio examined across different frequencies of loading for joint orientations of (a) $\theta = 30^{\circ}$, (b) $\theta = 45^{\circ}$, and (c) $\theta = 60^{\circ}$.

8.4.2 Effect of joint characteristics: The importance of joint properties in this study includes the influence of joint roughness and orientation. The effect of joint orientation and roughness on the shear modulus and damping ratio of rock joints was investigated by using resonant column testing.

8.4.2.1 Effect of joint roughness coefficient: The investigation delved into the impact of joint roughness coefficient across various strain amplitudes while maintaining constant confining pressure. Figure 8.9 illustrates the variation of shear modulus and

damping ratios concerning different JRC ranges (6-8, 12-14, and 18-20) and strain amplitudes for joint orientations of 30°, 45°, and 60°. The experimental outcomes reveal an increase in shear modulus values with elevated JRC, attributed to heightened interlocking and resistance against torsional displacement, aligning with the findings of Mohd-Nordin et al., 2014. Consequently, specimens with lower JRC exhibit higher damping ratios than those with higher JRC. Notably, the study demonstrates an accelerated rate of shear modulus decrement and damping ratio increase at higher strain levels. These trends persist consistently across varying confining pressures and joint orientations.

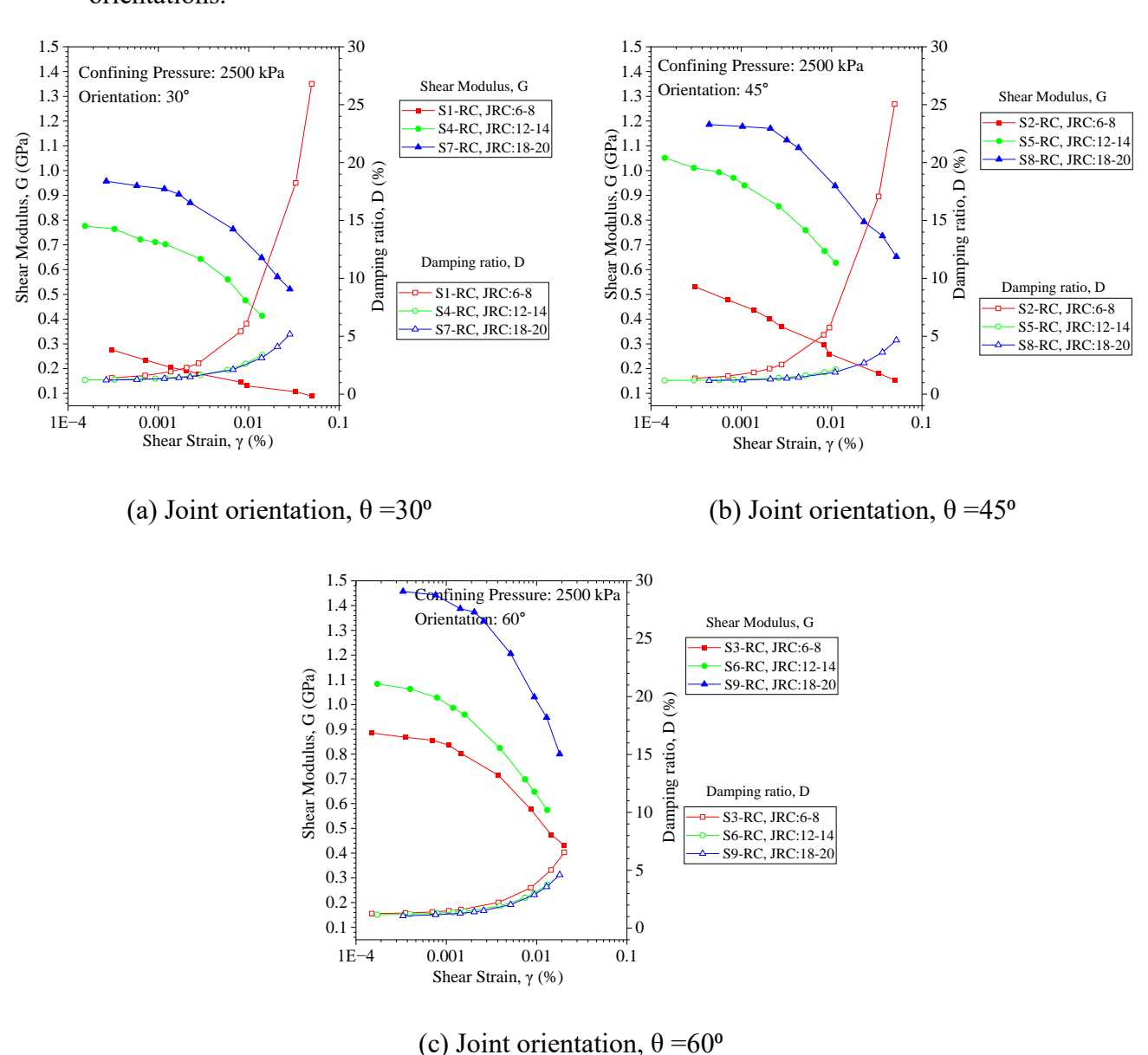
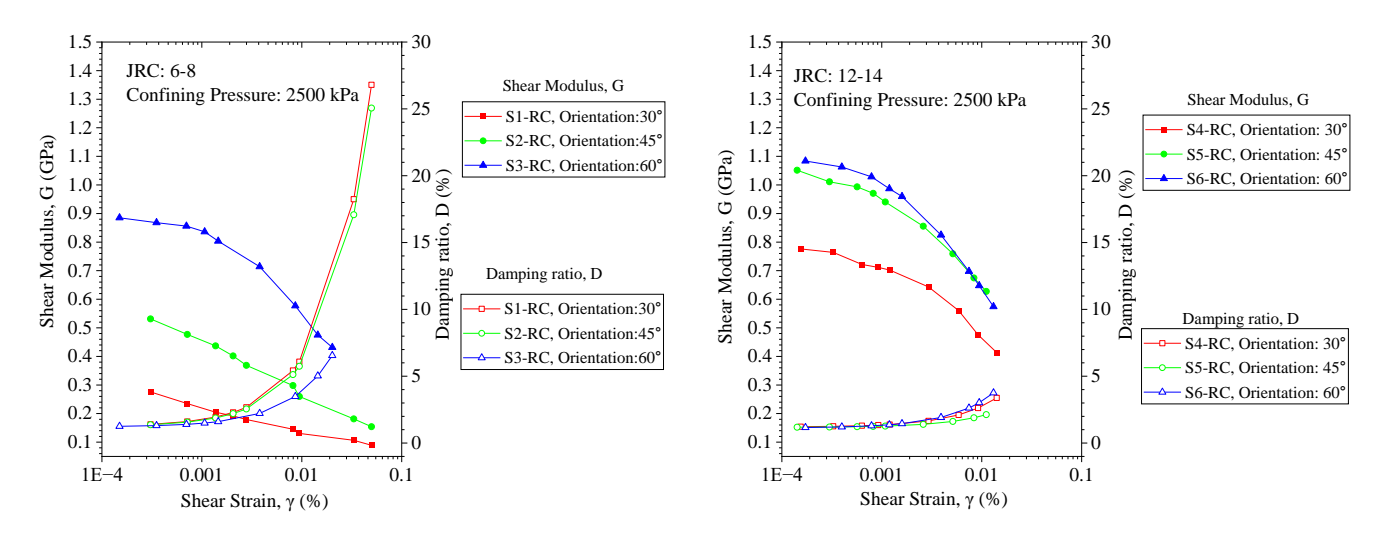
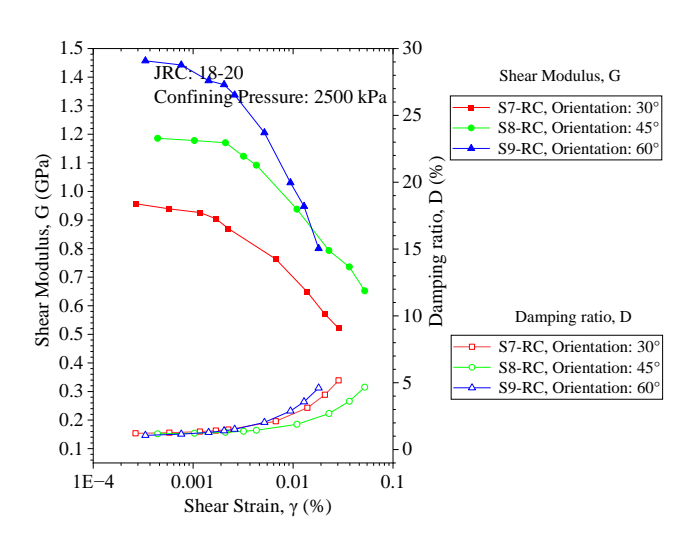


Figure 8. 9 Variation in shear modulus and damping ratio across varying joint roughness coefficients for joint orientations of (a) $\theta = 30^{\circ}$, (b) $\theta = 45^{\circ}$, and (c) $\theta = 60^{\circ}$.

8.4.2.2 Effect of Orientation: Resonant column testing was conducted to examine the impact of joint orientation on the shear modulus and damping ratio of jointed rocks. The tests were carried out at joint orientations of 30°, 45°, and 60°, with a constant confining pressure of 2500 kPa. Figure 8.10 shows the variations in shear modulus and damping ratio for jointed samples with different orientations (for JRC of 6-8, 12-14, and 18-20). The results indicate a consistent trend where shear modulus values increase, and the damping ratio decreases with a rise in joint orientation, aligning with the findings reported by Sebastian and Sitharam (2015). This observed pattern holds across all JRC values studied.



- (a) Joint roughness coefficient, JRC= 6-8
- (b) Joint roughness coefficient, JRC= 12-14



(c) Joint roughness coefficient, JRC= 18-20

Figure 8. 10 Changes in shear modulus and damping ratio examined across different joint orientations at Joint roughness coefficient of (a) JRC= 6-8, (b) JRC=12-14, and (c) JRC=18-20.

8.5 Discussions

In the preceding sections, the distinct influence of joint characteristics (joint roughness and joint orientation) and loading conditions (strain amplitude, confining pressure, and frequency of loading) on the dynamic response of jointed rock specimens has been thoroughly discussed. Building on the test results derived from RC and CTS experiments conducted on jointed rock specimens with diverse material and loading attributes, an attempt has been made to discern the cumulative impact of all parameters on the mechanical behaviour of the jointed rocks. To conduct this study, regression analysis was employed, encompassing multiple linear and multiple linear regression with proxies (theoretically modified). These analyses aimed to predict the combined effect of independent parameters on the shear modulus and damping ratio of jointed rocks. Four distinct models were examined to gauge the dependency of shear modulus and damping ratio across the variables outlined in Table 8.2.

Table 8. 2 List of models examined for different variables

Model	Test	Dependent variable	Independent variable
	performed		
M1		Shear Modulus (G)	1. Strain amplitude (γ)
M2	Resonant Column (RC)	Damping ratio (D)	 Confining pressure (σ) Joint roughness coefficient (R) Joint orientation (θ)
М3		Shear Modulus (G)	1. Strain amplitude (γ)
M4	Cyclic torsional shear (CTS)	Damping ratio (D)	 Confining pressure (σ) Joint roughness coefficient (R) Joint orientation (θ) Loading frequency (f)

Initially, regression analyses were fitted with various combinations, including the presence of an intercept in the model. The outcomes of goodness-of-fit measures are presented in Table 8.3 for comprehensive evaluation.

Table 8. 3 Outcomes of goodness-of-fit measures obtained from the regression analysis

	The equ	uation used:	$y = \beta_0 + (\beta_1)$	$*\gamma) + (\beta_2)$	$(\sigma) + (\beta_3)$	* R) +			
Model	$(\beta_4 * \theta) + (\beta_5 * f)$						$\left \begin{array}{c} \\ \\ \\ \end{array} \right $ S	Standard	F-value
Model			Coefficio	ents			IX	error	1-value
	β_0	eta_1	β_2	eta_3	eta_4	eta_5	-		
M1	-0.40	-8.86	6.81E-5	0.044	0.0107	0	0.83	0.134	570.3
	0	-10.49	3.99E-5	0.036	0.0058	0	0.95	0.158	2572.51
M2	6.055	335.18	-0.00023	-0.293	-0.0253	0	0.77	2.588	419.41
	0	360.13	0.000196	-0.161	0.0488	0	0.82	2.850	539.29
М3	-0.38	-6.29	4.28E-5	0.041	0.0091	0.024	0.81	0.133	2123.33
	0	-8.26	1.65E-5	0.033	0.0047	0.020	0.95	0.151	8882.5
M4	9.201	342.13	-0.00031	-0.494	-0.0383	-0.101	0.80	3.045	1898.8
	0	388.95	0.000319	-0.311	0.0669	-0.015	0.84	3.487	2567.96

Further, for theoretical validity, the independent variables considered were transformed according to the theoretical relation mentioned:

$$e^{y} = \beta_{0} * \gamma^{\beta_{1}} * \sigma^{\beta_{2}} * R^{\beta_{3}} * \theta^{\beta_{4}} * f^{\beta_{5}}$$
(8.1)

The results of the regression analysis based on the built-on theoretical transformed relation are given in Table 8.4.

Table 8. 4 Outcomes of goodness-of-fit measures obtained from the regression analysis of theoretical transformed relation

	The equation used: $e^y = \beta_0 * \gamma^{\beta_1} * \sigma^{\beta_2} * R^{\beta_3} * \theta^{\beta_4} * f^{\beta_5}$						Standard		
Models		Coefficients					R ²	error	F-value
	eta_0	eta_1	eta_2	eta_3	eta_4	eta_5			
M1	-3.33	-0.202	0.112	1.255	1.107	1	0.91	0.097	1241.12
	0	-0.152	0.022	0.784	-0.372	1	0.90	0.237	1077.27

	36.52	4.566	-0.641	-10.048	-5.213	1	0.483	3.944	112.24
M2									
	0	4.012	0.351	-4.878	11.022	1	0.525	4.599	132.99
	-2.89	-0.243	0.074	1.147	0.931	0.134	0.87	0.104	3774.93
M3									
	0	-0.187	-0.005	0.743	-0.357	0.131	0.89	0.215	4117.32
	55.35	8.85	-0.805	-16.088	-7.43	-0.609	0.62	4.167	788.20
M4									
	0	7.78	0.701	-8.36	17.211	-0.538	0.60	5.508	738.31

8.6 Summary

The objective of this study was to evaluate the dynamic response of frictional jointed rocks with varying joint orientations under diverse experimental conditions, including strain amplitude, confining pressure, and loading frequency. 3D moulds were used and validated for surface profile conformity based on established methods to ensure consistent joint orientation and roughness. Resonant column and cyclic torsional shear testing techniques were utilised to conduct experiments under varying conditions. The multiple linear regression analyses were performed to comprehensively capture the interplay of material and loading effects on rock response. The study yields the following key conclusions:

- 1. The shear modulus decreases, and the damping ratio increases with increased strain amplitude, a consistent trend observed across all experimental conditions.
- Increasing the confining pressure while keeping a steady strain amplitude leads to a
 larger shear modulus and reduced damping ratio. Furthermore, when the angle of
 orientation increases, the effect of confining pressure on dynamic characteristics
 becomes more pronounced.
- 3. Cyclic torsional shear testing shows that higher loading frequencies increase shear modulus and decrease damping ratios across all joint conditions.
- 4. Increased joint roughness and orientation lead to higher shear modulus values and lower damping ratios for a specific strain amplitude.
- 5. The multiple linear regression technique effectively predicts the shear modulus and damping ratio obtained through RC and CTS testing. Additionally, the comparison of goodness of fit between the simple and theoretically modified regression models

underscores the superiority of the former in accurately capturing the relationship between variables.

Chapter 9

Enhancing Energy Dissipation in Jointed Rocks: The Role of Natural Rubber Latex (NRL) as an Energy-Absorbing Layer

9.1 Introduction

This chapter delves into the dynamic properties of jointed rocks enhanced with natural rubber latex (NRL) as an energy-absorbing layer. Through a series of resonant column (RC) and cyclic torsional shear (CTS) tests, the chapter investigates the shear modulus and damping ratio of gypsum plaster specimens with plain and NRL-grouted joints across varying strain levels, joint spacings, and confining pressures.

Initially, the chapter compares theoretical predictions by Fratta and Santamarina (2002) with experimental results from RC testing, revealing a non-linear relationship between shear wave velocity, strain amplitude, and the significant influence of NRL thickness on the damping ratio. This is followed by a detailed examination of how increasing strain amplitude results in decreased shear modulus and increased damping ratio, consistent across different joint configurations and confining pressures.

Regression analyses for both RC and CTS testing highlight the sensitivity of NRL-grouted specimens to changes in joint spacing and loading frequency. These findings underscore the superior energy absorption and stability of NRL-grouted joints compared to plain joints, making them less reactive to changes in confining pressure and strain amplitude. The chapter concludes by affirming the practical implications of NRL as a damping material in jointed rock systems, providing a robust foundation for future research and applications in geotechnical engineering.

9.2 Materials

Gypsum Plaster has been used as a synthetic rock material to explore the dynamic properties of jointed rocks under distinctive experimental conditions. Natural rubber latex comes from the Hevea Brasiliensis tree. It is a milky blend of tiny rubber flakes (cis-1,4-polyisoprene) in water (Lim & Misni, 2016). Since it is sourced from an ecofriendly natural resource, NRL can be considered a sustainable grouting material for rock joints. Thus, NRL has been proven to be an eco-friendly grouting material for rock masses with joints. NRL is also easy to infuse as a liquid into the target rock mass, even

for existing structures. The natural rubber latex used in this study was procured from Kottayam, Kerala, India's Ms Asiatic Rubber Industries. <u>Table 9.1</u> provides the fundamental attributes of NRL as per Indian Standard codes.

Table 9. 1 Basic properties of Natural Rubber Latex used in the study

Parameter	Value
Total solid content (% by mass); IS 9316 (Part 4): 1988	60.05
Dry rubber content (% by mass); IS 3708 (Part 1):	61.7
1985	
Sludge Content (% by mass) ; <i>IS 3708 (Part 2): 1985</i>	0.014
Alkalinity as ammonia (% by mass); IS 3708 (Part 4):	Below detection limit
1985	
Koh number ; IS 3708 (Part 5): 2005	0.85
Mechanical stability time, (sec); IS 3708 (Part 6): 1985	724
Volatile fatty acid number; IS 3708 (Part 7): 2005	0.049
Copper content (ppm of total solids); IS 9316 (Part 7):	1.41
1987	

Some preliminary tests are conducted to determine how much NRL shrinks during drying. The wet formulation of NRL is applied between the joints of prefabricated specimens. The specimen with grout is then set aside to dry thoroughly. According to ASTM D 412-06a: 2013 and ISO 37:2017, the tensile stress-strain properties of the NRL used in this investigation are determined. The tensile strength test is conducted using the Zweick/Roell UTM at a loading rate of 200 mm/min, as indicated in Figure 9.1. The tensile stress-strain curve obtained is depicted in Figure 9.2. The maximum tensile strength of NRL is 2.42 MPa. As a hyperelastic material, it is observed that the Poisson's ratio of the NRL decreases as the longitudinal strain level increases, as depicted in Figure 9.3. The experimental data obtained from the tensile testing of NRL was fitted against the Mooney-Rivlin model according to the equation; $\sigma^* = 2\left(\lambda - \frac{1}{\lambda^2}\right) * \left(C_1 + \frac{c_2}{\lambda}\right)$, where σ^* is the tensile load per unit unstrained area pertaining to extension ratio ' λ ,' and C_1 and C_2 are the constants based on the material property. The extension ratio is the ratio between the initial and extended lengths. The constants C1 and C2 are 3.8E-5 MPa and 0.193 MPa, respectively, based on fitting experimental values at 95%

confidence limits. The ductility test is carried out at room temperature to determine the ductility of the dried NRL specimens as per IS 1201:1978. The wet NRL sample is placed in the briquette mould and allowed to dry in the open air for seven days, as depicted in Figure 9.4. The ductility of a dried NRL specimen is 17.5 cm.

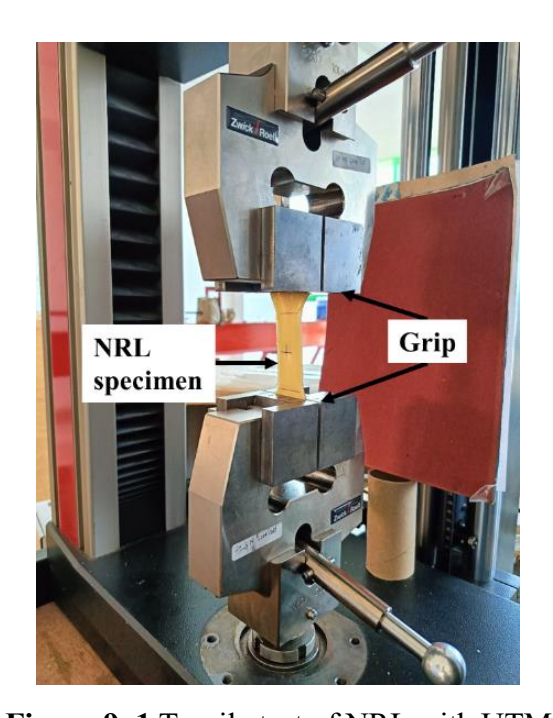


Figure 9. 1 Tensile test of NRL with UTM

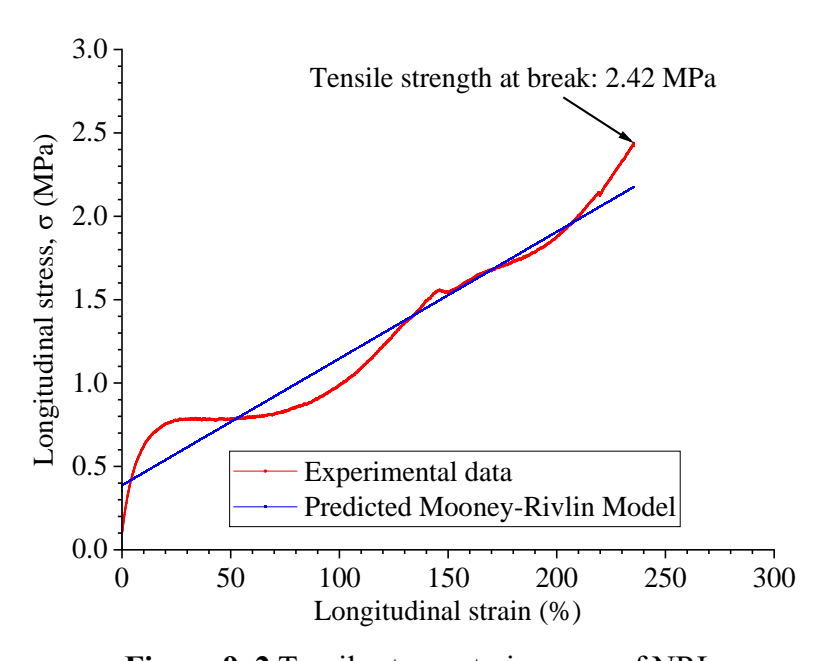


Figure 9. 2 Tensile stress-strain curve of NRL

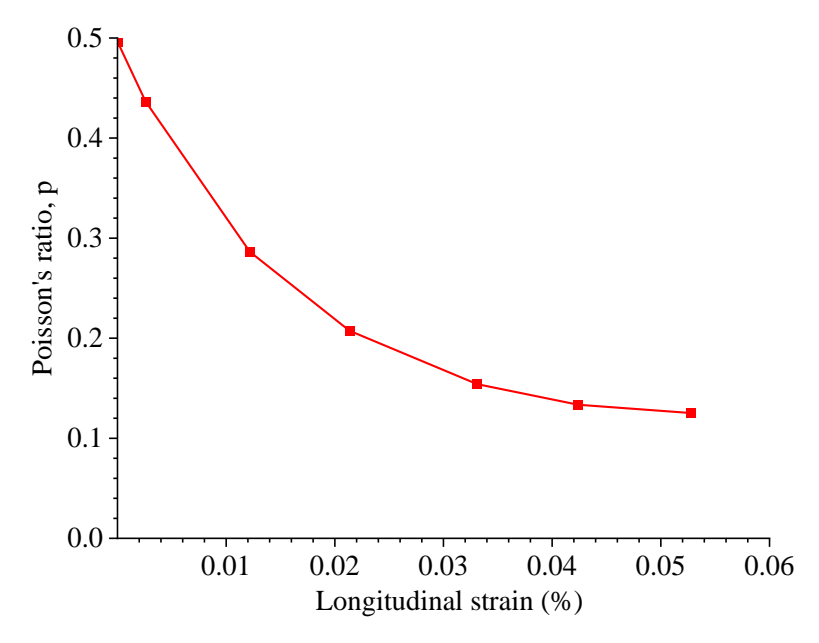


Figure 9. 3 Variation of Poisson's ratio with strain



Figure 9. 4 Typical view of dry and wet NRL specimen in briquette mould for ductility test

The resonant column testing was conducted to determine the shear modulus and damping ratio of NRL at various strain amplitudes. Figure 9.5 depicts the variation of shear modulus and damping ratio of NRL at varying strain levels.

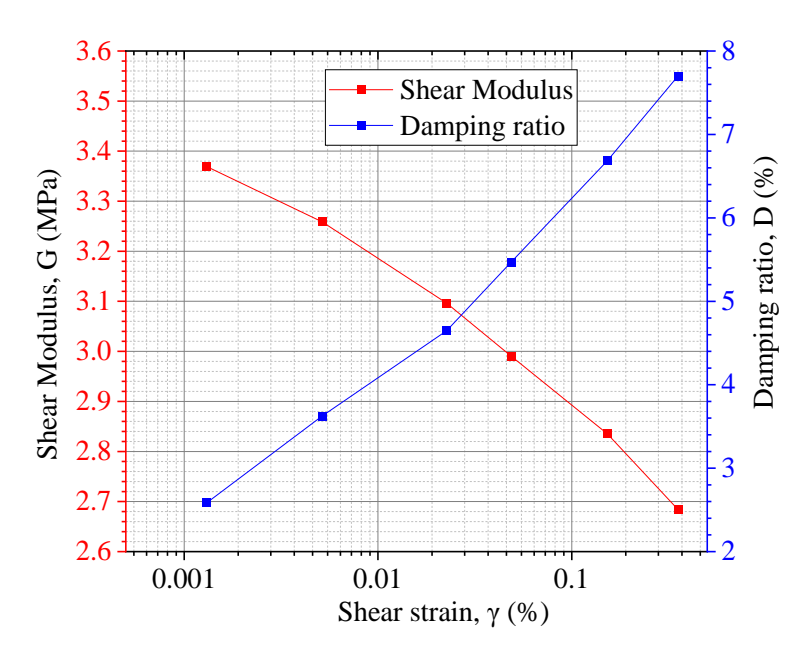


Figure 9. 5 Variation of shear modulus and damping ratio of NRL at different strain levels using RC testing

9.3 Test Plan

The study consists of two stages aimed at understanding the dynamic properties of jointed rocks under two different conditions. Initially, the influence of grouted NRL thickness is studied while keeping the number of joints constant. In this stage, the thickness of grouted NRL is varied with a single joint in the cylindrical gypsum plaster specimen, maintaining a joint spacing of 50 mm. NRL thicknesses of 2 mm, 3 mm, 4 mm, and 5 mm are examined. In the second stage, the NRL thickness is kept constant at 3 mm, and the number of joints is varied between 1, 2, 3, and 4, with joint spacings of 50 mm, 33.3 mm, 25 mm, and 20 mm, as shown in Figure 9.6. Resonant Column (RC) and Cyclic Torsional Shear (CTS) tests are conducted. Confining pressure is systematically varied from 0 kPa to 2500 kPa in 500 kPa increments. Additionally, a range of loading frequencies from 0.1 Hz to 10 Hz is applied under a constant confining pressure of 50 kPa to observe its effect on the NRL-grouted specimens. The combined influence of NRL thickness and joint spacing on the dynamic response of jointed rocks is explored comprehensively through these tests. The density of specimens with plain joints was 1.69 g/cc regardless of joint spacing. The density of a dry NRL specimen is 0.689 g/cc, which is considerably less than the density of gypsum plaster; consequently, the equivalent density of the gypsum plaster specimen grouted with NRL was utilised in all calculations. Single-jointed, 2-jointed, 3-jointed, and 4-jointed specimens have densities of 1.661 g/cc, 1.633 g/cc, 1.607 g/cc, and 1.583 g/cc, respectively. For this

study, the response of the jointed rock mass is analysed as an equivalent continuum material.



Figure 9. 6 Typical view of plain jointed and NRL grouted jointed Gypsum plaster specimens

9.4 Results from RC testing

Stage 1: The results of RC studies conducted on jointed NRL-grouted synthetic rock suggest that the shear moduli of specimens fall as the strain amplitude increases, as depicted in Figure 9.7. In addition, the shear modulus values drop as the thickness of the NRL layer increases. Increasing the thickness of the NRL layer reduces the shear modulus at a given strain level. Figure 9.8 illustrates that an increase in the thickness of the NRL layer increases the damping ratio values for a specific strain amplitude.

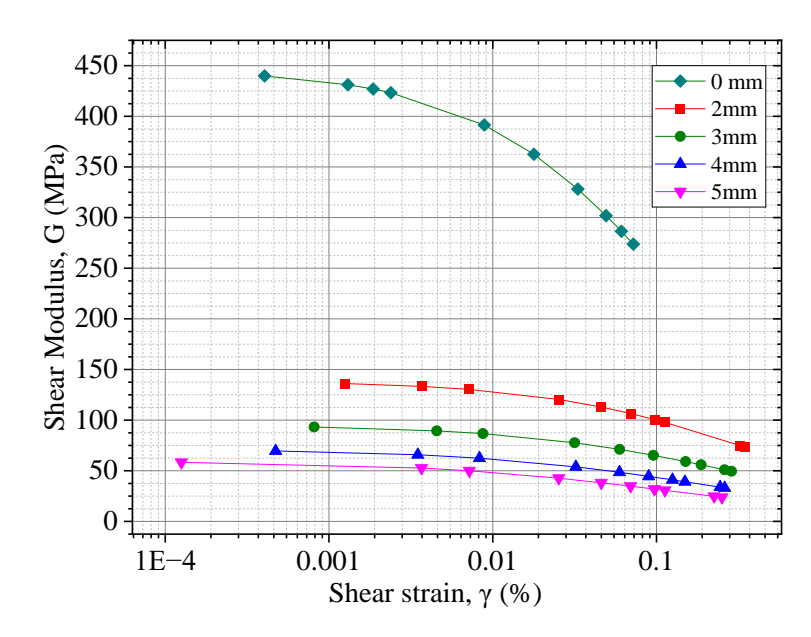


Figure 9. 7 Variation of shear modulus with strain level for various thicknesses of NRL-grouted layer

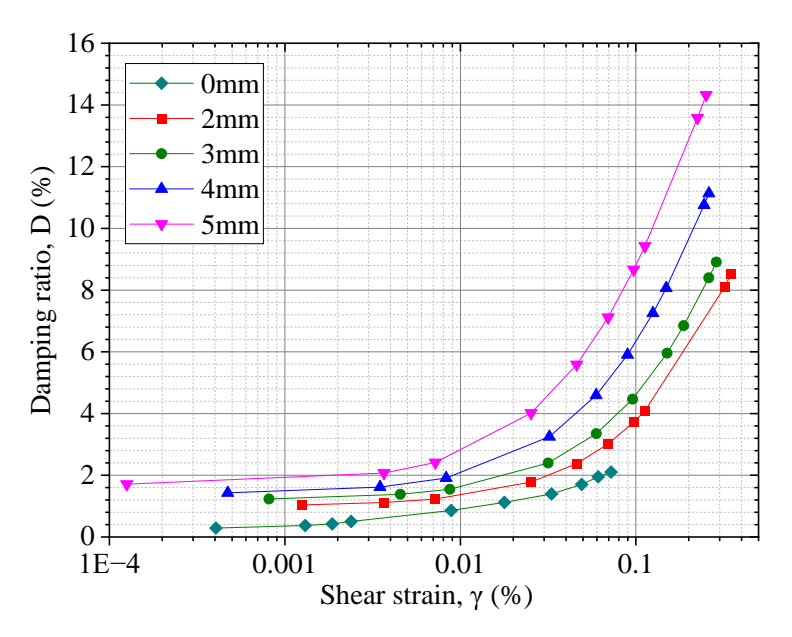


Figure 9. 8 Variation of damping ratio with strain level for various thicknesses of NRL-grouted layer

Fratta and Santamarina 2002, stated that if the wavelength of the incoming wave is significantly larger than the spacing of joints, then the medium can be analysed by considering it as an equivalent continuum medium with equivalent media properties. The expressions for equivalent velocity and damping ratio under long wavelength conditions, where the position of the joint is normal to the propagation of the wave, are given as:

$$V_{mass}^{long \lambda} = \sqrt{\frac{1}{\frac{1 - \eta \rho_{mass}}{V_r^2 \rho_r} + \frac{\eta \rho_{mass}}{\rho_r}}}$$
(9.1)

$$D_{mass}^{long \lambda} = \frac{\frac{\eta}{1 - \eta} \frac{G_r}{G_j} D_j + D_r}{\frac{\eta}{1 - \eta} \frac{G_r}{G_i} + 1}$$
(9.2)

Where, $\rho_{mass} = \rho_r (1 - \eta) + \rho_j \eta$; and $\eta = \frac{L_j}{L_{mass}}$ is the joint ratio; L_j , L_r , and L_{mass} are the length of the discontinuity, intact rock, and rock mass, respectively; ρ_j , ρ_r , and ρ_{mass} are the densities of discontinuity (i.e., NRL in this study), intact rock, and rock mass respectively; G_j and G_r are the shear moduli of infill material and intact rock respectively; and D_j and D_r are the damping ratios of infill material and intact rock respectively.

The values of shear modulus, G_i and G_r, and damping ratio, D_i and D_r of natural rubber latex and intact gypsum plaster have been obtained from the resonant column testing at varying strain levels ranging from 10^{-5} % to 10^{-1} % as given in Table 9.2. This study compares the theoretical approach offered by Fratta and Santamarina (2002) and the experimental results derived from RC testing conducted for NRL-grouted jointed specimens. Consistent with the approach suggested by Fratta and Santamarina (2002), the comparison analysis found that, in general, the equivalent shear wave velocity falls as the strain level and thickness of the grouted joint increase. In addition, the theoretical approach predicts a linear reduction in shear wave velocity with increasing strain amplitude, whereas the experimental results, as shown in Figure 9.9, reveal a non-linear relationship between the shear wave velocity and strain amplitude. Furthermore, the experimental results obtained from RC testing align with the findings of Fratta and Santamarina (2002) at low strain amplitude, i.e., 10⁻⁵%. Consistent with the findings of Fratta and Santamarina (2002), the equivalent damping ratio rises with increasing NRL thickness and strain amplitude. The experiment results and the variation in equivalent damping ratio values with increased joint thickness agree with Fratta and Santamarina (2002). Figure 9.10 demonstrates that a small change in the joint-grouted thickness substantially affects the equivalent damping ratio, and the fluctuation is non-linear. The notable variance between the theoretical and experimental results for shear modulus and damping ratio can be accounted for because the theoretical framework proposed by Fratta and Santamarina, 2002 overlooked the impact of strain amplitude on shear wave

velocity and damping ratio. In real-world scenarios, the behaviour of rock materials demonstrates a significant relationship between shear wave velocity, damping ratio, and strain amplitude, thus contributing to the observed distinctions.

Table 9. 2 Shear modulus and damping ratio of natural rubber latex and intact gypsum plaster

Shear strain, γ (%)	Shear Modulus of NRL, G _j (MPa)	Shear Modulus of intact rock, Gr (MPa)	Damping ratio of NRL, D _j (%)	Damping ratio of intact rock, D_r (%)
0.00001	3.723	3345.652	0.056	0.083
0.0001	3.527	3220.572	1.510	0.086
0.001	3.442	3187.322	2.136	0.111
0.01	3.246	2988.188	3.591	0.225
0.1	3.161	2964.141	4.217	0.391

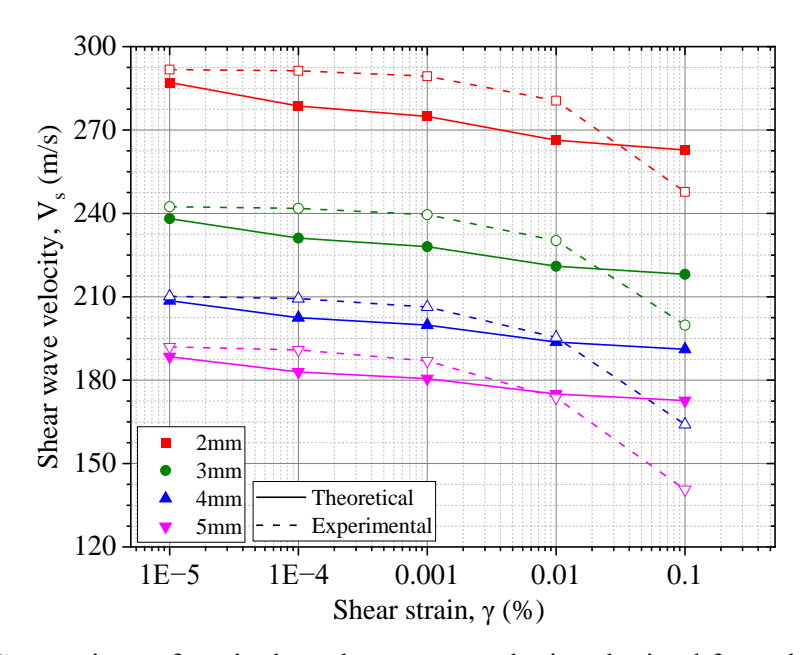


Figure 9. 9 Comparison of equivalent shear wave velocity obtained from theoretical and experimental results

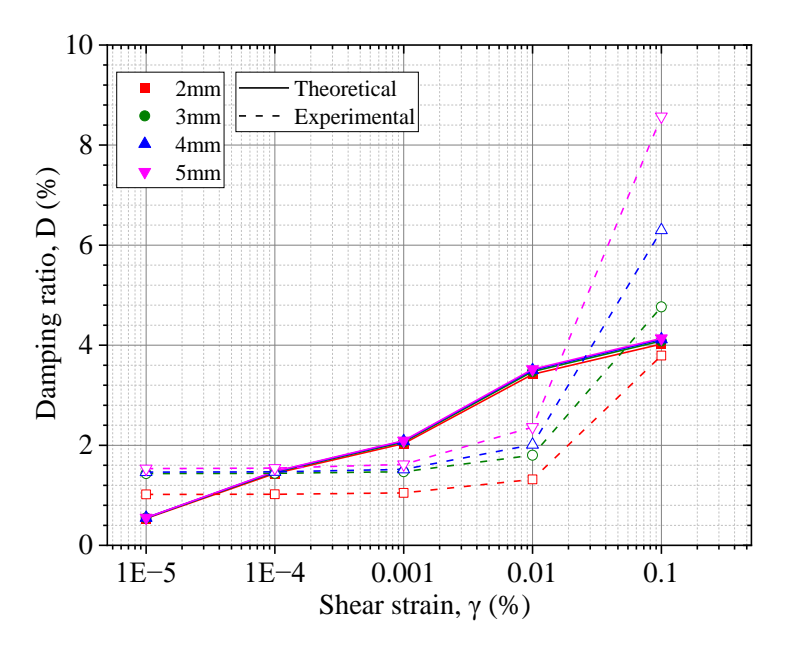


Figure 9. 10 Comparison of equivalent damping ratio obtained from theoretical and experimental analyses

Stage 2: The experimental results demonstrate that as the amplitude of shear strain increases, the shear modulus values decrease, and the damping ratio of the material increases, as depicted in Figures 9.11 and 9.12. A similar trend was found for all joint spacings and confining pressures. In particular, it has been observed that an increase in confining pressure causes a rise in the shear modulus and a decline in the damping ratio. Moreover, when the confining pressure increases, the nonlinearity related to the decrease in shear modulus with the increase in the strain level decreases. At any given strain level, the shear modulus values decline with an increased number of joints.

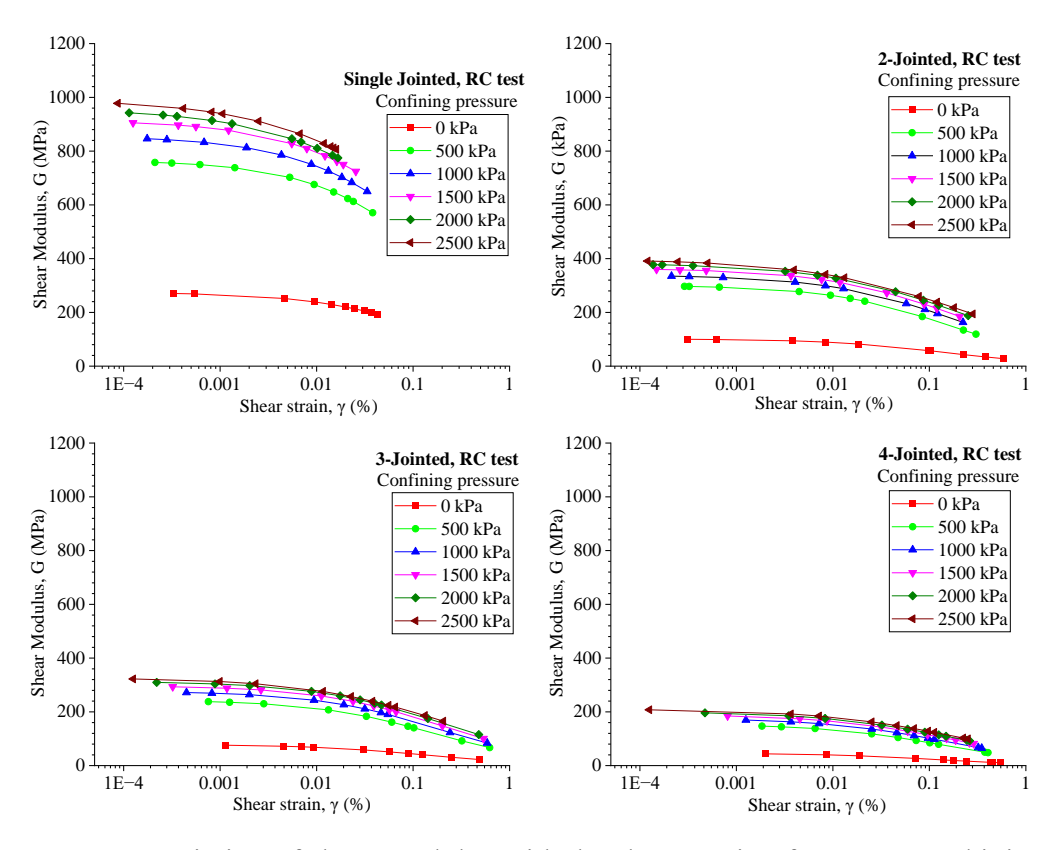


Figure 9. 11 Variation of shear modulus with the shear strain of NRL grouted jointed specimens under resonant column testing.

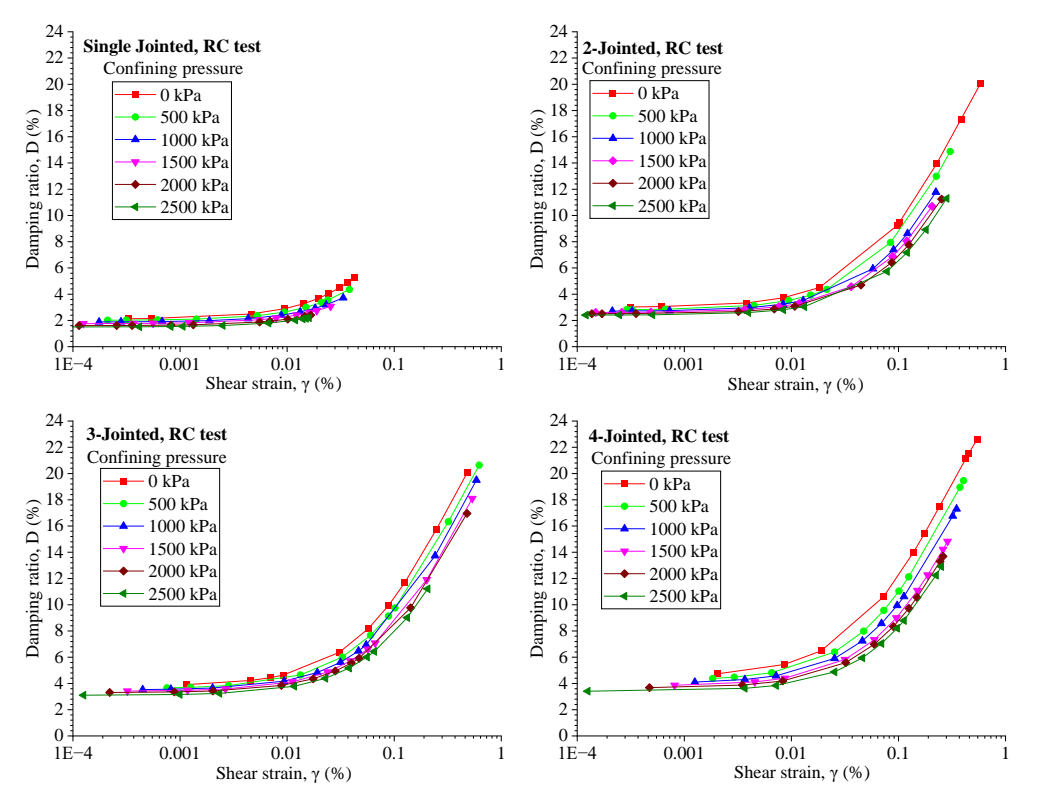


Figure 9. 12 Variation of damping ratio with the shear strain of NRL grouted specimens under resonant column testing

9.5 Results from cyclic torsional shear testing

The cyclic torsional shear testing of NRL grouted specimens demonstrates, as seen in Figure 9.13a, that the shear modulus values increase, and the damping ratio values reduce as the frequency of loading rises while the amplitude of loading remains constant. In addition, as depicted in Figure 9.13b, an increase in strain amplitude results in a declination in shear modulus and a rise in damping ratio while the loading frequency remains the same.

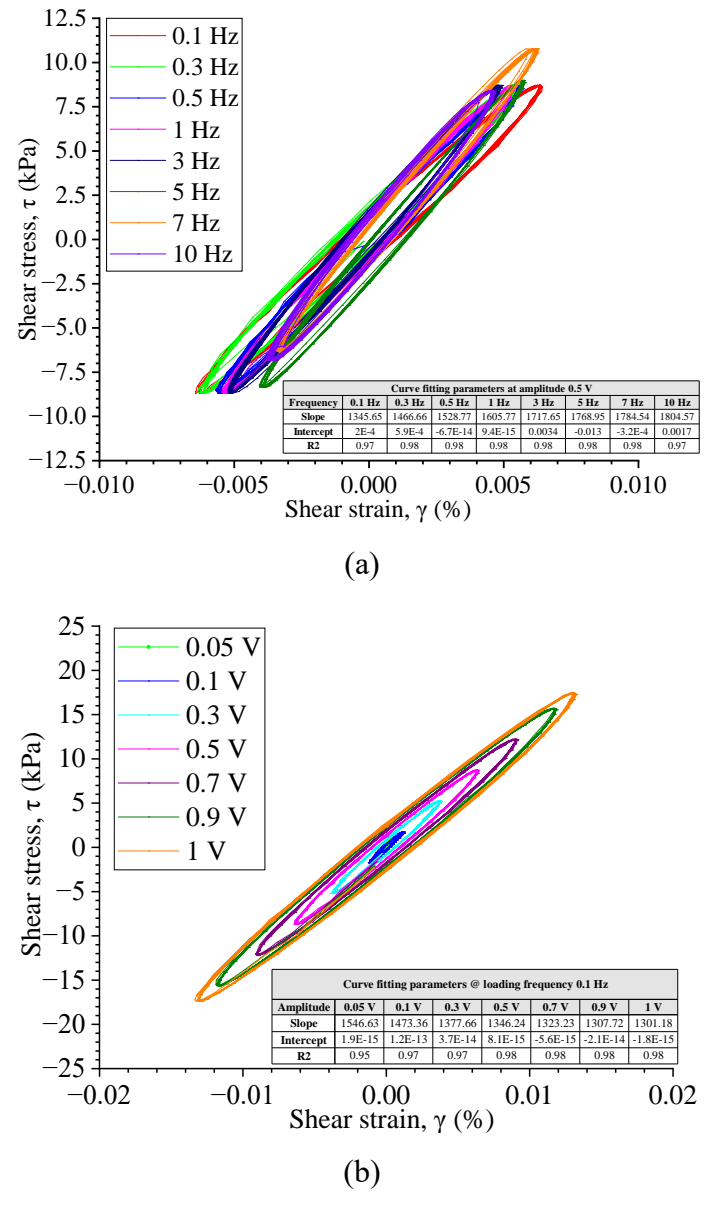


Figure 9. 13 Shear stress- shear strain curves obtained from CTS testing at **(a)** varying loading frequencies keeping the amplitude of shear strain constant, **(b)** varying amplitudes of shear strain keeping loading frequency constant

The cyclic torsional shear tests were conducted at a constant confining pressure of 50 kPa with various strain amplitudes and loading frequencies. As shown in Figures 9.14 and 9.15, for all joint spacings, the shear modulus values decline with a rise in strain amplitude and hike with an escalation in the loading frequency. Compared to cyclic torsional shear testing, resonant column testing yields greater shear modulus values at a given shear strain amplitude. The reason is the higher loading rate associated with the RC test than the CTS test. In RC testing, the specimen is exposed to torsional vibrations in which the loading frequency is considerably higher than the cyclic torsional shear loading applied in CTS. With an escalation in the number of joints, the influence of the loading frequency on the shear modulus diminishes.

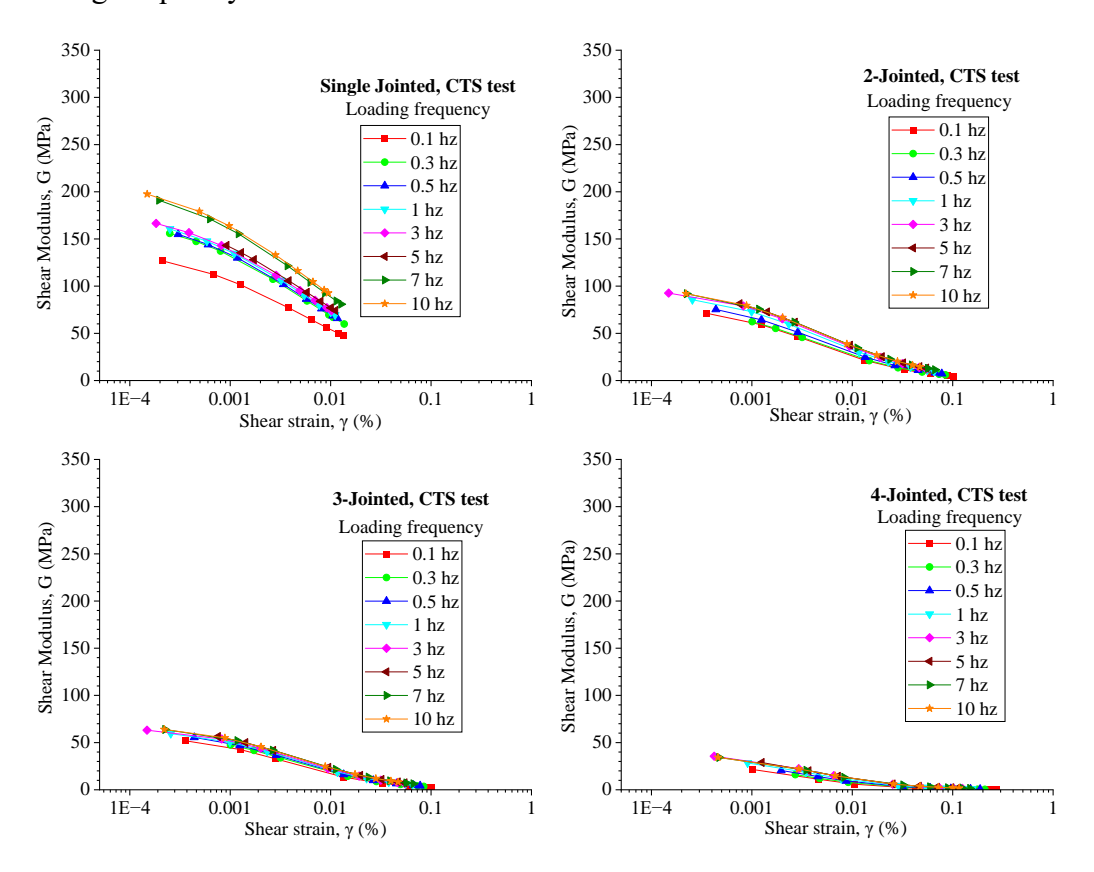


Figure 9. 14 Variation of shear modulus with the shear strain of NRL grouted jointed specimens under cyclic torsional shear testing.

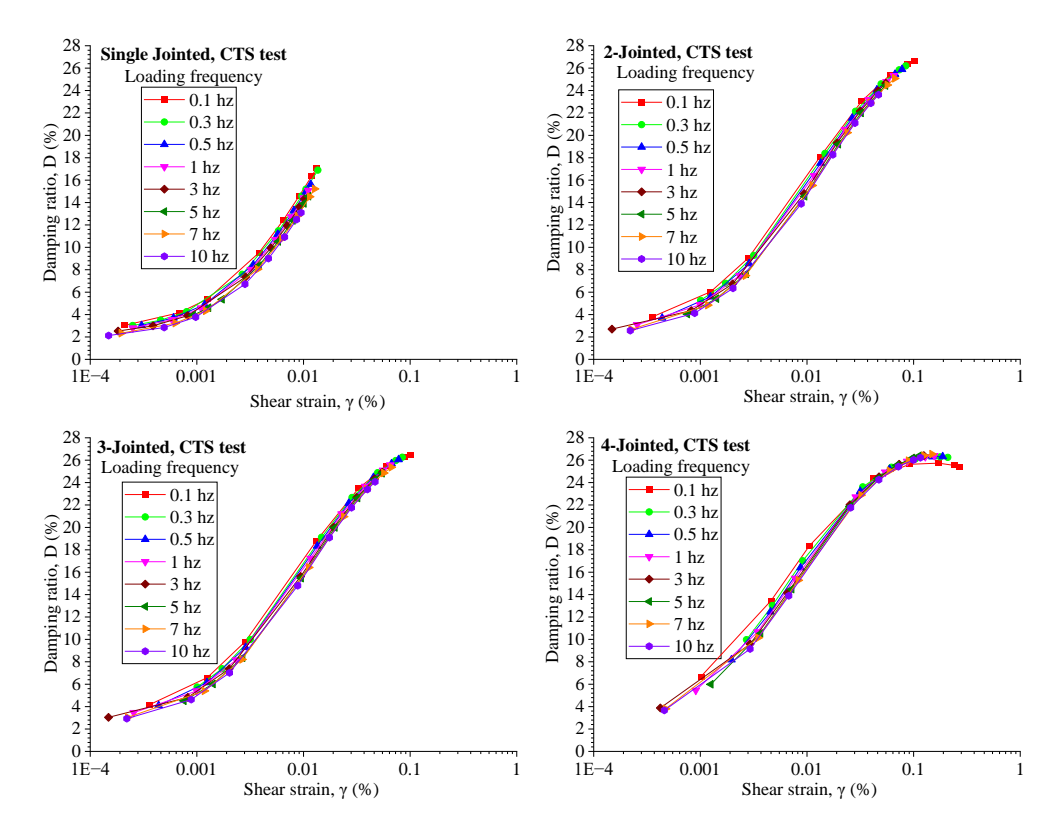


Figure 9. 15 Variation of damping ratio with shear strain of NRL grouted specimens under cyclic torsional testing

9.6 Analysis and Discussions

Comparing the NRL grouted specimens to the plain-jointed specimens, it was discovered that the NRL grouted specimens exhibit superior damping qualities due to their greater ductility. This study analysed the results of RC and CTS tests on plain-jointed and NRL-grouted gypsum plaster specimens using the MH model (Darendeli, 2001) and the RO material model (Ramberg-Osgood, 1943). Based on the data collected under various experimental settings, a correlation between material characteristics and experimental conditions has been suggested.

9.6.1 Effect of confining pressure: The rise in shear modulus and decline in damping ratio with increment in the confining pressure follows a power function, which can be stated as:

$$y = a \left(\frac{\sigma_n}{1kPa}\right)^b \tag{9.3}$$

Where y is the dependent variable, which can be either shear modulus (G) or damping ratio (D), a is the constant whose value depends on the material property at the confining pressure of 1 kPa, and b is the sensitivity constant.

With an increment in the number of joints, the sensitivity of the modification in shear modulus and damping ratio to a rise in confining pressure increases. In addition, the effectiveness of confining pressure on the dynamic properties of jointed rock specimens under varying shear strain amplitudes is not very significant, but a sudden increase in sensitivity was observed near the strain level of 0.1%. The same pattern has been observed for all joint conditions. With a reduction in joint spacing, the value of a decreases, and b rises. The findings of plain-jointed specimens from Chapter 7 reveal that plain-jointed specimens are more sensitive to the influence of confining pressure on dynamic properties than their NRL-grouted counterparts. Figures 9.16 and 9.17 depict the change of shear modulus and damping ratio with confining pressure for NRL grouted-jointed specimens.

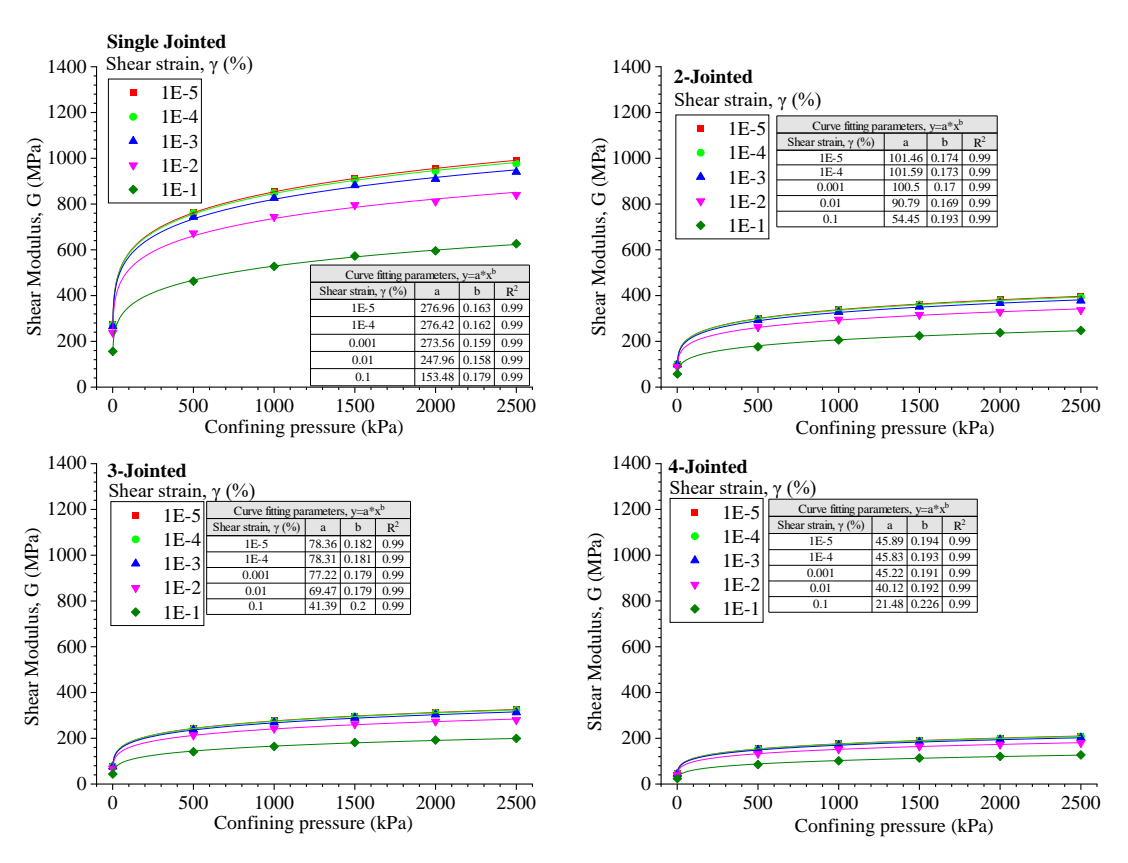


Figure 9. 16 Variation of shear modulus with confining pressure for NRL grouted jointed specimens

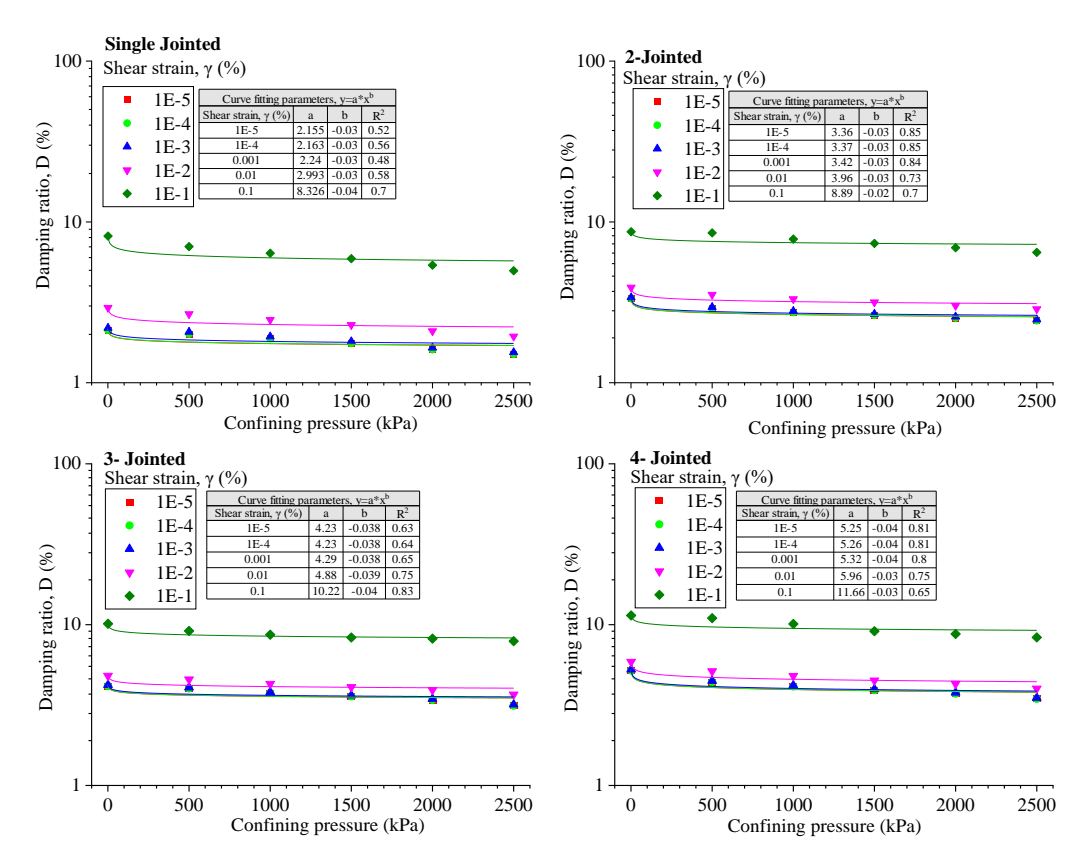


Figure 9. 17 Variation of damping ratio with confining pressure for NRL grouted jointed specimens

9.6.2 Effect of loading frequency: The experimental results from CTS testing demonstrate that loading frequency substantially affects the dynamic characteristics of NRL grouted-jointed rock specimens. Consistent with Xiao et al. (2008), increased shear modulus and reduced damping ratios are observed as loading frequency increases. The power function is followed by the change in the damping ratio and the shear modulus with a change in the loading frequency. By comparing the findings from Chapter 7, it becomes possible to determine that the NRL-grouted and plain-jointed rock specimens behaved similarly, i.e., the general trend of variation of the damping ratio and shear modulus with the magnitude of the shear strain is the same. The dynamic properties of plain-jointed specimens are more sensitive to variations in loading frequency when the shear strain amplitude is increased. On the contrary, for NRL grouted jointed rock specimens, the sensitivity of the change in dynamic properties with loading frequency and increase in shear strain level is less than that for plain jointed specimens. Figures 9.18 and 9.19 illustrate the deviation of shear modulus and damping ratio with the loading frequency for NRL grouted joint specimens.

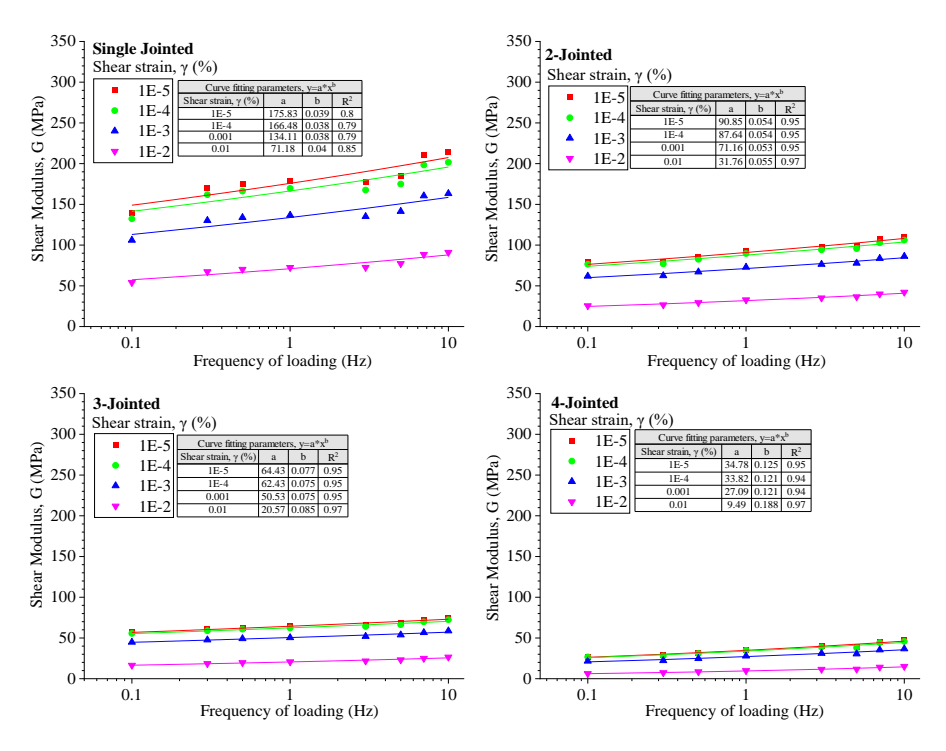


Figure 9. 18 Variation of shear modulus with the frequency of loading for NRL grouted jointed specimens

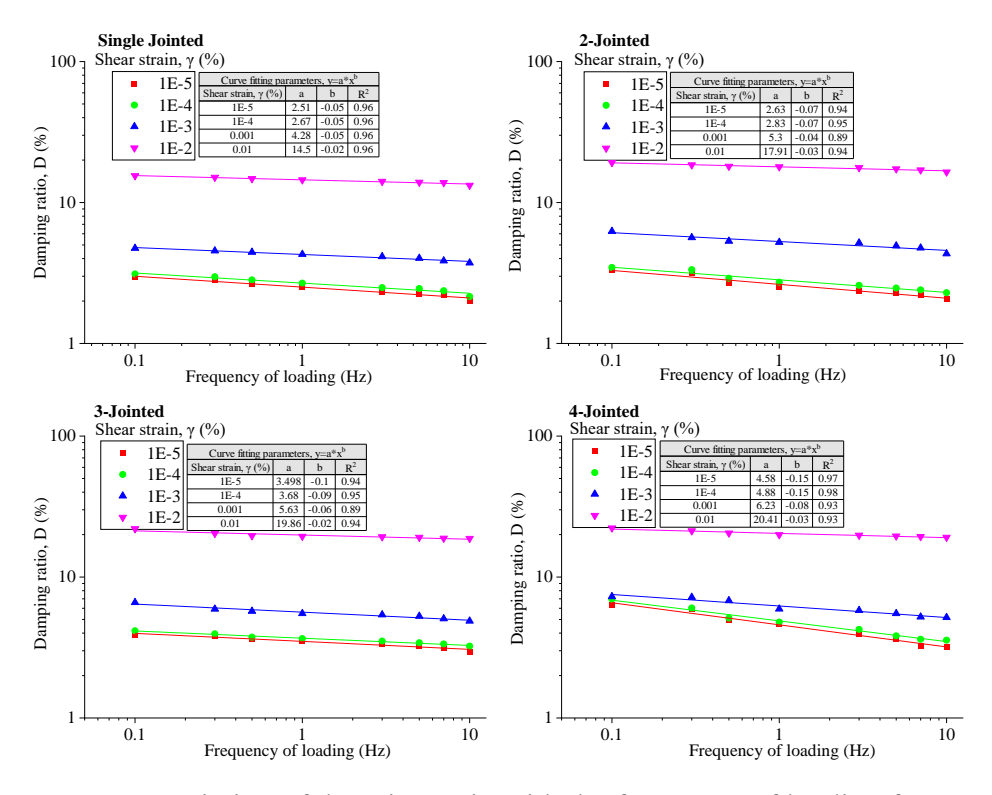


Figure 9. 19 Variation of damping ratio with the frequency of loading for NRL grouted jointed specimens

9.6.3 Curve fitting models: Normalized modulus reduction and material damping ratio curves have been obtained for NRL-grouted-jointed rock specimens with varying joint spacings. The RC and CTS testing outcomes have been fitted to the modified hyperbolic and Ramberg-Osgood models. It was discovered that both the MH and RO models fit the experimental data well. While fitting the experimental results of RC testing with the MH model, it was observed that the value of ' γ_{ref} ' raised with an increment in confining pressure, and ' δ ' declined with the increase in the number of joints. Likewise, previous findings showed that the value of ' γ_{ref} ' increased and ' δ ' decreased as the loading frequency increased during CTS testing. The curve fitting for NRL-grouted specimens subjected to RC and CTS testing is depicted in Figures 9.20 and 9.21, respectively. The values of the curve fitting parameters for the upper and lower bound curves of the MH and RO models are provided in Tables 9.3 and 9.4.

Table 9. 3 Results obtained from curve fitting performed for NRL grouted specimens under RC testing

Curve fitting parameters (Resonant Column testing), NRL grouted.						
Number of joints		Ramberg-Osgood Model		Modified hyperbo		
		r	α΄	γref	δ	
1	Upper bound	1.705	0.134	0.225	0.65	
	Lower bound	1.624	0.196	0.125	0.685	
2	Upper bound	1.663	0.195	0.185	0.725	
2	Lower bound	1.722	0.104	0.115	0.795	
3	Upper bound	1.657	0.182	0.215	0.705	
3	Lower bound	1.682	0.114	0.122	0.722	
4	Upper bound	1.697	0.202	0.189	0.707	
	Lower bound	1.712	0.114	0.105	0.691	

Table 9. 4 Results obtained from curve fitting performed for NRL grouted specimens under CTS testing

Curve fitting parameters (Cyclic torsional shear testing), NRL grouted.						
Number of joints		Ramberg-Osgood Model		Modified hyperbo		
		r	α΄	γref	δ	
1	Upper bound	1.702	1.404	0.0043	0.705	
	Lower bound	1.652	1.568	0.006	0.675	
2	Upper bound	1.782	1.502	0.0038	0.875	
2	Lower bound	1.752	2.315	0.0055	0.835	
3	Upper bound	1.863	1.875	0.0053	0.885	
3	Lower bound	1.829	2.465	0.0034	0.909	
4	Upper bound	2.013	2.207	0.0046	0.908	
7	Lower bound	1.959	3.156	0.003	0.995	

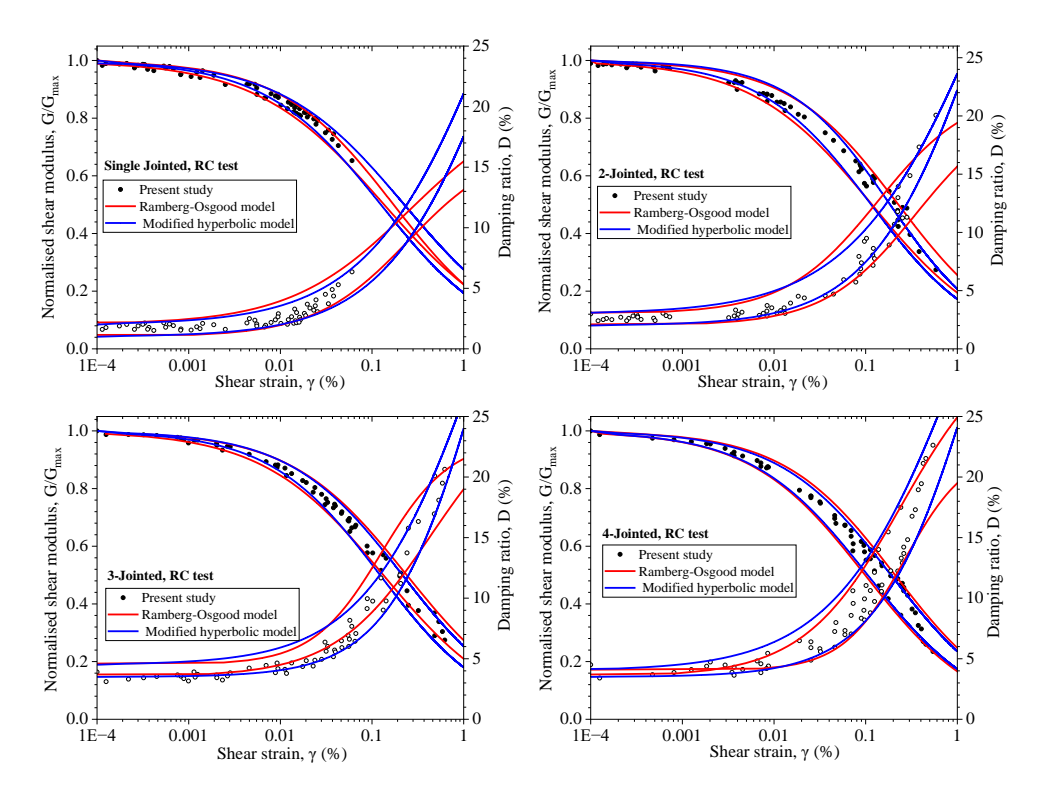


Figure 9. 20 Normalised modulus reduction and damping ratio curve of NRL grouted jointed specimen under RC testing

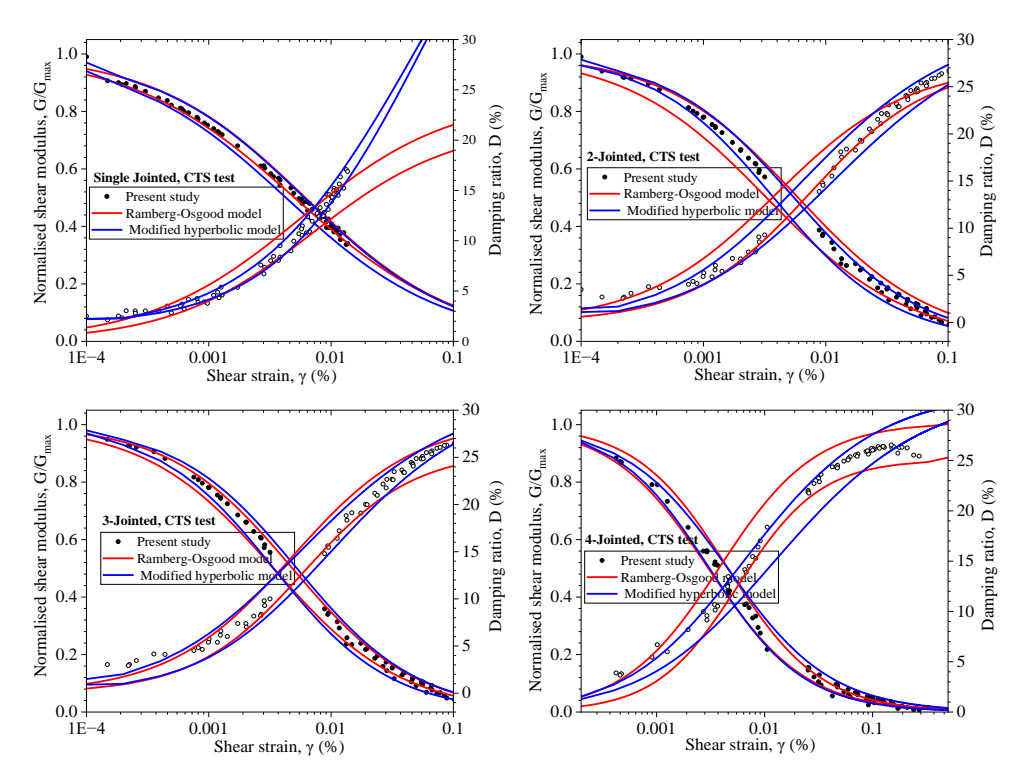


Figure 9. 21 Normalised modulus reduction and damping ratio curve of NRL grouted jointed specimen under CTS testing

9.6.4 Regression analysis: Based on experimental data gathered from different conditions of confining pressure, joint spacing, and shear strain amplitude, the regression analysis for RC testing has been performed for plain and NRL grouted jointed rock specimens. The proposed general form of the equation is as follows:

$$G = \zeta * (\sigma)^{\eta} * (s)^{\mu} * (\gamma)^{\varphi}, D = \zeta * (\sigma)^{\eta} * (s)^{\mu} * (\gamma)^{\varphi}$$
 9.4

Where ζ is the constant based on the material property; η is the confining pressure exponent; μ is the joint spacing exponent; φ is the shear strain amplitude exponent; s is the joint spacing in mm.

Similarly, regression analysis was performed for CTS testing based on the varying experimental conditions of loading frequency (f), joint spacing, and strain amplitude. The proposed equation for shear modulus and damping ratio can be written in its general form:

$$G = \zeta * (f)^{\varsigma} * (s)^{\mu} * (\gamma)^{\varphi}, D = \zeta * (f)^{\varsigma} * (s)^{\mu} * (\gamma)^{\varphi}$$
 9.5

Where ζ is the loading frequency exponent, μ and ϕ remain the same.

The outcomes of regression analysis performed for RC testing with a 95% confidence level are presented in Table 9.5. The regression analysis revealed that the value of ' η ' and ' φ ' obtained for the NRL grouted jointed rock specimen is less than that of the plain

jointed specimen, indicating that the NRL grouted specimens are less sensitive to changes in confining pressure and shear strain amplitude than the plain jointed specimens. The reason behind this is the adhesive nature and high ductility of NRL, which prevent the gypsum plaster blocks from reorienting themselves in response to a change in confining pressure and shear strain. In addition, the value of the joint spacing exponent, µ, is greater for the NRL grouted specimen than for the simple jointed specimen, indicating that the NRL grouted specimens are more sensitive to changes in the joint spacing than the plain jointed specimens. The reason could be the decrease in the equivalent density of the NRL grouted specimens as the number of joints increases. The results of regression analysis performed for CTS testing with a 95% confidence level are presented in Table 9.6. In contrast to RC testing, the value of the ' ζ ' exponent is less for NRL grouted jointed specimens than for plain grouted specimens, indicating that the NRL grouted specimens are less sensitive to the change in the loading frequency than the plain grouted specimens, as the adhesive nature of the NRL absorbs the energy and resists the movement of the gypsum plaster stones in accordance with the different loading frequency.

Table 9. 5 Results of regression analysis of RC testing

Outcomes of regression analysis of RC testing							
Joint Condition	Parameter	ζ	η	μ	φ	\mathbb{R}^2	
Plain jointed	Shear modulus, G (MPa)	4.375	0.329	1.311	-0.13	0.92	
J • • •	Damping ratio, D (%)	-0.0043	-0.049	-0.776	0.398	0.94	
NRL grouted	Shear modulus, G (MPa)	4.821	0.274	1.742	-0.116	0.95	
51 04104	Damping ratio, D (%)	-0.179	-0.044	-0.813	0.205	0.88	

Table 9. 6 Results of regression analysis of CTS testing

Outcomes of regression analysis of CTS testing							
Joint Condition	Parameter	ζ	S	μ	φ	R ²	
Plain	Shear modulus, G	4.099	0.141	2.946	-0.736	0.91	

jointed	(MPa)					
	Damping ratio, D (%)	1.841	-0.033	-0.043	0.408	0.91
NRL grouted	Shear modulus, G (MPa)	3.502	0.129	3.108	-0.500	0.90
grouted	Damping ratio, D (%)	1.740	-0.011	-0.078	0.371	0.95

9.7 Summary

This study aimed to utilise the NRL as an energy-absorbing layer within the jointed rocks. RC and CTS tests were conducted to determine the dynamic properties of the gypsum plaster after the plain joints were introduced. The results of the comparative study revealed that the variations of shear wave velocity and damping ratio strongly depend on the shear strain amplitude. Due to this, there is a large disparity between the findings of the experimental and the theoretical approach with increasing strain amplitudes. A comparative study has investigated the shear modulus and damping ratio of plain-jointed and NRL-grouted joints. From the study, the conclusions are listed below:

- Comparative analysis of the RC and CTS tests revealed that, at a certain strain amplitude, the lower shear modulus and higher damping ratio values were obtained from the CTS tests than those from the RC, and this trend was observed for all joint spacing conditions.
- Incorporating an NRL layer into the joints reduces shear modulus and increases
 the damping ratio than plain-jointed specimens; the same trend was observed
 during RC and CTS testing.
- At a specific strain amplitude, applying confining pressure raises the shear modulus and decreases the damping ratio, which holds for all test conditions. In addition, a comparison of plain-jointed and NRL-grouted joints under the influence of confining pressure reveals that the former is less sensitive than the latter.
- The impact of the loading frequency on plain and NRL-grouted joints reveals that the shear modulus escalates with a hike in the loading frequency, and the

- damping ratio decreases. The control of loading frequency on NRL-grouted, joined specimens is less than that of plain jointed specimens.
- The RO and MH models appropriately fit the results obtained from RC and CTS testing. In addition, the nonlinearity associated with the modulus reduction and damping ratio curves reduced with rising confining pressure, loading frequency, and joint spacing.
- The regression analyses of the RC and CTS test results indicate that NRLgrouted specimens are more sensitive to changes in joint spacing and less sensitive to changes in confining pressure, loading frequency, and strain amplitude than plain-jointed specimens.

Chapter 10 Conclusions

10.1 Introduction

The main objective of this research is to look into the dynamic behaviour of geomaterials in various experimental conditions. In an attempt to understand the deformational properties of geomaterials, resonant column (RC) and cyclic torsional shear (CTS) testing were carried out. The study covered two types of material behaviour: discrete and continuum. While intact gypsum plaster was used to simulate rocks and assess continuous behaviour, dry sand was employed to study discrete responses. To gain a thorough understanding of the dynamic properties of geomaterials, testing was undertaken at varied strain amplitudes, confining pressures, and loading frequencies. In addition, the effect of material qualities on dynamic properties was examined.

The dynamic response of dry sand was initially studied across a range of relative densities. The dynamic behaviour of rocks was next investigated, starting with tests on intact gypsum plaster and original rock specimens to identify broad characteristics. Then, rock joint features such as plain joints, joint spacing, roughness, and orientation were introduced. RC and CTS testing under various experimental situations allowed us to examine the individual and combined impacts of loads and joint features. Regression analysis of experimental data made it easier to propose empirical relationships.

Furthermore, natural rubber latex (NRL) was introduced into rock joints to investigate its effect on damping properties. The impact of NRL layer thickness on dynamic response was analyzed, indicating its effectiveness as a vibration-absorbing material and its potential to improve damping properties in rock joints.

As a result, this study offers a comprehensive understanding of geomaterials' discrete and continuum dynamic responses. Key contributions include the development of site-specific shear modulus and damping ratio curves for sand and an empirical correlation that incorporates strain amplitude, confining pressure, loading frequency, and sand relative density into account. Furthermore, the study of rock dynamic behaviour provided insights into the combined impacts of joint and loading features and an empirical correlation for forecasting rock dynamic response under various experimental

conditions. Furthermore, the usefulness of infilled NRL layers in improving the damping properties of rock joints was demonstrated.

10.2 Conclusions

The major conclusions drawn from the experimental and numerical studies presented in the thesis are:

10.2.1 Exploration of the deformational behaviour of sands with varying relative densities using resonant column and cyclic torsional shear testing techniques:

- With a specific relative density, increasing strain amplitude results in a decrease in shear modulus and an increase in damping ratio.
- At a specific relative density, raising confining pressure leads to higher shear modulus and lower damping ratio.
- Maintaining strain amplitude and confining pressure while increasing relative density leads to higher shear modulus and lower damping ratio.
- The shear modulus and material damping ratio obtained from Cyclic Torsional Shear (CTS) tests exhibit significant dependence on loading frequency across all shear strain amplitudes.
- The impact of relative density and confining pressure on the increase in shear modulus and decrease in damping ratio diminishes at higher strain levels, around 1%.
- Regression analysis of experimental data using a modified hyperbolic model reveals that increasing confining pressure raises the curvature coefficient, α, while lowering the scaling coefficient, β.
- The increase in damping characteristics and decrease in shear modulus with increasing shear strain amplitude is more pronounced in CTS testing compared to RC testing.

10.2.2 Determination of the dynamic response of intact rock under various strain amplitudes and loading frequencies:

• In resonant column testing, an increase in strain level corresponds to a decrease in shear modulus values and an increase in damping ratio.

- During cyclic torsional shear testing, a consistent trend of increasing loading rate
 with higher loading frequency and torque amplitude is observed across both
 sinusoidal and ramp waveforms.
- Elevating the loading rate leads to a reduction in shear strain in the material.
- Sinusoidal waveforms consistently exhibit notably higher loading rates than ramp waveforms for fixed loading frequency and torque amplitude combinations, highlighting the superior dynamicity of sinusoidal waveforms.
- Higher loading rates correlate with elevated shear modulus (G) and reduced damping ratio (D), while lower loading rates exhibit the opposite effect on these parameters.
- Curve fitting results emphasize the superior suitability of the RO model for describing modulus reduction behaviour, whereas the modified hyperbolic model is more adept for analyzing damping ratio dynamics.

10.2.3 Investigation of the surface roughness of jointed rocks using 3-D image processing techniques:

- Surface profiling achieved through smartphone-based photogrammetry offers realistic results compared to profilometry, attributed to its superior precision and reduced least count.
- JRC values derived from visual interpretation, Root Mean Square analysis, and fractal methods consistently fall within a comparable range across surface profiles obtained via photogrammetry, 3D scanning, and profilometry.
- Smartphone photogrammetry emerges as a cost-effective method for estimating JRC values with commendable precision.

10.2.4 Determination of dynamic properties of jointed rocks under varying joint and loading characteristics:

- Analysis comparing RC and CTS tests revealed that, under a certain strain amplitude, CTS tests produced lower shear modulus and higher damping ratio values than RC tests, consistent across all joint spacing conditions.
- Increasing the number of joints results in decreased shear modulus and increased damping ratio, a pattern observed in both RC and CTS testing.

- Application of confining pressure at a specific strain amplitude elevates shear modulus and reduces damping ratio across all test conditions, following a power function trend.
- Shear modulus increases, and the damping ratio decreases with rising loading frequency for all joint spacing conditions, following a power function trend.
- Nonlinearity in modulus reduction and damping ratio curves decreases with increasing confining pressure, loading frequency, and joint spacing.
- Increasing confining pressure while maintaining a constant strain amplitude yields higher shear modulus and lower damping ratio. Additionally, the influence of confining pressure on dynamic characteristics becomes more pronounced with increased orientation angle.
- Higher joint roughness and orientation lead to increased shear modulus values and decreased damping ratios at a specific strain amplitude.
- The dynamic response of frictional jointed rocks with varying orientations exhibits
 distinct deformational behaviour compared to plain jointed rocks, with the former
 not following a power function under varying confining pressure and loading
 frequency conditions.

10.2.5 Exploration of the dynamic properties of jointed rocks when infilled with natural rubber latex (NRL).

- Incorporating an NRL layer into the joints results in a reduction in shear modulus and a higher damping ratio compared to plain-jointed specimens. This trend is consistent across RC and CTS testing.
- Increasing the infilled NRL thickness leads to a decrease in shear modulus and an increase in damping ratio.
- The application of confining pressure at a specific strain amplitude enhances the shear modulus while reducing the damping ratio across all test conditions. A comparison between plain-jointed and NRL-grouted joints under confining pressure indicates that the former is less responsive than the latter.
- Loading frequency influences the shear modulus and damping ratio differently in plain and NRL-grouted joints. Shear modulus increases with higher loading frequencies while the damping ratio decreases. The influence of loading frequency on NRL-grouted joints is comparatively lower than on plain jointed specimens.

- Regression analysis of RC and CTS test results suggests that NRL-grouted specimens exhibit greater sensitivity to changes in joint spacing and lesser sensitivity to variations in confining pressure, loading frequency, and strain amplitude than plain-jointed specimens.
- Introducing NRL into rock joints increases damping compared to plain jointed rocks, making it an effective solution for applications requiring high vibration damping, such as in seismic and other vibrational loadings.

10.3 Scope for future work

- Study of the influence of a number of vibration cycles on the shear modulus and damping ratio of intact and jointed rocks.
- Assessment of frictional joint surface degradation and its effects on elastic wave propagation under cyclic torsional shear loading.
- Determination of directional dependency of surface foliations on the dynamic response of rocks.
- Investigation into the dynamic behaviour of obliquely striking waves across multiple parallel joints with frequency-dependent characteristics.
- Development of a statistical model capable of predicting the dynamic properties of rocks based on loading conditions and joint characteristics.
- Investigation into damping characteristics of different infill materials employing Resonant column and cyclic torsional shear testing methodologies.
- Study on the comparative analysis of wave propagation across complex joint characteristics using laboratory-derived and validated numerical models of RCA.

Appendix A

A.1 Calibration of RCA

In a resonant column apparatus (RCA), during torsional mode of vibration, the shear wave velocity (V_s) of a cylindrical specimen, which is fixed at its base and has a driving mass (M_o) attached to the top of the specimen, is obtained from the measured resonant circular frequency (ω_n) by using the following equation 1:

$$\frac{J_S}{J_O} = \frac{\omega_n L}{V_S} \tan\left(\frac{\omega_n L}{V_S}\right) \tag{A.1}$$

Here, J_s and J_0 refer to the mass polar moment of the inertia of the specimen and of the mass attached to the top of the specimen, respectively, and L is the length of the specimen.

On account of the complex geometry of the drive mechanism, its mass polar moment of inertia (J_0) is always determined by using a series of calibration tests carried out on metallic calibration bars (ASTM D4015). The procedure has been discussed in detail in the following section.

In a torsional mode of vibration, on the basis of Rayleigh's method, for a system with negligible damping, the circular frequency (ω_n) of the specimen which has one end fixed and other end free and having a mass at its free end (as shown in Figure A.1) can be expressed by using the following equations (Kumar & Clayton 2007):

$$\omega_n = \sqrt{\frac{K_T}{J_O + \frac{J_S}{3}}} \tag{A.2}$$

$$J_O + \frac{J_S}{3} = \frac{K_T}{\omega_n^2} \tag{A.3}$$

where K_T is the torsional stiffness of the specimen and (ii) J_s and J_O correspond to the mass polar moment of the inertia (about the vertical axis) of the specimen and of the drive system, respectively.

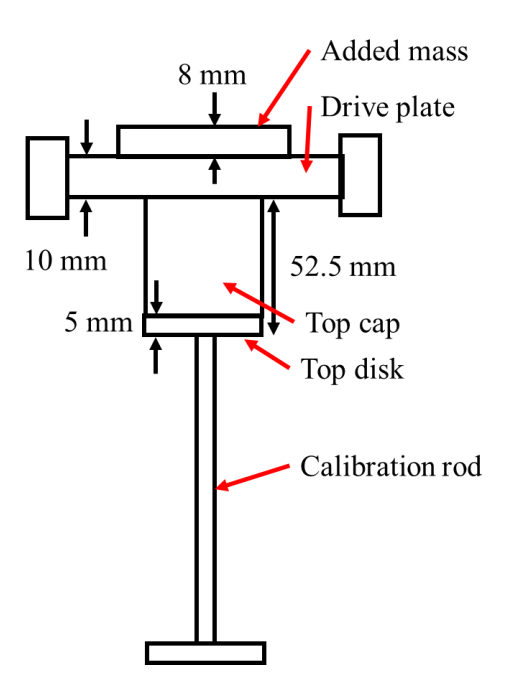


Figure A. 1 Basic configuration of calibration bar and additional mass in fixed-free torsional RCA

When an additional mass (m_I) , with the mass polar moment of inertia J_I about axis Y-Y, is attached to the top of the specimen, Equation (A.3) becomes:

$$J_O + J_1 + \frac{J_S}{3} = \frac{K_T}{\omega_n^2} \tag{A.4}$$

It should be noted that ω_n in Equation 4 corresponds to the resonant frequency of the specimen with an attachment of the additional mass on the top of the specimen. Therefore, for a calibration bar with a certain value of K_T , by varying the additional mass attached to the top of the specimen, the corresponding resonant frequency can be measured separately. From Equations A.3 and A.4, it can be observed that a plot of $J=J_1+J_s/3$ versus $1/\omega_n^2$ becomes a straight line. The negative intercept of this straight line on the J-axis provides the magnitude of J_0 , and the slope of the line gives K_T .

The calibration tests were conducted on three aluminium bars of diameters 15 mm, 12.5 mm, and 10 mm, and seven steel bars of diameters 13 mm, 15 mm, 17 mm, 18 mm, 19 mm, 20 mm, and 23.5 mm. Three Copper (Cu) calibration weights, which have the shape of a rectangular cuboid with 100 mm length, 20 mm width and 8 mm thick, were used as additional masses. Figure A.2 shows the calibration bars and the weights used in this study. Four separate tests were carried out for each calibration bar: (i) without the weight, (ii) with one weight, (iii) with two weights and (iv) with three weights. Figures A.3 and A.4 provide the corresponding plots associated with different

calibration bars. For the present study, the average value of J_O was found to be 35.19 kg-cm².

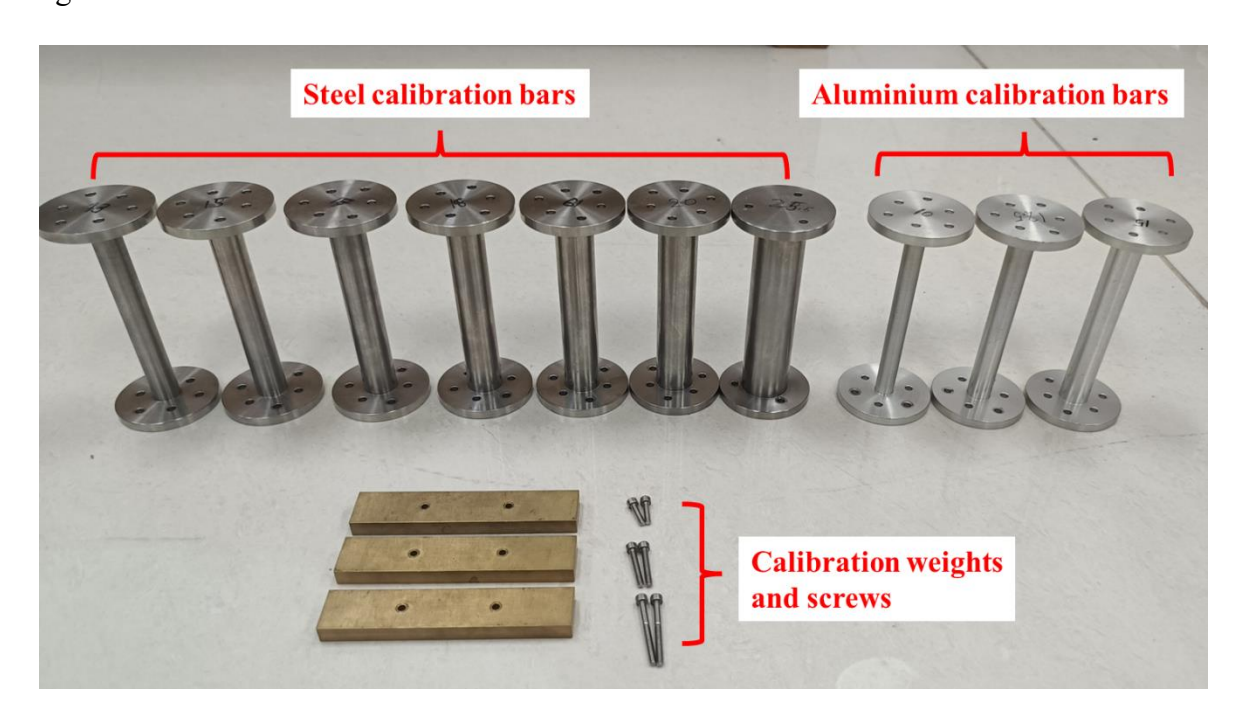


Figure A. 2 Calibration bars and additional weights used to obtain corrections in torsional vibrations

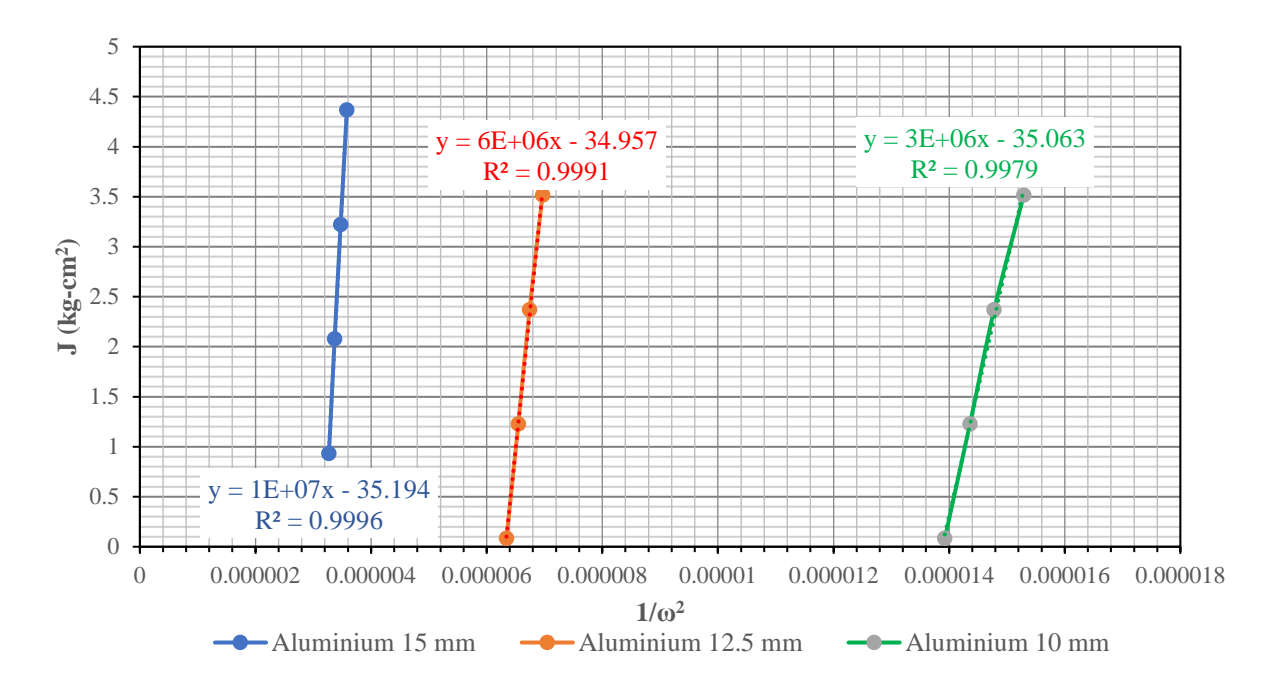


Figure A. 3 Calibration plot used to calculate the mass polar moment of inertia of the driving plate using the aluminium calibration bars.

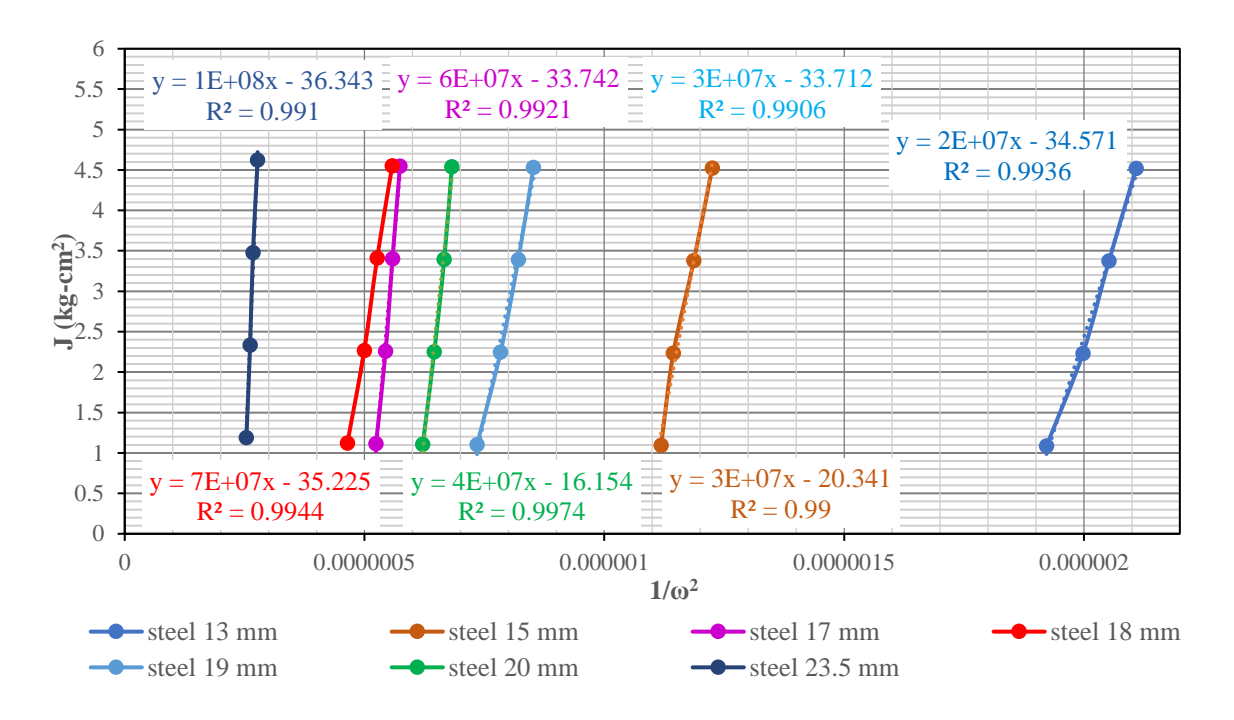


Figure A. 4 Calibration plot used to calculate the mass polar moment of inertia of the driving plate using steel calibration bars.

A.2 Need for corrections to be applied

The Resonant Column Apparatus (RCA) is typically employed to ascertain the lowstrain dynamic properties of geomaterials, given its limitations when testing rigid samples. The resonant frequencies obtained fell within the specified range for the apparatus used in this study. Nonetheless, it was imperative to verify the apparatus against predefined stiffness criteria. Challenges encountered in testing rigid samples include sample over-stiffness, insufficient fixity of the bottom pedestal, coupling problems between the sample and end platens, and the overestimation of damping due to back electromotive force (EMF) generated by magnets and solenoids.

• When stiff samples undergo resonance testing, their natural frequencies may interfere with those of the apparatus, rendering the apparatus base unfixed unless the base mass exceeds the specimen mass by a factor of 100, as per guidelines by Ashmawy and Drnevich (1994). ASTMD 4015 (2000) also stipulates fixity conditions for the bottom pedestal, requiring J_b / J_d > 100, where J_b represents the mass polar moment of inertia of the resonant column base, and J_d denotes the combined mass polar moment of inertia of the specimen and driving plate (J_S/3 + J_O). The fixity criteria outlined by ASTMD 4015 (2000) and Ashmawy and Drnevich (1994) were assessed against the RCA conditions and found to be

satisfactory. Additionally, Drnevich (1978) suggests that the upper limit of the shear modulus of the specimen should not exceed 10% of the material used in the apparatus fabrication. This criterion was validated against the shear moduli of gypsum plaster and stainless steel, confirming compliance.

- To prevent slippage of stiff samples from the base platens during vibration application, epoxy resins were applied to the ends of the samples, ensuring fixation to the end platens, and enhancing linear mode shape vibration, as highlighted by Khan et al. (2008).
- According to Faraday's law of induction, the movement of magnets in a magnetic field generates an electromotive force (EMF) opposing the change in magnetic flux, known as back EMF. This phenomenon, observed during damping tests with the resonant column apparatus, could lead to excessive dissipation of energy. To mitigate this, the apparatus employed an open circuit during free vibration decay, preventing the generation of back EMF by the movement between magnets and coils, thus correcting overestimations of damping values and underestimations of resonant frequencies.

Despite complying with specified stiffness limits outlined in various conditions, the stiffness of samples can occasionally result in an underestimation of natural frequency values during RCA testing, as noted by Kumar and Clayton (2007). This, in turn, may lead to an underestimation of shear wave velocity. To address this issue, corrective measures have been devised to adjust the resonance frequency values obtained and ensure the accurate determination of the actual natural frequencies of the samples.

A.3 Corrections for Resonant Frequencies

The necessary corrections for resonant frequencies were determined utilizing calibration bars of varying diameters. Aluminium and steel calibration bars with different diameters were used to ascertain the correction factors for resonant frequencies. Aluminium calibration bars measuring 10 mm, 12.5 mm, and 15 mm in diameter were utilized, possessing a shear modulus of 26.6 GPa. Furthermore, steel calibration bars with diameters of 13 mm, 15 mm, 17 mm, 18 mm, 19 mm, 20 mm, and 23.5 mm were employed to compute the correction factors, with a shear modulus of 66.05 GPa. The mass polar moment of inertia of the driving plate was determined to be 35.19 kg-cm².

The actual stiffness of each calibration bar was assessed using Equation A.5, followed by the determination of the actual resonant frequency corresponding to this stiffness, as per Equation A.6. The ratio of the actual resonant frequency to the obtained resonant frequency defines the correction factor for each aluminium and steel calibration bar. Tables A.1 and A.2 depict the actual and observed resonant frequencies of the aluminium and steel calibration bars, respectively.

It was observed that the trend of the correction factor corresponding to each resonant frequency follows a polynomial function, as illustrated in Figures A.5 and A.6 for the aluminium and steel calibration bars, respectively.

$$K_T = \frac{G \times \pi \times d^4}{32 \times L} \tag{A.5}$$

$$\omega_n = \frac{1}{2\pi} \sqrt{\frac{K_T}{J_o + \frac{J_S}{3}}} \tag{A.6}$$

Table A. 1 Actual and obtained resonant frequencies in torsional vibrations for aluminium calibration bar

Diameter	Obtained resonant	Actual resonant	Correction
of bar	frequency (Hz)	frequency (Hz)	factor
10	42.8	42.8	1.00
12.5	63.5	65.16	1.05
15	88	92.05	1.09

Table A. 2 Actual and obtained resonant frequencies in torsional vibrations for steel calibration bar

Diameter	Obtained resonant	Actual resonant	Correction
of bar	frequency (Hz)	frequency (Hz)	factor
13	114.8	114.81	1.00
15	151.5	152.85	1.01
17	185.7	196.33	1.05
18	201.9	220.11	1.09
19	219.9	245.25	1.11
20	233.6	271.74	1.16
23.3	322	441.75	1.37

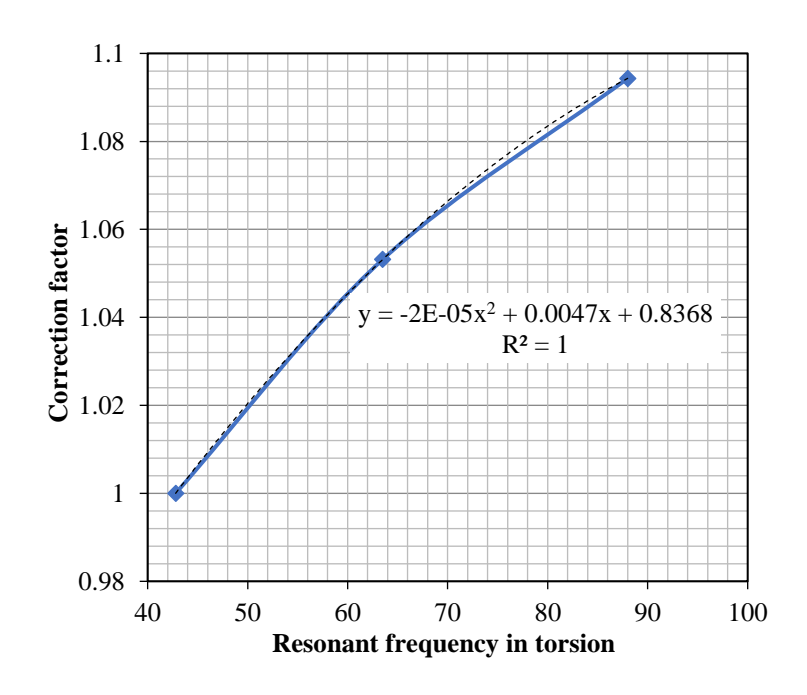


Figure A. 5 Correction factors obtained in torsional vibrations for aluminium calibration bars

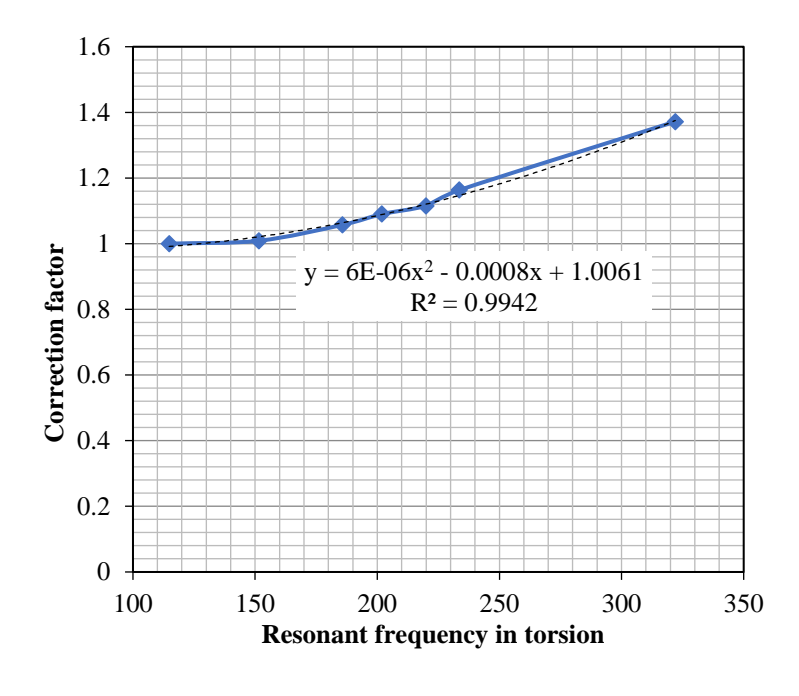


Figure A. 6 Correction factors obtained in torsional vibrations for steel calibration bars

References

- 1) Alarcon-Guzman, A. (1986). "Cyclic Stress-Strain and Liquefaction Characteristics of Sands". PhD. Thesis, Purdue University, Indiana.
- 2) Amadei, B. (1996). "Importance of anisotropy when estimating and measuring in situ stresses in rock." International Journal of Rock Mechanics and Mining Science & Geomechanical Abstract, 33(3), 293-325.
- 3) Anderson, D.G. and Stokoe, K.H. II (1978). "Shear modulus: A time-dependent soil property." In: Silver, M. & Tiedemann, D., Dynamic geotechnical testing: proceeding of a symposium on Dynamic Soil and Rock Testing in the Field and the Laboratory for Seismic Studies, 654, pp. 66–90.
- 4) Ashmawy, A. K., and Drnevich, V.P. (1994). "A general dynamic model for resonant column / quasi-static torsional shear apparatus." Geotechnical Testing Journal, ASTM, 17(3), 337-348.
- 5) ASTM D 2845-08. (2000). "Standard test method for laboratory determination of pulse velocities and ultrasonic elastic constants of rock", Annual book of ASTM Standards, West Conshohocken, PA, ASTM.
- 6) ASTM D 4015 -92. (2000). "Standard test methods for modulus and damping of soils by resonant column method," Annual book of ASTM Standards, West Conshohocken, PA, ASTM.
- 7) ASTM D4015-92, (2000). "Standard Test Methods for Modulus and Damping of Soils by the Resonant-Column Method," American Society for Testing and Materials, Annual Book of Standards.
- 8) ASTMD 412-06. (2021). "Standard test methods for vulcanized rubber and thermoplastic elastomers-Tension."
- 9) ASTMD 7012-23. "Standard test methods for compressive strength and elastic moduli of intact rock core specimens under varying states of stress and temperatures."
- 10) ASTME 122-17. (2022). "Standard practice for calculating sample size to estimate, with specified precision, the average for a characteristic of a lot or process."
- 11) Babanouri, N., Nasab, S. K., & Sarafrazi, S. (2013). "A hybrid particle swarm optimization and multi-layer perceptron algorithm for bivariate

- fractal analysis of rock fractures roughness." International Journal of Rock Mechanics and Mining Sciences, 60, 66–74.
- 12) Bae D, Kim K, Koh Y, Kim J (2011). "Characterization of joint roughness in granite by applying the scan circle technique to images from a borehole televiewer." Rock Mechanics and Rock Engineering, 44:497–504. https://doi.org/10.1007/s00603-011-0134-9
- 13) Bae, D., Kim, K., Koh, Y., & Kim, J. (2011). "Characterization of joint roughness in granite by applying the scan circle technique to images from a borehole televiewer." Rock Mechanics and Rock Engineering, 44, 497–504.
- 14) Bagde, M. N., & Petroš, V. (2005). "The effect of machine behaviour and mechanical properties of intact sandstone under static and dynamic uniaxial cyclic loading." Rock Mechanics and Rock Engineering, 38(1), 59–67. https://doi.org/10.1007/s00603-004-0038-z
- 15) Bar, Y. S., Bay, J.A. (2009). "Modifications of resonant column and torsional shear device for the large strain." Computers and Geotechnics 36 (2009) 944–952.
- 16) Barton, N. (1982). "Modelling rock joint behaviour from in situ block tests: Implications for nuclear waste repository design." Technical Report, Terra Tek, Inc., Salt Lake City, United States.
- 17) Barton, N. (1982). "Modelling rock joint behaviour from in situ block tests: implications for nuclear waste repository design." Office of Nuclear Waste Isolation ONWI-308: Columbus, OH; 1982. p. 96, ONWI-308
- 18) Barton, N. R., and Choubey, V. (1977). "The shear strength of rock joints in theory and practice." Rock Mechanics and Rock Engineering, 10, 1-54.
- 19) Barton, N., & Choubey, V. (1977). "The shear strength of rock joints in theory and practice." Rock Mechanics, 10, 1–54.
- 20) Belem, T., Souley, M., & Homand, F. (2007). "Modeling surface roughness degradation of rock joint wall during monotonic and cyclic shearing." Acta Geotechnica, 2, 227–248.
- 21) Bellotti, R., Ghionna, V.N., Jamiolkowski, M., and Robertson, P.K., (1989). "Design Parameters of Cohesionless Soils from In-situ Tests", Specialty Session, Sponsored by Committee A2L02-Soil and Rock Properties, National Research Council, Transportation Research Board, Washington, USA

- 22) Ben-Moshe, T., Frenk, S., Dror, I., Minz, D., & Berkowitz, B. (2013). "Effects of metal oxide nanoparticles on soil properties." Chemosphere, 90(2), 640–646. https://doi.org/10.1016/J.CHEMOSPHERE.2012.09.018
- 23) Boadu, F.K. and Long, L.T. (1996). "Effects of fractures on seismic-wave velocity and attenuation." Geophysical Journal International, 127(1), 86-110.
- 24) Borden, R. H., Shao, L., and Gupta, A. (1996). "Dynamic properties of Piedmont residual soils." Journal of Geotechnical Engineering, ASCE, 122(10), 813-821.
- 25) Bretar, F., Arab-Sedze, M., Champion, J., et al. (2013). "An advanced photogrammetric method to measure surface roughness: Application to volcanic terrains in the Piton de la Fournaise, Reunion Island." Remote Sensing of Environment, 135, 1–11. https://doi.org/10.1016/j.rse.2013.03.026
- 26) Brideau, M. A., Sturzenegger, M., Stead, D., Jaboyedoff, M., Lawrence, M., Roberts, N., Ward, B., Millard, T., & Clague, J. (2012). "Stability analysis of the 2007 Chehalis Lake landslide based on long-range terrestrial photogrammetry and airborne LiDAR data." Landslides, 9, 75–91.
- 27) Brown, E.T. (ed.) (1981). Rock Characterization, Testing and Monitoring: ISRM Suggested Methods. Oxford: Pergamon Press.
- 28) Brown, M., & Lowe, D. G. (2005). "Unsupervised 3D object recognition and reconstruction in unordered datasets." In Proceedings of the Fifth International Conference on 3-D Digital Imaging and Modelling (3DIM'05), Ottawa, ON, Canada, 13–16 June 2005 (pp. 56–63).
- 29) Bui, M. T. (2009). "Influence of some particle characteristics on the small strain response of granular materials." Ph.D. Thesis, School of Civil Engineering and the Environment, University of Southampton, UK. https://www.researchgate.net/publication/299462881
- 30) Carr, J.R., and Warriner, J.B. (1987). "Rock mass classification of joint roughness coefficient." Proceedings of the 28th US Rock Mechanics Symposium, Tucson, pp 72–86
- 31) Carrivick, J. L., Smith, M. W., & Quincey, D. J. (2016). "Structure from Motion in the Geosciences." John Wiley & Sons: Hoboken, NJ, USA.

- 32) Cascante, G., Vanderkooy, J., and Chung, W. (2003). "Difference between current and voltage measurements in resonant–column testing". Canadian Geotechnical Journal, 40 (4), 806 820.
- 33) Cengiz Kurtuluş, Maral Üçkardeş, Umut Sarı, Ş. Onur Güner, (2013). "Experimental studies in wave propagation across a jointed rock mass." Bulletin of Engineering Geology and the Environment, 2012, Volume 71, Number 2, Page 231. DOI 10.1007/s10064-011-0392-5
- 34) Cevik, A. Cabalar. (2009). "Modelling damping ratio and shear modulus of sand–mica mixtures using genetic programming." Expert Systems with Applications, 36 (4), 7749-7757.
- 35) Cha, M., Cho, G., and Santamarina, J.C. (2009). "Long wavelength P-wave and S-wave propagation in jointed rock masses." Geophysics, 74(5), E205-E214.
- 36) Chen, A. T. F., & Stokoe, K. H. (1979). "Interpretation of strain-dependent modulus and damping from torsional soil tests." Report No. USGS-GD-79-002, NTIS No. PB298479, U.S. Geologic Survey, Menlo Park, CA 94025, p.46.
- 37) Chen, S. J., Zhu, W. C., Yu, Q. L., & Liu, X. G. (2016). "Characterization of anisotropy of joint surface roughness and aperture by variogram approach based on digital image processing technique." Rock Mechanics and Rock Engineering, 49(3), 855–876.
- 38) Chowdhury, I., & Dasgupta, S. P. (2008). "Dynamics of Structure and Foundation-A Unified Approach." CRC Press, Florida, United States.
- 39) Christensen, R. M. (1971). "An Introduction to Theory of Viscoelasticity." Academic Press, New York, pp. 245.
- 40) Chun, C.G., and Carlos, S.J. (2001). "Unsaturated particulate materials—particle-level studies." Journal of Geotechnical and Geoenvironmental Engineering 2001;127(1):84–96. https://doi.org/10.1061/(ASCE)1090-0241(2001)127:1(84).
- 41) CloudCompare Omnia version: 2.9.1 Stereo, compiled with MSVC 1800 and Qt 5.9.1, windows 64-bit. Retrieved from http://www.cloudcompare.org/
- 42) Clustering Views for Multi-view Stereo (CMVS) algorithms (Furukawa et al., 2010). Retrieved from https://www.di.ens.fr/cmvs

- 43) Cresswell, A., Barton, M. E., and Brown, R. (1999). "Determining the maximum density of sands by pluviation." Geotechnical Testing Journal, 22, No. 4, pp. 324–328.
- 44) Darendeli, M. B. (2001). "Development of a New Family of Normalized Modulus Reduction and Material Damping Curves." Ph.D. Dissertation, University of Texas at Austin, 362p.
- 45) Deere, D. U., and Miller, R. P. (1966). "Engineering classification and index properties for intact rock." Technical Report No: AFWL TR 65-116, University of Illinois.
- 46) Dobry, R. and Vucetic, M. (1987) State of the art report: Dynamic properties and response of soft clay deposits. Proc. Int. Symp on Geotechnical Engineering of Soft Soils, Vol. 2, 51-87.
- 47) Dobry, R. and Vucetic, M. (1987). "Dynamic Properties and Seismic Response of Soft Clay Deposits." International Symposium on Geotechnical Engineering of Soft Soils, Vol. 2, Mexico City, 51-87.
- 48) Drnevich, V. P., (1967). "Effects of strain history on the dynamic properties of sand," Ph.D. Thesis, University of Michigan, 151 pp.
- 49) Drnevich, V.P. (1978). "Resonant-Column Problems and Solutions." Dynamic Geotechnical Testing, ASTM STP 654, p 384-398.
- 50) Drnevich, V.P. and Richart, F.E., Jr. (1970). "Dynamic Prestraining of Dry Sand." Journal of Soil Mechanics and Foundations Divisions, ASCE, Vol. 96, No.SM2 pp 453-469.
- 51) Drnevich, V.P., (1985). "Recent Developments in Resonant Column Testing." Richart Commemorative Lectures, Edited by R.D. Woods, Proceedings of a Session sponsored by the Geotechnical Engineering Division in conjunction with the ASCE Convention, Detroit, Michigan, p 79-107.
- 52) Du, S. (1994). "The directive statistical evaluation of rock joint roughness coefficient (JRC)." Journal of Engineering Geology, 2(3), 62–71. (in Chinese)
- 53) Emsley, S., Olsson, O., Stenberg, L., Alheid, H.J. and Falls, S. (1997). "ZEDEX – A study of damage and disturbance from tunnel excavation by blasting and tunnel boring." SKB International Cooperation Report 97-30. Stockholm: Swedish Nuclear Fuel and Waste Management Company.

- 54) Facciorusso J. (2021). "An archive of data from resonant column and cyclic torsional shear tests performed on Italian clays." Earthquake Spectra 2021;37(1):545–62. https://doi.org/10.1177/8755293020936692.
- 55) Fan, W., & Cao, P. (2019). "A new 3D JRC calculation method of rock joint based on laboratory-scale morphology testing and its application in shear strength analysis." Bulletin of Engineering Geology and the Environment. https://doi.org/10.1007/s10064-019-01569-0
- 56) Fardin, N., Feng, Q., & Stephansson, O. (2004). "Application of a new in situ 3D laser scanner to study the scale effect on the rock joint surface roughness." International Journal of Rock Mechanics and Mining Sciences, 41(2), 329–335. https://doi.org/10.1016/S1365-1609(03)00111-4
- 57) Fardin, N., Stephansson, O., & Jing, L. (2001). "The scale dependence of rock joint surface roughness." International Journal of Rock Mechanics and Mining Sciences, 38, 659–669.
- 58) Ferrero, A. M., Migliazza, M., Roncella, R., & Rabbi, E. (2011). "Rock slopes risk assessment based on advanced geostructural survey techniques." Landslides, 8, 221–231.
- 59) Fratta, D. and Santamarina, J. C., (1996). "Wave propagation in soils: Multimode, wide band testing in waveguide device" Geotechnical Testing Journal, ASTM, 19(2): 130-140.
- 60) Fratta, D., and Santamarina, J.C. (2002). "Shear wave propagation in jointed rock: State of stress." Geotechnique, 52(7), 495-505.
- 61) Frost J.D., 1989. Studies on the Monotonic and Cyclic Behaviour of Sands. PhD. Thesis, Purdue University, Indiana.
- 62) García-Luna, R., Senent, S., & Jimenez, R. (2021). "Using telephoto lens to characterize rock surface roughness in SfM models." Rock Mechanics and Rock Engineering, 54(5), 2369–2382. https://doi.org/10.1007/s00603-021-02373-7
- 63) Guo, H., Karekal, S., Poropat, G., Soole, P., & Lambert, C. (2011). "Pit wall strength estimation with 3D imaging." CSIRO, ACARP, Brisbane.
- 64) Gye-Chun, C., Jake, D., and Carlos, S. J. (2006). "Particle Shape Effects on Packing Density, Stiffness, and Strength: Natural and Crushed Sands." Journal of Geotechnical and Geoenvironmental Engineering, 132(5), 591–602. https://doi.org/10.1061/(ASCE)1090-0241(2006)132:5(591)

- 65) Haneberg, W. C. (2007). "Directional roughness profiles from three-dimensional photogrammetric or laser scanner point clouds." 1st Canada–U.S. Rock Mechanics Symposium, Vancouver, 101–106.
- 66) Hardin, B. O. and Drnevich, V. P., (1972). "Shear Modulus and damping in soils: Design equations and curves." Journal of soil mechanics and foundations division, ASCE, Vol. 98, No. SM7, pp. 667.
- 67) Hardin, B. O., and Drnevich, V. P. (1972). "Shear Modulus and Damping in Soils: Measurement and Parameter Effects." Journal of the Soil Mechanics and Foundations Division, Proceedings of the ASCE, 98(SM6), 603-624.
- 68) Hardin, B.O. and Richart, F.E. Jr. (1963). "Elastic Wave Velocities in Granular Soils." Journal of the Soil Mechanics and Foundations Division, ASCE, 89(SM1): 33-63.
- 69) Hardin, B.O., (1965). "The Nature of Damping in Sands." Journal of the Soil Mechanics and Foundations Division, ASCE, Vol. 91, No. SM1, pp. 63-97.
- 70) Hardin, B.O., and Blandford, G.E. (1989). "Elasticity of Particulate Materials." Journal of Geotechnical Engineering, 115(6), 788–805. https://doi.org/10.1061/(ASCE)0733-9410(1989)115:6(788)
- 71) Hardin, B.O., and Richart, F.E. Jr (1963). "Elastic Wave Velocities in Granular Soils." Journal of the Soil Mechanics and Foundations Division, 89(1), 33–65. https://doi.org/10.1061/JSFEAQ.0000493
- 72) Hardin, B.O., and Scott, G.D., (1966). "Generalized Kelvin-Voigt Used in Soil Dynamics Study." Journal of the Engineering Mechanics Division, ASCE, February, 143-156.
- 73) Hasan Ali Abbas, Zainab Mohamed & Mohd Mustaqim Mohd-Nordin, (2022). "Characterization of the Body Wave Anisotropy of an Interbedded Sandstone-Shale at Multi Orientations and Interlayer Ratios." Journal of Geotechnical and Geological Engineering, Volume 40, pages 3413–3429, (2022). https://doi.org/10.1007/s10706-022-02096-8
- 74) Hotar, V., and Novotny, F., (2005). "Surface profile evaluation by fractal dimension and statistic tools." Proceeding of 11th International Congress on Fracture (ICF), Turin, Italy, pp 20–25

- 75) Hu, X. Q., & Cruden, D. M. (1992). "A portable tilting table for on-site tests of the friction angles of discontinuities in rock masses." Bulletin of the International Association of Engineering Geology, 46(1), 59–62.
- 76) Hwang, S. K. (1997). "Investigation of the Dynamic Properties of Natural Soils." Ph.D. Dissertation, the University of Texas at Austin.
- 77) Idriss, I.M., M.ASCE, Ricardo, D., & Ram, D.S. (1978). "Nonlinear behavior of soft clays during cyclic loading." Journal of the Geotechnical Engineering Division, 104(12), 1427–1447. https://doi.org/10.1061/AJGEB6.0000727
- 78) Indraratna, B., and Haque, A. (2000). "Experimental and numerical modeling of shear behavior of rock joints". Proc. GeoEng 2000, An international conference of Geotechnical & Geological Engineering, Pennsylvania, vol. 1,
- 79) IS: 1201-1978. "Indian standard methods for testing tar and bituminous materials."
- 80) Isenhower, W.M., (1980). "Torsional Simple Shear/Resonant Column Properties of San Francisco Bay Mud." MS. Thesis, The University of Texas at Austin
- 81) Ishihara, K. (1996). "Soil Behavior in Earthquake Geotechnics". Oxford University Press Inc., New York.
- 82) Ismail Abd Rahim, (2018). "Sample type of tilt testing and basic friction angle value for the Ceocker Formation's fine sandstone of Sabah, Malaysia." ASM Science Journal, 11, SANREM, 215–223.
- 83) ISO 37:2005(E). "Rubber, vulcanized, or thermoplastic- Determination of tensile stress-strain properties." Fourth edition 2005-07-15. International standard
- 84) ISRM. (1978). "International Society for Rock Mechanics Commission on Standardization of Laboratory and Field tests." International Journal of Rock Mechanics and Mining Sciences & Geomechanics Abstract, 15, 319-368.
- 85) Iwasaki, T., & Tatsuoka, F. (1977). "Effects of grain size and grading on dynamic shear moduli of sands." Soils and Foundations., 17 No. 3, 19–35.

- 86) Jafarzadeh, F. Sadeghi, H. (2011). "Experimental study on dynamic properties of sand with emphasis on the degree of saturation." Soil Dynamic and Earthquake Engineering 32 (2012) 26 41.
- 87) Jiang, Y., Li, B., Tanabashi, Y., (2006). "Estimating the relation between surface roughness and mechanical properties of rock joints." International Journal of Rock Mechanics and Mining Sciences, 43:837–846.
- 88) Johnston, D.H. (1981). "Seismic Wave Attenuation." Geophysics Reprint Series, No. 2. Society of Exploration Geophysicists. Tulsa, Oklahoma, p. 123-135.
- 89) Jones, T.D. (1986). "Pore Fluids and Frequency-Dependent Wave Propagation in Rocks." Geophysics, v. 51, p. 1939-1953.
- 90) Kahraman, S., (2002). "The effects of fracture roughness on p-wave velocity." Engineering Geology, 63:347–350.
- 91) Kenneth, H. W., & E, W. H. (1968). "Stress History Effects on Dynamic Modulus of Clay." Journal of the Soil Mechanics and Foundations Division, 94(2), 371–389. https://doi.org/10.1061/JSFEAQ.0001101
- 92) Khan, Z. H., Cascante, G., and El Naggar, M.H. (2011). "Frequency dependent dynamic properties from resonant column and cyclic triaxial tests." Journal of the Franklin Institute, 348, 2011, pp:1363 1376.
- 93) Khan, Z. H., Cascante, G., and El Naggar, M.H., (2008a). "Linearity of the first torsional mode of vibration and base fixidity in resonant column." ASTM, Geotechnical Testing Journal, 31(1): 587 606.
- 94) Khan, Z. H., Cascante, G., El Naggar, M.H., and Lai, C. (2008b). "Measurement of frequency-dependent dynamic properties of soils using the Resonant-Column device." Journal of Geotechnical and Geoenvironmental Engineering, ASCE, 134(9): 1319-1326.
- 95) Kim, D.S., (1991). "Deformational Characteristics of Soils at Small to Intermediate Strains from Cyclic Tests." PhD. Thesis, The University of Texas at Austin.
- 96) Kim, J.W., Chong, S.H., Cho, G.C., (2018). "Experimental Characterization of Stress- and Strain-Dependent Stiffness in Grouted Rock Masses." Materials (Basel). 2018 Mar 29;11(4):524. doi: 10.3390/ma11040524. PMID: 29596371; PMCID: PMC5951370.

- 97) Kokusho, T., Yoshida, Y., & Esashi, Y. (1982). "Dynamic Properties of Soft Clay for Wide Strain Range." Soils and Foundations, 22(4), 1–18. https://doi.org/10.3208/SANDF1972.22.4_1
- 98) Kouretzis, G. P., Karamitros, D. K., & Sloan, S. W. (2015). "Analysis of buried pipelines subjected to ground surface settlement and heave." Canadian Geotechnical Journal, 52(8), 1058–1071. https://doi.org/10.1139/cgj-2014-0332
- 99) Kramer, S. L. (1996). "Geotechnical Earthquake Engineering." Prentice Hall, New Jersey.
- 100) Kulatilake, P. H. S. W., Balasingam, P., Park, J., & Morgan, R. (2006).
 "Natural rock joint roughness quantification through fractal techniques."
 Geotechnical and Geological Engineering, 24(5), 1181.
 https://doi.org/10.1007/s10706-005-1219-6
- 101) Kumar, J., and Clayton, C.R.I. (2007). "Effect of sample torsional stiffness on resonant column results". Canadian Geotechnical Journal, 44, 221-230.
- 102) Kumar, J., and Madhusudhan, B.N. (2010). "Effect of relative density and confining pressure on poisson ratio from bender and extender elements tests." Géotechnique, 60(7), 561-567.
- 103) Lai, C. G., Pallara, O., Lo Presti, D. C. and Turco, E. (2001). "Low-strain stiffness and Material Damping Ratio Coupling in Soils." Advanced Laboratory Stress-strain Testing of Geomaterials, Tatsuoka, T., Shibuya, S., and Kuwano, R. Eds, Balkema, Lisse, pp. 265-274.
- 104) Lama, R.D. and Vutucuri, V.S. (1978). "Handbook on mechanical properties of rocks-testing techniques and results." - Volume II. 1st ed. Clausthal, Germany: Trans Tech Publications.
- 105) Lamas, L.N. (1996). "An experimental and analytical study of the roughness of granite joints." In: Barla G (ed) Proc of the Eurock'96. Balkema, Rotterdam, p 117
- 106) Larsson, K. (2004). Mining Induced Seismicity in Sweden. Licentiate thesis 2004:80, Luleå University of Technology (Ltu), Luleå, Sweden.
- 107) Lee, Y.H., Carr, J.R., Barr, D.J., and Haas, C.J., (1990). "The fractal dimension as a measure of the roughness of rock discontinuity profiles." International Journal of Rock Mechanics and Mining Sciences, 27(6):453–464. https://doi.org/10.1016/0148-9062(90) 90998-h

- 108) Li, J.C., and Ma, G.W. (2009). "Analysis of blast wave interaction with a rock joint." Rock Mechanics and Rock Engineering, 43(6):777–787.
- 109) Li, N., Chen, W., Zhang, P., & Swoboda, G. (2001). "The mechanical properties and a fatigue-damage model for jointed rock masses subjected to dynamic cyclical loading." International Journal of Rock Mechanics and Mining Sciences, 38(7), 1071–1079. https://doi.org/10.1016/S1365-1609(01)00058-2
- 110) Li, Y., & Huang, R. (2015). "Relationship between joint roughness coefficient and fractal dimension of rock fracture surfaces." International Journal of Rock Mechanics and Mining Sciences, 75, 15–22.
- 111) Li, Y., and Zhu, Z. (2012). "Study on the velocity of P-waves across a single joint based on fractal and damage theory." Engineering Geology, 151:82–88.
- 112) Lim, H.M., and Misran, M. (2016). "Colloidal and rheological properties of natural rubber latex concentrate." Applied rheology, Vol 26(1). http://doi.org/10.3933/ApplRheol-26-15659
- 113) Lo Presti, D.C.F., and Pallara, O. (1997). "Damping Ratio of Soils from Laboratory and In-situ Tests", Proceedings, 14th International Conference on Soil Mechanics and Foundation Engineering, Hamburg, Germany, pp. 6-12
- 114) Lo Presti, D.C.F., Jamiolkowski, M., Pallara, O., and Cavallaro, A. (1996). "Rate and Creep Effect on the Stiffness of Soils," Proc. Conference on Measuring and Modeling Time-Dependent Soil Behavior, Held in Conjunction with the ASCE National Convention, Washington D.C., USA.
- 115) Lodde, P.F., (1982). "Dynamic Response of San Francisco Bay Mud." M.S. Thesis, The University of Texas at Austin.
- 116) Lowe, D. G. (2004). "Distinctive image features from scale-invariant key points." International Journal of Computer Vision, 60, 91–110.
- 117) Maerz, N.H., Franklin, J.A., and Bennett, C.P., (1990). "Joint roughness measurement using shadow profilometry." International Journal of Rock Mechanics and Mining Sciences, 27(5):329–343. https://doi.org/10.1016/0148-9062(90) 92708-m

- 118) Mahinroosta, R., & Oshtaghi, V., (2021). "The effect of particle shape on the deformation and stress reduction of a gravel soil due to wetting." Scientific Reports, 11(1). https://doi.org/10.1038/s41598-021-95731-y
- 119) Malagnini, L., 1996, "Velocity and Attenuation Structure of Very Shallow Soils: Evidence for Frequency Dependent Q", Bulletin of Seismological Society of America, 86(5): 1471-1486.
- 120) Malmgren, L., Saiang, D., Töyrä, J. and Bodare, A. (2007). "The excavation disturbed zone (EDZ) at Kiirunavaara mine, Sweden by seismic measurements." Journal of Applied Geophysics, 61(1), 1-15.
- 121) Mandelbrot, B. B. (1977). "Fractals--Form, Chance and Dimension." Freeman, San Francisco.
- 122) Masing, G. (1926) "Eigenspannungen und Verfestgung Beim Masing," Proceedings, Second International Congress of Applied Mechanics, pp.332-335.
- 123) Meng, J., & Rix, G. J. (2003). "Reduction of equipment-generated damping in resonant column measurements." Geotechnique, Vol. 53(5), 503-512.
- 124) Mohd-Nordin, M. M., Song, K.-I., Cho, G.-C., & Mohamed, Z. (2014). "Long-wavelength elastic wave propagation across naturally fractured rock masses." Rock Mechanics and Rock Engineering, 47(2):561-573. doi: 10.1007/S00603-013-0448-X
- 125) Murphy, W.F. (1982). "Effects of Partial Water Saturation on Attenuation in Massilon Sandstone and Vycor Porous Glass." Journal of the Acoustical Society of America 71(6), June, p. 1458-1467.
- 126) Murphy, W.F., Winkler, K.W. and Kleinberg, R.L., (1984). "Frame Modulus Reduction in Sedimentary Rocks: The Effect of Adsorption on Grain Contacts." Geophysical Research Letters. v. 1, p. 805-808.
- 127) Myers, N. O. (1962). "Characterization of surface roughness." Wear, 5, 182–189.
- 128) Ni, S.H. (1987). "Dynamic properties of sand under true triaxial stress states from resonant column/torsional shear tests." Ph.D. Dissertation, The University of Texas, Austin.
- 129) Nilsson, M., & Wulkan, F. (2011). "Determination of joint shear strength using photogrammetry." Luleå University of Technology, Luleå, Sweden.

- 130) Paixão, A., Muralha, J., Resende, R., & Fortunato, E. (2022). "Close-range photogrammetry for 3D rock joint roughness evaluation." Rock Mechanics and Rock Engineering. https://doi.org/10.1007/s00603-022-02789-9
- 131) Park, D., & Kishida, T. (2019). "Shear modulus reduction and damping ratio curves for earth core materials of dams." Canadian Geotechnical Journal, 56(1), 14–22. https://doi.org/10.1139/cgj-2017-0529
- 132) Paterson, M.S. (1978). "Experimental rock deformation the brittle field." Berlin Heidenberg: Springer-Verlag.
- 133) Payan, M., Senetakis, K., Khoshghalb, A., & Khalili, N. (2016). "Influence of particle shape on small-strain damping ratio of dry sands." Géotechnique, 66(7), 610–616. https://doi.org/10.1680/jgeot.15.T.035
- 134) Puri, N., Jain, A., Nikitas, G., Dammala, P. K., & Bhattacharya, S. (2020). "Dynamic soil properties and seismic ground response analysis for North Indian seismic belt subjected to the great Himalayan earthquakes." Natural Hazards, 103(1), 447–478. https://doi.org/10.1007/s11069-020-03995-w
- 135) Pyrak-Nolte, L.J., Myer, L.R. and Cook, N.G.W. (1990). "Anisotropy in seismic velocities and amplitudes from multiple parallel fractures." Journal of Geophysical Research, 95(B7), 11345-11358.
- 136) R. M. Rached, A. V. Garcia, and J. C. Santamarina, (2022). "Long-Wavelength Propagation in Fractured Rock Masses (3D Stress Field)." Journal of Geophysical Research: Solid EarthVolume 127, Issue 9 e2022JB024907
- 137) Ramamurthy, T., & Arora, V. K. (1994). "Strength predictions for jointed rocks in confined and unconfined states." International Journal of Rock Mechanics and Mining Sciences & Geomechanics Abstracts, 31(1), 9–22. https://doi.org/10.1016/0148-9062(94)92311-6
- 138) Ramana, Y.V. and Venkatanarayana, B. (1973). "Laboratory Studies on Kolar Rocks." International Journal of Rock Mechanics and Mining Science & Geomechanical Abstract, 10, 465-480.
- 139) Ramberg, W. and Osgood, W.R. (1943). "Description of stress-strain curves by three parameters." Technical Note no. 2, National Advisory Committee for Aeronautics (NACA). Washington, July 1943.
- 140) Ray, S. K., Sarkar, M., & Singh, T. N. (1999). "Effect of cyclic loading and strain rate on the mechanical behaviour of sandstone." International Journal

- of Rock Mechanics and Mining Sciences, 36(4), 543–549. https://doi.org/10.1016/S0148-9062(99)00016-9
- 141) Read, B.E. and Dean, G.D. (1978). "The determination of dynamic properties of polymers and composites." John Wiley and Sons, New York.
- 142) Read, W. T. J. 1950. "Stress Analysis for Compressible Viscoelastic Materials", Journal of Applied Physics, 21, 671-674.
- 143) Richart F. E., Hall J. R. and Woods R. D., (1970). "Vibrations of soils and foundations." Prentice Hall, Englewood Cliffs, pp. 414.
- 144) Rix, G. J., and Meng, J. (2005). "A non-resonance method for measuring dynamic soil properties." Geotechnical Testing Journal, 28(1), pp.1-8.
- 145) Roesler, S.K. (1979). "Anisotropic Shear Modulus due to Stress Anisotropy." Journal of the Geotechnical Engineering Division, 105(7), 871–880. https://doi.org/10.1061/AJGEB6.0000835
- 146) Rohilla, S., & Sebastian, R., (2023). "Determination of joint roughness coefficient using a cost-effective photogrammetry technique." Bulletin of engineering geology and the environment, 82(4). https://doi.org/10.1007/s10064-023-03135-1
- 147) Saada, A. S., (1985). "On Cyclic Testing with Thin Long Hollow Cylinders," Advances in the Art of Testing Soils Under Cyclic Conditions, ASTM STP, pp 1-28.
- 148) Salvini, R., Vanneschi, C., Coggan, J. S., & Mastrorocco, G. (2020). "Evaluation of the use of UAV photogrammetry for rock discontinuity roughness characterization." Rock Mechanics and Rock Engineering, 53(8), 3699–3720. https://doi.org/10.1007/s00603-020-02130-2
- 149) Schoenberg, M. and Sayers, M.C. (1995). "Seismic anisotropy of fractured rock." Geophysics, Vol 60(1), pp- 19-307. https://doi.org/10.1190/1.1443748
- 150) Sebastian, R., & Sitharam, T. G. (2015). "Long Wavelength Propagation of Elastic Waves Across Frictional and Filled Rock Joints with Different Orientations: Experimental Results." Journal of Geotechnical and Geological Engineering, 33(4), 923–934. https://doi.org/10.1007/s10706-015-9874-8
- 151) Sebastian, R., & Sitharam, T. G. (2016). "Long-wavelength propagation of waves in jointed rocks study using resonant column experiments and

- model material." Geomechanics and Geoengineering, 11(4), 281–296. https://doi.org/10.1080/17486025.2016.1139753
- 152) Sebastian, R., & Sitharam, T. G. (2018). "Resonant Column Tests and Nonlinear Elasticity in Simulated Rocks." Rock Mechanics and Rock Engineering, 51(1), 155–172. https://doi.org/10.1007/s00603-017-1308-x
- 153) Seed, H. B., Idriss, I. M., Shannon, Wilson, & Agbabian-Jacobsen Associates. (1970). "Soil moduli and damping factors for dynamic response analyses." University of California Berkeley Structural Engineers and Mechanics, NTIS No. PB197869, California University, Berkeley, [Report No. EERC70-10], p.48.
- 154) Seed, H.B., Wong, R.T., Idriss, I.M., Tokimatsu, K. (1986). "Moduli and damping factors for dynamic analyses of cohesionless soil." Journal of Geotechnical Engineering, 112(11), pp.1016–1032
- 155) Senetakis, K., Anastasiadis, A., & Pitilakis, K. (2012). "The small-strain shear modulus and damping ratio of quartz and volcanic sands." Geotechnical Testing Journal, 35(6), pp. 964–980. https://doi.org/10.1520/GTJ20120073
- 156) Senetakis, K., Anastasiadis, A., & Pitilakis, K. (2015). "A comparison of material damping measurements in resonant column using the steady-state and free-vibration decay methods." Soil Dynamics and Earthquake Engineering, 74, 10–13. https://doi.org/10.1016/J.SOILDYN.2015.03.009
- 157) Shibuya, S., Mitachi, T., Fukuda, F., and Degoshi, T. (1995). "Strain-Rate Effects on Shear Modulus and Damping of Normally Consolidated Clay." Geotechnical Testing Journal, 18(3), 365-375.
- 158) Shiming W, H GD, Richart FE. Capillary effects on dynamic modulus of sands and silts. Journal of Geotechnical Engineering 1984;110(9):1188–203. https://doi.org/10.1061/(ASCE)0733-9410(1984)110:9(1188)
- 159) Shirono, T., & Kulatilake, P. H. S. W. (1997). "Accuracy of the spectral method in estimating fractal/spectral parameters for self-affine roughness profiles." International Journal of Rock Mechanics and Mining Sciences, 34(5), 789–804.
- 160) Silver, M. L., & Seed, H. B. (1971). "Deformation characteristics of sands under cyclic loading." Journal of the Soil Mechanics and Foundations Division, ASCE, 97(8), 1081-1098.

- 161) Sireteanu, T., Mitu, A.M., Giuclea, M., Solomon, O., and Stefanov, D. (2014). "Analytical method for fitting the Ramberg-Osgood model to given hysteresis loops." Proceedings of the Romanian Academy-A, 15(1): 35-42.
- 162) SS-ISO 14837-1. (2005). Mechanical vibration Ground-borne noise and vibration arising from rail systems Part 1: General guidance.
- 163) SS-ISO 2631-1. (1997). Vibration and shock Evaluation of human exposure to wholebody vibration Part 1: General requirements.
- 164) Stokoe, K., and Isenhower M., (1980). "Dynamic Properties of Offshore Silty Samples." Proceedings of the 12th Annual Offshore Technology Conference. Houston, Texas.
- 165) Stoll, Robert D., (1978). "Damping in Saturated Soil." Proc. Specialty Conf. on Earthquake Engineering and Soil Dynamics, ASCE, New York, p. 969-975.
- 166) Stoll, Robert D., (1979). "Experimental Studies of Attenuation in Sediments." Acoustical Society of America 66(4), October, p. 1152-1160.
- 167) T. Ueng, & Chen, J.C. (1992). "Computational Procedures for Determining Parameters in Ramberg-Osgood Elastoplastic Model Based on Modulus and Damping Versus Strain." NASA STI/Recon Technical Report N, 94:10306U. http://doi.org/10.2172/6496483.
- 168) Tatone, B. S. A., & Grasselli, G. (2010). "A new 2D discontinuity roughness parameter and its correlation with JRC." International Journal of Rock Mechanics and Mining Sciences, 47, 1391–1400.
- 169) Tse, R., & Cruden, D. M., (1979). "Estimating joint roughness coefficients." International journal of rock mechanics and mining sciences & geomechanics abstracts, 16(5). https://doi.org/10.1016/0148-9062(79)90241-9
- 170) Tsuchida, H. (1970). "Prediction and countermeasure against liquefaction in sand deposits." Abstract of the Seminar of the Port and Harbour Research Institute, Ministry of Transport, Yokosuka, Japan, 3.1-3.33 (in Japanese)
- 171) Turk, N., Greig, M.J., Dearman, W.R., Amin, F.F. (1987) "Characterization of joint surfaces by fractal dimension." Proceedings of the 28th US Rock Mechanics Symposium, Tucson, pp 1223–1236.

- 172) Vaid, Y. P., & Negussey, D. (1984). "Relative Density of Pluviated Sand Samples." Soils and Foundations, 24(2), 101–105. https://doi.org/10.3208/SANDF1972.24.2 101
- 173) Varma, M., Maji, V. B., and Boominathan, A. (2021). "Influence of rock joints on longitudinal wave velocity using experimental and numerical techniques." International Journal of Rock Mechanics and Mining Sciences, 141:104699-. doi: 10.1016/J.IJRMMS.2021.104699
- 174) VisualSFM Version 0.5.22 (2014b) NVidia CUDA, Windows 64-bit (Wu et al. 2011; Wu 2013). http://ccwu.me/vsfm
- 175) Vucetic, M. (1994). "Cyclic Threshold Shear Strains in Soils." Journal of Geotechnical Engineering, ASCE, 120(12), 2208-2228.
- 176) Vucetic, M., and Dobry, R. (1991). "Effect of Soil Plasticity on Cyclic Response." Journal of Geotechnical Engineering, ASCE, 117(1): 89-107
- 177) Wang, C., Wang, L., & Karakus, M. (2019). "A new spectral analysis method for determining the joint roughness coefficient of rock joints." International Journal of Rock Mechanics and Mining Sciences, 113, 72–82.
- 178) Wang, Y.H., Cascante, G., and Santamarina, J.C. (2003). "Resonant column testing: The inherent counter EMF effect." Geotechnical Testing Journal, 26 (3), 342-352.
- 179) Watanabe, T. and Sassa, K. (1996). Seismic attenuation tomography and its application to rock mass evaluation. Inter-national Journal of Rock Mechanics and Mining Science & Geomechanical Abstract, 33(5), 467-477.
- 180) Westoby, M. J., Brasington, J., Glasser, N. F., Hambrey, M. J., & Reynolds, J. M. (2012). "Structure-from-Motion photogrammetry: A low-cost, effective tool for geoscience applications." Geomorphology, 179, 300–314. https://doi.org/10.1016/j.geomorph.2012.08.021
- 181) White, J.E., (1975). "Computed Seismic Speeds and Attenuation in Rocks with Partial Gas Saturation." Geophysics, v. 40, p. 224-232.
- 182) Wilson, S.D., and Dietrich, R.J., (1960). "Effect of Consolidation Pressure on Elastic and Strength Properties of Clay." Proceedings of the ASCE, Soil Mechanics and Foundations Division, Research Conference on Shear Strength of Cohesive Soils, Boulder, CO.
- 183) Winkler, K., and Nur, A., (1982). "Seismic Attenuation: Effects of Pore Fluids and Frictional Sliding." Geophysics. v. 47, p. 1-15.

- 184) Winkler, K., Nur, A., and Gladwin, M. (1979). "Friction and seismic attenuation in rocks." Nature, 227: 528-531.
- 185) Woo, I.K., Fleurisson, J.A., and Park, H.J. (2010). "Influence of weathering on shear strength of joints in a porphyritic granite rock mass in Jechon area, South Korea." Geosciences Journal 14(3):289–299
- 186) Woods, R. D. (1978). "Measurement of dynamic soil properties." Proc., ASCE Geotechnical Engineering Division Specialty Conference, Earthquake Engineering and Soil Dynamics, Vol. I, ASCE, New York, 91-178.
- 187) Wu, C., Wu, C. (2011). "VisualSFM: Version 0.5.22 for NVidia CUDA, windows 64-bit." Retrieved from http://ccwu.me/vsfm
- 188) Wu, Y.X., Liu, Q.S., and Liu, X.Y. (2011). "Study of relationship between joint roughness coefficient and statistical parameters." Chin J Rock Mech Eng 30:2593–2598 (in Chinese)
- 189) Xiao, J. Q., Ding, D. X., Xu, G., & Jiang, F. L. (2008). "Waveform effect on quasi-dynamic loading condition and the mechanical properties of brittle materials." International Journal of Rock Mechanics and Mining Sciences, 45(4), 621–626. https://doi.org/10.1016/j.ijrmms.2007.07.025
- 190) Xie, H.P., and Pariseau, W.G. (1994). "Fractal estimation of rock joint roughness coefficient." Sci China 24(5):524–530
- 191) Youash, Y.Y. (1970). Dynamical physical properties of rock: part, II, Experimental Results. In: Proceeding of the Second Congress of the International Society of Rock Mechanics, Belgrade, Yugoslavia, September 21-26 1970. Vol. 1.
- 192) Yu, X., and Vayssade, B. (1991). "Joint profiles and their roughness parameters." International Journal of Rock Mechanics and Mining Sciences 28(4):333–336. https://doi.org/10.1016/0148-9062(91)90182-1
- 193) Zhang, G., Karakus, M., Tang, H., Ge, Y., & Zhang, L. (2014). "A new method estimating the 2D joint roughness coefficient for discontinuity surfaces in rock masses." International Journal of Rock Mechanics and Mining Sciences, 72, 191–198.
- 194) Zhao, J., Zhao, X.B. and Cai, J.G. (2006). "A further study of P-wave attenuation across parallel fractures with linear deformational behaviour." Inter-national Journal of Rock Mechanics and Mining Science, 43, 776-788.

- 195) Zhao, L., Huang, D., Chen, J., Wang, X., Luo, W., Zhu, Z., Li, D., & Shi, Z. (2020). "A practical photogrammetric workflow in the field of the construction of a 3D rock joint surface database." Engineering Geology, 279, 105878. https://doi.org/10.1016/j.enggeo.2020.105878
- 196) Zhou, C.B., and Xiong, W.L. (1996). "Relation between joint roughness coefficient and fractal dimension." Journal of Wuhan University of Hydraulic and Electrical Engineering 29(5):1195–1197

List of Publications

Journal Publications:

- Sakshi Rohilla and Resmi Sebastian. (2023) "Resonant column and cyclic torsional shear tests on Sutlej River sand subjected to the seismicity of Himalayan and Shivalik hill ranges: A case study." Soil Dynamics and Earthquake Engineering (SDEE), 166(2023) 107766, doi.org/10.1016/j.soildyn.2023.107766
- 2. **Sakshi Rohilla** and Resmi Sebastian. (2023) "Determination of joint roughness coefficient using a cost-effective photogrammetry technique." *Bulletin of Engineering Geology and the Environment (BOEG)*, (2023) 82:125, doi.org/10.1007/s10064-023-03135-1
- 3. Sakshi Rohilla and Resmi Sebastian. "Determination of frequency-dependent dynamic properties of rocks using the non-resonance method." *International Journal of Geomechanics (GMENG)*, 2024, 24(8): 04024149, doi.org/10.1061/IJGNAI/GMENG-9752
- **4. Sakshi Rohilla**, Kallol Saha, and Resmi Sebastian. "Influence of natural rubber latex thickness on the behaviour of jointed rocks during shear wave propagation." *International Journal of Geomechanics (GMENG)*, 2024, 24(11): 04024254, doi:10.1061/IJGNAI/GMENG-9567
- 5. Sakshi Rohilla and Resmi Sebastian. "Dynamic characteristics of jointed rock masses with natural rubber latex dampening layer under seismic and explosive loading conditions." *International Journal of Geomechanics for Energy and the Environment*, Under Review
- 6. Sakshi Rohilla, Resmi Sebastian, and Aaditya Bhamidipati. "Dynamic properties of jointed rocks under diverse loading conditions: Insights from experimental and predictive modelling." *Tunnelling and Underground Space Technology incorporating Trenchless Technology Research*, Under Review

Conference Publications:

 Sakshi Rohilla and Resmi Sebastian. (2023) "Study of stress-dependent dynamic properties of jointed rocks using resonant column apparatus." In: Proceedings of the ISRM 15th International Congress on Rock Mechanics and Rock Engineering & 72nd Geomechanics Colloquium – Challenges in Rock

- Mechanics and Rock Engineering, Schubert, W. & Kluckner, A. (eds), Salzburg, Austria, October 9-14, 2023. Austrian Society for Geomechanics: Salzburg. pp.2308-2313.
- Sakshi Rohilla and Resmi Sebastian. (2022) "Influence of density on the dynamic properties of intact rock masses." Indian Geotechnical Conference 2022, GEOLEAP- Geotechnics: Learning, Evaluation, Analysis and Practice 15-17 December 2022, Kochi.